Studies of Infrared Response in Indium Antimonide under Hydrostatic Pressure

A thesis submitted by
David Michael Marks
to the University of St. Andrews
for the degree of
Doctor of Philosophy
September, 1993

Acknowledgments

I would like to thank the following people, whose help and support in one way or another shaped this dissertation:

First and foremost, my supervisor, Prof. R. A. Stradling, who has tenaciously goaded me forward over the years, and whose trained eye and keen understanding of physics have helped guide my efforts;

Malcolm H. Dunn, my St. Andrean advisor, for moral support and encouragement;

Zbyszek Wasilewski, friend and enthusiastic scientific collaborator, for many very useful discussions of physics and more; and Drs. Angus MacKinnon and Krzysztof Pastor for insights into mechanisms of narrowing.

For making it all so much pleasanter and smoother, thanks to postgraduate students Antony M. Thorley, Steve Najda, Chris J. Armistead, David A. Cowan, Carol Trager-Cowan, Stuart N. Holmes, Durig E. Lewis, Dr. Eleftherios Skuras ($\kappa\alpha\lambda\grave{\eta}\ \tau\acute{\upsilon}\chi\eta\ \kappa\alpha\iota\ \kappa\alpha\lambda\grave{\eta}\ \grave{\alpha}\nu\tau\acute{\alpha}\mu\omega\sigma\eta$!) and many others;

Bob Mitchell at St. Andrews and Derek Podger at Imperial College for technical expertise and assistance; Dougie W. Irons for endless attempts at thankless tasks and much good humor shared; and a host of other technical and shop staff;

In both Poland and the U. K., Paweł Kujawinsky, Dr. Tadeusz Suzki, Prof. Sylwester Porowski, Czesław Skierbiszewski and Przemek Wisniewski, for much help with Hall measurements and their interpretation, and great hospitality;

Dimitri Vvedensky, Mark Wilby and Kris Hampel of the IC Solid State Theory Department for informative discussions on physics, for assistance with *Mathematica* and other computer problems, and for access to their facilities;

Malcolm Clarke, Paul Jarvis, Brendon Molloy and Tom Weil of the Imperial College Computer Centre and Dan Moore of the Department of Mathematics for help with the TEX and PostScript implementations used to produce this thesis, and Phil Taylor of Bedford College for assistance with Metafont;

Mohan of the Mountains, for opening so many doors;

and finally, thanks to my friends, especially Rob and Clarissa Kennedy, and numerous relatives, for their support and encouragement throughout a long, long expatriation.

—DMM

DECLARATION

I, David M. Marks, hereby certify that this thesis has been composed by myself, that it is a record of my own work, and that it has not been accepted in partial or complete fulfilment of any other degree or professional qualification.

. . . .

David M. Marks Date

I was admitted to the Faculty of Science of the University of St. Andrews under Ordinance General No. 12 in October, 1982, and as a candidate for the degree of Ph.D. in September, 1983.

. . . .

David M. Marks Date

I hereby certify that the candidate has fulfilled the conditions of the Resolution and Regulations appropriate to the Degree of Ph.D.

. . . .

R. A. Stradling Date

In submitting this thesis to the University of St. Andrews, I understand that I am giving permission for it to be made available for use in accordance with the regulations of the University Library for the time being in force, subject to any copyright vested in the work not being affected thereby. I also understand that the title and abstract will be published, and that a copy of the work may be made and supplied to any *bona fide* library or research worker.

Abstract

High-pressure transport measurements on n-type bulk indium antimonide by Porowski *et al.* revealed the presence of, ostensibly, a single deep donor (possibly oxygen) that manifested itself as both a "substitutional" donor (i.e., showing no large lattice relaxation, or LLR) and a metastable donor. The electronic properties of the sample could be radically altered by varying the pressure at which the metastable sites were frozen out ("pressure-treatment").

Further investigation by Stradling and Wasilewski *et al.* using FIR spectroscopy proved that a single donor species ("A") was responsible for states apparently associated with the Γ, X or L minima.

Paralleling this work have been lengthy investigations by Mooney *et al.* into the nature of deep donors in GaAs and AlGaAs exhibiting persistent photoconductivity (PPC), the so-called DX centers. Recently, work by Dmochowski *et al.* has demonstrated the same phenomenon in GaAs and AlGaAs as in InSb, i.e., the manifestation of variously associated impurity states from a single donor.

For AlGaAs, the very successful negative-U model was proposed by Chadi and Chang to explain LLR, though this model vies with the phenomenon of correlation as an explanation for the observed mobility trends in AlGaAs.

The current thesis attempts to shed some light on the question of whether the negative-U model applies to indium antimonide. Hall measurements of high mobility samples were conducted over a range of pressures and with the sample pressure-treated. An extensive mathematical model (due to Szymańska and Dietl) was invoked to tie mobility measurements to impurity concentrations and polar optical phonon population.

Narrowing of the cyclotron resonance peaks with the application of hydrostatic pressure, over only a very narrow range of pressures, had been observed previously by Wasilewski. One of the samples studied in the present work, on the other hand, exhibited this narrowing over the entire range of pressures applied. This made possible a comprehensive study of cyclotron resonance linewidths as a function of pressure. It was hoped that analysis of these data could elucidate scattering mechanisms involved in the sample. It was found that the narrowing was greatest in the case of long-wavelength excitation (i.e., low magnetic fields), and virtually unobservable for the short wavelengths, in contrast to the results of Wasilewski. Correlation of impurity ions is

apparently responsible for the narrowing.

Cyclotron resonance was also recorded with the sample in the pressure-treated state.

Samples of indium antimonide were also optically investigated in the mostly intrinsic near-infrared regime (1–10 μ). It was discovered that the application of hydrostatic pressure enhanced the responsivity for one of the samples by at least two orders of magnitude over that at ambient pressure, and that a portion of this increase is due to an increased electron lifetime, ostensibly due to hole-trapping centers. A near-infrared spectrum was also obtained for a sample in the pressure-treated state. It was found that a high energy ($\sim$300 meV) absorption occurs, perhaps indicating the vertical (optical) separation of the neutral relaxed impurity state and the ionized state.

Table of Contents

List of Figures

List of Symbols

Below is the list of mathematical and physical symbols, and their denotations, as used in this thesis. Generally, characters set in the math-italic font (e.g., A, b) are scalar quantities or the magnitudes of vector quantities, while characters set in bold-oblique font (e.g., $\boldsymbol{A}$, $\boldsymbol{k}$) denote vectors, and those in bold ($\mathbf{M}$), tensors. For specific values of constants germane to indium antimonide, see Table 1.1.

a	Contribution to conduction band wavefunction; screening length in nonparabolic band
$_{\mathrm{a}}$ (subscript)	Ambipolar quantity
a_{B}	Bohr radius
a_i	Scattering length or distance of interaction
$\boldsymbol{a_q}$	Unit polarization vector
a_0	Lattice constant
a^*	Bohr radius of defect
A	Area of detector; half electron energy width of disordered crystalline solids
A'	Higher band parameter (InSb)
$\boldsymbol{A}$	Magnetic vector potential
$\mathcal{A}$	Laser cavity loss from absorption at end mirrors
$\mathcal{A}_{ij}$	Einstein coefficient for spontaneous emission between states i and j
b	Ratio of carrier mobilities, $\mu_{\mathrm{e}}/\mu_{\mathrm{h}}$; contribution to conduction band wavefunction; impact parameter
$_B$ (subscript)	Magnetic field-associated quantity
$B, \boldsymbol{B}$	Magnetic field, magnetic induction
B_{c}	Cyclotron resonance magnetic field value
ΔB	Cyclotron resonance linewidth (FWHM)
$\Delta B_{1/2}$	Cyclotron resonance linewidth (HWHM)
$\mathcal{B}_{ij}$	Einstein coefficient of stimulated emission between states i and j
c	Contribution to conduction band wavefunction; speed of light (esu)
$_{\mathrm{c}}$ (subscript)	Cyclotron resonance-associated quantity
c.c.	Complex conjugate
d	Ionic separation; grating line separation; diameter of laser resonator
D	Optical deformation potential constant
$\boldsymbol{D}_i$	Electric displacement vector of a crystal
$\mathfrak{D}$	Interband optical mode scattering operator
$\mathfrak{D}$ (+ subscript)	Diffusion length

$\mathfrak{D}$	Optical deformation potential constant
D^*	Spectral detectivity
e	Base of natural logarithms
e	Charge of proton (esu); electron itself
$\boldsymbol{e}$, e_{ikl}	Piezoelectric constant tensor, elements
e (subscript)	Electron-associated quantity
e_{pz}	Piezoelectric constant
e^*	Effective charge of polar atom
E	Absolute energy of the electron
E'	Energy relative to valence band maximum
E_{g}	Energy-gap
$E_{\mathrm{g};0}$	Energy-gap at ambient pressure
E_{e}	Impurity center electron emission energy
E_{P}	Impurity center photoionization energy
E_0	Donor binding energy
E_∞	Impurity center capture activation energy
$\boldsymbol{E}$	Electric field vector
$\mathcal{E}_j$	Electric field component
f (subscript)	Final scattering state
f	Fermi-Dirac distribution function; scattering factor; optical modulation frequency; focal length
Δf	Bandwidth
f_0	Equilibrium Fermi-Dirac distribution function
f_0'	Energy derivative of equilibrium Fermi-Dirac distribution function
F (subscript)	Fermi level-associated quantity
$F(\lambda, k_{\mathrm{F}})$	II scattering cross-section factor for mobility
$F(\boldsymbol{r})$	Hydrogen-like envelope function
$F_i(\eta)$	Fermi integral of order i
g	Landé g-factor; degeneracy
g^*	Effective Landé g-factor
g_{L}	Coupling constant for long-range (Coulombic) polar-phonon coupling
g_{S}	Coupling constant for short-range elastic deformation potential
g_0	Landé g-factor at Γ-minimum
$g(\epsilon)$	Density of states function
G	Photoconductive gain
$h, \hbar$	Planck's constants
h (subscript)	Hole-associated quantity
H_0	Unperturbed Hamiltonian operator
$\boldsymbol{H}$	Magnetic intensity
$\mathcal{H}$	Hamiltonian operator
H (subscript)	Hall-associated quantity
i (subscript)	Initial scattering state
I	Detector current; intensity of radiation
I_{p}	Photocurrent

J	Rotational quantum number
$k, \boldsymbol{k}$	Reciprocal lattice wavevector
k_B	Boltzmann's constant
k_e^{TF}	Thomas-Fermi momentum
K	Second rotational quantum number
$\mathcal{K}$	Electromechanical coupling coefficient
$\mathcal{K}_n$	Modified Bessel function
l	Magnetic length, cyclotron orbit radius; length of detector
$_l$ (subscript)	Longitudinal acoustic wave-associated quantity
l	Low-field angular momentum quantum number
L	Reduced conduction band energy; laser cavity length
L_a	Ambipolar diffusion length
$L(\phi_i)$	Scattering operator
L'	Higher band parameter (InSb)
L_z	Length of semiconductor sample in direction of magnetic field
$\hat{\mathcal{L}}$	Orbital angular momentum operator
m_c	Cyclotron resonance electron effective mass
m_e^*	Electron effective mass
m_e^{DS}	Density-of-states electron effective mass
m_h	Hole/valence band effective mass
m_h^{DS}	Density-of-states hole effective mass
m_{hh}^*	Heavy hole mass
m_{lh}^*	Light hole mass
m_0	Free electron mass
m_0^*	Band-edge effective mass of electron
m	Low-field magnetic quantum number
M	Higher band parameter (InSb); orbital angular momentum quantum number
$\overline{M}$	Reduced mass of unit cell
$\mathbf{M}$	Effective mass tensor
n, n_e	Electron concentration; order of grating reflection
$\boldsymbol{n}$	Index of refraction
n	Low-field principal quantum number
$\mathfrak{n}$	Impurity electron band index
n_i	Intrinsic electron concentration
N	Number of cells in crystal; Landau level quantum number
N'	Higher band parameter (InSb)
N_A	Acceptor concentration
$N_B(\epsilon)$	Density of states in a magnetic field
N_c	Conduction band "density of states"
N_D	Donor concentration
N_{D^+}	Ionozed donor concentration
N_{D^0}	Neutral donor concentration
N_I	Impurity ion concentration
N_T	Conduction band "density of states" in a magnetic field

N_X	Concentration of metastable states
$\mathcal{N}_i$	Occupation number of i th Maxwellian distribution state
p	Hole concentration
p_i	Intrinsic hole concentration
$\boldsymbol{p}$	Electron canonical momentum
P	Pressure, kilobars (1 kbar = 100 MPa); power spectrum
$\boldsymbol{P}$	Polarization vector
$\mathcal{P}$	s-p Momentum matrix element
$\mathfrak{P}$	Power absorbed from EM wave
$\boldsymbol{q}$, q	Wavevector (or magnitude) of a phonon, reciprocal length
q_0	Reciprocal Debye screening length
Q	Generalized lattice configuration coördinate; quadrupole moment
Q_c	Laser cavity efficiency
Q_q	Quantum efficiency
$Q_{\boldsymbol{q}}$	Normal coördinates
$\mathcal{Q}$	Electric dipole matrix element
r_H	Hall factor
r_T	Scattering radius
$\boldsymbol{r}$	Radius vector
R	Resistance of detector; resolution of grating
R_H	Hall coefficient
$R_\pm$	State transition rate for phonon emission (+) and absorption (−)
$\boldsymbol{R}$	Position vector of ionic cores or unit cell
$\Re$	Real part; responsivity
Ry	Rydberg
Ry*	Effective Rydberg
$s_{1,2}$	Surface recombination velocities; monochromator slit width
S_{kl}	Acoustic strain tensor
$S_\pm$	Kohn-Luttinger amplitude of s-basis functions; state transition probability for phonon emission (+) or absorption (−)
$\boldsymbol{S}$	Poynting vector
$\hat{\boldsymbol{S}}$	Spin vector operator
t	Thickness of detector
T	Temperature, degrees Kelvin
T_e	Electron temperature
$\mathcal{T}$	Transmission per round trip in laser cavity
$\mathcal{T}$	Intraband optical mode scattering operator
$u(\boldsymbol{r})$	Periodic portion of Bloch function
$\boldsymbol{u}$, $\boldsymbol{u}(\boldsymbol{R})$	Optical displacement
U	Screened ionic impurity potential; effective Hubbard correlation energy
$U(\omega)$	Density of stimulating radiation
v	velocity
V	Volumetric normalization constant; constant volume

V_s	Signal voltage
$V_0(\boldsymbol{r})$	Unperturbed crystal periodic potential
w	Width of detector
W	Scattering transition rate
$W(\epsilon)$	Electron scattering probability, angularly integrated
$\mathcal{W}$	Energy width of DX band
x	Optical propagation distance
$X_\pm$, $Y_\pm$, $Z_\pm$	Kohn-Luttinger amplitudes of p-basis functions
Z	Atomic number
α	Absorption coefficient; rate of decay of impurity wavefunction
α_j	Bloch basis function contribution to impurity wavefunction
$\alpha_u(T)$	Fraction of ionized impurity atoms uncorrelated at temperature T
$\boldsymbol{\alpha}$	Polar constant
β	Conductivity electric field dependence, $(1/\sigma)[d\sigma/d(E^2)]$
β_{BH}, β_{CW}	Ionized impurity screening constants
γ	Dimensionless magnetic field; pressure coefficient of band-gap; ratio of longitudinal to transverse effective mass
Γ	Halfwidth at half-maximum of a resonance curve; conduction band minimum
Γ_D	Rate of depopulation of excited state
Γ_{IR}	Empty FIR laser cavity loss
Δ	Spin-orbit splitting
Δ_{F-C}	Franck-Condon shift energy
$\Delta(\omega, \omega_c; k_z)$	Cyclotron resonance peak shift
ϵ	Electron energy above the conduction band minimum
ϵ_D	Donor energy, relative to conduction band minimum
ϵ_F	Fermi energy, or chemical potential, relative to Γ-minimum
$\boldsymbol{\epsilon}$, ϵ_{ij}	Dielectric tensor, elements
$\epsilon_{L-\Gamma}$	Energy of L-associated level above the Γ-minimum
$\epsilon_{X-\Gamma}$	Energy of X-associated level above the Γ-minimum
ϵ_0	Permittivity of free space
ε	Relative pairing energy (see Chapter III)
ε_{ac}	Deformation potential constant
ε'	Reduced conduction band energy ($= E_g/(E_g + 2\epsilon)$)
η	Reduced Fermi energy; quantum efficiency
θ	Scattering angle
θ_i	Angle of incidence
Θ	Debye temperature
$\boldsymbol{\kappa}$	Extinction coefficient
$\kappa \begin{cases} \kappa_0 \\ \kappa_\infty \end{cases}$	Static or D.C. dielectric constant High frequency dielectric constant
λ	Wavelength, cm; electron localization parameter
λ, λ_e	Screening length
Λ	Lorentzian lineshape function

μ_B	Bohr magneton
μ_0^*	Magnetic moment of electron
μ	Mobility
μ_d	Dipole moment
ν	Frequency, Hz
Ξ (+ subscript)	Deformation potential tensor, components
ρ	Charge density
ρ_n	Scattering parameters
ϱ	Mass density
σ	Conductivity; standard deviation
σ_a	Absorption cross-section
$\hat{\boldsymbol{\sigma}}$	Pauli spin matrix operator
τ_{CR}	Cyclotron resonance lifetime, inverse of Γ
τ_{DC}	Momentum relaxation time
τ_E or $\tau(\epsilon)$	Energy relaxation time
τ_h	Hole recombination lifetime
τ_r	Photoconductive recombination lifetime
τ_t	Photoconductive carrier transit time
ϕ	Polarization potential
φ	Wannier function; Bloch function
Φ	Photon flux
$\Phi(\epsilon)$	Perturbation function
ψ	Electronic Bloch wavefunction; impurity atom electron wavefunction
ω	Angular frequency, rad sec^{-1}
ω_c	Cyclotron resonance frequency
ω_{LO}	Longitudinal optical phonon frequency
ω_p	Plasma frequency
ω_{TO}	Transverse optical phonon frequency
$\Delta\omega_{1/2}$	Resonance linewidth at half-maximum
Ω	Cell volume, cm^{-3}
* (superscript)	Effective Mass Approximation-associated quantity

CHAPTER I

Introduction

This thesis is concerned with certain electronic and optical properties of bulk n-type indium antimonide in generally extreme conditions, i.e., under high magnetic fields, high hydrostatic pressure, low temperature, and laser illumination, although not always at the same time. Indium antimonide has been under intense scrutiny for well over thirty years: The motivation for this investigative effort, and for the studies of photoconductivity and impurity behavior undertaken herein, is manifold.

1.1 Indium Antimonide as an Exceptional Semiconductor

Beginning in the 1950's, indium antimonide was investigated along with other intermetallic polar compounds when it was discovered they possessed semiconductor qualities. Early cyclotron resonance experiments revealed a very small electron effective mass and a spin-split conduction band. Optical measurements confirmed a very narrow energy gap which was strongly temperature-dependent. Ground-breaking work was done by KANE (1957) to elucidate the band structure of indium antimonide, work that has subsequently been exploited and extended for a wide variety of other semiconductors. Kane showed that by virtue of the small effective mass and large spin-orbit interaction in indium antimonide, the conduction band is highly nonparabolic, a result which is very significant in questions of transport and scattering mechanisms within the semiconductor, and which evinces itself quite noticeably in experiments involving magnetic fields.

The question of indium antimonide's high electron mobility, and the factors that limit it, was first extensively probed by EHRENREICH (1957, 1959). Initially, work on this topic had been conducted using the relaxation time approximation, but Ehrenreich applied the

Boltzmann equation to the system, and thereby was able to quantify polar optical mode scattering as well as heavy hole scattering.

BARRIE (1956) and BATE ET AL. (1965) presented expressions for electron mobility valid under special conditions (such as high temperature). Bate *et al.* showed that electron-electron scattering was significant at elevated temperatures.

More recently, more ambitious efforts by ZAWADZKI & SZYMAŃSKA (1971) and SZYMAŃSKA & DIETL (1978) have attempted (with impressive success in the latter case) to model mobility in indium antimonide, as well as in various II-VI compounds, under a wide variety of conditions, including low temperature and high hydrostatic pressure.

A theoretical review of this range of topics is presented in Chapter II. Table 1.1 lists the values of material parameters of indium antimonide introduced in the theory and used throughout this thesis.

1.2 Impurity Studies in Indium Antimonide

Among the most important features characterizing semiconductors is that of the dependence of many of their properties on the nature and number of their defects, which are typically impurity atoms often not strikingly different from those of the host lattice, in numbers representing often not more than 1/10,000,000 of 1% of the atoms present. KOHN (1957) presented the first extensive model of "shallow" donors, i.e., those with loosely bound electrons, which could be adequately described in terms of effective mass theory (EMT).

This theory was unsuited to many impurities, however, and deep donor and tight-binding models, such as that of TOYOZAWA (1978) proliferated. No model, however, has had nearly the success of EMT.

In particular, for many years, the phenomenon of persistent photoconductivity and *DX* behavior in general has been a topic of fevered investigation. First in indium antimonide (notably by POROWSKI ET AL., 1974), and later in gallium arsenide (e.g., LANG & LOGAN, 1977), it was observed that certain deep donors exhibited a large Stokes shift and large lattice relaxation, and thereby affected, often adversely, the characteristics of numerous devices, such as FETs. This problem has spurred on an era of vigorous searching for possible electronic and atomic mechanisms to explain often contradictory findings.

Among the more recent and more successful of explanations for these effects has been the negative-*U* model proposed by CHADI & CHANG (1988), a model that has proved not a little contentious, with enthusiastic support from, e.g., MOONEY (1990), and less enthusiasm emanating from, e.g., MAUDE ET AL. (1987).

TABLE 1.1: Material parameters of indium antimonide used in this thesis.

Material Parameters	Symbols	Values	References
Energy gap, 1.8°K, 1 bar	$E_{g;0}(0)$	0.237 eV	LANDOLT & BÖRNSTEIN, 1987
Energy gap temperature dependence: $E_g(T) = E_{g;0}(0) - aT^2/(b+T)$	a b	0.6 meV K^{-1} 500 °K	LITTLER & SEILER, 1986
Energy gap pressure dependence: $E_g(P) = E_{g;0} + \gamma P$	γ	14 meV kbar^{-1}	HUANG ET AL., 1984
Defect level energy pressure dependence (relative to the Γ-minimum): d_L (deep donor) d_X (metastable defect)	 $\partial\epsilon_{L-\Gamma}/\partial P$ $\partial\epsilon_{X-\Gamma}/\partial P$	 -10.5 meV kbar^{-1} -20 meV kbar^{-1}	DMOWSKI ET AL., 1982
Momentum matrix element	$\mathcal{P}$	9.07×10^{-8} eV cm	PIDGEON & GROVES, 1969
Higher band perturbation parameters	A' M L' N'	0 -5.5 -2.7 -4.4	PIDGEON & GROVES, 1969
Electron effective mass	m_e^*		SUMMERS ET AL., 1968
cyclotron resonance mass, 4.2°K	m_c	0.0138 m_0	
band-edge effective mass:	m_0^*		
60°K		0.0134 m_0	STRADLING & WOOD, 1968
160°K		0.0127 m_0	
Hole effective mass	m_h	0.40 m_0	BAGGULEY ET AL., 1963
TO-phonon frequency	ω_{TO}	3.481×10^{13} sec^{-1}	LANDOLT & BÖRNSTEIN, 1987
LO-phonon frequency	ω_{LO}	3.707×10^{13} sec^{-1}	
Dielectric constants	κ_0 κ_∞	17.9 15.7	KAHLERT & BAUER, 1973
Spin-orbit splitting	Δ	0.9 eV	PIDGEON & BROWN, 1966
Landé g-factor at band-edge, for $n < 10^{15}$ cm^{-3}	g_0^*	-50.6	LANDOLT & BÖRNSTEIN, 1987
Landé g-factor energy dependence: ($\varepsilon' = E_g/(E_g + 2\epsilon)$, with $\epsilon \equiv$ energy above Γ-minimum)	$\partial g/\partial\varepsilon'$	-60	LANDOLT & BÖRNSTEIN, 1987
Lattice constant	a_0	6.48 Å	ZAWADZKI & SZYMAŃSKA, 1971
Deformation potential, lattice dilatation constant	Ξ_d	14.6 eV	LANDOLT & BÖRNSTEIN, 1987
Melting point		530°C	MADELUNG, 1964

One complication that may, at least in indium antimonide, provide an alternative explanation for various observations in this field is that of correlation, the electric field-neutralizing effect of a non-random distribution of impurities (O'REILLY, 1989). ANDERSON (1958) and MOTT (1967) were among the first to consider the effect on electron conduction of disorder in semiconductors. CUEVAS (1967) and FALICOV & CUEVAS (1967) investigated electron mobility in Ge, and discovered that an increased concentration of ionized impurities in fact led to increased screening of scatterers and elevated mobility. This work was extended in the 1970's, largely by Russian scientists such as Éfros, Shklovskiĭ, Baranovskiĭ and others (see, e.g., BARANOVSKIĬ, 1980), who examined rigorously the effects on the Fermi energy and on the density of states of monopole and dipole interactions in a disordered semiconductor. KOSSUT (1990) discovered via a computer simulation that these correlative effects would enhance mobility in semiconductors under hydrostatic pressure, over a range of electron concentrations.

The effects of heterogeneity on a larger scale, i.e., actual impurity "phase" separation, was investigated by PIOTRZKOWSKI ET AL. (1986), who successfully modeled anomalous mobility behavior in indium antimonide.

Some of the effects of impurities on indium antimonide, and in particular the examination of metastable states, are discussed in Chapter IV, and the results are exhibited in Chapters VII and VIII.

1.3 Magnetic fields and Cyclotron Resonance in Indium Antimonide

At the same time that Kane was investigating the band structure of indium antimonide, YAFET ET AL. (1956) and KEYES & SLADEK (1956) examined the effects, both theoretically and experimentally, of a magnetic field on the energies of the band states of donors in indium antimonide. The phenomenon of freeze-out was successfully predicted, though the decrease in electron mobility was larger than expected. The application of weak magnetic fields and of strong magnetic fields proved mathematically tractable, but intermediate fields were problematic in this regard. ARMISTEAD ET AL. (1982) investigated shallow impurity states experimentally in this regime, while MAKADO & MCGILL (1986) examined the problem theoretically.

Beginning in the 1960's, effort was concentrated on the information about electron scattering processes that could be gleaned from the linewidths of cyclotron resonances in indium antimonide. While KUBO (1957) had rigorously derived an expression for the absorbed power in a resonance peak, many of the complexities of lineshape, such as asymmetry and

peak shift, were not considered. HINDLEY (1964) considered the effect on the lineshape in a *parabolic* band of a number of scattering modes, while the effects of ionized impurities in indium antimonide were examined both theoretically and experimentally by KAWAMURA ET AL. (1964), KAWABATA (1967), KAPLAN (1973) and LARSEN (1973), the last of whom also considered the importance of correlation in Stark broadening. Most recently, a pair of papers by KOBORI ET AL. (1990) (**I** & **II**) has examined linewidth due to many scattering mechanisms from both theoretical and experimental standpoints, and has beautifully illustrated the difficulties involved in constructing accurate, conclusive models in this field.

WASILEWSKI ET AL. (1986) reported the anomalous narrowing of cyclotron resonance and "impurity-shifted cyclotron resonance" in indium antimonide upon the application of high hydrostatic pressure. These studies have been extended in the current thesis and are discussed at length in Chapters III and VIII.

1.4 Indium Antimonide as an Infrared Detector

Much of the impetus for the aforementioned studies of indium antimonide has been provided by the search for ever more sensitive infrared detectors covering an ever greater portion of the spectrum.

The Second World War saw a spirited development of the lead chalcogenides as both photoconductive and photovoltaic infrared detectors, especially on the part of Germany. Subsequently, development was pursued in both the United Kingdom and the United States. While lead selenide was useful at wavelengths out to 8 μ, a search for a narrow-gap semiconductor was launched in order to extend the detectable spectrum even further (SMITH ET AL., 1968). While indium antimonide cut off at 300°K only at 7.5 μ, it was available as a very pure single crystal material, in contrast to the chalcogenides, and exhibited remarkably high mobility, a key asset for a photoconductive detector.

Indium antimonide was developed as a detector in numerous forms:

- *Photoconductors:* In the U.K., most development concentrated on photoconductors, often p-type in order to exploit the high mobility of the electrons to enhance the minority sweep-out effect;
- *Photovoltaics:* In the U.S., on the other hand, photovoltaic cells were more popular, usually comprising a thin layer of p-type material diffused over the surface of an n-type slab;
- *The photoelectromagnetic (PEM) effect:* In this case, a semiconductor in a magnetic field is illuminated on one surface, creating a Hall-like voltage by virtue of the greater

mobility of the electrons on one side of the detector. This effect has been exploited to eliminate cooling and biasing requirements (KRUSE, 1962);

- *Extrinsic detectors:* Shallow impurities in indium antimonide, even at the lowest temperatures, do not freeze out. However, the application of pressure or of a magnetic field will result in freeze-out at even liquid nitrogen temperature. In this way, the response of indium antimonide as a photoconductor can be extended to well beyond 1000 μ;
- *Rollin detectors (or hot electron bolometers):* By virtue of the λ^2 dependence of EM wave absorption for free electrons (see Chapter V), and of the very low effective mass of the electrons in indium antimonide, the effective temperature of the electrons may be elevated substantially above that of the lattice (the adiabatic effect). Because the mobility is highly energy-dependent, this radiation absorption is seen as a change in mobility, which shows up in the photoconductive mode, especially if the resistance of the detector has been increased with a magnetic field (KINCH & ROLLIN, 1963);
- *Putley detectors:* PUTLEY (1965) described the use of cyclotron resonance at high magnetic fields as a detection mechanism in indium antimonide, the chief advantages of which were the great increase in resistivity in the sample at 4.2°K in a magnetic field, and its tunability, a hitherto unattained feature.
- *Heterodyne detectors:* PUTLEY (1977) reviews the use of indium antimonide, in conjunction with a maser, to act as a very long wavelength ($\sim$1 mm) heterodyne detector. This type of detection was not investigated at all in the current work.

Most recently, molecular beam epitaxy has been used to produce detectors of variable quality (see Chapter VIII), while liquid phase epitaxially-grown devices have been available commercially for several years.

In the current work, hydrostatic pressure has been used as a variable to increase the dark resistance of the indium antimonide sample, in both the intrinsic photoconductive and Putley modes of detection. General detector theory is presented in Chapter V, and results in Chapter VIII. Some technical specifics concerning the so-called "figures of merit" are presented briefly in Appendix 1. Finally, some of the mathematics required to interpret the results in line with the theory presented in Chapter II are presented in the form of a *Mathematica* program in Appendix .

CHAPTER II

Theory of Band Structure and Transport in Indium Antimonide

In this chapter are set out some of the fundamental equations relating to indium antimonide that are necessary for the quantitative analysis of many of the data in later chapters. Initially, the bulk properties of indium antimonide are described. There follows a discussion of the electron statistics used to determine the occupation of conduction band states, and successive sections treat effective mass, the Kane theory of energy-wavevector relationships, electron mobility and scattering, and Hall measurements.

2.1 Indium Antimonide: Band Structure and Properties

Indium antimonide is a direct-(narrow)-gap semiconductor of the zincblende structure (see Figs. 2.1, 2.2 below and Table 1.1) with a very small electronic effective mass. As such, it has long been the detector of choice for work in the 3–5 μ region, as its high mobility enhances its detectivity (see Chapter V). It has been available in very high purity form ($N_D - N_A \approx 5 \times 10^{13}\,cm^{-3}$) for well over thirty years. It is to this day grown on boules (typically ~5–6 cm in diameter) by the Czochralski method,* though LPE-grown commercial detectors have been common for many years, and MBE-grown material has in recent years made its debut.

KANE (1957) proposed an extensive band model for indium antimonide (see below, § 2.4 and Fig. 2.4 therein). It has a spherical conduction band minimum, obviating the need for orientational considerations. Its conduction band is, however, highly nonparabolic, which

* A single-crystal "seed" is immersed in a melt of the semiconductor, and slowly "pulled", or withdrawn while being rotated, to grow a single crystal.

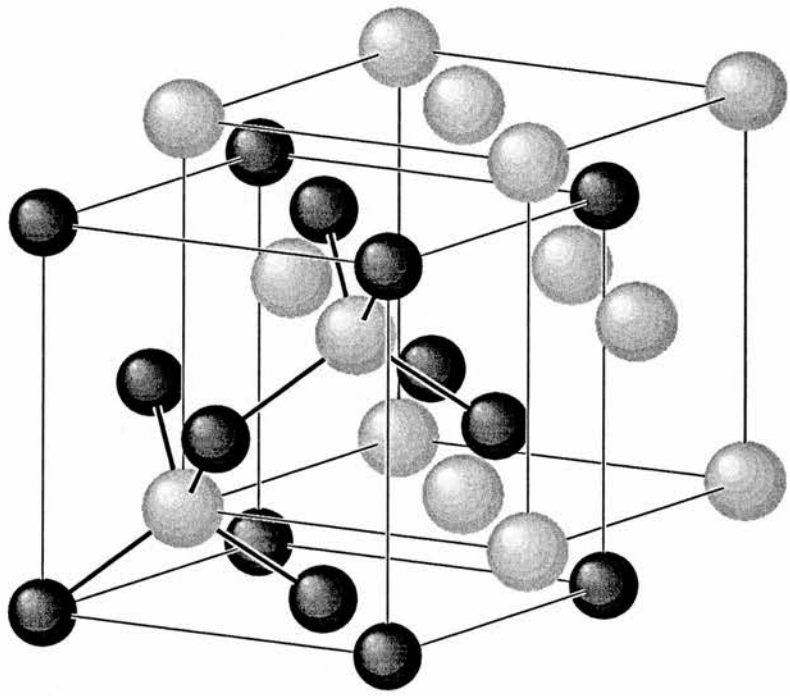

FIG. 2.1: The zincblende crystal structure of indium antimonide, showing the two equivalent inter-penetrating FCC lattices. The larger (light gray) atoms are indium, with a diameter of 1.44 Å, while the smaller (partially ionic) antimony atoms have a diameter of 1.36 Å (drawing not to scale).

results in some notable features in its Landau level spectrum (see Chapters III and VIII). Also of note, especially with regard to the pressure studies herein undertaken, is the nature of its higher conduction band minima. In common with the other III-V semiconductors, the Γ-minimum is flanked by two "subsidiary" sets of minima in the L ($\{111\}$) and X ($\{100\}$) directions.

A free atom with outer (valence) electrons of s- and p-nature can be thought of as a two-level system where the p-level is at the higher energy. As atoms are assembled into rows, and the rows into lattices, level-splitting occurs due to perturbations, and the two levels broaden into two bands. Free-electron theory rationalizes this such that the parabolic $E - k$ curve obtained from $E = \hbar^2 k^2 / 2m_e^*$ is modified to include interactions of the nearly-free electron with the lattice. At the Brillouin zone edge, Bragg reflection of the electron's associated wave results in the mixing of two running waves to form a standing wave, which results in an energy gap. Hence, a series of bands and gaps is built up in the zone. In the case of the s- and p-orbitals in particular, tight-binding theory pictures the s-like state as

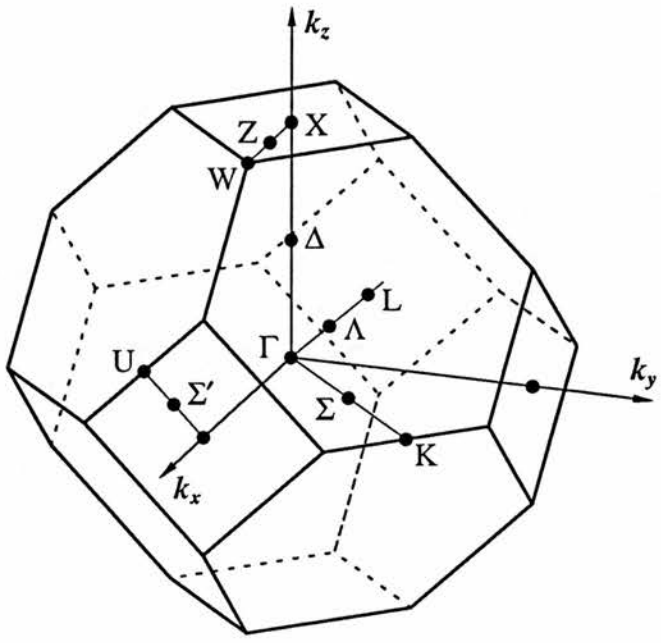

FIG. 2.2: The Brillouin zone of the zincblende crystal structure, showing principal points. The enclosed volume is half that of the cube defined by the planes of the six square faces.

originating from a chain of spherically symmetric electron clouds (s-states) modified into a Bloch function:

$$\psi_k(\boldsymbol{r}) = \sum_{\boldsymbol{R}} \varphi(\boldsymbol{r} - \boldsymbol{R}) e^{i\boldsymbol{k}\cdot\boldsymbol{R}} .$$

Here, $\varphi(\boldsymbol{r} - \boldsymbol{R})$ is the so-called Wannier function, which in narrow-gap semiconductors can be approximated by the atomic wavefunctions of an atom with an equilibrium core position of $\boldsymbol{R}$. At the center of the zone, $k = 0$, and the successive s-electrons are all of the same parity, resulting in a high, repulsive potential. At the edge of the zone, $e^{i\boldsymbol{k}\cdot\boldsymbol{r}} = -1$, and ψ changes sign on each atom, resulting in maximum overlap. Therefore, the band at this point is of lower energy. For the p-electrons, in contrast, a chain of orbitals comprises longitudinally oriented "dumbbells", aligned in a head-to-tail fashion, minimizing overlap, and lowering energy, while at the zone edge, the reverse holds true. In fact, the energy levels would cross if they were of different symmetry; but as the states are of the same symmetry, "anticrossing" behavior is what is actually observed.

The behavior of this band structure under hydrostatic pressure is considered here. A theoretical treatment of this system has been published by GORCZYCA (1982), who included

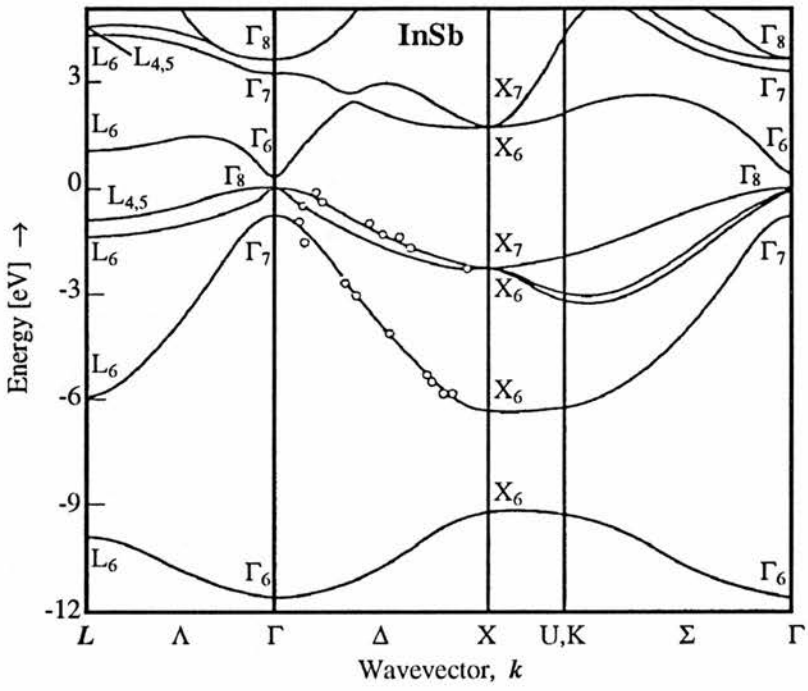

FIG. 2.3: Band diagram of indium antimonide, reprinted and adapted from LANDOLT-BÖRNSTEIN.

non-local corrections to the pseudo-potential, involving the use of a variable effective mass and including the spin-orbit interaction, which is large in indium antimonide.

When hydrostatic pressure is applied to the crystal, diminishing the lattice constant while maintaining the same symmetry,* the level-splitting is increased, and the levels move apart. In indium antimonide, the band-gap is seen to increase at 14 meV/kbar (HUANT ET AL., 1984), a value similar in all III-V semiconductors. Hydrostatic pressure compresses the wavefunctions of shallow impurity atoms as well, an effect similar to the application of a magnetic field (see Chapter III).

The subsidiary minima, labelled L and X, are also shown in the figure.

The salient effect of hydrostatic pressure is to increase the effective mass (see below) of the electrons of the semiconductor by altering the band curvature. Also important however (see below) is the decrease in the dielectric constant.

* The actual change in lattice constant is minute: In indium antimonide, the change over 1 kbar is 0.15% at 300°K, and a bit less at lower temperatures. Also of note is that the zincblende phase of indium antimonide, InSb I, exists only up to ~30 kbars, depending on temperature. At least three higher pressure phases are known to exist.

2.2 Effective Mass

The electron's effective mass, for which there are several definitions, varies strongly with pressure.

The definition wherein the group velocity $v_k = d\omega/dk$ is defined as* $(1/\hbar)\nabla_k\epsilon(k)$ leads via the Boltzmann equation (see § 2.5.1) to the "momentum" effective mass utilized in transport (velocity) problems:

$$\mathbf{M}_e^* = \frac{\hbar^2 k}{\partial\epsilon/\partial k}. \tag{2.1}$$

where $\mathbf{M}_e^*$ is the effective mass tensor. (In the general non-spherical case, effective mass is anisotropic, i.e., the acceleration of an electron will not in general be in the same direction as the applied force.) Throughout the present work, the scalar version of Eq. 2.1 will be employed. The major difference between conduction band electrons in the subsidiary minima and those in the Γ-minimum is one of effective mass.

For parabolic bands only, and therefore at the bottom edge of a nonparabolic band as well, the first derivative of energy with respect to k-vector is equal to the second derivative times k: $m_e^* = \hbar^2(\partial^2\epsilon/\partial k^2)^{-1}$.

m_e^{DS}, the so-called density-of-states mass of the electron (the weighted average of the effective mass within the conduction band, discussed in the next section) depends on contributions from the vicinity of the Fermi energy, and these depend on the particular scattering mechanisms involved. Again, in a completely parabolic conduction band, this value would equal that of the m_e^* discussed in the previous paragraph.

The cyclotron resonance mass, m_c, as discussed in Chapter III, is strongly dependent on a number of parameters, such as temperature, magnetic field and the wavelength used to excite resonance. This strong dependence results chiefly from the large nonparabolicity of the conduction band.

2.3 Fermi-Dirac Statistics

In order to quantify the scattering mechanisms and resulting transport properties in indium antimonide, it will be necessary to develop expressions relating electron concentration, mobility and energy.

* This definition leads to the current associated with an electron in state k being equal to ev_k.

2.3.1 *Intrinsic Semiconductors*

The intrinsic electron concentration n_i can be expressed by an integral

$$n_i = \int_0^\infty f_0(\epsilon) g(\epsilon) d\epsilon, \tag{2.2}$$

where ϵ signifies the energy of free electrons relative to the bottom of the conduction band, $f_0(\epsilon)$ is the equilibrium occupation probability of any energy level, and $g(\epsilon)$ is the density of states in phase space, which comprises both real space and k-space (with crystal momentum in any direction given by $\hbar k$). In a semiconductor with a spherical (isotropic) band, the constant energy surfaces in k-space are spheres. A differential volume of phase space is thus equal to $4\pi\hbar^3 k^2 dk$, while the electron states occupy a volume of h^3 (except that 2 electrons per state are allowed by the Pauli exclusion principle). Therefore, Eq. 2.2 can be rewritten

$$n_i = \frac{1}{\pi^2} \int_0^\infty f_0(\epsilon) k^2 \frac{dk}{d\epsilon} d\epsilon. \tag{2.3}$$

The occupation probability function is that given by the Fermi-Dirac distribution:

$$f_0(\epsilon) = \frac{1}{\exp[(\epsilon - \epsilon_F)/k_B T] + 1}. \tag{2.4}$$

Here, ϵ_F is the so-called Fermi energy, equal to the electronic chemical potential.* ϵ_F is chosen so as to make the integral of the Fermi-Dirac distribution function equal to the electron concentration.

In the case of a parabolic conduction band, where $\epsilon = \hbar^2 k^2 / 2 m_e^{DS}$ (and m_e^{DS} is the density-of-states mass described above), Eq. 2.3 can be rewritten in a form dependent on the electron mass and the Fermi energy:

$$n_i = \frac{\sqrt{2}}{\pi^2 \hbar^3} (m_e^{DS} k_B T)^{\frac{3}{2}} F_{\frac{1}{2}}(\eta), \tag{2.5}$$

where $F_i(\eta)$ is the Fermi integral of order i:

$$F_i(\eta) = \int_0^\infty \frac{x^i dx}{1 + \exp(x - \eta)}. \tag{2.6}$$

* The Fermi energy by this definition, which is strictly valid only at 0°K, would also be equal to the energy needed to add one electron from infinity to the system; but see § 4.6.

Here, $x = \epsilon/k_B T$, and η is the so-called reduced Fermi energy, $\epsilon_F/k_B T$. It is seen then that in the general case even the zero-pressure value of m_e^{DS} cannot be easily derived precisely unless the Fermi energy is known. In the intrinsic case, however, where Maxwell-Boltzmann statistics apply by virtue of the elevated temperature, the high energy tail of the Fermi-Dirac distribution can be estimated by a simple exponential function, wherein the 1 in Eq. 2.6 can be neglected. In this case the Fermi energy relative to the conduction band minimum can be approximated using the following formula:

$$\epsilon_F = -\frac{1}{2}E_g + \frac{3}{4}k_B T \ln (m_h^{DS}/m_e^{DS}), \tag{2.7}$$

where m_h^{DS} is the density-of-states mass of the holes. This was derived by setting $n_i = p_i$ in an intrinsic semiconductor, where p_i is the intrinsic hole concentration, also given by Eq. 2.5, but with m_h^{DS} substituted for m_e^{DS}. In order to solve analytically for the Fermi energy, it must be factored out of the Fermi integral, which can be done only by neglecting the 1 in the denominator of the integrand. Eq. 2.7 is therefore applicable only in classical cases, and not if the Fermi energy is very close to the band-edge.

A variant of Eq. 2.5, Eq. 2.8, connects m_e^{DS} with the band-gap, independently of the Fermi energy. While 2.5 is widely applicable, Eq. 2.8 relies on the fact that the high-energy tail of the Fermi-Dirac distribution function resembles a Maxwell-Boltzmann (classical) distribution, and is applicable only to non-degenerate semiconductors. In this case,

$$n_i = \frac{1}{4}\left(\frac{2k_B T}{\pi\hbar^2}\right)^{\frac{3}{2}} m_h^{DS\,\frac{3}{4}} m_e^{DS\,\frac{3}{4}} \exp\left(-E_g(P)/2k_B T\right), \tag{2.8}$$

where P indicates hydrostatic pressure. The value of the energy gap dominates this expression through the exponential term. Therefore, when the logarithm of each side is taken, the variation of effective mass with the band-gap plays a minor role. The virtually direct dependence of $\ln n_i$ on pressure (see Chapter VII) therefore indicates that $E_g \approx E_{g;0} + \alpha P$ (where the subscript 0 refers to zero pressure), or in other words, that dE_g/dP is virtually constant.

To solve Eq. 2.8, the expression for m_h^{DS} in indium antimonide is needed:

$$m_h^{DS} \approx (m_{lh}^{*\,\frac{3}{2}} + m_{hh}^{*\,\frac{3}{2}})^{\frac{2}{3}} \quad \text{and} \quad m_e^{DS} \approx m_e^* .$$

Here, the asterisks refer to effective masses, the subscript 'e' to the electron, and the subscripts 'lh' and 'hh' to the light and heavy holes respectively. The valence band effective

mass is virtually both temperature- and pressure-independent and a density-of-states mass of 0.40 m_0, derived from cyclotron resonance experiments (BAGGULEY ET AL., 1963), is applicable here,* where m_0 is the mass of the free electron. (From now on, effective masses will be expressed in units of m_0.) This figure actually reflects the mass of the heavy holes, as the mass of the light holes, 0.015, is negligible.

2.3.2 *Extrinsic Semiconductors*

The ionization energy of a donor $\Delta\epsilon_D$ in a semiconductor can be determined as follows. If N_D is the total concentration of donors, N_{D^0} the concentration of neutral donors, and N_{D^+} that of ionized donors, then probability that an impurity state at energy ϵ_D is occupied is

$$\frac{1}{1+\exp[(\epsilon_D-\epsilon_F)/k_BT]}=\frac{N_{D^0}}{N_D}, \tag{2.9}$$

meaning that

$$\frac{N_{D^+}}{N_D}=1-\frac{N_{D^0}}{N_D}=\frac{1}{1+\exp[(\epsilon_F-\epsilon_D)/k_BT]}. \tag{2.10}$$

This can be rearranged to

$$N_{D^+}=\frac{N_D}{\frac{g_D n}{N_c}\exp\frac{\Delta\epsilon_D}{k_BT}+1}, \tag{2.11}$$

where g_D has been introduced to account for the impurity spin degeneracy, and the conduction band density of states is

$$N_c=2\left(\frac{2\pi m_e^*(P)k_BT}{h^2}\right)^{\frac{3}{2}}.$$

In an n-type semiconductor, $N_{D^+}\approx n+N_A$, where N_{D^+} is the concentration of ionized donors and N_A is the total concentration of acceptors. Substituting this into Eq. 2.11 gives

$$\frac{n(n+N_A)}{N_D-N_A-n}=\frac{N_c}{2}\exp\left(\frac{-\Delta\epsilon_D}{k_BT}\right), \tag{2.12}$$

* This is because the heavy hole band, which dominates the mass of the holes, is parabolic to the extent that the cyclotron resonance mass and that for transport may be treated equivalently.

where the denominator of 2 in Eq. 2.12 reflects spin degeneracy (at suitably high temperatures) for indium antimonide, where the multiplicity of the conduction band minimum is unity.

2.4 Kane's Theory

KANE (1957) solves for the band structure of indium antimonide near the Γ-minimum by employing $\boldsymbol{k}\cdot\boldsymbol{p}$ theory to treat exactly the interaction of the s-like Γ_6 conduction band minimum with the p-like Γ_7 and Γ_8 valence maxima, which are split by the spin-orbit interaction, Δ. Because indium antimonide has a very narrow band-gap (responsible for the very low effective mass of the conduction band electrons as well as for the extreme nonparabolicity of the band), interactions with higher and lower bands are treated with second-order (rather than first order) perturbation theory. A separate treatment is done by Kane of the terms linear in $\boldsymbol{k}$, which dominate very close to $\boldsymbol{k} = 0$, which are finite in materials lacking inversion symmetry, and which are responsible for a maximum in the valence band—located at ~0.3% of the distance from the Γ-minimum to the zone boundary at (111)—of $\sim 10^{-4}$ eV above the value at $\boldsymbol{k} = 0$. In the present treatment, linear terms will be ignored.

Hall data, magnetoresistance measurements and the existence of a single sharp cyclotron resonance maximum are cited to supply various physical constants and to test agreement with experiment. However, the theory is strictly valid only at 0°K (EHRENREICH, 1956), and scattering mechanisms (such as electron-phonon coupling) are not explicitly considered.*

The Schrödinger equation for an electron in a crystal is

$$\left[\frac{p^2}{2m_0} + V_0(\boldsymbol{r}) + \frac{\hbar}{mo}\boldsymbol{k}\cdot\boldsymbol{p} + \frac{\hbar}{4m_0{}^2c^2}\left(\nabla V \times (\boldsymbol{p}+\boldsymbol{k})\right)\cdot\hat{\sigma}\right]\Psi_k = E_k\Psi_k. \qquad (2.13)$$

The second term above, $V_0(\boldsymbol{r})$, is the unperturbed crystal periodic potential, while the third term represents the so-called $\boldsymbol{k}\cdot\boldsymbol{p}$ interaction. The fourth term represents the spin-orbit interaction. $\hat{\sigma}$ is the Pauli spin matrix operator, and E_k refers to the total energy of the electron taken with respect to the top of the valence band, in contradistinction to ϵ, which will always mean energy with respect to the bottom of the conduction band.

* In particular, according to Ehrenreich, if the effective mass is to be derived from the Kane theory, the temperature-dependence of band-gap must be that due only to lattice dilatation and not to lattice vibration. This value is $(\partial E_{g;0}/\partial T)_P = -9.6 \times 10^{-5}$ eV/°K. However, according to RAVICH (1965), it is the *total* derivative (equal to $\sim 2.9 \times 10^{-4}$ eV/°K) that should be used to calculate to change in effective mass at the band-edge.

For small k, ($\hbar k \ll p$), and for $\Psi_k = u_k(r)e^{ik\cdot r}$, Eq. 2.13 can be approximated by

$$\left[\frac{p^2}{2m_0} + V_0(r) + \left(\frac{\hbar}{m_0}\right) k\cdot p + \left(\frac{\hbar}{4m_0^2c^2}\right)(\nabla V \times p)\cdot\hat{\sigma}\right] u_k(r) = E_k u_k(r).$$

This equation is solved by expanding the Bloch amplitudes, as a function of k, in terms of the eight unperturbed (uncoupled) periodic Luttinger-Kohn amplitudes, at $k = 0$: $S_\pm$, representing the s-basis functions, and $X_\pm$, $Y_\pm$ and $Z_\pm$, representing the p-basis functions, where the $\pm$ subscript refers to spin states.

After solving the secular equation resulting from the 8×8 interaction matrix for the four bands with spin, the perturbation energies due to the more distant bands are estimated and incorporated into the expression for electron energy. The following highly nonparabolic relation for the conduction band energy ϵ as a function of k ($\epsilon = 0$ at the Γ-minimum) is obtained (see Fig. 2.4):

$$\epsilon(\epsilon + E_g)(\epsilon + E_g + \Delta) - k^2\mathcal{P}^2(\epsilon + E_g + \frac{2}{3}\Delta) = 0, \tag{2.14}$$

where:

- $\epsilon + E_g = E - (\hbar^2k^2/2m_0)\left[1 + a^2A' + b^2M + c^2L' + \frac{1}{5}(b^2 - 2c^2)(L' - M - N')\right]$ (SZYMAŃSKA & DIETL, 1978);* where a, b and c give the contributions to the conduction band wavefunction from s-like and from two different components of p-like basis functions, respectively, and A', L', M and N' are perturbing contributions from higher bands;
- $\mathcal{P}$ is the s-p momentum matrix element $-i(\hbar/m_0)\langle S \mid p_z \mid Z\rangle$, representing the coupling between the conduction and valence bands ($\mathcal{P} \approx 9.07 \times 10^{-8}$ eV cm, often quoted as $E_\mathcal{P} = (2m_0/\hbar^2)\mathcal{P}^2 \approx 20$ eV); and
- Δ is the spin-orbit coupling energy in eV:

$$\Delta = \frac{3\hbar i}{4m_0^2c^2}\langle X \mid (\nabla V \times p)_z \mid Y\rangle,$$

where V is the periodic potential and p is the momentum operator for the electron. $\Delta \approx 0.9$ eV (LANDOLT-BÖRNSTEIN) independent of pressure or temperature.

* Hereafter referred to as *S&D*.

The coefficients a, b and c above are given by the following equations, in which $E' \equiv \epsilon + E_{g;0}$:

$$\begin{aligned} a^2 &= \frac{1}{D}\left(\Delta + \frac{3}{2}E'\right)(\Delta + E')E', \\ b^2 &= \frac{\Delta^2}{3D}(E' - E_{g;0}), \\ c^2 &= \frac{2}{3D}\left(\Delta + \frac{3}{2}E'\right)^2(E' - E_{g;0}), \end{aligned} \tag{2.15}$$

where

$$D = \left(\Delta + \frac{3}{2}E'\right)(\Delta + E')E' + (\Delta + E')^2(E' - E_{g;0}) + \frac{1}{2}(E' - E_{g;0})E'^2 .$$

However, if $\epsilon \ll 2\Delta/3$, then these coefficients reduce to simpler expressions:

$$a^2 = L, \qquad b^2 = \frac{1-L}{3} \qquad \text{and} \qquad c^2 = \frac{2(1-L)}{3},$$

where $L = \epsilon/(E_{g;0} + 2\epsilon)$. Close to the band-edge, $a \approx 1$ and $b,\ c \approx 0$, so the conduction band is extremely s-like.

If $k \approx 0$, a simpler equation than Eq. 2.14 results, describing parabolic bands:

$$\epsilon = E_g + \frac{\hbar^2 k^2}{2m_0} + \frac{\mathcal{P}^2 k^2}{3}\left(\frac{2}{E_g} + \frac{1}{E_g + \Delta}\right). \tag{2.16}$$

Using Eq. 2.1, Eq. 2.16 can be differentiated with respect to k, inverted, and multiplied by $\hbar^2 k/m_0$ to produce

$$\frac{m_0^*}{m_0} = \left[1 + \frac{2m_0\mathcal{P}^2}{3\hbar^2}\left(\frac{3E_g + 2\Delta}{E_g(E_g + \Delta)}\right)\right]^{-1},$$

where m_0^* is the electron effective mass at $k = 0$, the bottom of the conduction band. The second addend in the large brackets is $\sim$80, so the 1 can be neglected. The conduction band-edge effective mass of the electron is a function of the energy gap, which varies both with pressure and temperature. At 0°K then, if $m_{0;0}^*$ is the band-edge mass at zero pressure, taking the ratio of m_0^* to $m_{0;0}^*$ from the equation above produces for parabolic bands (or at $k \approx 0$)

$$\frac{m_0^*}{m_{0;0}^*} \approx \left(\frac{\Delta + \frac{3}{2}E_{g;0}}{E_{g;0}\left(\Delta + E_{g;0}\right)}\right)\left(\frac{E_g(P)\left(\Delta + E_g(P)\right)}{\Delta + \frac{3}{2}E_g(P)}\right), \tag{2.17}$$

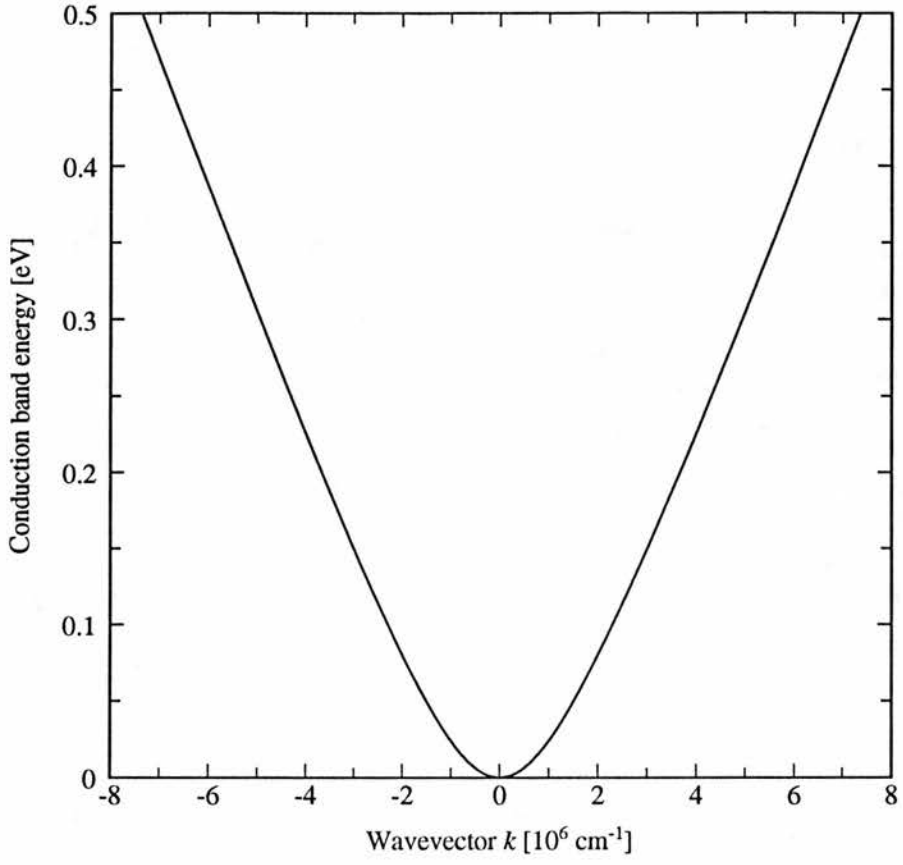

FIG. 2.4: A plot of conduction band energy above the Γ-minimum *vs.* wavevector, using band parameters for 77°K and ambient pressure.

where all subscripts ";0" refer to the values of mass and energy gap at zero pressure. The approximation sign in Eq. 2.17 reflects the fact that while most of the temperature and pressure effect on mass is due to the dilatation of the lattice, some is due to electron-phonon coupling (LANG, 1961 and RAVICH, 1965).

On the other hand, a useful approximation to Eq. 2.14 for the case where $\Delta \gg E_{g;0}, k\mathcal{P}$ (applicable to indium antimonide for small k ($\epsilon < E_{g;0}$) and because $\Delta/E_{g;0} \approx 4.5$) is

$$\epsilon = \frac{\hbar^2 k^2}{2m_0} + \frac{1}{2}E_{g;0} + \left({E_{g;0}}^2 + \frac{8}{3}\mathcal{P}^2 k^2 \right)^{\frac{1}{2}} . \tag{2.18}$$

In this equation, the split-off valence band is viewed as a lower band which does not to first order influence the conduction band electrons. This is the so-called two-band model, which approximates the nonparabolicity of the conduction band. In this case, the relation between the conduction band energy and the electron wavevector takes on a particularly simple form,

i.e., $\hbar^2k^2/2m_0^* = \epsilon(1 + \epsilon/E_{g;0})$. With Eq. 2.1, this means that the effective mass can be expressed by

$$m_e^* = m_0^* \left(1 + \frac{2\epsilon}{E_{g;0}}\right). \tag{2.19}$$

According to ZAWADZKI & SZYMAŃSKA (1971),* this approximation is not of suitable precision for optical experiments, but is accurate enough to describe transport in indium antimonide up to energies corresponding to $n \approx 10^{19}\,\mathrm{cm}^{-3}$, or $\sim$0.5 eV. By using Eqs. 2.1 and 2.18 evaluated at $k = 0$, it is seen that

$$\frac{1}{m_0^*} \equiv \frac{1}{\hbar^2 k}\frac{\partial\epsilon}{\partial k}\bigg|_{k=0} = \frac{1}{m_0} + \frac{4\mathcal{P}^2}{3\hbar^2 E_{g;0}},$$

and therefore that

$$\mathcal{P}^2 = \frac{3\hbar^2 E_{g;0}}{4}\left(\frac{m_0 - m_0^*}{m_0 m_0^*}\right).$$

This will prove useful for putting various energy integrals in terms of m_0^*.

2.5 Electron Scattering and Mobility

Subsequent to Kane's landmark paper in 1957, several investigators over the years endeavored to analyze the scattering processes in semiconductors in general and in III-V compounds in particular using the newly available correct *nonparabolic* energy-wavevector relationships to determine the density of states required in scattering equations (see below); eventually, *Z&S* pointed out that it was insufficient to consider the effect of the nonparabolic band-shape on the density of states alone, and that the actual scattering matrix elements were effected as well by the nonparabolicity. EHRENREICH (1957, 1959) first attempted to quantify several scattering modes (described below): polar optical phonon (PO) interaction, optical deformation potential (OD) (or non-polar optical phonon) interaction, polar acoustical phonon (piezoelectric or "piezoacoustic") (PE) interaction, non-polar acoustical deformation potential (AD), and charge-center (CC), which comprises ionized impurity scattering (II) as well as the effects of holes and electron screening. BATE ET AL. (1965) showed that at liquid nitrogen temperatures, in pure samples, electron-electron scattering was also significant. Most authors have disregarded neutral impurity scattering in the case of indium antimonide,

* Hereafter referred to as *Z&S*.

as it is deemed to be insignificant relative to that of ionized impurities, even at the lowest temperatures. Whether this can be said to be true at high pressures as well remains moot.

Z&S treated numerous scattering mechanisms over a wide range of temperatures and electron concentrations using the relaxation time approximation (see below). In order to derive the energy-dependent relaxation times $\tau(\epsilon)$, which are proportional to the product of the density of states $g(\epsilon)$ (see Eq. 2.3) and the angularly integrated scattering probability for the scattering mode in question, $W(\epsilon)$, it was necessary to derive the correct forms for $W(\epsilon)$, reflecting the nonparabolicity of the band. Until then, many authors had been using power functions of ϵ for $W(\epsilon)$, a procedure valid only for parabolic bands.

The majority of these processes can be modeled as elastic collisions, i.e., the electron can be viewed as a particle whose velocity is virtually unchanged from collision to collision, by virtue (in indium antimonide, at least) of its extremely small mass. This permits conduction to be modeled with the so-called relaxation time approximation (RTA), wherein mobility is proportional to the mean time between collisions, and, more significantly, that in the case of more than one scattering mechanism, a reduced mobility can be estimated from a reduced relaxation time given by

$$1/\tau = 1/\tau_1 + 1/\tau_2 + 1/\tau_3 + \ldots ,$$

where the various τ_i are the relaxation times for each mode of elastic scattering. In the case of PO scattering, however, the interaction is highly inelastic due to the fact that the phonon energy is comparable to that of the electrons, and the RTA is inapplicable, except either at very low temperatures where on average the time spent by an electron in the interaction is very small (DAVYDOV & SHMUSHKEVICH, 1940), or at temperatures above the Debye temperature (283°K in indium antimonide) (see below). Many authors (EHRENREICH, 1957, 1959; BATE ET AL., 1965; and others) therefore limited their models of mobility, thermoelectric power, etc. to temperatures at or above the Debye limit, or assumed that at low temperatures it was completely absent. However, as EHRENREICH (1959) pointed out, a valid expression for mobility can be derived if one is willing to employ the Boltzmann transport equation, which can be solved by the variational procedure. EHRENREICH (1959) did this for high temperatures and concentrations.

S&D provided, at last, a complete set of expressions for the individual scattering mechanisms, including electron-electron scattering terms (not considered here), and a variationally derived scheme for determining mobility (see below). LITWIN-STASZEWSKA ET AL. (1981), who also supply many constants for indium antimonide, applied this to their own data, and found excellent agreement. In particular, a glance at curve (4) in Fig. 2.5 shows extremely

close resemblance to Fig. 7.9 in the present work. Below are the equations pertinent to the present work.*

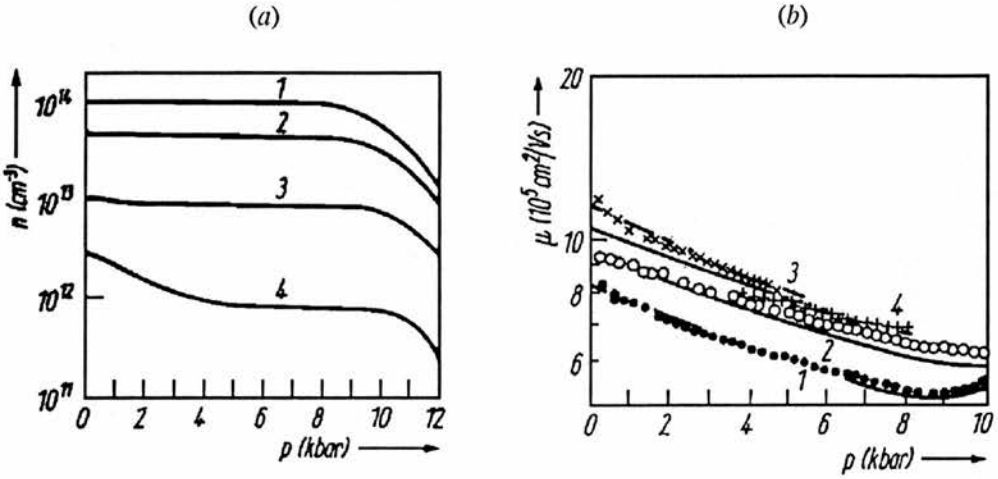

FIG. 2.5: Illustration of the close agreement between the mobility model of SZYMAŃSKA & DIETL (1978) and the measured mobility in indium antimonide in a wide variety of conditions (reprinted from LITWIN-STASZEWSKA ET AL., 1981). (*a*): Electron concentration *vs.* pressure for indium antimonide; in curve (1), "normal" conditions; curves (2)–(4), increasing degrees of high-pressure freeze-out onto metastable states (see Chapter IV). Note the close similarity of curve (4) to Fig. 7.9. (*b*): Measured mobility corresponding to curves in (*a*); tokens, experimental; solid lines, calculated.

2.5.1 The Boltzmann Equation

In order to treat various transport problems on a statistical basis, wherein the steady state *distributions* of carriers subject to thermal gradients, electric and magnetic fields, diffusion processes, collisions, etc. are examined, rather than individual carriers themselves, Boltzmann introduced the function $f_k(\boldsymbol{r})$, which is equal to the number of carriers of wavevector $\boldsymbol{k}$ in the differential neighborhood of $\boldsymbol{r}$. In a homogeneous, isotropic semiconductor in steady

* It was found necessary to do this rather complete analysis of mobility in indium antimonide, which is shown at length in Appendix 2, in order to adequately model the temperature-dependent mobility results presented in Chapter VII. The use of textbook equations such as the Brooks-Herring model (see below) proved very inconsistent, and did not provide the accuracy required to make conclusions regarding observed impurity-limited mobility.

state in an applied electric field in the x-direction (but with no magnetic field or temperature gradient present), the Boltzmann equation is

$$-f_0'\frac{\hbar k_x}{m_e^*}\left(|e|E_x+\frac{d\epsilon_F}{dx}\right)=f_0'k_x\mathcal{T}\big(\Phi(\epsilon)\big)+f_0'k_x\Phi(\epsilon)\left(\mathcal{D}+\sum_s\frac{1}{\tau_s}\right),$$

where $f_0'=\partial f_0/\partial\epsilon$ (f_0 is the unperturbed Fermi distribution function), $\Phi(\epsilon)$ is a perturbation function defined by setting the perturbation $f_k(\boldsymbol{r})-f_0(\epsilon)$ equal to $-f_0'k_x\Phi(\epsilon)$, $\mathcal{T}\big(\Phi(\epsilon)\big)$ arises (as explained below) from inelastic intraband polar and non-polar optical mode scattering, $\mathcal{D}$ from interband* polar and non-polar optical mode scattering, and the τ_s are the relaxation times of the various elastic scattering processes.

When the variational technique is used to solve this equation as per *S&D*, using the first Born approximation,† an expression for the electrical conductivity σ is found, from which the Hall mobility may be derived:

$$\sigma=-\frac{e}{3\pi^2}\frac{d_{a^{(0)},a^{(0)}}}{d},$$

where

$$d=\begin{vmatrix} d_{00} & d_{01} & \cdots \\ d_{10} & d_{11} & \cdots \\ \vdots & \vdots & \ddots \end{vmatrix} \qquad \text{and} \qquad d_{\alpha,\beta}=\begin{vmatrix} 0 & \alpha_0 & \alpha_1 & \cdots \\ \beta_0 & d_{00} & d_{01} & \cdots \\ \beta_1 & d_{10} & d_{11} & \cdots \\ \vdots & \vdots & \vdots & \ddots \end{vmatrix}$$

are the determinants of infinite matrices, but can be evaluated to satisfactory precision, according to *S&D*, by considering only those elements for which $i,j=0,1,2$. In these expressions,

$$a_i^{(k)}=\left\langle\phi_i\left(\frac{\epsilon-\epsilon_F}{k_BT}\right)^k\right\rangle \qquad \text{and} \qquad d_{ij}=d_{ji}=\langle\phi_iL(\phi_j)\rangle\,.$$

* Between the conduction band and heavy-hole valence band.

† Also called the adiabatic approximation; *viz.*, that the electron, by virtue of its tiny mass relative to that of the ion cores, is unaffected by the *motion per se* of the cores, instantaneously adjusting its state to any momentary ionic distribution.

The angle brackets refer to statistical integrals for arbitrary nonparabolic bands. For a generalized quantity $A(\epsilon)$, its mean value is given by

$$\langle A(\epsilon)\rangle = \int_0^\infty \left(-\frac{\partial f_0}{\partial \epsilon}\right) A(\epsilon)k^3(\epsilon)d\epsilon\,.$$

The quantities ϕ_i are the trial functions which are used in the variational procedure to estimate $\Phi(\epsilon)$. *S&D* refer to $\phi_i = (\epsilon/k_B T)^i$ as the most common choice for a non-degenerate semiconductor. Finally (prior to examining individual scattering terms in the sections below), the scattering operator $L(\phi_i)$ is given by

$$L(\phi_i) = \frac{m_e^*}{|e|}\mathcal{T}(\phi_i) + \phi_i\frac{m_e^*}{|e|}\mathcal{D} + \phi_i\sum_s \frac{1}{\mu_s}, \tag{2.20}$$

where $\mu_s = |e|\tau_s/m_e^*$, and the various τ_s are presented below.

2.5.2 *Polar Optical Phonon Scattering*

PO scattering results from the long-range electric fields that arise from LO phonons, i.e., the relative movements of atoms or ions of opposite polarity within a unit cell, that momentarily destroy local charge neutrality in a polar crystal. It has long been appreciated as the predominant scattering mode in indium antimonide at room temperature.

The long range nature of PO scattering implies, by virtue of its few k-components, that most of the scattering events will be intra-valley. The scattering is in general highly inelastic because of the large magnitude of $\hbar\omega_{LO}$ (many meV), a quantity that stays fairly constant over the entire Brillouin zone. However, interactions are constrained to those phonons near the zone center (i.e., those with large wavelength).

The polar interaction energy is given by

$$\mathcal{H}_{PO} = \int \rho(\boldsymbol{R})\phi(\boldsymbol{R})\,d\boldsymbol{R}, \tag{2.21}$$

where $\boldsymbol{R}$ is the vector to a unit cell, ρ refers to charge density, and ϕ is the electric potential arising from the polarization of the lattice. This polarization, $\boldsymbol{P}(\boldsymbol{R})$, is given by $e^*\boldsymbol{u}(\boldsymbol{R})/\Omega$, where e^* is *defined* as the effective charge, dealt with at length below, on each atom in the

unit cell, Ω is the latter's volume, and $\boldsymbol{u}(\boldsymbol{R})$ is the "optical displacement" within the unit cell: Polarization is equivalent to a bound space charge density given by $-\nabla \cdot \boldsymbol{P}$. When $\boldsymbol{u}(\boldsymbol{R})$ is expanded in terms of plane waves oriented with respect to the symmetry of the crystal, only those modes effecting a change in the distance between adjacent crystal planes will give rise to a polarization; i.e., the longitudinal modes.

Eq. 2.21 can be rewritten as

$$\mathcal{H}_{\mathrm{PO}} = \int \nabla \cdot \boldsymbol{D}(\boldsymbol{R})\phi(\boldsymbol{R})\, d\boldsymbol{R} = -\int \boldsymbol{D}(\boldsymbol{R}) \cdot \boldsymbol{P}(\boldsymbol{R})\, d\boldsymbol{R}. \tag{2.22}$$

Using the substitutions

$$\boldsymbol{D}(\boldsymbol{R}) = -\nabla \left[\frac{e}{|\boldsymbol{r} - \boldsymbol{R}|} \exp(-q_0 |\boldsymbol{r} - \boldsymbol{R}|) \right] \tag{2.23}$$

(wherein the exponential term represents the screening of a Thomas-Fermi potential and q_0 is the reciprocal Debye screening length) and

$$\boldsymbol{u}(\boldsymbol{R}) = \frac{1}{\sqrt{N}} \sum_{\boldsymbol{q}} [Q_{\boldsymbol{q}} \boldsymbol{a}_{\boldsymbol{q}} \exp(i\boldsymbol{q} \cdot \boldsymbol{R}) + \text{c.c.}],$$

the expansion of $\boldsymbol{u}(\boldsymbol{R})$ into plane waves, where N is the number of unit cells in the crystal, the $Q_{\boldsymbol{q}}$ are the normal coördinates, $\boldsymbol{a}_{\boldsymbol{q}}$ is the unit polarization vector, and "c.c." stands for the complex conjugate, the Hamiltonian can be integrated and rewritten

$$\mathcal{H}_{\mathrm{PO}} = -\frac{1}{\sqrt{N}} \frac{ee^*}{\Omega} \sum_{\boldsymbol{q}} \frac{q}{q^2 + q_0^2} [iQ_{\boldsymbol{q}} \exp(i\boldsymbol{q} \cdot \boldsymbol{r}) + \text{c.c.}]. \tag{2.24}$$

With a transition rate from first order perturbation theory given by

$$W = \int \frac{2\pi}{\hbar} |\langle \mathrm{f} | \mathcal{H}_{\mathrm{int}} | \mathrm{i} \rangle|^2 \, \delta(E_{\mathrm{f}} - E_{\mathrm{i}})\, dS_{\mathrm{f}}, \tag{2.25}$$

where $\langle \mathrm{f}|$ and $|\mathrm{i}\rangle$ are the final and initial states, and the integral is over all final states S_{f}, the following form is obtained for the PO scattering rate, assuming spherical *parabolic* bands,

and neglecting screening:

$$W(k) = \frac{\Omega}{2\pi\overline{M}\hbar\omega_{\mathrm{LO}}v_{\mathrm{e}}}\left(\frac{ee^*}{\Omega}\right)^2\left[n(\omega_{\mathrm{LO}})\sinh^{-1}\left(\frac{E_k}{\hbar\omega_{\mathrm{LO}}}\right)^{1/2}\right.$$
$$\left. + [n(\omega_{\mathrm{LO}})+1]\sinh^{-1}\left(\frac{E_k}{\hbar\omega_{\mathrm{LO}}}-1\right)^{1/2}\right], \tag{2.26}$$

where $\overline{M}$ is the reduced mass of the unit cell. The second term in the large brackets, which corresponds to phonon emission, is to be set equal to 0 if $E_k < \hbar\omega_{\mathrm{LO}}$, i.e., if there is not sufficient energy to emit a phonon.

The effective charge used above has profound consequences for the permittivities, at different frequencies, of a semiconductor. At high frequencies, the ionic contribution to the polarization becomes negligible, while at low frequencies, both it and the electronic component are important. It can be shown (RIDLEY, 1988) that

$$e^{*2} = \overline{M}\Omega\omega_{\mathrm{LO}}^2\left(\frac{1}{\kappa_\infty}-\frac{1}{\kappa_0}\right). \tag{2.27}$$

In the case of III-V compounds, this can be approximated by

$$\left(\frac{e^*}{e}\right)^2 \approx 3\left(\frac{1}{\kappa_\infty}-\frac{1}{\kappa_0}\right). \tag{2.28}$$

S&D use the quasi-static approximation initially in order to express the screening among conduction band electrons. This approach is valid when $v_0 q \gg \omega_{\mathrm{LO}}$, where v_0 is the Fermi velocity, q is the longitudinal optic phonon wavevector and ω_{LO} is its frequency. When $v_0 q \not\gg \omega_{\mathrm{LO}}$, the electron mobility is slightly overestimated. For a non-degenerate semiconductor, this is equivalent to requiring that $k_{\mathrm{B}}T \gg \hbar\omega_{\mathrm{LO}}$, which is valid for narrow-gap semiconductors over almost the entire regime wherein free electron screening is significant. In indium antimonide, in particular, below room temperature, the approximation is not valid, but screening is in this case insignificant anyway due to the very low electron concentration.

The resulting expression for $\mathcal{T}_{\mathrm{PO}}$ in Eq. 2.20 is:

$$\mathcal{T}_{\mathrm{PO}}\big(\Phi(\epsilon)\big) = \frac{e^2\kappa_{\mathrm{L}}\omega_{\mathrm{TO}}^2}{\hbar^2\kappa_\infty^2\overline{\omega}_{LO}f_0 k}\{m_+^* f_{0+}(N_q+1)V_+\big(\Phi(\epsilon)\big) + m_-^* f_{0-}N_q h_-(\epsilon)V_-\big(\Phi(\epsilon)\big)\}.$$

Here, κ_L is the lattice contribution to the static dielectric constant, and is equal to the difference between κ_0 and κ_∞; $\overline{\omega}_{LO}$ is a mean value of $\omega_{LO}(q)$ (the dispersion of which with respect to q would complicate further calculations); N_q is the optical phonon number, which, based on Bose-Einstein statistics is $[\exp(\hbar\overline{\omega}_{LO}/k_B T) - 1]^{-1}$;

$$h_-(x) = \begin{cases} 1 & \text{if } x \geq \hbar\overline{\omega}_{LO} \\ 0 & \text{if } x < \hbar\overline{\omega}_{LO}; \end{cases}$$

and finally

$$V_{\pm}(\Phi(\epsilon)) = \frac{1}{2}\left(\Phi - \frac{k_{\pm}^2 + k^2}{2k^2}\Phi_{\pm}\right)\left[\rho_{0\pm} + \rho_{1\pm}\frac{k_{\pm}^2 + k^2}{2kk_{\pm}} + \rho_{2\pm}\left(\frac{k_{\pm}^2 + k^2}{2kk_{\pm}}\right)^2\right]$$

$$\times\left[\ln\left(\frac{1 + \lambda_e^2 K_{\pm}^{(+)^2}}{1 + \lambda_e^2 K_{\pm}^{(-)^2}}\right) - \frac{4\lambda_e^2 k_{\pm} k}{(1 + \lambda_e^2 K_{\pm}^{(+)^2})(1 + \lambda_e^2 K_{\pm}^{(-)^2})}\right]$$

$$+\left\{-\left(\Phi - \frac{k_{\pm}^2 + k^2}{2k^2}\Phi_{\pm}\right)\left(\rho_{1\pm}\frac{1}{4\lambda_e^2 kk_{\pm}} + \rho_{2\pm}\frac{k_{\pm}^2 + k^2}{4\lambda_e^2 k^2 k_{\pm}^2}\right)\right.$$

$$\left. + \Phi_{\pm}\frac{1}{4\lambda_e^2 k^2}\left[\rho_{0\pm} + \rho_{1\pm}\frac{k_{\pm}^2 + k^2}{2kk_{\pm}} + \rho_{2\pm}\left(\frac{k_{\pm}^2 + k^2}{2kk_{\pm}}\right)^2\right]\right\}$$

$$\times\left[4\lambda_e^2 kk_{\pm} - 2\ln\left(\frac{1 + \lambda_e^2 K_{\pm}^{(+)^2}}{1 + \lambda_e^2 K_{\pm}^{(-)^2}}\right) + \frac{4\lambda_e^2 k_{\pm} k}{(1 + \lambda_e^2 K_{\pm}^{(+)^2})(1 + \lambda_e^2 K_{\pm}^{(-)^2})}\right]$$

$$+\left[\rho_{2\pm}\frac{1}{8\lambda_e^4 k^2 k_{\pm}^2}\left(\Phi - \frac{k_{\pm}^2 + k^2}{2k^2}\Phi_{\pm}\right) - \Phi_{\pm}\left(\rho_{1\pm}\frac{1}{8\lambda_e^4 k^3 k_{\pm}} + \rho_{2\pm}\frac{k_{\pm}^2 + k^2}{8\lambda_e^4 k^4 k_{\pm}^2}\right)\right]$$

$$\times\left[4\lambda_e^4 kk_{\pm}(k_{\pm}^2 + k^2) - 8\lambda_e^2 kk_{\pm} + 3\ln\left(\frac{1 + \lambda_e^2 K_{\pm}^{(+)^2}}{1 + \lambda_e^2 K_{\pm}^{(-)^2}}\right)\right.$$

$$\left. - \frac{4\lambda_e^2 k_{\pm} k}{(1 + \lambda_e^2 K_{\pm}^{(+)^2})(1 + \lambda_e^2 K_{\pm}^{(-)^2})}\right]$$

$$+\Phi_{\pm}\rho_{2\pm}\frac{1}{16\lambda_e^6 k^4 k_{\pm}^2}\left[3\lambda_e^2(K_{\pm}^{(+)^2} - K_{\pm}^{(-)^2}) - \lambda_e^4(K_{\pm}^{(+)^4} - K_{\pm}^{(-)^4})\right.$$

$$+\frac{1}{3}\lambda_e^6(K_{\pm}^{(+)^6} - K_{\pm}^{(-)^6}) - 4\ln\left(\frac{1 + \lambda_e^2 K_{\pm}^{(+)^2}}{1 + \lambda_e^2 K_{\pm}^{(-)^2}}\right)$$

$$\left. + \frac{4\lambda_e^2 k_{\pm} k}{(1 + \lambda_e^2 K_{\pm}^{(+)^2})(1 + \lambda_e^2 K_{\pm}^{(-)^2})}\right].$$

In this expression, the subscripts $\pm$ indicate that the corresponding quantity is evaluated at $\epsilon \pm \hbar\bar{\omega}_{\mathrm{LO}}$; $K_{\pm}^{(+)} = k_{\pm} + k$; $K_{\pm}^{(-)} = k_{\pm} - k$; $\lambda_e^2 = \kappa_e/(k_e^{\mathrm{TF}})^2$, where κ_e is a formally defined quantity which will, in the present circumstances, be replaced simply by κ_∞, and k_e^{TF} is the

Thomas-Fermi momentum, given by

$$(k_e^{\mathrm{TF}})^2 = \frac{4e^2}{\pi\hbar^2}\int_0^\infty \left(-\frac{\partial f_0}{\partial \epsilon}\right) m_e^* k \, d\epsilon;$$

and $\rho_{n\pm} = \rho_n(k, k_\pm)$, where the various $\rho_n(k, k')$ are scattering parameters for an electron being scattered from $\boldsymbol{k}$ to $\boldsymbol{k}'$:

$$\rho_0(k,k') = (aa')^2 + \frac{1}{4}(bb')^2 + bb'\frac{bc'+cb'}{\sqrt{2}} + \frac{(bc'+cb')^2}{2},$$

$$\rho_1(k,k') = 2(aa')(bb'+cc'),$$

$$\rho_2(k,k') = \frac{3}{4}(bb')^2 + bb'\frac{bc'+cb'}{\sqrt{2}} + 2(bb')(cc') - \frac{1}{2}(bc'+cb')^2 + (cc')^2.$$

In these expressions, the coefficients are those given in Eq. 2.15, with the primes indicating that they must be evaluated at the energy corresponding to phonon emission or absorption, i.e., at $\epsilon \pm \hbar\overline{\omega}_{\mathrm{LO}}$. In non-degenerate indium antimonide, the dispersion of ω_{LO} is very minor, so in the present calculations, $\overline{\omega}_{\mathrm{LO}}$ will be replaced universally by the constant ω_{LO} from Table 1.1. Furthermore, by the same token, the screening length λ_e will be replaced by the simply evaluated

$$\lambda = \sqrt{\frac{\kappa_\infty k_{\mathrm{B}} T}{4\pi e^2 n}}.$$

The interband scattering term in this instance is given by another very lengthy expression; however, in the case of indium antimonide, the band-gap is larger than the LO-phonon energy, so the $\mathcal{D}_{\mathrm{PO}}$ contribution to Eq. 2.20 vanishes.

2.5.3 *Optical Deformation Potential Scattering*

OD scattering reflects the deformation by optical modes of the periodic lattice potential, resulting in comparatively short-range but immediate energy variations in the electron wavefunctions.

The interaction Hamiltonian for electrons and optical phonons is*

$$\mathcal{H}_{\mathrm{PO}} = \mathfrak{D}_o \cdot \boldsymbol{u} \tag{2.29}$$

where $\mathfrak{D}$ is the optical deformation potential constant, and $\boldsymbol{u}$ is the relative displacement of the two different atoms in the unit cell.

It is found empirically that acoustic strain is connected to the polarization of a crystal by the relation

$$\boldsymbol{D}_i = \sum_j \epsilon_{ij} \mathcal{E}_j + \sum_{k,l} e_{ikl} S_{kl}, \tag{2.30}$$

where the ϵ_{ij} are elements of the dielectric tensor, e_{ikl}, the elements of the piezoelectric constant tensor, $\boldsymbol{e}$, and S represents the strain tensor.

Since the free charge is 0, $\boldsymbol{D} = 0$, and the elements of the polarization vector are given by

$$P_i = \frac{1}{\kappa} \sum_{k,l} e_{ikl} S_{kl}. \tag{2.31}$$

The interaction Hamiltonian is thus given by

$$\mathcal{H}_{\mathrm{OD}} = \int \boldsymbol{D}(\boldsymbol{R}) \boldsymbol{P}(\boldsymbol{R})\, d\boldsymbol{R}, \tag{2.32}$$

with $\boldsymbol{D}(\boldsymbol{R})$ in this case given by Eq. 2.23, as screening is important.

As OD scattering becomes comparable to that of other modes only at $n \approx 10^{19}\ \mathrm{cm}^{-3}$, it will be ignored.

* This equation has a few variants, depending on definitions used. See, e.g., RIDLEY (1988).

2.5.4 *Acoustic Phonon Scattering*

Piezoelectric scattering, like PO scattering, is usually an intra-valley event. Because the energy of the phonon is so small (~1 meV), collisions are approximately elastic. However, it should be noted that an electron's wavevector may change direction appreciably in such an interaction, even though its magnitude is fundamentally constant. Because of the need to satisfy both energy and momentum conservation, there is a limitation in the range of phonon wavevector that may interact with an energy. In the case of PE and AD scattering, only the long-wavelength modes (from the zone center) may interact.

Briefly, the interaction potential brought about by the deformation of the lattice is given by

$$\mathcal{H}_{\mathrm{AD}} = \sum_{ij} \Xi_{ij} S_{ij}, \tag{2.33}$$

where Ξ_{ij} is an element of the deformation potential tensor, equal to the change in energy of the band-edge per unit of elastic strain. Strain is defined by the strain tensor

$$S_{ij} = S_{ji} = \frac{1}{2}\left(\frac{\partial u_i}{\partial x_j} + \frac{\partial u_j}{\partial x_i}\right), \tag{2.34}$$

where u_i represents the displacement of a unit cell in the ith direction, i.e., x_i, x_j or x_k. This strain represents the differential displacement of one cell relative to its neighbor. In cubic crystals, there are three independent components to the strain tensor, commonly denoted Ξ_{d}, Ξ_{u} and Ξ_{p}. The symmetry of the Γ, X and L valleys lowers this number to two, Ξ_{d} and Ξ_{u}. The former, which in indium antimonide is 14.6 eV for the Γ-minimum (LANDOLT-BÖRNSTEIN, 1987), relates to pure dilation of the lattice, while the latter corresponds to pure shear consisting of uniaxial stretch along the major axis and symmetrical compression along the other two minor axes. While the Γ-minimum is independent of Ξ_{u}, it does depend on Ξ_{d}, which can be altered with hydrostatic pressure.

There is no significant acoustic phonon scattering in indium antimonide at room temperature or below, except in samples of the highest electron concentration (i.e., $n \approx 10^{19}$ cm^{-3}).

2.5.5 *Charge Center Scattering*

Charge center (CC) scattering refers to relatively localized electron scattering events due to Coulombic interaction with either ionized impurities (II scattering) or holes. Perturbation treatments in this case would in many instances be insufficient, as the strong core potentials involved can radically alter an electron's state.

The general approach for II scattering is to consider the impurities dispersed throughout the semiconductor with a Holtsmark distribution, wherein interactions are divided into the almost constant but weak many-body interactions, and the less frequent but strong two-body interactions. Further simplification may be made by employing the Born approximation, but only for fast electrons: The rule of thumb is that to do so, $k^2 r_T^2$ must be $\gg 1$, where r_T is a characteristic scattering radius, which in the case of impurity ions is the effective Bohr radius, a^* (see Chapter IV). In the opposite extreme ($k^2 r_T^2 \ll 1$), the method of phase shifts of partial waves is often used. CC scattering is largely intra-valley, though inter-valley capture and emission processes are observable (RIDLEY, 1988). In all the treatments discussed below, the approximation is made that the mobility depends on the overall concentration of impurity ions, N_I. However, the scattering cross-sections of attractive and repulsive potentials are in fact different (SEEGER, 1982). Further, no account is taken in them of either correlation effects (see § 4.6) or heterogeneity effects (see §§ 4.7 and 8.2, and PIOTRZKOWSKI ET AL, 1986), which are responsible for various anomalies in the mobility.

A remaining mathematical difficulty is that because the Coulombic potential is long-ranging, an infinite scattering cross-section is present. Numerous approaches to the problem have appeared over the years, as CC scattering is well-known to be the dominant scattering mechanism at low temperatures, and therefore has generated much interest. Two classic approaches are the Conwell-Weisskopf and the Brooks-Herring models.

Conwell and Weisskopf in 1950 employed classical Rutherford scattering theory, wherein an impact parameter b (the closest approach of an electron to a scatterer) is related to a scattering angle θ by the simple formula

$$b = \frac{Z\sqrt{\mathrm{Ry}^*}}{k\sqrt{\epsilon(k)}} \cot\left(\frac{\theta}{2}\right). \tag{2.35}$$

A maximum impact parameter is invoked, equal to half the average distance between ionized impurities, $N_I^{1/3}$. This results in a minimum scattering angle in Eq. 2.37 (see below), and a

finite scattering cross-section σ equal simply to $\pi b_{\max}^2$.

The final mobility formula is of the same form as the later Brooks-Herring equation (see Eq. 2.38 below), but here the bracketed term is of the form $\log(1+\beta_{\mathrm{CW}}^2)$, where

$$\beta_{\mathrm{CW}} = \frac{\kappa}{16}\left(\frac{T}{100°\mathrm{K}}\right)\left(\frac{2.35\times10^{19}\,\mathrm{cm}^{-3}}{N_{\mathrm{I}}}\right)^{\frac{1}{3}}. \tag{2.36}$$

The Brooks-Herring treatment of 1951 removed the infinities by invoking exponential carrier screening. While the resulting formula works well at high carrier concentrations, it breaks down when screening is absent, as the infinities return.

The momentum relaxation time in the Brooks-Herring model,

$$\tau_{\mathrm{m}} = \frac{1}{Nv2\pi\int_0^\pi \sigma(\theta)(1-\cos\theta)\sin\theta d\theta}, \tag{2.37}$$

was calculated by averaging over a Maxwell-Boltzmann distribution. The resulting mobility expression is

$$\mu_{\mathrm{CC}} = \frac{\dfrac{3.68\times10^{20}\,\mathrm{cm}^{-3}}{N_{\mathrm{I}}}\left(\dfrac{\kappa}{16}\right)^2\left(\dfrac{T}{100°\mathrm{K}}\right)^{\frac{3}{2}}}{\left(\dfrac{m_e^*}{m_0}\right)^{\frac{1}{2}}\left[\log(1+\beta_{\mathrm{BH}}^2)-0.434\beta_{\mathrm{BH}}^2/(1+\beta_{\mathrm{BH}}^2)\right]}, \tag{2.38}$$

where β_{BH} is a screening constant proportional to the Debye length:

$$\beta_{\mathrm{BH}} = \left(\frac{\kappa}{16}\right)^2\left(\frac{T}{100°\mathrm{K}}\right)\left(\frac{m_e^*}{m_0}\right)^{\frac{1}{2}}\left(\frac{2.08\times10^{18}\,\mathrm{cm}^{-3}}{n}\right)^{\frac{1}{2}}. \tag{2.39}$$

The major difference between the formulae these different models yield is that β_{CW} depends not on n but on N_{I}. As a result, the Conwell-Weisskopf mobilities differ from those predicted by the Brooks-Herring model rather dramatically at very high or very low carrier concentrations.

The behavior of μ_{CC}, the charge-center-scattering-limited mobility as a function of (low) temperature may be examined using relations presented by BATE ET AL. (1965) and BARRIE (1956). Generalizing for a nonparabolic energy band,

$$\mu = \frac{\sigma}{ne} = \frac{e\displaystyle\int_0^\infty \tau_{\mathrm{m}}k^2\left(\frac{d\epsilon}{dk}\right)\left(-\frac{\partial f_0}{\partial\epsilon}\right)d\epsilon}{3\hbar^2\displaystyle\int_0^\infty f_0k^2\left(\frac{d\epsilon}{dk}\right)^{-1}d\epsilon}. \tag{2.40}$$

For a nonparabolic band, τ_{CC}, the relaxation time corresponding to charge center scattering is given by

$$\frac{1}{\tau_{CC}} = \frac{2\pi e^4 N_I}{\hbar\kappa^2}\frac{1}{k^2 d\epsilon/dk}\left\{\ln[1+(2ka)^2] - \frac{1}{1+(1/2ka)^2}\right\},$$

where N_I is the concentration of ionized impurities, κ is the pressure-dependent dielectric constant ($\kappa \approx 16.27\exp(-0.011P)$,* where P is the hydrostatic pressure in kilobars), and a is a screening length calculated for a nonparabolic band:

$$a^2 \approx \frac{\kappa k_B T}{2\pi n e^2}\frac{F_{1/2}(\eta)}{F_{-1/2}(\eta)}\left[1+\frac{5k_BT}{2E_g}\left(\frac{F_{3/2}(\eta)}{F_{1/2}(\eta)} - 3\frac{F_{1/2}(\eta)}{F_{-1/2}(\eta)}\right)\right],$$

where $E_g \gg \epsilon_F, k_BT$.

For indium antimonide at low temperatures, *Z&S* provide the following formula:

$$\frac{1}{\tau_{CC}} = \frac{2\pi e^4 N_I m_e^*}{\hbar^3 k^3 \kappa_0^2} F_{CC}, \tag{2.41}$$

where

$$F_{CC} = \ln(1+\xi) - \frac{\xi}{1+\xi} + 4A'\left[1+\frac{1}{1+\xi} - \frac{2}{\xi}\ln(1+\xi)\right]$$
$$+ 2B'\left[1 - \frac{4}{\xi} + \frac{6}{\xi^2}\ln(1+\xi) - \frac{2}{\xi(1+\xi)}\right],$$

in which $\xi = 4k^2\lambda^2$ (λ is the screening length), while

$$A' = b^2\left(\frac{b}{2} - c\sqrt{2}\right)^2 - (b^2+c^2)$$

and

$$B' = (b^2+c^2)^2 - b^2\left(\frac{b}{2} - c\sqrt{2}\right)^2,$$

with the values a, b and c given by Eq. 2.15. The aforementioned screening length is given for the general case as

$$\lambda^2 = \frac{\kappa_s}{(k_e^{TF})^2 + (k_h^{TF})^2},$$

* ZAWADZKI & WŁASAK, 1984: The best fit to their results.

where κ_s is the static dielectric function comprising κ_∞ and κ_L, the lattice contribution to the static dielectric constant, k^{TF} refers to Thomas-Fermi momentum and the scripts 'e' and 'h' refer to electrons and holes respectively. In the case of non-degenerate semiconductors, however, the above expression for screening length is simply:

$$\lambda = \sqrt{\frac{\kappa_0 k_B T}{4\pi e^2 n}}.$$

Eq. 2.41 can also be applied to electron-hole scattering, if N_I is replaced by p. According to EHRENREICH (1957), however, hole scattering is negligible in indium antimonide below ~500°K.

2.5.6 *Neutral Impurity Scattering*

The mobility as limited by neutral impurity scattering, wherein the scattering cross-section is $\sigma \approx 20a^*/k$ for $ka^* < 0.5$,* is (SEEGER, 1982):

$$\mu = \frac{e}{20a_B\hbar}\frac{m_e^*/m_0}{\kappa N_I} \approx \frac{1.44 \times 10^{22}\,\mathrm{cm}^{-3}}{N_I}\frac{m_e^*/m_0}{\kappa}, \tag{2.42}$$

a quantity independent of temperature, where in this case N_I refers to the concentration of neutral impurities. In indium antimonide, this mobility may work out to $\sim 10^6$ cm^2 V^{-1}sec^{-1}, substantially higher than that observed. As such, it has been regarded as unimportant at all temperatures, but this may not be the case with a very impure sample of, say, $N_I \approx 10^{15}$ cm^{-3}, where the mobility would be only $\sim 10^5$ cm^2 V^{-1}sec^{-1}.

2.6 Hall Experiments

The Hall coefficient R_H is equal to r_H/nec in the low field limit, where the Hall factor, r_H, is equal to $\langle\tau_m^2\rangle / \langle\tau_m\rangle^2$ for spherical energy surfaces,† and where τ_m is the momentum

* Due to ERGINSOY, 1950.

† For ellipsoidal surfaces, a factor of

$$\frac{3\gamma(\gamma+2)}{(2\gamma+1)^2},$$

where γ is the ratio of the longitudinal to the transverse effective mass, must be included in r_H.

relaxation time. When ionized impurity scattering, dominant at 77°K, is considered alone, for example, $r_H \approx 315\pi/512 \approx 1.93$, if τ is taken to be proportional to $\epsilon^{3/2}$ (where ϵ is the conduction band energy), but this is dependent on the material, temperature and pressure. r_H is normally defined in the low magnetic field limit where $\mu B \ll 1$, as the Hall constant R_H approaches $1/ne$ only in the high-field limit in a single carrier system. In indium antimonide, this low-field limit would correspond to a field at 77°K of $\ll 0.02$ T, or at 290°K of $\ll 0.15$ T. For an energy-independent scattering mechanism, r_H would equal 1.

CHAPTER III

Magnetic Fields and Cyclotron Resonance in Indium Antimonide

In this chapter, the variation with magnetic field of the band structure of indium antimonide and of the wavefunctions of impurities in the bulk are discussed. The theory of cyclotron resonance is reviewed, as well as that of the linewidths and lineshapes of the resonance peaks. It will prove convenient to work in the dimensionless magnetic field $\gamma = \hbar\omega_c/2\mathrm{Ry}^*$, where ω_c is the cyclotron frequency (see below) and Ry^* is the effective Rydberg (see Chapter IV), i.e., the binding energy of an electron to a hydrogen-like donor ($1\,\mathrm{Ry}^* = m_e^* e^4/2\hbar^2\kappa^2 = (m_e^*/m_0\kappa^2) \times 13.6\,\mathrm{eV}$). In indium antimonide at 4.2°K, $1\,\mathrm{Ry}^*_{(P=0)} = 0.653\,\mathrm{meV}$, and at $B = 1\,\mathrm{T}$, $\gamma \approx 6.5$.

3.1 Charge Carriers in a Magnetic Field

3.1.1 Free Electron in a Magnetic Field

The classical Hamiltonian of a free electron in a magnetic field is

$$\mathcal{H} = \frac{(\boldsymbol{p} - e\boldsymbol{A})^2}{2m_0} + V(\boldsymbol{r}), \tag{3.1}$$

where $\boldsymbol{A}$ is the magnetic vector potential, and the canonical conjugate momentum of an electron is $\boldsymbol{p} - e\boldsymbol{A}$. Quantum mechanically, this is expressed as

$$\mathcal{H} = \frac{(-i\hbar\nabla - e\boldsymbol{A})^2}{2m_0} + V(\boldsymbol{r}). \tag{3.2}$$

If $\boldsymbol{B}$ is taken as $(0, 0, B)$, then one possible solution for the vector potential is $\boldsymbol{A} = (-yB, 0, 0)$, and in free space ($V = 0$) the wavefunction of the electron, ψ, satisfies the Schrödinger equation

$$-\frac{\hbar^2}{2m_0}\nabla^2\psi - \frac{i\hbar eB}{m_0}\frac{y\partial\psi}{\partial x} + \frac{e^2B^2y^2}{2m_0}\psi = E\psi(\boldsymbol{r}). \tag{3.3}$$

This is a separable equation, with $\psi(x, y, z) = e^{i(k_x x + k_z z)}\varphi(y)$. It can be demonstrated (KIREEV, 1978) that Eq. 3.3 can then be rewritten as

$$-\frac{\hbar^2}{2m_0}\frac{d^2\varphi(y')}{dy'^2} + \frac{m_0{\omega_c}^2y'^2}{2}\varphi(y') = \left(E - \frac{\hbar^2k_z^2}{2m_0}\right)\varphi(y'), \tag{3.4}$$

where y' represents a translation transformation of the original coördinate y by a constant $\hbar k_x/eB$ and $\omega_c = eB/m_0$. Eq. 3.4 is that for a harmonic oscillator, with solutions

$$E - \frac{\hbar^2k_z^2}{2m_0} = \hbar\omega_c\left(N + \frac{1}{2}\right). \tag{3.5}$$

Eq. 3.5 describes an electron with motion unconstrained in the direction parallel to the magnetic field, but quantized in the perpendicular plane into discrete orbits of radii

$$r_N \approx \sqrt{\frac{2\hbar}{m_0\omega_c}\left(N + \frac{1}{2}\right)} = \sqrt{\frac{2\hbar}{eB}\left(N + \frac{1}{2}\right)} \tag{3.6}$$

(where the approximation sign reflects the fact that these are only expectation values of radial position, which does not, as a quantum mechanical operator, commute with energy). The various solutions for the energy are the so-called Landau levels of quantum number N, and ω_c is the cyclotron resonance frequency.

In a crystal, there exists a periodic potential V, which can be taken into account by replacing the free electron mass by an effective mass m_e^*. The solutions for the Landau levels in this case, if the magnetic field is taken to be in the z-direction, are as before:

$$\epsilon = (N + 1/2)\hbar\omega_c + \hbar^2k_z^2/2m_e^*,$$

where now $\omega_c = eB/m_e^*$. The electrons in a spherically symmetric conduction band will again be constrained to circular orbits in the x-y plane, and unconstrained in the z-direction.*

* Inasmuch as most semiconductor conduction bands deviate from perfect sphericity, the radii of Eq. 3.6 (in which m_0 must be replaced by m_e^* anyway) are only approximate.

Each orbit is separated energetically by $\hbar\omega_c$. This implies that the resulting quantization phenomena such as magnetic permeability/susceptiblity oscillations (the de Haas-van Alphen effect in metals and degenerate semiconductors) and the Shubnikov-de Haas effect and its two-dimensional analog, the quantum Hall effect, will be visible only in fields and at temperatures such that $k_B T \ll \hbar\omega_c$, i.e., the thermal broadening is less than the level separation. This can be expressed as the requirement that B (Tesla) $\gtrsim (m_e^*/m_0)\, T(°\mathrm{K})$. (The de Haas-van Alphen effect, furthermore requires that $\epsilon_F \gg k_B T$, and that $\mu B \gg 1$.)

The so-called "quantum limit" is reached when only the lowest band ($N = 0$) is populated.*

The per unit volume density of states in a magnetic field can be expressed as

$$N_B(\epsilon) = \frac{\hbar\omega_c}{2}\left[2\pi\left(\frac{2m_e^*}{h^2}\right)^{\frac{3}{2}}\right]\sum_{N=0}^{\nu}[\epsilon - \hbar\omega_c(N + 1/2)]^{-\frac{1}{2}}, \tag{3.7}$$

where ν is the number of Landau levels accessible to electrons of energy ϵ, i.e., $\nu \leq (\epsilon - \hbar\omega_c/2)/\hbar\omega_c < \nu + 1$. This results in the well-known series of apices of state density, each of which decreases as $\epsilon^{-1/2}$ (see Fig. 3.1).

(In Eq. 3.7, the magnetic moment of the electron, and hence the energy-splitting (Zeeman splitting) resulting therefrom, has been neglected. The electron has a magnetic moment $\boldsymbol{\mu}_0^*$ of magnitude equal to the Bohr magneton ($\mu_B = e\hbar/2m_0 \equiv 58\,\mu\mathrm{eV\,T^{-1}}$) multiplied by g^*, the effective Landé g-factor of the electron, which in indium antimonide at 4.2°K is -50.6.† The energy-splitting is equal to the scalar product of $\boldsymbol{\mu}_0^*$, the magnetic field induction $\boldsymbol{B}$, and the difference of the spin quantum numbers $\hat{S} = \pm 1/2$: $\Delta\epsilon_\pm = \hat{S}_\pm \boldsymbol{\mu}_0^* \cdot \boldsymbol{B}$, or about $1.47\,\mathrm{meV\,T^{-1}}$ in indium antimonide.)

For a non-degenerate semiconductor, in the classical approximation (see § 2.3), if the

---

* The lowest allowed energy, $\frac{1}{2}\hbar\omega_c$, is the so-called zero-point energy, and its difference from 0 is a manifestation of the uncertainty principle.

† $g^* = 2\left(1 - \dfrac{m_0/m_e^* - 1}{2 + 3E_g/\Delta}\right)$ for $E_g \ll$ energies of higher bands, i.e., $\lesssim 1$ eV. For a free electron, $g = 2.0036$.

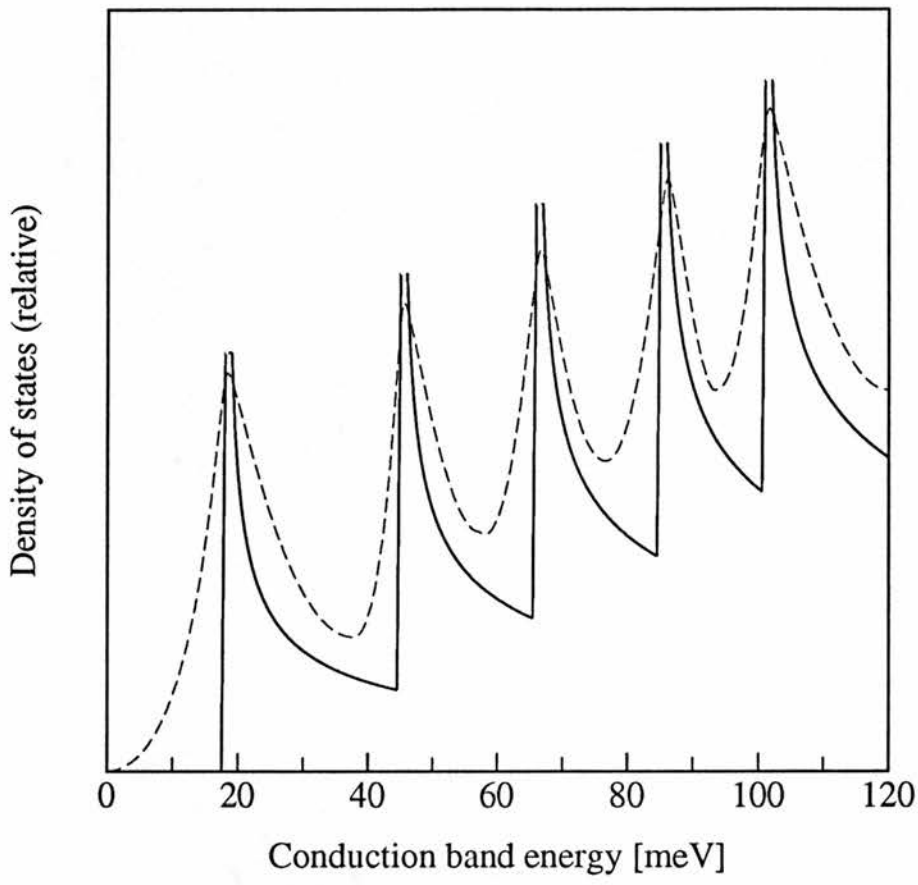

FIG. 3.1: Density of states for Landau levels in indium antimonide at 5 T. The solid lines show the theoretical result, while the dashed line shows a typical real situation, where scattering has smoothed out the infinities (see § 3.3.4). In indium antimonide, the magnitude of the spin-splitting (not shown here) is about one third the spacing of the Landau levels.

Fermi energy is known, then the electron concentration can be expressed as

$$n = \hbar\omega_c \left[2\pi \left(\frac{2m_e^*}{h^2} \right)^{\frac{3}{2}} \right] \exp\left(\frac{\epsilon_F(B)}{k_B T} \right) \times \sum_{N=0}^{\nu} \int_{\hbar\omega_c(N+1/2)}^{\infty} \frac{1}{\sqrt{\epsilon - \hbar\omega_c(N+1/2)}} \exp\left(-\frac{\epsilon}{k_B T} \right) d\epsilon. \tag{3.8}$$

(This is the magnetic field equivalent of Eq. 2.5.) This expression can be rearranged (KIREEV,

1978) to

$$n = \left(\frac{\hbar\omega_c}{2k_BT}\right) N_c \exp\left(\frac{\epsilon_F}{k_BT}\right) \left[\sinh\left(\frac{\hbar\omega_c}{2k_BT}\right)\right]^{-1}. \tag{3.9}$$

The magnetic field-dependent Fermi energy $\epsilon_F(B)$ can be found in a weak magnetic field ($\hbar\omega_c \ll k_BT$) to be $k_BT \ln(n/N_c)$, which is identical to the expression in Eq. 2.5. In a strong magnetic field,

$$\epsilon_F(B) = k_BT \ln \frac{2nk_BT}{N_c\hbar\omega_c} + \frac{\hbar\omega_c}{2}.$$

In each of these cases, N_c, as usual, is the effective number of states in the conduction band,

$$N_c = 2\left(\frac{2\pi m_e^{DS} k_BT}{h^2}\right)^{\frac{3}{2}}. \tag{3.10}$$

YAFET ET AL. (1956) express a quantity similar to N_c:

$$N_T = \frac{eH}{\pi^2\hbar^2 c}(2m_e^{DS}k_BT)^{\frac{1}{2}}, \tag{3.11}$$

such that N_T need merely be multiplied by the exponential term to yield n.

3.1.2 Free Carrier Absorption

If κ_r and κ_i are the real and imaginary parts respectively of the complex dielectric constant κ_0, the complex index of refraction and the extinction coefficient (see below) can be shown to be:

$$\boldsymbol{n} = \sqrt{\frac{1}{2}\left(\kappa_r + \sqrt{\kappa_r^2 + \kappa_i^2}\right)} \qquad \text{and} \qquad \boldsymbol{\kappa} = \sqrt{\frac{1}{2}\left(-\kappa_r + \sqrt{\kappa_r^2 + \kappa_i^2}\right)}. \tag{3.12}$$

Then, the coefficient of absorption of light in a semiconductor of complex index of refraction $\boldsymbol{n}$ is given by (KIREEV, 1978)*

* In this case what is meant by "absorption coefficient", also called the "attenuation constant" (JACKSON, 1975), is the quantity α such that the *intensity* of a beam in an absorptive medium falls off as $e^{-\alpha x}$. This is to be contrasted with the latter term's use to denote $\alpha/2 = k_i$, the (real) coefficient of the imaginary part of the wavevector, which is the rate at which the electric field *amplitude* falls off (as used, e.g., by LORRAIN & CORSON, 1970). This is again in contradistinction to the use of the former term by, e.g., LANDAU & LIFSHITZ (1960) and BLEANEY & BLEANEY (1976), to describe κ, the (real) coefficient of the imaginary part of the refractive index (here referred to as the "extinction coefficient"), which is equal to ck_i/ω.

$$\alpha = \frac{4\pi\sigma_0}{cn} = \frac{4\pi}{cn}\frac{e^2\langle\tau_{CR}\rangle}{m_e^*}n. \tag{3.13}$$

n, however, is dependent on the frequency of the incident light, ω. It can be shown that Eq. 3.13 may be expressed in terms of ω by

$$\alpha = \frac{4\pi ne^2}{cm_e^*}\frac{b}{\omega^2 + b^2}, \tag{3.14}$$

where $b \equiv \sqrt{\kappa}/\langle\tau_{CR}\rangle$. In the regime where $\omega^2 \ll b^2$, α remains virtually constant:

$$\alpha\Big|_{\omega^2 \ll b^2} \approx \alpha_0 = \frac{4\pi\sigma_0}{c\sqrt{\kappa}} = \frac{4\pi e^2\langle\tau_{CR}\rangle}{c\sqrt{\kappa}m_e^*}n.$$

On the other hand, for $\omega^2 \gg b^2$, we get from Eq. 3.14

$$\alpha\Big|_{\omega^2 \gg b^2} = \alpha_0\frac{\kappa}{\langle\tau_{CR}\rangle^2}\frac{\lambda^2}{4\pi^2}.$$

From this it can be seen that at higher frequencies, $\alpha \propto \lambda^2$, in which case $\alpha < \alpha_0$. Further, the point at which this transition occurs is $\omega_{trans} \approx \sqrt{\kappa}/\langle\tau_{CR}\rangle$. In practice, however, the actual dependence of α on λ will vary strongly among different modes of scattering. The reason for this is that in fact a perfectly free (i.e., undamped or unscattered) electron *cannot* absorb a photon, as momentum and energy could not be conserved simultaneously in this case. Absorption must proceed via interaction with the lattice, wherein electrons are scattered between energy states. In the simple case of a non-degenerate semiconductor with a parabolic conduction band, the approximation $\alpha \propto \lambda^p$ may be used, where the value of p is 3/2, 5/2 or 7/2 for acoustic phonon, optical phonon and impurity ion scattering, respectively (see Chapter II).

3.1.3 *Cyclotron Resonance*

Quantum mechanically, the salient feature of electrons in the Landau levels is that they can absorb or emit energy $\hbar\omega_c$, for instance in the form of radiation, and thus move between levels, i.e., they can exhibit cyclotron resonance. The probability of a transition from the Nth level to the $(N+1)$th is proportional to $(N+1)/m_e^*$.

It can be seen from classical physics that an electron in crossed (static) magnetic and electric fields in free space processes in a cycloid about the $\boldsymbol{B}$-vectors with frequency ω_c, and with drift velocity $\boldsymbol{v}_d = \boldsymbol{E} \times \boldsymbol{B}/B^2$. This occurs as well in semiconductors in the photoconductivity experiments described in Chapters VI and VIII, provided the Hall effect is not present (i.e., when the carriers would be restrained by the voltage created as they migrate toward one edge of the sample).

(This is of course in contrast with the case when $\boldsymbol{E} \parallel \boldsymbol{B}$, wherein the electron proceeds in a helix along the common vector, with its velocity component in that direction constant. This difference in motion evinces itself in, e.g., the Shubnikov-de Haas effect: When $\boldsymbol{E} \parallel \boldsymbol{B}$, scattering will simply "misdirect" an electron traveling in the direction of the fields, lowering the net current, or in effect, raising the resistance. In contrast, when $\boldsymbol{E} \perp \boldsymbol{B}$, a cycloidally (transversely) drifting electron will not be misdirected; it can be shown that small but finite scattering will lead to an increase in the conductivity, such that $\sigma_{xx} \approx nm_e^*/\tau B^2$, as the cycloidally drifting electrons tend to scatter preferentially in the direction of the applied E-field. The electron will likely be scattered into a volume of phase space that contains a greater density of states: In fact, the Landau levels, with a density of states dependent on both kinetic and potential energy, have higher densities of states *up* the potential gradient, and in some cases a velocity of this direction is imposed on the carriers.)

In the case of a plane-polarized oscillating electromagnetic field, it can be shown that the complex longitudinal velocity component of an electron is*

$$v = \mu E \frac{1 + i\omega\tau_{CR}}{(1 + i\omega\tau_{CR})^2 + \dfrac{e^2 {\tau_{CR}}^2}{{m_e^*}^2} B^2}$$

* In the expressions in this section, the relaxation time τ_{CR} is introduced. As will be made clear later, the lifetime associated with cyclotron resonance is distinct from that associated with, for example, DC conductivity, or many other phenomena.

$$= \mu E \frac{[1 + (\omega_c{}^2 + \omega^2)\tau_{CR}{}^2] + i\omega\tau_{CR}[(\omega_c{}^2 - \omega^2)\tau_{CR}{}^2 - 1]}{[1 + (\omega_c{}^2 - \omega^2)\tau_{CR}{}^2]^2 + 4\omega^2\tau_{CR}{}^2}.$$

The real part of the conductivity therefore is

$$\sigma(\omega) = e\mu n \frac{1 + (\omega_c{}^2 + \omega^2)\tau_{CR}{}^2}{[1 + (\omega_c{}^2 - \omega^2)\tau_{CR}{}^2]^2 + 4\omega^2\tau_{CR}{}^2}, \tag{3.15}$$

from which the following expression for optical absorption may be derived:

$$\alpha(\omega) = \alpha_0 \frac{1 + (\omega_c{}^2 + \omega^2)\tau_{CR}{}^2}{[1 + (\omega_c{}^2 - \omega^2)\tau_{CR}{}^2]^2 + 4\omega^2\tau_{CR}{}^2}. \tag{3.16}$$

This absorption represents the work done by the electric field component in displacing the electrons.

In order to observe cyclotron resonance in a semiconductor, it is necessary that electron collisions be kept below a certain limit: The rule of thumb is that an electron must be able to proceed uninterrupted through about one radian, or $\omega_c > 1/\tau_{CR}$. In this way, the electron can absorb at least one cycle of incoming circularly polarized radiation before a collision destroys its phase coherence with that radiation. With far-infrared laser excitation of 118.8 μ, for instance, it is necessary that $\tau_{CR} \gtrsim 10^{-13}$ s. Low temperatures and high magnetic fields are necessary to keep τ_{CR} and ω_c, respectively, large.

The sharpness of a cyclotron resonance can be expressed as

$$\begin{aligned} \omega_c\tau_{CR} &= \frac{\omega_c}{\Delta\omega_{1/2}} \\ &= \frac{B_c}{\Delta B_{1/2}}, \end{aligned} \tag{3.17}$$

where the '1/2' subscripted values refer to halfwidths of the resonances at half-height (but see § 3.3).

When $\omega_c{}^2\tau_{CR}{}^2 \gg 1$, Eq. 3.16 implies that for $\omega \ll \omega_c$, the absorption coefficient becomes independent of ω, and is approximately α_0/μ^2B^2. When $\omega \gg \omega_c$, $\alpha(\omega) \approx \alpha_0/\omega^2\tau_{CR}{}^2$. At frequencies near resonance, the absorption coefficient is maximal, with a value of approximately $\alpha_0/2$.

A cyclotron mass can be defined for electrons in cyclotron resonance. The effective mass of the electron in a highly nonparabolic band such as that of indium antimonide is very magnetic field dependent. In the general case (SHOCKLEY, 1950), the quasi-classical equation of motion of an electron in crossed magnetic and electric fields (the so-called Faraday configuration) can be written

$$\frac{d(\hbar k)}{dt} = \frac{e}{\hbar}[\nabla_k \varepsilon \times B].$$

This equation neglects both the electric field E and $1/\tau_m$ in the resonance state. It can be rewritten in cylindrical coördinates

$$\hbar \frac{dk_\varphi}{dt} = \hbar k \frac{d\varphi}{dt} = \frac{e}{\hbar} B \frac{\partial \varepsilon}{\partial k},$$

which after some rearrangement becomes

$$\hbar^2 \frac{k d\varphi}{\partial \varepsilon / \partial k} = eB dt = m_c \omega_c dt.$$

Integrating this over one revolution gives

$$m_c = \frac{\hbar^2}{2\pi} \oint \frac{k \, d\varphi}{\partial \epsilon / \partial k}.$$

PALIK ET AL. (1961) demonstrated that the effective cyclotron resonance mass m_c as defined by the equation $m_c = eB/\omega_c c$ varies strongly with magnetic field, becoming larger at higher fields due to nonparabolicity. Using the conduction band energy derived by BOWERS & YAFET (1959), based on Kane's model, an effective mass associated with a transition between two energy levels was expressed:

$$\frac{1}{m_c(B)} = \left(\frac{c}{\hbar e B}\right)[E(1,\ 0,\ +) - E(0,\ 0,\ +)], \tag{3.18}$$

where the +-sign refers to spin state, and

$$E(l,\ 0, \pm) = \frac{1}{2} E_g \left\{1 + \left[1 + 2\left(2l + 1 \mp \frac{1}{2}|g * |(m_0^*/m_0)\right)(\hbar\omega_{c;0}/E_g)\right]^{\frac{1}{2}}\right\}. \tag{3.19}$$

In Eq. 3.19, which is the magnetic field analog of Kane's expression, Eq. 2.18, $\omega_{c;0}$ refers to the cyclotron resonance frequency associated with the mass at the bottom of the band, m_0^*.

3.2 "Impurity-Shifted" Cyclotron Resonance

3.2.1 Hydrogenic Atom in a Magnetic Field

In the following chapter, the theory of shallow donors will be discussed, and Eq. 4.4, describing a donor electron in a semiconductor will be introduced. With the additional feature of a magnetic field applied to the hydrogenic system, the Hamiltonian of this electron can be expressed as

$$\left[\frac{1}{2m_0}(i\hbar\nabla + eA)^2 - \frac{e^2}{\kappa_0 r} + V_p(r) + \mu_B B \cdot \hat{S}\right] F'(r) = \epsilon F'(r)\,, \tag{3.20}$$

where $e^2/\kappa_0 r$ represents a screened ionic impurity potential, $V_p(r)$ is the lattice periodic potentialand $F'(r)$ refers to an envelope function, with the prime denoting the presence of a magnetic field. This equation ignores the effects of crystal anisotropy and of a nonparabolic conduction band. Calculations based on a parabolic band structure are reliable in nonparabolic semiconductors for the ground state only up to $\gamma \approx 10$ ($\sim$1.5 T in indium antimonide), and not even that for higher states (TRZECIAKOWSKI, 1986). Furthermore, use of the simple dielectric constant κ_0 ignores two screening problems: the so-called dynamical screening effects of polarons, and the effect on the screening potential itself of the magnetic field. According to LARSEN (1968), the effect of the former is negligible in indium antimonide at low carrier concentrations.

As above, the lattice potential and free electron mass can be replaced by the effective mass, while the spin and lattice potential together give rise to the effective Landé g factor. However, as above, the spin adds only a constant value to the energy, and so for the time being will be neglected. In a weak magnetic field ($\gamma \ll 1$), perturbation theory can be used to solve for the eigenenergies, while in a medium field ($\gamma \gtrsim 1$), the variational approach must be employed. Once the field becomes strong ($\gamma \gg 1$), the perturbation technique may be used again.

Taking the magnetic field $\boldsymbol{B}$ in the z-direction, setting $\boldsymbol{A} = \frac{1}{2}\boldsymbol{r} \times \boldsymbol{B}$ (the so-called symmetric gauge, where $\boldsymbol{A} = (-\frac{1}{2}yB, \frac{1}{2}xB, 0)$), Eq. 3.20 then simplifies to

$$(\mathcal{H}_0 + \mathcal{H}_1)\, F'(r) = \epsilon F'(r),$$

where

$$\mathcal{H}_0 = \frac{-\hbar^2\nabla^2}{2m_e^*} - \frac{e^2}{\kappa_0 r},$$

and the perturbation due to the magnetic field (the Zeeman interaction) is

$$\mathcal{H}_1 = \frac{-i\hbar\omega_c}{2}\left(\frac{x\partial}{\partial y} - \frac{y\partial}{\partial x}\right) + \frac{m_0{\omega_c}^2}{8}(x^2 + y^2).$$

Eq. 3.20 can be put conveniently into cylindrical polar coördinates and made dimensionless by expressing energy in Rydbergs, distance in units of the Bohr radius, and magnetic field in units of γ:

$$\left[-\nabla^2 + \gamma\hat{\mathcal{L}}_z + \frac{\gamma^2\rho^2}{4} - \frac{2}{r}\right] F'(\boldsymbol{r}) = \epsilon F'(\boldsymbol{r}), \tag{3.21}$$

where $\hat{\mathcal{L}}_z$ is the dimensionless operator $-i(\partial/\partial\phi)$, which yields the z-component of the orbital angular momentum, and where the coördinates are ρ, ϕ, z.

The solutions to Eq. 3.21, ignoring momentarily the Coulombic term, are of the form

$$F^0_{MNk} = \phi_{NM}(x, y)e^{ik_z z}$$

(where the ϕ_{NM} are the associated Laguerre polynomials), with eigenenergies $\epsilon_{NMk} = 2(N + 1/2)\gamma + \epsilon_z$, $N \geq M$. Here, M is the quantum number of $\hat{\mathcal{L}}_z$, N is the principal quantum number, k_z is the wavenumber of the electron in the z-direction (permitted to be $2\pi n_z/L_z$, where L_z is the length of the sample parallel to the magnetic field, and n_z is an integer), and ϵ_z is the kinetic energy in the z-direction, equal to $\hbar^2k^2/2m_0$, while the superscript 0 refers to the zeroth-order of a perturbational treatment of the Coulombic term. The limiting radius of these cylindrical wavefunctions is given by $[(2N-2M+1)\hbar/m_0\omega]^{1/2}$, which in the low temperature or quantum limit implies that the orbital radius is proportional to $\sqrt{2|M|+1}$, with the ground state corresponding to $M = 0$. The ionization energy is the difference between this ground state and the $M \to \infty$ states, wherein the Coulombic energy is so low, due to the large orbital radius, that the states are virtually free.

In a weak magnetic field ($\gamma \ll 1$), the Lorentz force is not comparable to the Coulombic force, and the electronic wavefunction is not radically altered by the field, although it is compressed in a plane normal to the magnetic field vector, and the energy of the parallel state is lower than that of the anti-parallel state. The ground state wavefunction is still proportional to $\exp(-\beta r^2)$, where β is a variational parameter.*

ARMISTEAD ET AL. (1982) investigated shallow impurity states in n-GaAs and n-InP in the intermediate field regime, where $\gamma \approx 1$. The mathematics becomes complicated, and

* Wavefunction compression, albeit isotropic, also results from the application of hydrostatic pressure.

the variational technique is usually applied. This will not be discussed here, but see e.g., MAKADO & MCGILL (1986) and WINTGEN & FRIEDRICH (1986).

When $\gamma \gg 1$, the electronic wavefunction is cigar-shaped, having become significantly smaller in the direction transverse to the field. This results in a dramatic lowering of the associated Coulombic energy (i.e., an increase in binding energy). In this case, the only permissible transitions between the ground state and the continuum states are those wherein the continuum state has $M = \pm 1$, where the positive and negative signs are for left and right circularly polarized radiation, respectively.

In the high field limit, for right circularly polarized light, and in the Faraday configuration, with the Poynting vector $\boldsymbol{S} \parallel \boldsymbol{B}$,* the selection rule is $\Delta N = \pm 1$, $\Delta M = -1$, and $\Delta\lambda$ even; while for plane polarized light, $\Delta N = 0$, $\Delta M = 0$, and $\Delta\lambda$ odd. (Left circularly polarized light is different from right only in that $\Delta M = +1$.)

The ionization energy of an impurity in a magnetic field will depend on the shift of the ground state relative to that of the continuum, and is therefore generally field-dependent. The magnetic field-spin interaction energies are equal in the ground state and the conduction band, and so do not contribute to the ionization energy field-dependence.

Neglecting spin, the conduction band energy in a magnetic field (the zero-point energy given in § 3.1) is given by

$$\frac{\hbar\omega_c}{2} = \frac{e\hbar}{2m_e^* c} H.$$

The energy of the ground state rises with increasing magnetic field, but not as fast as that of the conduction band. Therefore, ionization energy tends to increase with field.

TRZECIAKOWSKI ET AL. (1986) conclude that the chief effect of nonparabolicity on impurity-associated Landau levels is that of deepening all levels. This effect increases with γ and with N. The difference between the parabolic and nonparabolic energies in indium antimonide, for instance, is about 20% at ~3 T.

In a strong field, the conduction band of indium antimonide is broken up into Landau levels. WALLIS (1958) showed that the nonparabolicity of the conduction band in indium antimonide resulted in a successive "flattening" in the curvature of higher levels due to the increasing effective mass. A fourth order term proportional to $\hbar^4[k_z^4 + 4(eB/\hbar)(N + \frac{1}{2})k_z^2 + 4(eB/\hbar)^2(N + \frac{1}{2})^2]$ must be added to the energy of Eq. 3.5. This expression can be

* The complementary Voigt configuration, where $\boldsymbol{S} \perp \boldsymbol{B}$, tends to moderate the sharp peaks and valleys of the density of states of the Landau levels by virtue of a k_z^2 term that removes the singularities.

approximated to first order (ROBERT, 1979) simply by using for the effective mass in Eq. 3.5 the approximate value given by Eq. 2.19 from the Kane theory. This results in a set of bands as depicted in Fig. 3.2 (see § 3.3).

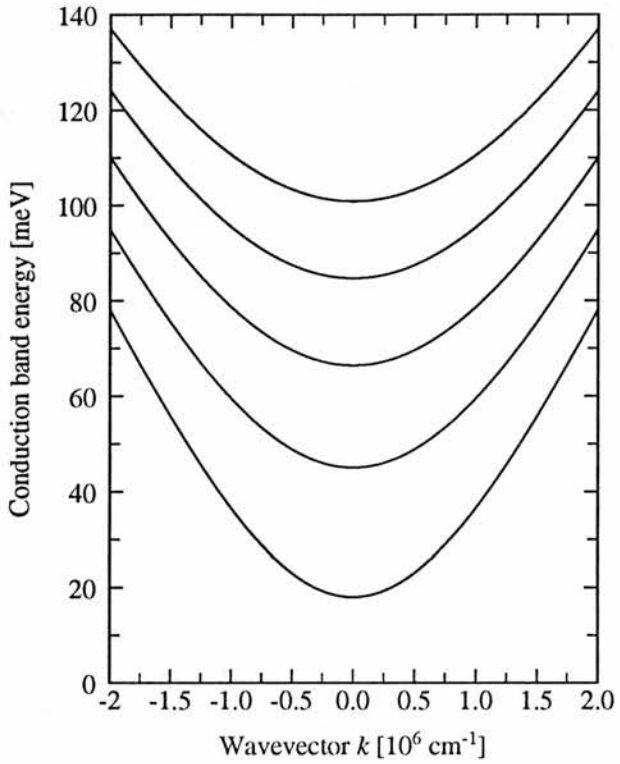

FIG. 3.2: The first few Landau levels of InSb, at 5 T, showing the effect of non-parabolicity of the conduction band. Because the "fundamental" $N = 0 \rightarrow 1$ absorption at $k_z = 0$ is accompanied by a continuum of smaller energy transitions within the same pair of bands, as well as by still lower energy transitions between higher bands, cyclotron resonance at fixed frequency is accompanied by a long tail into higher magnetic fields as the level separations successively increase.

The levels that appear due to impurity atoms tend to "track" with the Landau levels for $\gamma > 1$, i.e., their energies remain very similar (to within a few meV) to those of the free electrons as magnetic field varies. There remains a quasi-hydrogenic hierarchy to the quantum numbering of these labels, to the point that many authors use the low-field (nlm) notation (e.g., "$2p_{-1}$") even in the high-field limit, where properly, the high-field (NMk) notation should be employed. The "equivalence" is tenuous, and is only straightforward for the

lowest quantum numbers: One criterion of equivalence is that of nodal surface conservation, as examined by KAPLAN ET AL. (1969). The conservation rules in this case are as follows:

$$\begin{aligned} \mathsf{n} - \mathsf{l} - 1 &= N - \frac{1}{2}(M + |M|) \\ \mathsf{l} - |\mathsf{m}| &= \begin{cases} 2\lambda, & \text{for } \lambda \text{ even}, \\ 2\lambda - 1, & \text{for } \lambda \text{ odd}. \end{cases} \end{aligned} \tag{3.22}$$

Under a Landau level of any given N will exist the quasi-hydrogenic n levels, while both m and M refer to the orbital angular momentum quantum number, which is preserved in the transition from low to high field. For instance, the lowest "1s" level is labeled (000), while the $2p_{+1}$ level is (110) and the $2p_{-1}$ is $(0\bar{1}0)$.

The $M = +1$ states are tied to the first Landau level.

The absorption coefficient for impurity transitions (in the high field limit only, and for circularly polarized light) is given by

$$\alpha(\omega) = \frac{8\pi N_{\mathrm{I}} |\mathcal{Q}|^2}{hc\kappa^{1/2}} \left[\frac{\omega_{\mathrm{c}} \Delta\omega_{1/2}}{(\omega - \omega_{\mathrm{c}})^2 + (\Delta\omega_{1/2})^2} \right], \tag{3.23}$$

where N_{I} is the impurity concentration and $\mathcal{Q}$ is the electric dipole matrix element.

3.2.2 *Magnetic Freeze-out of Shallow Donors*

YAFET ET AL. (1956) describe the magnetic freeze-out of electrons onto shallow donor states using EMT. Freeze-out arises from two effects. First, in the absence of a magnetic field, if the impurity concentration is high enough, the individual atomic impurity wavefunctions may broaden into a band and raise the highest of the impurity electron energies to the ionization level. A magnetic field will spatially reduce the impurity electronic wavefunctions, and therefore the width of the impurity band as well.

Second, the ground state energy increases with magnetic field at a lower rate than the continuum energy, leading to a net increase in the ionization energy. For a simple donor atom with an isotropic effective mass, an increase in binding energy from 1–5 Ry* is predicted over the range $0 < \gamma < 30$.

3.3 Cyclotron Resonance Linewidths and Lineshapes

The above-mentioned time constant τ_{CR} is not the same quantity used in drift velocity calculations, τ_{DC}. The two quantities may differ significantly because of differing sensitivities to small-angle scattering, especially in the case of ionized impurity scattering (KAPLAN ET AL., 1973), for instance (see below). Still, cyclotron resonance linewidth studies are of great importance in characterizing various scattering mechanisms. Some of these mechanisms and their effects on lineshapes are discussed below. Of signal importance in the analysis of lineshapes is the phenomenon of correlation, which will be further discussed in § 4.6.

3.3.1 Overview of Line-Broadening

Line-broadening is the result of numerous processes or phenomena that tend to break the symmetry of a physical picture, e.g., nonparabolicity in a conduction band or random electric fields (in the case of inhomogeneous broadening), or it may result from the various relaxation times given in, e.g., Eqs. 3.16 and 5.22.*

Broadening may be classified as either homogeneous (symmetric lineshape) or inhomogeneous. The former arises, for example, from the natural linewidth of a radiative process, such as laser action or cyclotron resonance, and is a consequence of the uncertainty principle: The finite lifetime of an excited state leads to an uncertainty in the energy width of a resonance. In the case of cyclotron resonance in semiconductors, this linewidth is of negligible proportion. Collision broadening is also homogeneous, even when the scattering process is energy-dependent.

In the idealized situation of an energy-independent scattering mechanism, the lineshape for a single transition is given by the Lorentzian function:

$$A(\omega_{ji}, \omega) = \frac{\Gamma}{(\omega_{ji} - \omega)^2 + \Gamma^2}, \tag{3.24}$$

where $\hbar\omega_{ji} = \epsilon_j - \epsilon_i$. The effect of energy-dependence in τ will be to broaden the wings of the curve while sharpening the maximum (as in Fig. 8.30).

* It is necessary to distinguish the following relaxation times: τ_{DC} is the momentum relaxation time, or that time for the electron population to be randomized after an electric field pulse. τ_E is the energy relaxation time, the mean time required for an electron to relax its energy back to equilibrium after optical or electric excitation. τ_{CR}, mentioned above, is equal to the experimental value of the inverse of the halfwidth at half-height of the cyclotron resonance peak, i.e., $1/\Delta\omega_{1/2}$. KAWABATA (1967) stated that τ_{CR} was the relaxation time of the electric current, rather than that of the electron eigenstates. In the case of energy-independent scattering, τ_{CR} will equal τ_{DC}.

The time-averaged power absorbed by the conduction band electrons in cyclotron resonance at ω_c from a circularly polarized EM wave, derived from the formula by KUBO (1957), is

$$\mathfrak{P}(\omega) = \frac{1}{2}\mathcal{E}^2\Re[\sigma_{+-}(\omega)], \tag{3.25}$$

where

$$\Re[\sigma_{+-}(\omega)] = \frac{2e^2}{m_e^*\Omega}\sum_{k_z}\frac{f[\epsilon_0(k_z)]\Gamma(\omega,\omega_c;k_z)}{[\omega-\omega_c-\Delta(\omega,\omega_c;k_z)]^2+[\Gamma(\omega,\omega_c;k_z)]^2}, \tag{3.26}$$

in which $f[\epsilon_0(k_z)]$ is the distribution function for the $N = 0$ Landau level, $\Delta(\omega,\omega_c;k_z)$ is a peak shift and $\Gamma(\omega,\omega_c;k_z)$ is the linewidth, by which is meant the halfwidth at half-maximum.

Inhomogeneous broadening may come as well from two sources. As seen in Fig. 3.2, the highly nonparabolic conduction band of indium antimonide results in an asymmetric broadening of the cyclotron resonance line toward higher field, with a linewidth proportional to the resonant field. This broadening may be enhanced by polaron effects (i.e., the additional effective mass imposed on the electron in a polaron increases the nonparabolicity of the conduction band). However, at low temperatures, low electric fields and low electron concentrations, this broadening represents only a few percent of the total linewidth of the cyclotron resonance.

The second source of inhomogeneous line broadening is the Stark effect. LARSEN (1973) found that the major portion of the inhomogeneous broadening of the $1s \rightarrow 2p_{\pm}$ transitions derives from Stark broadening (see below).

It is seen, therefore, that Eq. 3.17 (i.e., $\omega_c\tau_{CR} = B_c/\Delta B_{1/2}$) represents an idealized situation of energy-independent scattering in the classical limit ($k_BT \gg \hbar\omega_c$). In general, $\mu = f/\Delta B$, where f is a weighting term arising from averaging scattering terms over the entire conduction band, roughly analogous to the Hall factor r_H (see § 2.6). When τ_{CR} is energy-dependent, the lineshape deviates from the Lorentzian form expressed above, with significant sharpening of the peak and broadening of the wings of the curve in the case of a power curve dependence (see, e.g., Fig. 8.30).

HINDLEY (1964) calculated the lineshape functions for a parabolic conduction band averaging the scattering over the conduction band by assuming an energy-dependence $\tau_{CR}(E) \propto E^p$, a rather too simplified picture. For AD scattering (deformation potential-coupled acoustic phonons) ($p = -1/2$), f was found to be 0.94, agreeing reasonably well

with experiment in the classical regime ($k_B T \gg \hbar\omega_c$), while for II scattering ($p = 3/2$), the deviation is $f = 0.55$.

In general, linewidth calculations of the type reviewed below are complicated by a number of factors (STRADLING[b]):

- correlation effects, discussed below, and which will be taken up further in the next chapter (§ 4.6), ;
- a changing electron concentration, and therefore a changing ionized impurity concentration as well, due to magnetic freeze-out (discussed in § 3.2.2), which is very large in indium antimonide: Two thirds of conduction band electrons may freeze out in indium antimonide at liquid helium temperatures and 2 T;
- nonparabolicity, mentioned above, which may be enhanced by polaron effects;
- in nonparabolic conduction bands, spin-up and spin-down transitions have slightly different energies. If these are unresolved from one another, their overlap may confuse the measurement.
- the applied electric bias may influence the linewidth. This quantity may not be constant, as constant current sources are often used to measure photoconductivity, and resistance changes dramatically with field.

In the discussion that follows, the quantity l is a magnetic length, $(\hbar/eB)^{1/2}$, equal to the ground state cyclotron orbit radius (see Eq. 3.6) (typically on the order of 10^{-6} cm at high field), and a_i is the distance of interaction. As a rule of thumb, when $l/a_i < 1$, τ_{CR} and τ_{DC} will not be equal. Conversely, when $l/a_i \gg 1$, the two relaxation times are roughly equal, but not necessarily in the quantum limit (see MEYER, 1962).

3.3.2 The Stark Effect on Shallow Impurities

The random electric fields from impurity ions broaden the energy levels of shallow impurities in an effect known as Stark broadening, the chief contributor to linewidth at low temperatures and low impurity concentrations. LARSEN (1973) showed that transitions are shifted (up or down, by an amount proportional to $N_I^{4/3}$) and their linewidths inhomogeneously broadened by the quadratic Stark effect,* which is accompanied by energy shifts (proportional to N_I)

* Individual atomic transition energies are *not* broadened by the Stark effect: These remain infinitely sharp, but shifted due to the perturbing potential of ionized donors. Rather, it is the ensemble of variously shifted transitions that produce the finite linewidth. The appellation "quadratic" refers to terms arising from second-order perturbation theory.

due to the quadrupole moment of a neutral impurity in an electric field gradient. The perturbing ionic potentials predominantly effect the spatially more extensive excited states rather than the ground state energies, and by the same token diminish in effect with increasing magnetic fields. A halfwidth in units of the effective Rydberg of

$$\Gamma = \left(\frac{4\pi^2}{3^{5/2}}\right)\left(\frac{N_I a^{*3}}{2}\right)\left(\frac{\Delta Q}{e a^{*2}}\right) \tag{3.27}$$

was derived, where ΔQ is the change in quadrupole moment entailed in the transition in question. A shift in the line maximum of $\sim 0.132\,\Gamma$ results if all impurity charges are of the same sign.

Using the Monte Carlo technique, Larsen produced a number of lineshapes and lineshifts intended for comparison with the results of FIR magnetospectroscopy on n-GaAs from, e.g., STILLMAN ET AL. (1971) and Stradling. "Tails" of inhomogeneous broadening extended variously into higher or lower energies. For the $1s \rightarrow 2s$, $1s \rightarrow 2p_{-1}$ and the $1s \rightarrow 2p_{+1}$ transitions, calculations agreed with experiment only when the electrically measured value of N_I was reduced by 50%, in which case both linewidth and lineshape agreed to within experimental and theoretical uncertainty (i.e., Monte Carlo statistical error). However, the $1s \rightarrow 2p_0$ transition, which was expected to be broadened mostly by the quadrupole interaction, was 70% broader in experiment than predicted, while adjusting the value of N_I resulted in an inaccurate lineshape. Van der Waals interactions were investigated in an attempt to account for this discrepancy, but were found to be too weak. The question then was raised about the correlative effects present in a semiconductor (see below).

Larsen included the following points in his analysis of the Stillman linewidths to account for the apparent discrepancy in N_I. If the joint probability of finding concentrations N_A and N_{D+} of acceptors and ionized donors, respectively, in a given volume of semiconductor is taken to be

$$\exp\left(-\frac{(N_A - \langle N_A\rangle)^2}{2\sigma^2}\right)\exp\left(-\frac{(N_{D+} - \langle N_A\rangle)^2}{2\sigma^2}\right), \tag{3.28}$$

where the angle brackets denote mean values, the mean values of acceptors and ionized donors are equal, and σ represents the standard deviation, then it can be seen that the distributions of $N_A - N_{D+}$ and $N_A + N_{D+}$ are uncorrelated and independent (i.e., a change in one does not affect the values available to the other). The first of these quantities represents the concentration of negative charge in the region, while the latter is equal to N_I. It is expected that electrons will migrate into regions of net positive charge and thus decrease N_I

therein. However, a decrease of 50% in N_I would require the complete neutralization of all donors within such a region.

GOLKA ET AL. (1977) reported on studies, in zincblende semiconductors (including n-GaAs), of inter-excited state transition linewidths inhomogeneously broadened by the presence of impurity ions. Experimentally, it was found that two impurity transition linewidths approximately doubled as temperature was elevated from 4°K to 10°K.

Using a very simple model, it was shown that fairly good agreement between theory and experiment concerning the temperature dependence of the broadening (at low temperatures) could be obtained.* The quadratic Stark interaction mixes states of opposite parity, which can cause normally forbidden transitions, such as $1s \rightarrow 2s$ and $1s \rightarrow 3d_{+1}$. The quadrupole moments of states may interact with the electric field gradient.

Golka *et al.* also investigated the question of correlation, and outlined the following schema: In a random distribution of equal numbers of positively and negatively charged impurity ions, there exists a pairing energy, $e^2/\kappa r$, equal to the drop in potential experienced by one ion at a radius r from an oppositely charged ion. The mean value of this energy, $\langle E \rangle$, is equal to the above expression for pairing energy evaluated at the mean separation $\langle r \rangle$, where $\frac{4}{3}\pi \langle r \rangle^3 = 1/N_D$. It is proposed that at very low temperatures, where $k_B T$ is less than this pairing energy, electrons will migrate only between nearest neighbors, creating a population of randomly distributed dipoles with a very low potential energy. This "correlated" dipole field, falling off as $1/r^3$, is much weaker, on average, than that arising from the same collection of ions sharing a random point charge distribution, falling off as $1/r^2$, which would arise at higher temperatures. As the inhomogeneous linewidth is to first order proportional to the electric field intensity, the linewidth increases with temperature. This continues until the dipoles are on average as large as the mean ion separation, beyond which temperature no further broadening is seen (see below).

When uncorrelated (randomly distributed) charges are responsible for approximately all of the broadening, the following temperature dependence is postulated for the linewidth:

$$\Gamma(T) = \Gamma_0 + (\Gamma_\infty - \Gamma_0)\alpha_u(T).$$

Here, Γ_0 is the 0°K (minimum) linewidth, Γ_∞ is the high temperature limit, and $\alpha_u(T)$ is the fraction of ionized impurity atoms uncorrelated at temperature T. This is approximately

* Broadening between neutral impurities alone is very substantially less, except in uncompensated samples, and that due to phonons, at low temperatures, may be neglected.

that portion of donors with binding energies smaller than $k_B T$:

$$\alpha_u(T) = \int_0^{k_B T} p(E)\, dE,$$

where $p(E)d(E)$ is the fraction of ionized donors with binding energy between E and $E+dE$, which can be expressed as

$$p(E)dE = 3\varepsilon^{-4} \exp(-\varepsilon)^{-3}\, d\varepsilon,$$

where ε is $E/\langle E\rangle$.

Therefore, $\alpha_u(T) = \exp[-(\langle E\rangle / k_B T)^3]$. While no attempt is made to quantify Γ_0 or Γ_∞, aside from the remark that their difference should decrease with increasing compensation, it is observed that the derived form agrees approximately with experiment.

3.3.3 Linewidth and Phonon Scattering

KOBORI ET AL. (1990) (**I**) studied numerous modes of phonon scattering and line broadening of cyclotron resonance in a few semiconductors, employing absorption spectroscopy. In acoustic phonon scattering, if the cyclotron resonance energy is small compared to the electron's thermal energy, the cyclotron radius of curvature is large compared with the phonon wavelength, and $l/a_i \gg 1$, as a_i must be taken to be the wavelength of an acoustic phonon. In this case, but not in the quantum limit, $\tau_{CR} \approx \tau_{DC}$ (MEYER, 1962). Acoustic deformation potential scattering was investigated over a large temperature range in Ge and Si, where II scattering was constant, and where optical phonon energy is much greater than $\hbar\omega_c$, thus removing these scattering modes from consideration. Previously, in many investigations, a $T^{3/2}$ dependence between 2 and 100°K, agreeing with DC measurements, had been observed, whereas the results of Kobori *et al.* showed an approximately proportional dependence on T in the extreme quantum limit, and a $T^{3/2}$ dependence only in the classical limit. In Si below 4°K, in fact, a sublinear dependence on T was observed. As with II scattering, a $B^{1/2}$ dependence on magnetic field was observed.

PE scattering was studied from 20–60°K in n-CdS, where the acoustic deformation potential has a much lower relaxation rate. A roughly proportional temperature-dependence was observed.

Indium antimonide was investigated for the case of PO scattering by using a highly compensated sample to eliminate carrier-carrier scattering. Linewidth is found to be independent of temperature (due to the predominance of II scattering) as high as 30°K, above which it becomes supra-proportional, due to the onset of PO scattering. They attempted then to determine α, the polaron coupling constant, by fitting their linewidth results with a theoretical formula for the PO scattering relaxation rate. While the experimental fit gives $\alpha = 0.087$, in theory, by Eq. 5.36, the value should be 0.026. No explanation is offered for the discrepancy.

3.3.4 Ionized Impurity Scattering in the Quantum Limit

Just as it does in the classical limit (see § 2.5.5), II scattering presents theoretical difficulties in the quantum limit; specifically, the need to treat both screening and small angle scattering in the quantum limit.

KAWAMURA ET AL. (1964) investigated adiabatic (i.e., intra-Landau level*) scattering by the long range Coulomb potential ($1/a_i < 1$) and obtained data on very pure Ge ($n \approx 10^{12}$ cm^{-3}) in order to determine Γ. The temperature-independent (largely phenomenological) result was

$$\Gamma = 0.915 \frac{e^2 \sqrt{N_I}}{m_e^{*\frac{1}{4}} \hbar^{\frac{3}{4}} \kappa \omega_c^{\frac{1}{4}}}. \tag{3.29}$$

In the applied semiclassical theory, $\Gamma \propto N_I$, and the $\sqrt{N_I}$ dependence was ascribed to the cyclotron radius being smaller than the screening length of the Coulomb interaction.

KAWABATA (1967), on the other hand, investigated the short-range point defect potential ($l/a_i > 1$) wherein the chief scattering mode is non-adiabatic (i.e., inter-Landau level). An electron-impurity coupling parameter λ was invoked, and it was deduced that in the extreme quantum limit, $\tau_{CR} \propto BT^{1/2}/N_I \propto 1/\lambda^2$, an N_I-dependence again not borne out by experiment. (It should be pointed out that for CC scattering, $\tau_{DC} \ll \tau_{CR}$, and $\tau_{DC} \propto T^{3/2}$. Whereas τ_{DC} is determined by the lifetimes of electron eigenstates, τ_{CR} is determined by the relaxation times of currents.)

KAPLAN ET AL. (1973) studied cyclotron resonance in indium antimonide at liquid helium temperatures with high-resolution far-infrared (~70–200 μ) transmission spectroscopy.

* For both ionized and neutral impurity scattering, intra- (as opposed to inter-) Landau level scattering is dominant at low temperatures.

a_i in this case is the screening length of the Coulombic field of the ionized impurities. For a non-degenerate semiconductor, at $T = 0°K$ in the high magnetic field approximation, the screening length a_i is $(\hbar/4m_e^*\omega_p)^{1/2}$ (SHIN ET AL., 1972), where ω_p is the plasma frequency, given by $(4\pi ne^2/m_e^*)^{1/2}$. In indium antimonide at 4.2°K, typically $\omega_p \approx 5 \times 10^{12}$, giving a screening length of 2×10^{-6} cm.

It was discovered that for low magnetic fields, where $l/a_i > 1$, linewidths decreased with increasing magnetic field, while for $l/a_i < 1$, linewidths increased with increasing magnetic field. This latter high-field result was in qualitative (but only rough quantitative) agreement with the results of SHIN ET AL. (1972), in whose model anisotropic adiabatic scattering is the dominant scattering mechanism. However, so-called K_2 "vertex correction" terms ("scattering-in" and "scattering-out"), which take into consideration the influence of small wavevector Fourier components of the scattering potential on the cosine of the scattering angle, were omitted in this model. These terms are in fact vital in a consideration of ionized impurity scattering, so this model was found to be inadequate; and in fact, in other semiconductors, the linewidth continues to decrease with increasing magnetic field. This suggests that at high magnetic fields there is significant broadening from the inhomogeneous change in effective mass.

The results at low magnetic field were found to be in agreement with the theory of KAWABATA (1967), concerning non-adiabatic scattering from unscreened Coulombic centers, involving terms which usually dwindle at high magnetic field, and which are found not to be additive with those of the adiabatic case. In this instance, the relaxation time is given by

$$\tau^{NA} \approx \frac{\hbar\omega_c\kappa_L^2}{2\pi e^4 N_I}(2m_e^* k_B T)^{\frac{1}{2}}. \tag{3.30}$$

Acoustic phonon scattering was found to be negligible in the region 4.5–15°K, as evidenced by constant linewidth throughout the range at every wavelength.

MCCOMBE ET AL. (1976), investigating indium antimonide, discovered that linewidth in the quantum limit at high magnetic fields is, in agreement with many theoretical predictions, proportional to $\sqrt{N_I}$, and, again, that a minimum in linewidth with respect to magnetic field could be found, though as yet were unable to offer a satisfying explanation of this. They further demonstrated that linewidth is independent of temperature below ~30°K, and therefore that phonon contributions to linewidth are negligible in this regime; also that linewidth is independent of carrier concentration, thus indicating that screening of the ionized impurities was not a significant factor in linewidth either (but see § 3.3.5).

FUJITA & LODDER (1976), using the theory of proper connected diagrams, calculated that at liquid helium temperatures, for a very pure semiconductor,

$$\Gamma = 1.403 \frac{e^2 \sqrt{N_I}}{m_e^{*\frac{1}{4}} \hbar^{\frac{3}{4}} \kappa \omega_c^{\frac{1}{4}}}. \tag{3.31}$$

This was in fundamental agreement with Kawamura's results (see Eq. 3.29), but for the difference in constant coefficient, i.e., 0.915 *vs.* 1.403. This calculation was simply an application of a more general formula derived in their work, that for conductivity lineshape, based on Eq. 3.26 above. In this case, the peak shift $\Delta(\omega, \omega_c; k_z)$ was neglected. The neglect of this shift may be responsible for other theoretical and experimental discrepancies (see Kobori's results below).

NICHOLAS & SARKAR (1982) examined the problem above of linewidth temperature dependence at low temperatures in an effort to replace the originally derived $T^{-1/2}$ dependence with a form that reflected the narrowing at low temperatures. Beginning with a statement of proportionality between the halfwidth and the density of states, an expression for the latter including the spreading and high-energy "tailing" of the apices shown in Fig. 3.1 (resulting from a consideration of multiple II scattering in a highly compensated semiconductor) was invoked. Additionally, consideration was made of carriers whose energy was below the so-called mobility edge, which become localized in resonant backscattering and do not contribute to the conductivity in Eq. 3.15 (which, strictly, must be evaluated by an energy integral). These modifications to the calculation resulted in a dramatic difference in the final values of linewidth, which were found to agree functionally with the observed behavior, i.e., to increase roughly linearly with temperature below a characteristic temperature.

KOBORI ET AL. (1989) (**II**) also conclude that the linewidth is independent of temperature in quite pure, but compensated ($N_A/N_D \approx 1$) indium antimonide below ~30°K, where ionized impurity scattering is dominant. Scattering decreases at shorter wavelengths and higher magnetic fields with a $B^{-1/2}$ dependence. In their analysis, they considered only elastic scattering in the quantum limit, such that the only allowed transitions are $N = 0 \rightarrow N = 0$, $N = 1 \rightarrow N = 1$ and $N = 1 \rightarrow N = 0$. The relaxation rate is $\Gamma(k_z) = \Gamma^{\text{intra}}(k_z) + \Gamma^{\text{inter}}(k_z)$,* with individual rates given by

$$\Gamma^{\text{intra}}(k_z) = \frac{\pi}{\hbar} N_I \sum_q |v_{e-\text{imp}}(q)|^2 t^2 e^{-t} \, \delta[\epsilon(k_z - q_z) - \epsilon(k_z)] \tag{3.32a}$$

* This is an application of Matthiessen's summing rule, which is valid only when each individual resonance width Γ is proportional to N_I (SRINIVAS ET AL., 1983).

and

$$\Gamma^{\text{inter}}(k_z) = \frac{\pi}{\hbar} N_{\text{I}} \sum_q |v_{\text{e-imp}}(q)|^2 t e^{-t} \delta[\epsilon(k_z - q_z) - \epsilon(k_z) + \hbar\omega_c], \tag{3.32b}$$

where $t \equiv l^2 q_\perp^2/2 \equiv l^2(q_x^2 + q_y^2)$.

When a screened Coulomb potential is substituted in the above equations for $v_{\text{e-imp}}(r)$, and the approximations $k_z = 0$ and $lq_s = 0$ are made (where q_s is the reciprocal of the Debye screening length), the following expressions for the II scattering-limited rates are derived:

$$\frac{1}{\langle \tau_{\text{II}}^{\text{intra}} \rangle} \equiv \frac{1}{\langle [\Gamma_{\text{II}}^{\text{intra}}]^{-1} \rangle} = \sqrt{2\pi^3} \frac{N_{\text{II}} e^4}{\kappa^2 m_e^{*1/2}} (\hbar\omega_c)^{-1} (k_B T)^{-1/2} \tag{3.33a}$$

and

$$\frac{1}{\langle \tau_{\text{II}}^{\text{inter}} \rangle} \equiv \frac{1}{\langle [\Gamma_{\text{II}}^{\text{inter}}]^{-1} \rangle} = \sqrt{2}\pi \frac{N_{\text{II}} e^4}{\kappa^2 m_e^{*1/2}} (\hbar\omega_c)^{-3/2} [1 + 2e\text{Ei}(1)], \tag{3.33b}$$

where N_{II} is the concentration of ionized impurities and Ei(1) is the exponential integral function

$$\text{Ei}(x) = \int_x^\infty \frac{e^{-u}}{u}\, du.$$

3.3.5 The Electron-Electron Interaction and Linewidth

PASTOR (1987) investigated the behavior of cyclotron resonance linewidth in very pure n-CdTe at 4.2°K as influenced by the electron-electron interaction. This was possible because of cadmium telluride's unique persistent cyclotron resonance mechanism (PASTOR ET AL., 1986): Heterogeneous regions are formed at low temperature, with holes being trapped in high resistivity defect-rich regions, and electrons accumulating (and persisting) in low resistivity regions. It is possible with illumination then to increase the electron concentration in a limited region without increasing the proportion of ionized scatterers. It was discovered that the linewidth was increased by ~50% over two orders of magnitude of electron concentration, with a $\sqrt{n}$ dependence, paralleling that on impurity concentration. This was not as much as would be expected based on the mobility decrease of DC measurements: BATE ET AL. (1965) show that even in a non-degenerate semiconductor, electron-electron scattering

can enhance II scattering to the effect of lowering mobility to 60% of its value from II scattering alone, but with an overall proportionality to n.

GORNIK ET AL. (1978) shows that the chief limitation on electron lifetime in indium antimonide is intraband electron scattering, giving $\tau_{CR} \sim 10^{-10}$ sec for $n \gtrsim 10^{13}\,\mathrm{cm}^{-3}$.

3.3.6 Neutral Impurity Scattering and Linewidth

NI scattering may determine linewidth in the case of low temperatures and uncompensated samples (i.e., II scattering is largely absent or diminished). KOBORI ET AL. (1989) **II** proceed from the results of ERGINSOY (1950) (see § 2.5.6) by introducing a model potential, renormalized according to the EMA, with which to solve Eqs. 3.32. By approximating k_z to be 0, the following expressions for scattering rates from neutral *donors* are derived (a distinct scattering cross-section is presented for neutral acceptors, but it is stated that the results are expected to be approximately equal):

$$\frac{1}{\langle \tau_{ND}^{intra} \rangle} \equiv \frac{1}{\langle [\Gamma_{ND}^{intra}]^{-1} \rangle} = \frac{15\pi}{8} \frac{N_{ND} a^* \hbar}{m_e^*} \left(\frac{\hbar\omega_c}{k_B T} \right)^{1/2} \tag{3.34a}$$

and

$$\frac{1}{\langle \tau_{ND}^{inter} \rangle} \equiv \frac{1}{\langle [\Gamma_{ND}^{inter}]^{-1} \rangle} = \frac{5 N_{ND} a^* \hbar}{m_e^*}, \tag{3.34b}$$

where the subscript 'ND' refers to neutral donors. Eq. 3.34a is seen to predict a square-root magnetic field dependence which is entirely at odds with the quoted results for n-GaAs, which show a linewidth sharply *decreasing* as magnetic field increases. This problem is initially addressed by generalizing Erginsoy's result for higher energy scattering. With this modification, a rough agreement with experimental magnetic field dependence is achieved, but at a linewidth an order of magnitude larger than observed. One possible explanation for this discrepancy is posited; namely, the neglect of the cyclotron resonance peak shift.

Some of the above results, as presented in the papers of Kobori *et al.*, on linewidth dependence on various factors in the low temperature limit, are summarized in Table 3.1.

TABLE 3.1: Approximate dependences of cyclotron resonance linewidth, limited by specific scattering modes, on various factors.

Scattering mode	Ionized Impurity	Neutral Impurity	Acoustic Phonon (deformation potential)
Intra-Landau level	$N_I \kappa^{-2} m_e^{*1/2} B^{-1} T^{-1/2}$	$N_{ND} a^* m_e^{*-3/2} B^{1/2} T^{-1/2}$	$m_e^{*1/2} B T^{1/2}$
Inter-Landau level	$N_I \kappa^{-2} m_e^* B^{-3/2} T$	$N_{ND} a^* m_e^{*-1} B T$	$m_e^* B^{1/2} T$

3.3.7 Line-Narrowing with Hydrostatic Pressure

WASILEWSKI ET AL. (1982) reported the dramatic narrowing (by an order of magnitude) with hydrostatic pressure of the cyclotron resonance and impurity-shifted cyclotron resonance lines in indium antimonide. The samples exhibiting this behavior, in the region of ~4–7 kbars, were uncompensated. Above this pressure, the sample, at liquid helium temperature, became highly resistive (on the order of 10 MΩ), and could not easily be examined, as it loaded the preamplifier.

The mechanism responsible was not clear, but certain possibilities could be ruled out at once:

- *Deionization of impurities:* While ionized impurity scattering is responsible for broadening of the cyclotron resonance line, deionization in the medium pressure region investigated occurs for only, say, one third, and at most one half, of all donors (see § 4.5). With a $N_I^{1/2}$ dependence, scattering alone could not make an order of magnitude difference.
- *Increase of effective mass:* Again, even a doubling of the effective mass could not explain such a large change.
- *Decrease of self-absorption:* If the observed narrowing were due to a decrease in free-electron concentration and a consequential decrease in over-absorption, then narrowing should be visible as well in a very thin (say ~10 μ) sample, with no pressure applied. While there is some narrowing, the effect is again quite small compared to that with pressure applied, which at any rate causes further narrowing in thin samples (see Chapter VIII).

Two ideas have been presented to explain these findings. The first relies on the correlative effects mentioned earlier with respect to the Stark effect; *viz.,* in this case, in a fairly compensated sample, the deionization of donors is not random, as a significant rise in potential energy would result from deionized donors existing very close to ionized acceptors. Therefore, it is hypothesized, the electrons are likely to distribute themselves in such a way as to create neutral but isolated donors, and ionized donor-ionized acceptor pairs, whose dipolar fields would in general be much weaker than the monopolar fields responsible for large Stark effects.

Another possibility (WASILEWSKI, 1985 and PIOTRZKOWSKI ET AL., 1986) is that two distinct phases exist in indium antimonide, a high purity and a low purity phase, leading to anomalous mobility effects as described in § 4.7. If the electron migration due to differing Fermi levels in each phase leaves a small population of electrons in the high purity regions (accounting for the observed increase in resistivity), then minimal II scattering (proportional to $N_I^{1/2}$), and therefore, minimal linewidth, will result. This model is supported in WASILEWSKI (1985) by the disappearence from an indium antimonide sample's photoconductivity spectrum of a particular shallow donor upon the application of high pressure. Although the donor remains shallow, it apparently contributes very little to the photocurrent because of the low electron occupation in its region.

The regions of high purity would necessarily have to be considerably larger than the cyclotron radius of an electron ($\sim 0.5\,\mu$) in order for the narrowing to actually be observed. Therefore, a size of several microns across would be expected.

CHAPTER IV

Impurities and Metastable States in III-V Compounds

4.1 Introduction

It is, arguably, the defects in semiconductors that imbue them with their more interesting or valuable properties. Here, "defects" is meant in the largest sense, including not merely structural defects such as dislocations and vacancies, but surface states and impurities as well, which also distort the lattice, and even lattice distortions brought on by external factors such as temperature, pressure or magnetic field.*

In indium antimonide, which is easily grown quite pure (i.e., $n \approx 10^{13}\,\mathrm{cm}^{-3}$),† some defects have been well characterized:

Mechanical stress (resulting in plastic deformation), as that from polishing, is known to introduce dislocations into indium antimonide. These dislocations are usually associated with undesirable or spurious results, such as negative magnetoresistance, and the appearance of surface etch pits at the point of emergence from the bulk of an edge dislocation. One of the most common types of dislocation in III-V materials (MADELUNG, 1964) is the so-called "60° dislocation", which extends in the [111] direction. Depending which atom of the pair is exposed along this defect, it may act as a row of acceptors or donors. On the other hand, the electron mobility in MBE-grown indium antimonide containing high concentrations of misfit dislocations can be very high; it therefore appears that dislocations are almost completely electrically inactive (STRADLING[a]), due to reconstruction of the core.

* Defects such as vacancies and interstitial substitutions are thermodynamically driven events; as such, there will *always* be finite (possibly metastable) concentrations of these defects.

† Uncompensated indium antimonide is always of n-type.

Dislocations may effect the electron mobility in indium antimonide in various ways. For instance, for current perpendicular to the axis of plastic deformation (or in other words, perpendicular to the induced dislocations), scattering increases and the mobility drops, while for current parallel to the dislocations, no effect is seen.

Plastic deformation by compression has been seen to result in the creation of interstitials and vacancies, while grain boundaries have been observed to act like donors (MADELUNG, 1964).

As is true in most III-V semiconductors, zinc and cadmium (which are bivalent) are acceptors in indium antimonide, substituting for the trivalent In atom, and are quite shallow, with ionization energies of ~7.5 meV each (MADELUNG, 1964). Other acceptors are magnesium, silicon and germanium, a shallow acceptor, while copper, silver and gold are double acceptors. Silicon, however, is a donor in MBE-grown indium antimonide (STRADLING[a]).

Sulfur, selenium and tellurium substitute on Sb^+ sites, becoming shallow donors (i.e, Sb^+ is replaced by $Te^{++} + e^-$), as they are in all III-V compounds. The remaining member of this family, oxygen, is somewhat problematic (see below), but it forms a deep level in many semiconductors.

A further problem in the growth of semiconductors, with indium antimonide no exception, is the diffusion of the various atoms, host and impurity, during the formation (cooling) process. Different atoms may diffuse into or out of individual grains (though most impurities tend to cluster at grain boundaries) and by different mechanisms (e.g., interstitial "hopping", bond exchanges, etc.). But diffusion may lead to various problems in the final product: Heterogeneity, or a separation of phases in the extreme case; and to certain "correlation" effects (see § 4.6 for discussion of *electron* correlation effects) which may more subtly influence the electronic behavior of the semiconductor: In this case, impurity ions of opposite charge may be drawn toward each other, creating dipolar fields which scatter carriers differently from monopolar fields. There is no evidence that this occurs in high purity indium antimonide as used in the present studies, where the Coulombic force is very weak at the average impurity ion separation. (This effect is likely to be present simply by virtue of the motion of individual electrons between ions when the sample is cold, but different behavior observed between bulk indium antimonide and MBE-grown material, which are formed at different temperatures, indicates the actual formation distribution may be important as well (O'REILLY, 1989).)

Because of the large radius associated with the small effective mass of indium antimonide (see below), the donor impurity atomic wavefunctions overlap significantly, thus creating

a separate impurity band, even in the purest material currently available ($N_D \sim N_A \sim 10^{14}$ cm^{-3}). These donors cannot be frozen out merely by lowering the sample temperature; rather, a magnetic field is required (see Chapter III).

4.2 Shallow Donors and EMT

KOHN (1957) develops a theory of hydrogenic donor states wherein the wavefunction of the electron of an impurity atom, $\psi(\boldsymbol{r})$, can be expressed as

$$\psi(\boldsymbol{r}) = \sum_j \alpha_j F_j(\boldsymbol{r}) \varphi_j(\boldsymbol{r}),$$

viz., a normal conduction band Bloch function $\varphi(\boldsymbol{r}) = u(\boldsymbol{r}) e^{i\boldsymbol{k}\cdot\boldsymbol{r}}$ modified by a "hydrogen-like" envelope function $F(\boldsymbol{r})$. The summation is over j multiple minima, and the various α_j are numerical coefficients or vectors reflecting the contribution of each Bloch basis function to each irreducible group representation of the impurity atom symmetry. This derivation rests on two approximations (see below), but provides some very useful results.

Using for a screened impurity ionic potential the form $U(r) = -e^2/\kappa_0 r$, where κ_0 is the static dielectric constant,* the Hamiltonian of the electron of the impurity ion can be expressed as $(H_0 + U)\psi = E\psi$, where H_0 is the Hamiltonian due to the host lattice, and ψ, the impurity wavefunction, is a linear combination of the wavefunctions of the unperturbed electron:

$$\psi = \sum_{\mathfrak{n},\boldsymbol{k}} A_{\mathfrak{n}}(\boldsymbol{k}) \psi_{\mathfrak{n},\boldsymbol{k}}.$$

Here, $\psi_{\mathfrak{n},\boldsymbol{k}}$ is a Bloch function

$$\psi_{\mathfrak{n},\boldsymbol{k}} \equiv \frac{1}{V^{\frac{1}{2}}} u_{\mathfrak{n},\boldsymbol{k}}(\boldsymbol{r}) e^{i\boldsymbol{k}\cdot\boldsymbol{r}},$$

where V is a volumetric normalization constant and $u_{\mathfrak{n},\boldsymbol{k}}$ is a periodic function, with $\boldsymbol{k}$ a wavevector in the first Brillouin zone, and $\mathfrak{n}$ the energy band index. The resulting equation,

* Use of the static (rather than the high-frequency "dynamic") dielectric constant is justified, according to Kohn, by virtue of the low frequency (relative to that of other electrons) of the impurity atom electron, $Ry^*/2\hbar$. That is, since $Ry^* < \hbar\omega_{LO}$, in its large orbital radius and slow motion, it encounters widely averaged fields from much faster-moving charges involved in polarization of the crystal. κ_0 and κ_∞ are the "plateaux" of the dielectric function on either side of ω_{LO}, with $\kappa_0 > \kappa_\infty$.

after taking the scalar product with $\psi_{\mathfrak{n},k}$, is

$$(E_{\mathfrak{n}}(k) - E)A_{\mathfrak{n}}(k) + \sum_{\mathfrak{n}',k'} \langle \mathfrak{n}k|U|\mathfrak{n}'k'\rangle \, A_{\mathfrak{n}'}(k') = 0, \tag{4.1}$$

where the matrix element

$$\begin{aligned}\langle \mathfrak{n}k|U|\mathfrak{n}k'\rangle &\equiv \int_{\infty} \psi^*_{\mathfrak{n},k} \left(-\frac{e^2}{\kappa_0 r}\right) \psi_{\mathfrak{n}',k'} d\boldsymbol{r} \\ &= \frac{1}{V} \int_{\infty} u^*_{\mathfrak{n},k} u_{\mathfrak{n}',k'} e^{i(k'-k)\cdot r} \left(-\frac{e^2}{\kappa_0 r}\right) d\boldsymbol{r}.\end{aligned}$$

If the periodic function $u_{\mathfrak{n},k}u_{\mathfrak{n}',k'}$ is expanded in a Fourier series with coefficients $C^{\nu}_{\mathfrak{n},k;\mathfrak{n}',k'}$ in terms of the reciprocal lattice vectors $\boldsymbol{K}_{\nu}$, the matrix element may be expressed so:

$$\langle \mathfrak{n}k|U|\mathfrak{n}'k'\rangle = \sum_{\nu} C^{\nu}_{\mathfrak{n},k;\mathfrak{n}',k'} \left(-\frac{4\pi e^2}{V\kappa_0 |\boldsymbol{K}_{\nu} + \boldsymbol{k}' - \boldsymbol{k}|^2}\right). \tag{4.2}$$

At this point, the first of two approximations may be explained. Because the Coulombic attraction between the electron and the impurity ion is greatly reduced by the dielectric constant, relative to that in the hydrogen atom, the spatial extent of the electron wavefunction is comparatively enormous. Therefore, only those values of $\boldsymbol{k}$ close to 0 will contribute substantially in the Fourier transform; i.e., the wavefunction will resemble a grouping of Bloch waves from near the conduction band minimum. This will be quantified in Eq. 4.3.

Now due to the orthonormality of ψ, if $\boldsymbol{k} = \boldsymbol{k}' = 0$, then in Eq. 4.2:

$$C^{0}_{\mathfrak{n},0;\mathfrak{n}',0} = \begin{cases} 1 & \mathfrak{n} = \mathfrak{n}' \\ 0 & \mathfrak{n} \neq \mathfrak{n}' \end{cases}$$

Therefore, most of the contribution to the impurity electron wavefunction will be made by terms in Eq. 4.1 where $\mathfrak{n} = 0$. In effect, this approximation neglects interband matrix elements in the expression. Kohn demonstrates that in order of magnitude, $A_{\mathfrak{n}\neq 0}/A_0 \sim (E_0 a_{\mathrm{B}}/E_{\mathrm{g}} a^*)$, where E_0 is the ionization energy. Using for the latter the effective Rydberg of indium antimonide (see below), this ratio equates to between 10^{-5} and 10^{-6}, thus confirming the argument above.

This leads to the following substitutions in Eq. 4.1:

$$A_{\mathfrak{n}}(k) \to 0, \text{ for } \mathfrak{n} \neq 0$$

$$E_0(k) \to \frac{\hbar^2 k^2}{2m_e^*}$$

$$\langle 0k|U|0k'\rangle \to -\frac{4\pi e^2}{V\kappa_0|k-k'|^2}.$$

This results in the final expression in momentum space of the Schrödinger equation:

$$\left(\frac{\hbar^2}{2m_e^*}k^2 - E\right) A_0(k) - \frac{4\pi e^2}{V\kappa_0}\sum_{k'}\frac{1}{|k-k'|^2}A_0(k') = 0,$$

which is identical to that for an electron orbiting a Coulombic potential of $-e^2/\kappa_0 r$. The sum is properly taken only over the wavevectors of the first Brillouin zone, but the second approximation is here invoked; *viz.*, that the perturbing potential of the impurity atom, $U(\boldsymbol{r})$, varies spatially so slowly that its Fourier components $U(\boldsymbol{k}) = \int_\infty U(\boldsymbol{r})\exp(-i\boldsymbol{k}\cdot\boldsymbol{r})\,d^3\boldsymbol{r}$ outside the first Brillouin zone may be neglected. Therefore, the summation above is taken over all $\boldsymbol{k}'$.

Fourier transforming from $\boldsymbol{k}$-space to real space, a function

$$F(\boldsymbol{r}) = \frac{1}{V^{\frac{1}{2}}}\sum_{\boldsymbol{k}} A_0(k)e^{i\boldsymbol{k}\cdot\boldsymbol{r}} \tag{4.3}$$

is found such that

$$\left[-\frac{\hbar^2}{2m_e^*}\nabla^2 + U(\boldsymbol{r}) - E\right] F_{\mathfrak{n}}(\boldsymbol{r}) = 0. \tag{4.4}$$

In this scheme, an effective Bohr radius a^* and an effective Rydberg energy Ry* for the donor electron can be defined, equal to those for the hydrogen atom ($a_B = 0.529$ Å and 1 Ry = 13.6 eV) multiplied by an appropriate scaling factor:

$$a^* = \frac{\kappa_0}{m_e^*/m_0}a_B \qquad \text{and} \qquad \text{Ry}^* = \frac{m_e^*/m_0}{\kappa_0^2}\text{Ry},$$

where 1 Ry $= m_0 e^4/2(\kappa_0\hbar)^2$. In indium antimonide, this means that the effective Bohr radius extends for about a hundred unit cells.

In this notation, the ground state wavefunction for the electron is

$$F(\boldsymbol{r}) = \frac{1}{(\pi a^{*3})^{\frac{1}{2}}} e^{-r/a^*}. \tag{4.5}$$

If Eq. 4.3 is inverted to solve for $A_0(\boldsymbol{k})$, and Eq. 4.5 is employed, it is found that

$$A_0(\boldsymbol{k}) = \frac{8\pi^{\frac{1}{2}}}{V^{\frac{1}{2}} a^{*\frac{5}{2}}} \frac{1}{\left[k^2 + \left(\frac{1}{a^*}\right)^2\right]^2}.$$

This means that at values of $k \gtrsim 1/a^*$, $A_0(\boldsymbol{k})$ becomes negligible. In particular, in indium antimonide, since $a^* \approx 640\,\text{Å}$ (assuming $m_e^*/m_0 = 0.014$ and $\kappa_0 = 17$) while the lattice constant $a_0 = 6.48\,\text{Å}$, $A_0(\boldsymbol{k})$ is $\sim 1.4 \times 10^{11}$ as great at the zone center as at the zone edge. It is worth noting as well that, from Eq. 4.5, the electron probability function (proportional to the square of the modulus of $F(\boldsymbol{r})$) tends to "concentrate", becoming larger and narrower, about the impurity ion with an m_e^{*3} dependence. This has profound consequences for the observation of shallow states under hydrostatic pressure.

It is because of the admixture of band states of widely varying k-values within the impurity wavefunction that phonons over a wide spectrum of wavevectors may interact strongly with the impurity. However, an excited electron will tend to absorb strongly interacting phonons of low wavevector ($k \lesssim 1/a^*$), which can excite it to the more closely spaced higher states, and it is less likely to emit the large wavevector phonons ($k \gtrsim 1/a^*$) resulting from large transitions to ground state. Therefore, impurity state transitions between the lower lying states brought about by photo-absorption may result in eventual "photothermal ionization", making these transitions visible as a photoconductive "pulse" (see Chapter VIII).

Finally, it can easily be shown that $F(\boldsymbol{r})$ is indeed an "envelope" function as initially claimed. The impurity electron wavefunction, as derived above, is

$$\psi(\boldsymbol{r}) \approx \sum_{\boldsymbol{k}} A_0(\boldsymbol{k}) \psi_{0,\boldsymbol{k}}(\boldsymbol{r})$$

$$= \frac{1}{V^{\frac{1}{2}}} \sum_{\boldsymbol{k}} A_0(\boldsymbol{k}) u_{0,\boldsymbol{k}}(\boldsymbol{r}) e^{i\boldsymbol{k}\cdot\boldsymbol{r}}.$$

But in $u(\boldsymbol{r})$ as well, $k \neq 0$ may be neglected, so

$$\psi(\boldsymbol{r}) \approx \frac{1}{V^{\frac{1}{2}}} u_{0,0}(\boldsymbol{r}) \sum_{\boldsymbol{k}} A_0(\boldsymbol{k}) e^{i\boldsymbol{k}\cdot\boldsymbol{r}}$$

$$= u_{0,0}(\boldsymbol{r}) F(\boldsymbol{r}).$$

The energy of the electron may in fact be significantly different from that predicted by this effective mass theory, or EMT, and for many possible reasons, the primary one being the central cell effect. This effect, wherein the core potential in the central cell of the impurity varies from the ideal Coulombic potential, arises from any of three sources: *1)* A true "chemical shift", arising from the difference between the core potential of the impurity atom and that of the host; *2)* lattice distortion around the impurity atom due to steric factors; and *3)* the breakdown of the dielectric continuum approximation at small distances, where the dielectric constant approaches its free space value.

The chemical shift, which is proportional to the density of the electron wavefunction at the impurity site (DMOCHOWSKI ET AL., 1990), may be quite dramatically evinced in many semiconductors in magnetic field spectra that show Zeeman splitting (see Chapter III). The shift may vary from a few percent for large quantum number $\mathfrak{n}$, wherein the electron is far removed from the defect, to several hundred percent for the ground state, in the case of high effective mass, as in GaP. However, the effect is often visible in many semiconductors (to $\sim$1%) even in no magnetic field. On the other hand, because of the node in the wavefunction at the origin, the effect essentially disappears on all odd parity states, and even for $\mathfrak{n} = 2$. In indium antimonide, the effect can be observed only in high magnetic fields or at high pressure: At 10 T ($\gamma \approx 50$) and 6 kbars, the effect is $\sim$10% for the "A" donor (see below).

Another source of error in EMT is its neglect of conduction band nonparabolicity, which in indium antimonide (see Chapter II) deepens the $1s$ state. In high magnetic fields, due to its association with the $\mathfrak{n} = 1$ Landau level, the $2p_+$-like state is most affected (STRADLING, 1980).

Finally, both spin and polaron interactions may complicate the picture. Polarons (interactions between electrons and LO phonons) contribute mostly to a deepening of the ground state resulting from the substitution of the band-edge mass by the polaron mass (STRADLING, 1980).

4.3 Deep Donors

Deep donors are those donors whose behavior is governed by their core potentials, which more resemble deep rectangular-well potentials (with eigenenergies increasing as n^2) than Coulombic potentials of hydrogenic donors (whose eigenenergies converge as $1/n^2$ toward a continuum). These donors may be treated approximately with tight-binding theory rather than with EMT in order to describe their electronic properties.* The word "deep" in this instance describes not so much a large negative energy that might be associated with these donors (for in fact so-called deep levels can exist as resonant states in narrow-gap semiconductors), but rather the fact that the donor levels are governed by bands well removed, energetically, from each other. Thus, the deep levels may not follow a unique band in the case of hydrostatic pressure application or variable alloying, but may exhibit a manifold nature as various experiments are performed, apparently being dominated by any of two or more bands under different conditions. Notably, the Stokes shift, the difference between the thermal and optical ionization energies, may be enormous, the latter being several times larger than the former (see below).

Only a treatment which takes into account the interaction between the electronic state of the defect and the vibrational state of the lattice ("vibronic" coupling) can explain the large Stokes shift. TOYOZAWA (1978) concludes that the defect-lattice energy is given by $E = (\lambda^2 - g_S\lambda^3 - g_L\lambda)E_K$, where the so-called electron localization parameter λ is equal to a_0/a^* (a_0 is the host lattice constant and a^* is the Bohr radius of the defect); g_S is a coupling constant for the short-range, elastic deformation potential, proportional to the charge density and hence to λ^3; g_L is the coupling constant for long-range Coulombic polar-phonon coupling, inversely proportional to radius, or $\propto \lambda$; and E_K is the electron kinetic energy for $\lambda = 1$. When $\lambda \ll 1$, the state is hydrogenic. When $\lambda \approx 1$, the electronic wavefunction is highly localized. The two states may involve a single donor atom, but are likely to be separated by a large energy since the electron-lattice interaction energy is inversely proportional to the square of the electron wavefunction radius for acoustical phonons (STONEHAM, 1979). (Optical phonons, on the other hand, exhibit a coupling constant with a $1/a^*$ dependence, and therefore couple more readily than do acoustic phonons to delocalized states.)

While the ionic core potential of a deep impurity may be little affected by small changes in the lattice constant, the application of hydrostatic pressure is known to effect profoundly

* It is also possible in many cases to adapt the Kohn-Luttinger theory above by not neglecting the higher order A_n terms.

the surrounding lattice (POROWSKI & TRZECIAKOWSKI, 1983), possibly due to a substantial difference in its local compressibility from that of the pure lattice (for example, see next section).

4.4 *DX* Centers

Certain poorly understood deep donors, responsible for, among other things, persistent photoconductivity (PPC) at low temperatures, have been under observation in various II-VI and III-V semiconductors for well over twenty years (LANG & LOGAN, 1977). In particular, work on GaAs and the AlGaAs alloys has revealed the presence of the so-called *DX* centers* (LANG & LOGAN, 1979) and Saxena's donors (SAXENA, 1981), through a variety of experimental techniques. Given the industrial importance of these compounds, it is vital to achieve a better understanding of these defects; specifically, their chemical and structural identity, means of processing to intentionally introduce or remove them, and the physical principles underlying their remarkable behavior. The PPC centers, for example, were seen to profoundly influence modulation doping (STORMER ET AL., 1981), transport in 2D systems (NISHINCHI ET AL., 1983), and FET and HEMT performance (ARNOLD ET AL., 1981), though not DH (double-heterojunction) laser or HBT (heterojunction bipolar transistor) performance, which would be expected of a hole-trapping center (MOONEY, 1990).

Early work on PPC (LANG & LOGAN, 1977) revealed that at low temperatures, photoconductivity may persist in numerous semiconductors even days beyond actual illumination, and can be quenched only by warming the sample. Capacitance and optical measurements subsequently revealed (LANG & LOGAN, 1979) a confusing picture wherein it appeared that an occupied donor lay deep within the band-gap, but after excitation was found to be resonant with the conduction band. In $Al_xGa_{1-x}As$ with $x \lesssim 0.2$, this relaxation or Franck-Condon energy was several times the donor binding energy. This led to the perplexing question of how a resonant state, normally expected from EMT to be highly delocalized, could effect such a large lattice relaxation (LLR), and thus appear to be very well localized and associated primarily with the Γ-, L- or X-minimum.

This situation, as seen in indium antimonide for example (see § 4.5), may be depicted in the configuration-coördinate diagram seen in Fig. 4.1. In this figure, the abscissa is an abstract or generalized lattice parameter Q, a significant variation in which reflects LLR. The ordinate is the total energy of the system, including the energy of the electron and that of

* So named because they are *D*onors, associated with an unknown defect X, or are found to be associated, at least apparently, with the X-minimum of the conduction band.

the elastic deformation of the lattice. The parabolas represent the adiabatic potential curves of the defect center. The parabolas centered at Q_Γ represent the donor in its "shallow" (i.e., non-metastable) state:* the higher parabola represents the (positively) ionized donor and its electron in the conduction band; the lower parabola, the (neutral) deionized shallow donor in the unrelaxed state. The parabola centered at Q_X represents the donor in its relaxed state.

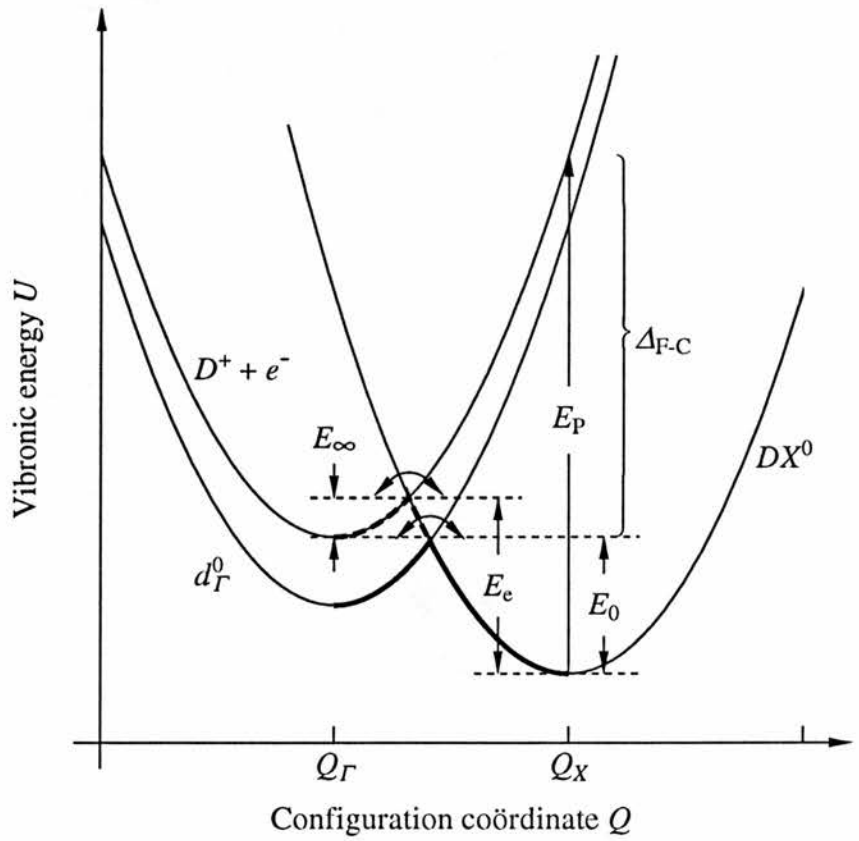

FIG. 4.1: Configuration coördinate diagram depicting large lattice relaxation as observed in indium antimonide (see text, and also § 4.5). Upper left parabola: Donor positively ionized, electron in conduction band; lower left parabola: Neutral d_Γ donor; right parabola: Occupied *DX*-center exhibiting LLR. The vertical transition from the *DX* state to the conduction band represents photoionization, and is a much larger energy than that measured in a Hall experiment, *viz.*, the difference between the capture energy, E_∞, and the emission energy, E_e. The curved arrows represent two possible paths for energy capture by the *DX* level. Δ_{F-C} is the Franck-Condon shift.

One of the salient features of this type of diagram is that it reveals how activation or

* Also called the "substitutional" state (MOONEY, 1991).

ionization energies measured by different means can vary so radically from one another, and how phenomena like PPC can arise: Superposed on the parabola at Q_X is an arrow denoting the optical excitation of an electron to the conduction band. In this case, there is neither sufficient time nor thermal energy to bring about a lattice reconfiguration, so a large quantum of energy, E_P, is required for ionization in a strictly vertical transition. On the other hand, emission of an electron from the donor in the X state over the higher barrier may result from a thermally activated lattice reconfiguration with only the energy E_e. This may be succeeded by the recapture of the electron by the ionized donor, but only if the electron attains E_∞, the capture activation energy required to surmount the barrier.* The difference between E_e and E_∞ is the donor-binding energy E_0, and is what Hall measurements of free-electron concentration as a function of temperature can reveal. The difference between E_P and E_0 is the Franck-Condon energy.

DX behavior is observed with virtually all substitutional donors, cationic or anionic, in GaAs, AlGaAs, and many other III-V and II-VI compounds. Metastable donors are found as well in silicon. In $Al_xGa_{1-x}As$, the *DX* center is the dominant state for $x > 0.22$. Initially, *DX* donors were enigmatic in their identity as well as in their nature. A defect-complex was proposed by LANG & LOGAN (1979), as it seemed unlikely that an isolated donor could effect such LLR. Subsequent research with GaAs exhibiting PPC has indicated that a *DX* level exists 260 meV above the bottom of the conduction band, and is occupied only when the material is heavily doped or subjected to hydrostatic pressure (at 24 kbar the band structure of GaAs becomes almost identical to that of $Al_{0.24}Ga_{0.76}As$, and similar centers become evident, at least up to 30 kbar). As the defect appears to have substantial contributions from minima removed from the zone center, it was thought likely to be of low symmetry; although there was the opinion that the deep state is actually a separate level, distinct from the shallow level, of *s*-like symmetry (HJALMARSON ET AL., 1986). MORGAN (1986) suggested the Jahn-Teller effect† as a possible explanation for metastability in $Al_xGa_{1-x}As$.

BAJ ET AL. (1976) investigated similar behavior in CdTe:Cl, in which a pressure-induced low-temperature metastable state associated with the chlorine impurity was found to have thermal and optical ionization energies of 80 and 1050 meV respectively. The relaxation

* Alternatively, tunneling may be possible, but this would depend on specific parameters of the impurity and the host lattice; or, the electron may be captured by the non-metastable state of the donor at Q_L.

† This is a form of LLR wherein electron states which are degenerate by virtue of the symmetry of a crystal may be split by a distortion of the crystal. The Jahn-Teller theorem states that for each such degenerate orbital, there exists a normal mode of vibration such that distortion will occur spontaneously and lower the overall energy.

time (i.e., the exponential population decay time constant) was found to be strongly pressure-dependent, and is maximum when the capture energy is equal to the emission energy (see Fig. 4.1); the same was found to hold true in indium antimonide.

Another example of a deep state, apparently stabilized by Jahn-Teller distortion, is that of the $EL2$ defect in gallium arsenide. $EL2$ is an antisite defect, in this case, an arsenide ion in the gallium position. It has a normal effective mass-like ($EL2^0$) state, and a metastable ($EL2^*$) state located at a higher energy, and normally unpopulated. It can, however, be populated either by illuminating the sample at low temperature, or by pressurizing it to ~3 kbar, whence it is resonant with the Γ-minimum, and at which point it accepts an electron from the conduction band, apparently as a negative-U center (POROWSKI & SADOWSKI) (see below).

As discussed in Chapter III, FIR photoconductivity has been used to help characterize both shallow and deep donors in GaAs and AlGaAs. Interstate transitions give rise to enhanced photoconductivity through photothermal ionization, and central cell structure becomes evident at high magnetic fields, allowing impurity identification. Numerous investigators have demonstrated the existence of hydrogen-like levels closely (though not solely) associated with the Γ, L^* and X† minima, thus implying that these centers are in fact donors, rather than defect complexes. Furthermore, the transition of a donor from a shallow state to a deep state with increasing pressure has been observed with this method (WASILEWSKI ET AL., 1982).‡

One recent explanation of deep center metastability agreeing well with many (but not all—see below) experiments (see MOONEY, 1991) is the negative-U model, described by CHADI & CHANG (1988). Normally, a donor atom in a crystal lattice possesses a positive U:¶ i.e., energy is raised when a donor ion receives a second electron, due to the repulsion between the two electrons. On the other hand, if the acquisition of the first electron results in LLR, it is possible for a metastable state to arise, in that the overall energy of the system has been reduced, and this second ionization is likely in the presence of a second electron.

The configuration-coördinate diagram for this schema (as discussed by MOONEY (1991) for AlGaAs) may be seen in Fig. 4.2.

---

* WASILEWSKI ET AL. (1982).

† DOBACZEWSKI ET AL. (1988) and DMOCHOWSKI ET AL. (1988)

‡ It should be pointed out, as CHADI & CHANG (1988) argue, that for many systems, this apparent tracking of the defect state with the L-minimum is purely fortuitous, having nothing to do with the L band.

¶ $U \equiv$ the effective Hubbard correlation energy.

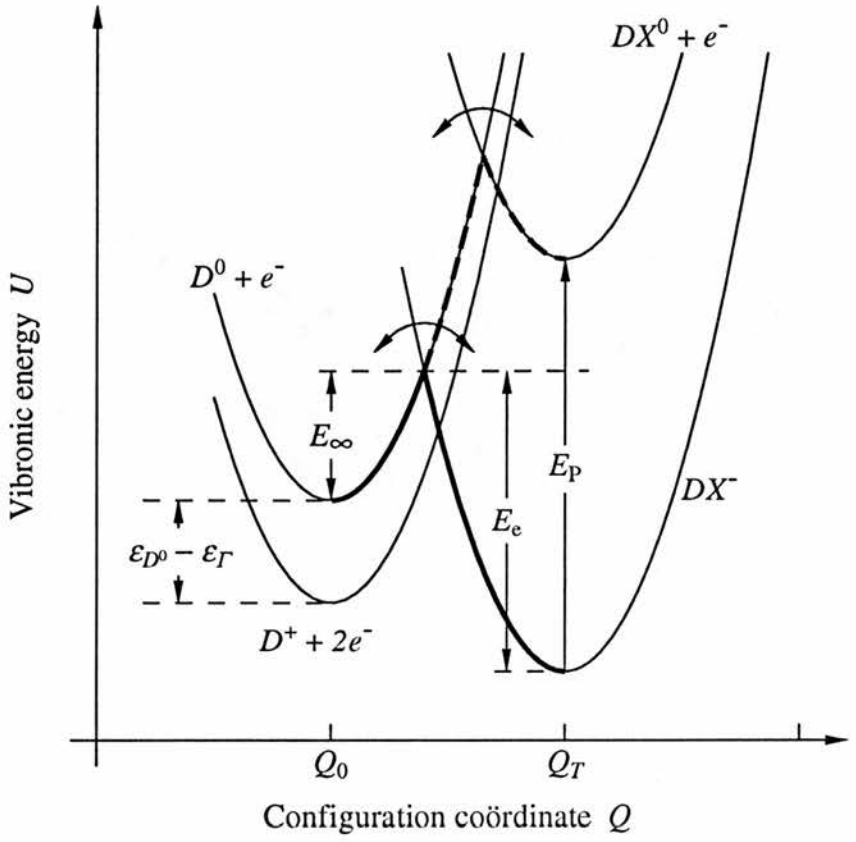

FIG. 4.2: Configuration coördinate diagram depicting negative-U model of LLR (see text and MOONEY, 1991).

The parabolas centered at Q_T correspond to the deep, metastable DX level arising from LLR. The lower of the two represents the occupied state found deep in the gap. This may correspond in fact to a negatively charged donor, and in this case there is likely to be an excited neutral state (through which a postulated two-step photoionization proceeds), corresponding to the higher parabola on the same side. Excitation of an electron into the conduction band from either of the two DX levels (or electron capture therefrom) requires sufficient energy to surmount the barriers between the states (shown in thicker solid and dashed lines with curved arrows), although tunneling may occur, depending on the barrier breadth and height. The upper barrier appears to have a height of $\sim$100 meV, corresponding to a comparatively short-lived excited state.

The two parabolas centered on Q_0 represent the donor in the "substitutional" configuration, the lower being positively ionized with both electrons in the conduction band, and the higher being an *excited* one-electron state D^0. This excited state, lying above the positively

ionized state, is postulated in order to agree with kinetic studies (THEIS & MOONEY, 1990) indicating a two-step thermal capture process.

Optical excitation, involving no phonon coupling, reveals a large ionization energy, as shown. However (as is evident from experiments that achieve thermal equilibrium between the lattice and the electrons) once the LLR has been effected, the energy of the electrons, which return to the bottom of the conduction band, is only slightly greater than when they occupy the donor site. There exists, therefore, an energy barrier (shown with a thicker line) that prevents the electron and donor level from spontaneously relaxing. Once the electrons are rethermalized with only a small energy, however, the metastability is lost, and the original state reappears.

The rationale for having hypothesized a negative-U model initially was the pseudopotential calculations done for a single Si donor atom in GaAs, showing the stability conferred on the distorted configuration once a Si-As bond was broken. However, in the case of AlGaAs, there are four non-equivalent substitutions of Al for Ga atoms. There are also four *DX* levels observed in GaAs/AlAs superlattices, lending some experimental support to the negative-U model. Also cited by Mooney in support of the model are EXAFS experiments, the absence of an EPR signal from the centers, consistent with paired electrons, DLTS measurements, Mössbauer spectra and photoconductivity experiments demonstrating that photoionization of the centers removes two electrons. Only one magnetic susceptibility experiment is cited as negative evidence.

MAUDE ET AL. (1987) investigated Shubnikov-de Haas oscillations and PPC, particularly with regard to mobility, in highly doped n-type AlGaAs as a function of carrier concentration and pressure. The behavior observed was largely consistent with that observed in highly S-, Se- and Te-doped indium antimonide by KOŃCZEWICZ ET AL. (1977) (with Hall and thermoelectric power measurements) and POROWSKI ET AL. (1981) (with Shubnikov de Haas measurements) (see below). (This is not surprising inasmuch as III-V compounds share nearly identical band structures and pressure coefficients.) The results were seen to be *qualitatively* consistent (MAUDE ET AL., 1989) with a model of a deep donor which is singly ionized at ambient pressure, and deionized at high pressure. This was concluded on the basis of applying the BARRIE (1956) model of mobility limited by screened ionized impurity scattering for a nonparabolic conduction band (in the Born approximation) to the system in question:

$$\mu = \frac{Cn}{N_I m_e^*(k_F)^2 F(\lambda, k_F)}, \tag{4.6}$$

where C is a constant, $m_e^*(k_F)$ is the pressure-dependent effective mass at the Fermi energy, and $F(\lambda, k_F)$ is a term proportional to the scattering cross-section. It was observed that the formula predicts for the deionization model an increase of mobility with pressure, largely due to precipitous drops in the scattering cross-section and the impurity ion concentration. On the other hand, the formula predicts, contrary to experiment, a decrease in mobility for the negative-U model, as n decreases, removing screening and lowering the Fermi velocity,* while N_I remains constant. However, according to CHADI ET AL., (1989), the negative-U model *does* predict the observed increase in mobility with pressure: In the case of highly doped samples, the value of the density of states needed to calculate the screening parameter λ ($\lambda^2 \approx 4\pi e^2 g(\epsilon_F)/\kappa$) used in Eq. 4.6 is:

$$g(\epsilon_F) = \frac{3n}{2\epsilon_F} + \frac{n(P=0) - n(P)}{\mathcal{W}}, \tag{4.7}$$

where $\mathcal{W}$ is the energy-width of the *DX* level distribution. The second addend in Eq. 4.7, neglected by MAUDE ET AL., (1989), will allow an accurate match between theory and experiment for $\mathcal{W} = 0.03$ to 0.04 eV, an experimentally consistent value, while the neutral donor model would require a value of $\mathcal{W} = 0.2$ eV, which is not consistent.

Furthermore, even without the use of Eq. 4.7, Eq. 4.6 may be found to predict an increase in mobility in the negative-U model by virtue of certain correlation effects (see O'REILLY (1989), who argues that the uniform electron distribution screening model implicit in Eq. 4.7 is inappropriate in any case due to the highly localized nature of the donor electrons): When ionized donors and acceptors are located near each other in a semiconductor, the potential energy, relative to a neutral pair or a neutral-ion pair, is lowered. The dipolar fields arising from this effect are on average of much shorter extent ($\propto 1/d^3$, where d is the ionic separation) than monopolar fields arising from unpaired ions ($\propto 1/d^2$), giving rise to less scattering. If largely monopolar ionized impurity fields were to be replaced by dipolar fields as the *DX* centers became negatively charged, the net mobility could thereby increase (see § 4.6).

YAMAGUCHI ET AL. (1990) presented a theoretical simulation of Si-doped GaAs, $Al_xGa_{1-x}As$, and AlAs/GaAs superlattices, using a 64-atom "supercell", as opposed to the 18-atom model of Chadi and Chang. They calculated total energy, considering the Hellmann-Feynman force and using the *ab initio* self-consistent pseudo-potential method. Their results, in consonance with previous work they cite, imply that the negative-U center

* In the simple Rutherford model, $\tau \propto v_F^3$.

is metastable even at high hydrostatic pressures. Rather, a deep substitutional donor of A_1 symmetry and a higher lying T_2 level are implicated to explain various photoluminescence and photoconductivity results.

Finally, KOŃCZYKOWSKI ET AL. (1974) (see below) cooled to 77°K a single sample of indium antimonide at various pressures, and measured the Hall coefficient against pressure in each case (see Fig. 4.4). The higher the cool-down pressure (above 7 kbar), the lower the free electron concentration in general, as more metastable states were occupied. However, at the highest pressure measured, electron concentration was equal from trial to trial, i.e., independent of the cool-down pressure. This is strong evidence against the negative-U model in this case (see the discussion below).

4.5 Metastable Donors in Indium Antimonide

POROWSKI ET AL. (1980) reviewed earlier Hall measurements, involving variable hydrostatic pressure, temperature and magnetic field, on pure n-InSb ($N_D - N_A \lesssim 10^{15}\,\mathrm{cm}^{-3}$). These measurements (KOŃCZYKOWSKI ET AL., 1972; POROWSKI ET AL., 1974; POROWSKI & SOSNOWSKI, 1976; and DMOWSKI ET AL., 1976) revealed the presence of two donor levels, one of which was metastable. The summarized results can be seen in the following figures.

In Fig. 4.3 (*a*), the Hall coefficient is plotted for three pressures (applied at room temperature) against temperature in a cooling process. However, these curves do not reflect equilibrium conditions, and the path by which they were attained is important. The samples were pressurized as indicated while at room temperature, and were subsequently cooled. It was found that for pressures $\lesssim 7$ kbar, the Hall coefficient does not change significantly with respect to pressure or temperature. However, for pressures above 7 kbar, deionization of two donor levels is apparent. Freeze-out on to the deeper of the two levels continues as the temperature is lowered, until approximately 100°K. At this point, the electron concentration is relatively stable until the temperature is lowered by another 30°K, when the temperature is low enough to freeze electrons out on to the shallower donor level. At 9.2 kbar, the donor levels are deeper still, and each leg of the freeze-out is correspondingly higher on the plot. It was also noted that while in the temperature region of 90–115°K, electrons transferred from the Γ-minimum to the deeper level over the course of minutes, below 90°K such transfer was so slow as to be virtually unobservable, apparently amounting to 270 days at 77°K. It was thus concluded that a barrier of $\sim$0.3 eV exists between this level and the Γ-minimum,*

* For a simple thermally activated process the time constant τ may be linked to the barrier height E_B by $\tau \propto \exp(E_B/k_BT)$.

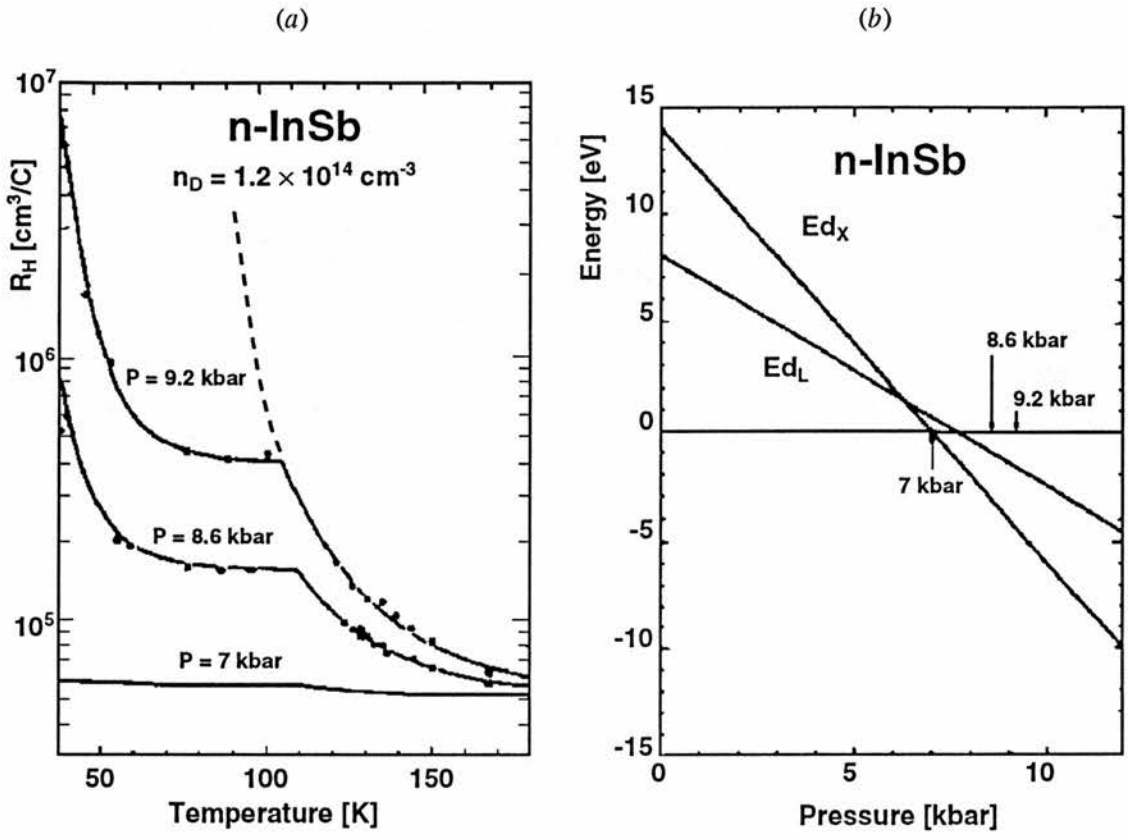

FIG. 4.3: (*a*): Hall coefficient *vs.* temperature for different hydrostatic pressures. As temperature is lowered above 100°K, the deeper donor deionizes. At ~100°K, it becomes metastable; further cooling deionizes only the shallower donor, and the equilibrium condition indicated by the dashed line is not attained. (*b*): "L-" and "X-associated" (see text) donor energies relative to the Γ-minimum *vs.* pressure. The pressures corresponding to the measurements in (*a*) are marked with arrows. (Reprinted and adapted from POROWSKI ET AL., 1980.)

conferring on the former a measure of metastability. The equilibrium state prevented by this metastability is indicated approximately by the dashed line.

The energetics of this system are depicted in part (*b*) of the figure. Here it is seen that the metastable state indeed exhibits mainly the character of the X-minimum ($d\epsilon_{X-\Gamma}/dP = -20\,\mathrm{meV\,kbar^{-1}}$, where the subscript '$-\Gamma$' implies that the energy is relative to the Γ-minimum), while the other exhibits mainly that of the L-minimum ($d\epsilon_{L-\Gamma}/dP = -10.5\,\mathrm{meV\,kbar^{-1}}$). However, the convention adopted by Porowski for labeling these as "X-" and "L-associated" states is not actually meant to imply that the states are genuinely located at these minima, as there are significant contributions to their

respective wavefunctions from all parts of the band. Strictly, the convention implies no more nor less than the similarity of pressure coefficients of conduction band energy.

It was initially guessed and eventually concluded from FIR experiments (see below) that these two states, which cross into the gap at about 7 and 8 kbar, respectively, represent two non-equivalent lattice sites of the same donor, which, by virtue of its depth relative to that of known donors (S, Se and Te), appears to be oxygen, a prevalent contaminant.*

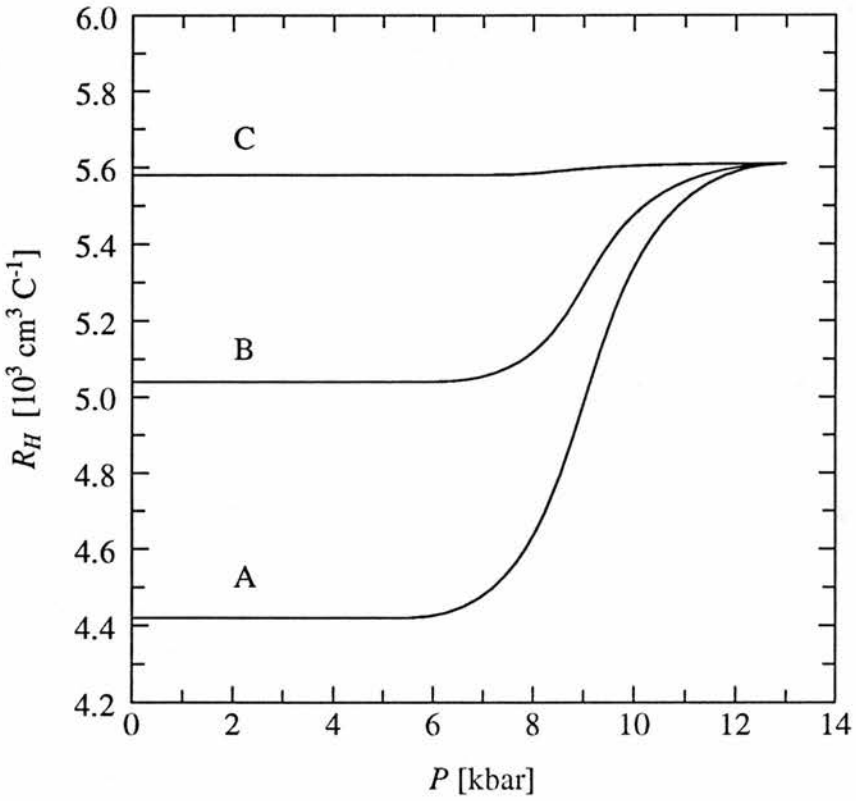

FIG. 4.4: Hall coefficient *vs.* pressure at 77°K for different cool-down pressures P_c (i.e., the pressure at which the sample is cooled from room-temperature to 77°K, whence it may be pressurized and depressurized reversibly): Curve (A), $P_c < 7$ kbar (for several values of P_c); (B), $P_c = 8.5$ kbar; (C), $P_c = 11$ kbar. (From KOŃCZYKOWSKI ET AL., 1974.)

At the same time as the above measurements were performed, a complementary set of data was assembled, and is displayed in Fig. 4.4. In this case, a single *uncompensated*

* This is speculative. The depths of donors increase with electronegativity, for which there are many different definitions and scales. Si and Ge are possibilities as well.

sample of indium antimonide was cooled down isobarically to 77°K at numerous pressures. Once the sample was cold, its metastable states were in effect inert, and pressure could be changed isothermally and reversibly, leaving only non-metastable donors to influence the Hall coefficient. The data show that when cool-down was carried out at pressures below 7 kbar, the donor level was completely ionized (i.e., R_H remained low and constant) at low pressures (also below 7 kbar), regardless of the cool-down pressure. Subsequently, over the range from 7–11 kbar, a transition region, wherein the "L" level crossed the Γ-minimum, occurred, giving "freeze-out". This was followed by a saturation region where once again R_H was constant, but high, presumably meaning that all the "L" levels were occupied. After cool-down at higher pressures, R_H starts off at correspondingly higher values, indicating that electrons had been frozen out onto the metastable level during cool-down. However, as the pressure was varied following each cool-down, a saturation region is reached at the highest pressures in which R_H is invariant from trial to trial. This behavior is eminently consistent with a picture of a semiconductor in which a constant number of electrons, Δn, is divided between a population of "normal" (i.e., non-metastable) states d_L, and another of metastable states d_X, such that, simply, $N_L + N_X = \Delta n$, with N_X being determined by the initial cool-down pressure.

This behavior would not be expected in a *compensated* sample, as was examined in the present work (see Chapter VII): In such a case, if the number of acceptors were larger than the number of non-"A" donors, then the electron concentration would be lowered beyond the values observed in Fig. 4.4. In particular, the sample resistance would become arbitrarily large with enough acceptors, lowering the electron concentration far enough that the saturation point observed in Fig. 4.4 is never reached, as there would be too few conduction band electrons to guarantee occupation at any given pressure.

If these metastable states were *DX* centers stabilized by the negative-U effect, it could be expected that the differing populations N_X in each trial would freeze out differing numbers $2N_X$ of electrons, and three different Hall coefficients would be measured at the highest pressure, which is clearly not the case: i.e., if the non-metastable "L" states freeze out only one electron, then the saturation limit of curve (A) would be expected to remain at $R_H = 5.6 \times 10^3\,\mathrm{cm^3\,C^{-1}}$. However, curve (C) would be shifted upwards with its saturation limit at $\sim 6.8 \times 10^3\,\mathrm{cm^3\,C^{-1}}$ (assuming $r_H = 1$). Curve (B) would be expected to correspond to ~50% occupancy of the metastable levels, initially. This would leave an equal number of normal levels, but these, accepting only one electron each, would freeze out half as many electrons as they would if they too were metastable (as in curve (C)), and therefore a final

saturation point of $R_H \approx 6.5 \times 10^3\,\mathrm{cm^3\,C^{-1}}$ should appear.

It therefore appears that Kończykowski *et al.* have obtained strong evidence, in this sample, for a positive-U donor in indium antimonide. However, the experiment needs to be repeated for a number of samples of varying carrier concentration.

It must also be noted that while these states are observed in a narrow gap material, they are ~0.5 eV removed from their actual respective subsidiary conduction band extrema, which precludes describing them by EMT; they are in fact deep donor states. There is expected to be, therefore, significant admixture of states and corresponding symmetries. STRADLING (1985) demonstrated this admixture using Fourier transform spectroscopy in the far infrared, as illustrated in Fig. 4.5. In this experiment, a high magnetic field was used to achieve substantial freeze-out, and to Zeeman-split shallow Γ-associated donor levels, allowing sharper resolution among them. At low pressure, the $1s \rightarrow 2p_0$ transition energy for this deep donor ("A") tracks approximately with the Γ-minimum,* but at 6 kbar it suddenly breaks and tracks approximately with the L-minimum, reflecting the deepening of the ground state from $1s(\Gamma)$ to $1s(L)$.

This anticrossing behavior indicates that the two states involved share a symmetry, therefore necessarily interacting with one another.† (These measurements involve very small ground state energies—i.e., on the order of a few meV—and therefore must be conducted at liquid helium temperatures. It is therefore not possible to observe any admixture with the relaxed "X"-associated state, which, as noted above, is accompanied by a 300 meV barrier.)

In Fig. 4.5 (*b*), the $1s \rightarrow 2p_-$ transition is plotted as a function of magnetic field. This transition is sufficiently sharp to allow resolution of the shallow donors (B, C and D).

It should be noted that by virtue of its metastability, "A" may be used to freeze out electrons at low temperatures by first pressurizing the indium antimonide to above 7 kbar, cooling it to below 100°K, thus trapping electrons on the donor sites, and finally depressurizing the sample while still cold. This restores the original ambient energy gap and effective mass, thus allowing a spectroscopic comparison of its impurity energy and population levels in the normal and metastable states. It is found that in an uncompensated sample, the Γ-like state of donor "A" disappears completely from the spectrum when this is done, illustrating that

* i.e., as the ground state energy varies approximately as that of the Γ-minimum.

† Anticrossing occurs when a perturbation mixes states of matching symmetry, and a quantum mechanical "repulsion" results: If two such states, E_1 and E_2, interact through a potential operator V, such that $H_{12} = \langle 1|V|2\rangle$ (using standard bra-ket notation), then second-order perturbation theory reveals that $E_1' = \frac{1}{2}\{E_{21}+E_{11} \pm [(E_{21}-E_{11})^2+4H_{12}^2]^{1/2}\}$, where the prime indicates the perturbed state, $E_{11} \equiv E_1+H_{11}$ and $E_{21} \equiv E_2 + H_{22}$.

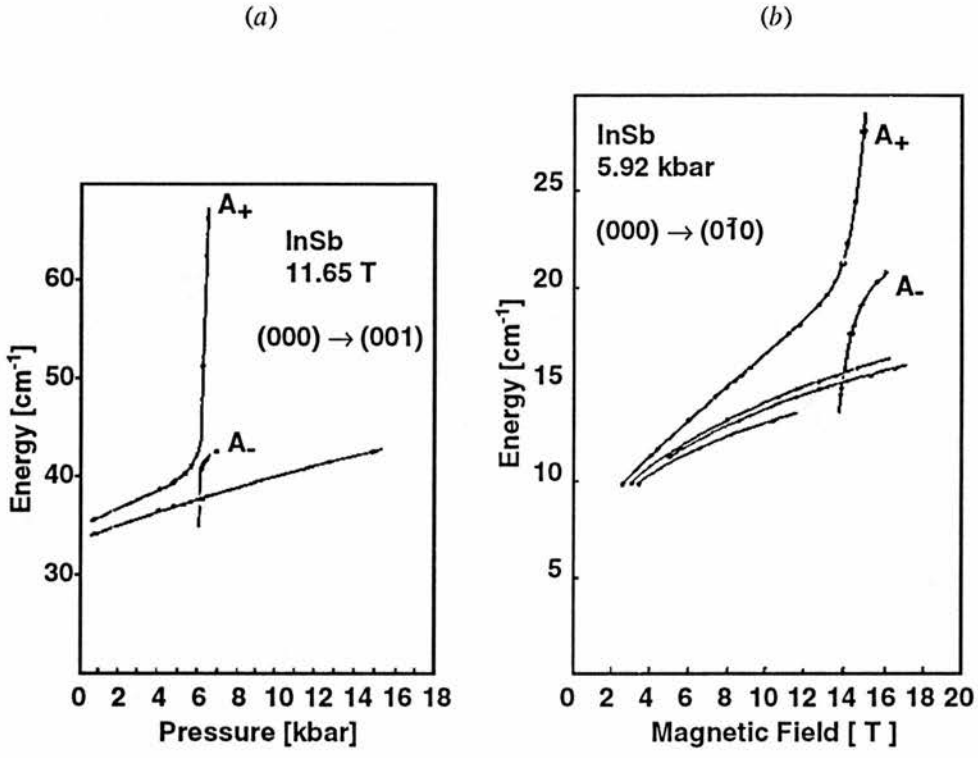

FIG. 4.5: (*a*): Anticrossing behavior of donor "*A*" is exhibited at 6 kbar for the $1s \rightarrow 2p_0$ transition, indicating admixture of Γ and L states. (*b*): The sharper $1s \rightarrow 2p_-$ transition is shown, resolving shallow donors *B*, *C* and *D*. (Reprinted and adapted from STRADLING, 1985.)

the two donor states represent one donor species (Fig. 4.6).

The anticrossing between Γ and "*L*" states shown in Fig. 4.5, taken with the results of Fig. 4.6, show that all three types of level (Γ, deep non-metastable ("*L*") and deep metastable ("*X*")) all involve the same donor species "*A*".

Highly uncompensated samples like those studied in Figs. 4.4 and 4.6 would be expected to become highly resistive, or insulating, at the highest pressures were the negative-*U* model correct: The concentration of donor "*A*" is known from spectroscopic studies, as in Fig. 4.6, to comprise approximately half of the donor atoms. Therefore, if each donor *A* atom froze out two electrons, there would be approximately no carriers left in the band. Compensated samples, on the other hand, are highly resistive at the highest pressures anyway, as pointed out above, so cannot as straightforwardly be used as an indicator.

Finally, it appears that donors in III-V semiconductors in general can be expected to exhibit three types of levels: Shallow Γ-like levels and two deep levels, one of A_1 (fully

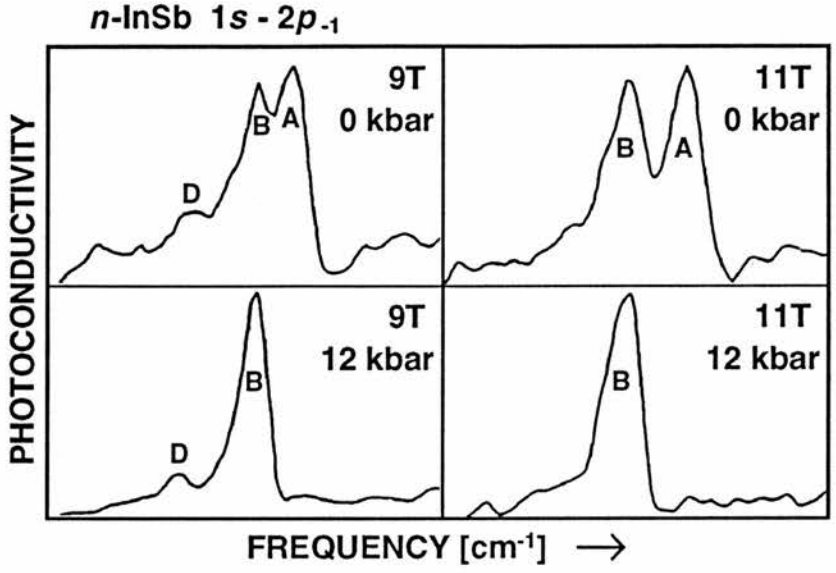

FIG. 4.6: Far-infrared data demonstrating that all states (shallow, deep and metastable) of donor "*A*" indeed represent one impurity species (Reprinted and adapted from STRADLING, 1985). If it is assumed that the integrated intensities of the peaks accurately represent the concentrations of the active centers, it should be possible with Hall measurements of the type illustrated in Fig. 4.4 to estimate the number of carriers that can be frozen out by a donor.

symmetric) symmetry, but non-metastable, and another of metastable *DX* character. This conclusion is invited partly by the work of DMOCHOWSKI ET AL., (1990, '91, '91) wherein impurity states associated with various identified donors (S, Si and Ge) in high-purity GaAs were investigated using FIR transmission and high pressure (up to 30 kbar), as well as photoluminescence. Shallow to deep A_1 state transitions were observed for both sulfur and silicon. Previous work with, e.g., DLTS, had confirmed that *DX*-like levels are extant under hydrostatic pressure in GaAs doped with S, Ge or Si.

4.6 Correlative Effects among Impurity Ions in Semiconductors

ANDERSON (1958) was one of the first workers to address the question of the effects of localized potentials on transport in semiconductors. In particular, the question of spin diffusion among donor electrons in silicon prompted the construction of a model of a semiconductor wherein impurities were modeled as a band of sufficient disorder and low concentration that Drude-like conduction was not possible, but quantum tunneling, or "hopping" conduction, was. (Because the band must be sufficiently "rarefied" to eliminate wavefunc-

tion overlap which would lead to a Drude-like situation, energy conservation, even allowing for quantum mechanical violations, requires phonon assistance.) The theory presented by Anderson in this case,* largely a tight-binding approach, was constrained to interactions which, like the localized potentials discussed above, fell off very quickly with distance, i.e., faster than $1/r^3$, and which certainly therefore could not include the Coulomb potential. At any rate, the salient conclusion of the work was that localization, and the cessation of conduction, would occur when the variation in site potential was greater than the width of the band which would result from the overlap of the impurity states.

MOTT (1967) published a review of the ensuing work on disordered systems, which included a number of inquiries into the density of states of a disordered system. In particular, the question arose of whether a gap in the density of states would exist in such a system. Mott concluded that for a one-dimensional system, a gap would not arise in a completely random system, but would in a system of limited disorder. For a three-dimensional system, the question was left open, but a primary concern was the definition of localization. Mott proposed that while the distinction between "localized" and "non-localized" was qualitative, a population of electrons, characterized as being within a specific energy band, whose mean contribution to conductivity diminished toward zero as the frequency of the applied electric field approached zero could be said to be localized.

ZIMAN (1968, '69) pointed out the distinction between cellular disorder, wherein, as in Anderson's model, variations in potential occur from atom to atom, and structural disorder, wherein the periodicity of the lattice is disturbed.

COHEN ET AL. (1969) reported on studies in amorphous semiconducting alloys and presented a band model to account for the effects of localized states, by which the authors meant states whose wavefunctions decrease exponentially from a given site. These states, it was proposed, originate from the variation in valence bond characteristics (e.g., coördination number) associated with a given atom (resulting from the compositional and translational disorder typical of glassy solids), and give rise to a "smeared" valence band that extends into the conduction band (and *vice versa*). This overlap results in electrons from the valence band falling into lower conduction band states, with the Fermi level coming to rest somewhere

* This was one of the first implementations (beginning a long tradition in this subject) of the Markoff statistical method for random variables, as modified by Holtsmark. In this case, a random variation in potential energy is imposed on the distribution of "sites" (e.g., individual atoms, or, in the case of the Holtsmark distribution, stars in space), leading to a treatment where the overall potential felt at any one site can be separated into a background potential due to the large site population at long range and a local potential due to a nearest neighbor.

toward the minimum of the two tails, surrounded, energetically, by charged (localized) states within each band. Furthermore, it is supposed that certain valence bonding requirements are not satisfied, and there result broken bonds that also expose Coulomb potentials (AMBEGAOKAR ET AL., 1971). The final position of the Fermi level is influenced by the distribution of these Coulombic potentials, which must self-adjust, by means of hopping conduction, for example, to attain the lowest total energy. This difference in conduction mechanism at the energy of the localized states, where the normal band conduction (finite at $T = 0$) is replaced by a thermally activated process, gives rise to a "mobility gap". Within this gap, the charged localized states may serve as traps for carriers.

In particular, the authors cite experiments with photoconductivity and intense transient electric fields wherein conductivity was seen to decay rapidly after an initial stimulation, but persisted for hours at low temperatures at levels still orders of magnitude greater than normal. This metastability (not involving lattice relaxation) was ascribed to the existence of traps in the vicinity of the Fermi level which give rise to supra-equilibrium concentrations of carriers, and which relax only by the slow process of hopping conduction.

AMBEGAOKAR ET AL., 1971 examined hopping conductivity in amorphous semiconductors (Ge, Si and C), and using Mott's model and a percolation method for calculation, derived Mott's conduction rule for disordered solids, which states that

$$\sigma_{DC} \propto \exp[-(\zeta\alpha^3/g_0 k_B T)^{1/4}, \tag{4.8}$$

where ζ is a dimensionless constant, α is the rate of decay of the impurity wavefunction, and g_0 is the density of states. In their model, the authors tentatively assumed that there was no correlation between occupation numbers at different sites. Furthermore, Mott's rule depends on the continuity of the density of states at the Fermi level. But Ambegaokar *et al.* proposed that the density of states germane to Eq. 4.8 would be lower than that for the material as a whole.

In a series of papers beginning in seventies (e.g., ÉFROS & SHKLOVSKIĬ, 1974; ÉFROS, 1976; GEL'MONT & ÉFROS, 1976; BARANOVSKIĬ ET AL., 1978; and BARANOVSKIĬ ET AL., 1980), the question of the nature of the Fermi energy and its associated density of states in disordered (doped or amorphous) crystalline solids, and their precise dependence on the energetics of large ensembles of electrons, was investigated using various mathematical models. Results were generated for systems of various dimensions.

The key points of the model of ÉFROS & SHKLOVSKIĬ (1975), for instance, included that the Coulomb potential represents a long-range interaction, and that for a three-dimensional crystal it results in a "soft Coulomb gap", i.e., a drop to zero, at one energy only, in the density of states near the Fermi level brought on by the Coulomb potential.

Without going into the mathematics of the self-consistent approach eventually presented in ÉFROS (1976) or the computer model of GEL'MONT & ÉFROS (1977), this effect can be thought of as follows: A system in its lowest energy configuration at $T = 0$ cannot be stabilized further by a redistribution of charges. In particular, the transfer of an electron between localized sites should result in an increase of potential energy, as the initial site must be below the Fermi level, and the final site above. Furthermore, this exchange of sites cannot be stabilized by Coulombic terms to the extent that this stabilization energy exceeds the energy of the transfer, for that would contradict the initial construction. But it is because of the long-range nature of the Coulomb interaction (specifically, in that it falls off more slowly than $1/r^3$) that an electron cannot simply be moved out of a given volume. Therefore, if an energy interval of width ϵ centered about the Fermi energy is imagined, two states $\epsilon_i < \epsilon_F$ and $\epsilon_j > \epsilon_F$ cannot be separated by a distance R that is less than $e^2/\kappa\epsilon$, for then their mutual interaction energy would be greater than ϵ. This implies a maximum concentration of states of ϵ^3/e^6 and a maximum density of states therefore of ϵ^2/e^6, implying that as ϵ vanishes, so must the density of states. The energy width $e^3 g_0^{1/2}$, the range of energies in which the density of states must fall below g_0, is called the Coulomb gap. It is also pointed out in this work that the shallow energy levels interact strongly with small energy electron-hole pairs. ÉFROS (1976) further states that due to polaron interactions (many-particle excitations) and correlation, this gap, in the three dimensional case, is not soft, but diminishes to 0 exponentially.

Éfros and Shklovskiĭ conclude that at low temperatures, conduction should be given by $\sigma_{DC} \propto \exp[-(e^2\alpha/\kappa T)^{1/2}]$.

BARANOVSKIĬ ET AL. (1980) examined dipole excitations, as well as excitations of higher multipoles, which are considered to be very weakly interacting for the most part (although quadrupole excitations play a large role in determining the specific heat at low temperatures). The compactness principle was introduced, which states that if the displacement r of a *low energy* dipole exceeds a value $r_0 = a_0^{3/2}\sqrt{A}/e$, where $2A$ is the energy width of the system, the probability of formation of that dipole tends to vanish with increasing r. This is a manifestation of the Coulomb gap, in that a large dipole arm in effect transforms the dipole into two individual charges, which themselves are forbidden within the Coulomb gap. It is

stated that it is the dipole excitations that determine the AC conductivity of a sample, while the monopole excitations determine the low temperature DC (hopping) conductivity. This is because the dipoles are of low energy (small dipole arm) and comparatively large distance from one another, and are as such "disconnected".

On the other hand, the dielectric properties of the material are significantly affected by the dipole population, as pairs will alter their polarization in the presence of a newly added charge, stabilizing it. This effect is, in ionic crystals, the so-called "polaron shift".

O'REILLY (1989), in response to the negative-U model controversy (see § 4.5), calculated pressure-dependent mobility values in degenerate Sn- and Si-doped GaAs for DX^0, uncorrelated DX^- and correlated DX^- models. It was shown that in a random distribution of impurity atoms, 50% of the impurities have an impurity neighbor within a distance of $\sim 0.55 N_I^{-1/3}$, a distance less than half that expected if the impurities were arranged in an FCC lattice. Therefore, electrostatic interactions may become significant at a lower doping level than initially guessed. In fact, O'Reilly shows that energy is lowered by 43 meV in a sample of doping $N_I = 1 \times 10^{19}\,\mathrm{cm}^{-3}$ if a DX^- donor and a d^+ donor form at the above median separation. Using the Born approximation, and taking the scattering cross section for two positive donors a small distance L apart to be $\sigma_2(L) = \sigma_2 - \sigma_d(L)$, where σ_2 is the scattering cross section for a monopole of charge $+2e$ and $\sigma_d(L)$ is that for a dipole of length L, an expression for mobility involving the pressure-dependent "trap-out" fraction f is derived. This expression is dominated by a term $(1-f)/(1-2f)$, which drives the mobility upward with pressure, in agreement with experiment. On the other hand, the expression breaks down for large degrees of trap-out ($f \gtrsim 0.5$), predicting infinite mobilities.

KOSSUT ET AL. (1990) computer-modeled the effects of correlation on the pressure- and concentration-dependent mobility of electrons in HgSe:Fe and heavily doped GaAs, and compared the results with experiment. In this model, some donors must be neutral, and the extent of impurity hybridization must be small, as in highly relaxed impurities such as DX centers, or when symmetries are "incompatible", as in HgSe:Fe In all cases reported, the experimental mobility was higher than would be expected from uncorrelated impurities.

Correlative effects with respect to cyclotron resonance were discussed at length in § 3.3.

4.7 Mobility Anomalies in Heterogeneous Samples

PIOTRZKOWSKI ET AL. (1986) examined mobility in high purity indium antimonide, which was studied in the present work as well, under conditions of high pressure freeze-out as described above in § 4.5. As seen in Fig. 4.7, Piotrzkowski *et al.* observed a number of

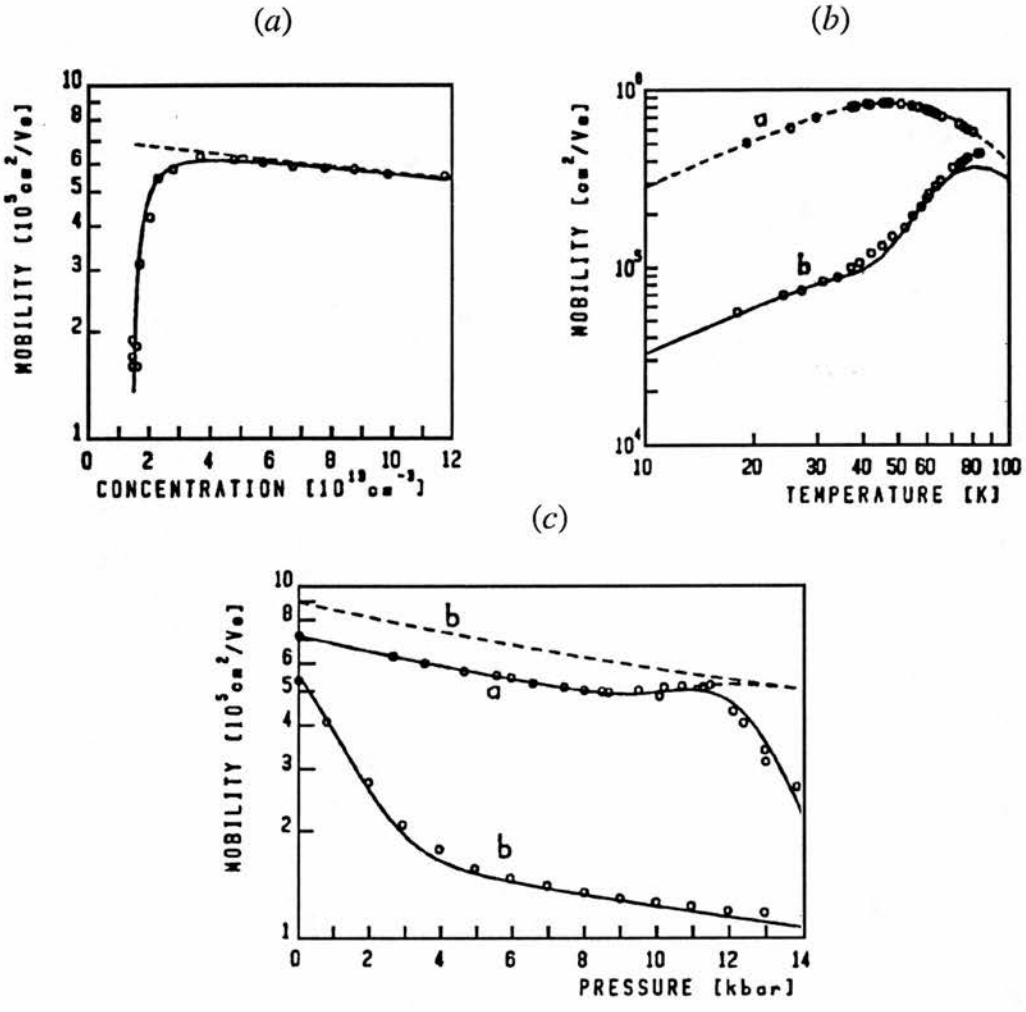

FIG. 4.7: Anomalous mobility effects in indium antimonide after high-pressure freeze-out: (*a*): Mobility *vs.* electron concentration subsequent to freeze-out; (*b*): Mobility *vs.* temperature; (*c*): Mobility *vs.* pressure. In each case where they appear, curve (a) results from no freeze-out ($n \approx 4 \times 10^{13}\,\mathrm{cm}^{-3}$), and (b) from virtually total metastable freeze-out ($n \lesssim 2 \times 10^{13}\,\mathrm{cm}^{-3}$). Dashed lines represent homogeneous samples, while solid lines are given by the model of PIOTRZKOWSKI ET AL. (1986) (see text).

unusual features in the dependence of mobility on a number of variables.

In part (*a*) of the figure, electron concentration, measured at 77°K and 6 kbar, has been determined by previous freeze-out of the metastable centers at various pressures (above 7 kbars). It is seen that at the lowest concentration (i.e., where the largest portion of met-

astable donors has been frozen out at the highest pressure), mobility plummets to ~15% of its "expected" value, i.e, that indicated by the dashed line, which represents the results for a homogeneous sample. Part (*b*) shows the dependence of mobility at ambient pressure on temperature below 100°K. Curve (a) depicts the sample's behavior when $n \approx 4 \times 10^{13}$ cm^{-3} (i.e., untreated), while in curve (b) $n \approx 2 \times 10^{13}\,cm^{-3}$. Finally, part (*c*) also illustrates the difference in mobility at 77°K between extremes of electron concentration, in this case curve (a) representing $n \approx 1.2 \times 10^{14}\,cm^{-3}$ (no freeze-out) and the lower curve (b) corresponding to $n \approx 1.6 \times 10^{13}\,cm^{-3}$ (virtually all donor "*A*" frozen out). It is seen that at the lowest pressure, even though electron concentration *remains constant* for curve (b) (see Fig. 4.4) mobility drops with pressure far more than expected due to increased effective mass alone. (In all cases in these figures, the dashed line corresponds to the results of a homogeneous sample.)

Piotrzkowski *et al.* posited a simple model wherein the sample comprised periodic layers of two alternating impurity concentrations, arranged perpendicularly to the flow of current. Such "growth striations" (periodic inhomogeneities) are typical in melt-grown crystals. In this scheme, the high purity (uncompensated) phase contains an electron concentration at 77°K (n_{77}) greater than that of the donor "*A*" species (N_{D^A}) (which represents no more than half of the impurities present), while in the low purity phase, because of compensation, $n_{77} < N_{D^A}$ (however, the concentration of donor "*A*" itself is assumed to be equal in the two types of layers). In this case, as hydrostatic pressure is increased, the electrons will be expected to diffuse from the high purity to the low purity region, as many more sites will be available there to trap them. This results in the eventual rise of a back voltage, preventing any further current flow into the low purity regions, which will be depleted. This leaves a very small population of electrons in the conduction band or in the pure regions to contribute to conductivity.

The solid lines in each figure are the calculated results of the model, when the purer of the two phases had $N_D - N_A \approx 10^{12}\,cm^{-3}$, i.e., was very pure.

It therefore appears that at the highest pressures, electrons are trapped in metastable states at sites in the impure regions, which are depleted, leaving ionized donors in the pure regions, which determine the conductivity.

CHAPTER V

Theory of Photoconductive Detectors and Noise

5.1 Introduction

To begin with, a simple model of intrinsic photoconductivity in semiconductors, particularly applicable to indium antimonide, will be described. Spectra shapes, noise mechanisms, and voltage/current relationships (including derivations of figures of merit*) will be examined.

It is assumed that the semiconductor detector is a rectangular prism of exposed surface area A, with length l, width w, and thickness t. This material, it will be initially assumed, is free of defects, including impurities and surface states. Further, let the material have electron and hole concentrations n and p, respectively, which at equilibrium will equal n_0 and p_0, and which will be incremented under photoexcitation by Δn and Δp. It is assumed that the fractional change in the carrier concentration is very small, as is the case in indium antimonide in most instances, and therefore that any current or voltage changes induced by photoexcitation will be second order. Let the electron and hole mobilities be μ_e and μ_h respectively. Let b be the electron to hole mobility ratio, η the quantum efficiency, R the resistance of the detector, and e the charge of an electron. The detector is exposed to an incident flux Φ photons/cm^2-s, where the wavelength λ of these photons is no greater than $\lambda_{co} = hc/E_g$, the cut-off wavelength for the band-gap. An electric field E is applied lengthwise to the sample by two ohmic (infinite recombination speed) contacts.

When photons impinge upon the semiconductor surface, then, $\eta\Phi A$ are absorbed, creating as many electron-hole pairs, assuming no two-photon processes, and assuming negligible

* Explanations of figures of merit germane to this discussion, i.e., responsivity, detectivity, etc., are to be found in Appendix 1, along with expressions for their ideal limits.

trapping (of minority carriers). Within the lifetime of a majority carrier, it may be conducted to the attracting electrode, only to be replaced at the opposite electrode by another identical carrier simultaneously, as a result of charge conservation. This may of course happen repeatedly to each of the multitude of carriers, resulting in a photogain G, often of many hundreds; that is, each photon absorbed has on the average produced G, or approximately τ_r/τ_t, current carriers, where τ_r is the mean recombination lifetime of the carriers, and τ_t is the mean transit time for the carriers between electrodes. This means that the induced photocurrent is

$$I_p = \eta \Phi A G e, \tag{5.1}$$

while the spectral signal-voltage (V_s) responsivity (see Appendix 1, *viz.*, current *vs.* constant energy interval) is

$$\Re_\lambda(V_s) = \frac{e\eta\lambda G R}{hc}, \tag{5.2}$$

which, for a spectrally flat (energy *vs.* wavelength) source yields a sawtooth shape cutting off at λ_{co}.

In order to determine G, assume the dark current in the detector is

$$I = ewt(n\mu_e + p\mu_h)E. \tag{5.3}$$

Then the photocurrent above is also

$$I_p = ewt(\mu_e \Delta n + \mu_h \Delta p)E, \tag{5.4}$$

and the gain is therefore

$$G = \frac{wtE(\mu_e \Delta n + \mu_h \Delta p)}{\eta \Phi A}. \tag{5.5}$$

Notice in Eq. 5.5 that G is effectively proportional to $\Delta\sigma$, the change in conductivity, and to E, which, for constant current is proportional to $1/\sigma$. Since responsivity is proportional to G, this shows that it is also proportional to $\Delta\sigma/\sigma \approx \Delta\sigma/\sigma_0$. It can be shown (LONG, 1977) that for minority carrier holes, in the presence of negligible trapping, the Δp that appears in Eq. 5.5 can be expressed as a function of the applied electric field:

$$\Delta p = \frac{\eta\Phi\tau_h}{t}\{1 - z_h[1 - \exp(-1/z_h)]\} \equiv \frac{\eta\Phi\tau_h}{t} f(z_h), \tag{5.6}$$

where τ_h is the hole lifetime and $z_h \equiv \mu_h \tau_h E/l$. Eq. 5.6 expresses the minority carrier sweepout effect, which effectively reduces the minority lifetime by lowering the hole concentration through recombination in the contacts, and is particularly pronounced in small samples ($l <$ minority carrier diffusion length).

It may be mentioned here, especially with regard to sweepout, that much of the literature makes reference to certain "ambipolar" quantities. VAN ROOSBROECK (1953) shows that under the assumption of certain standard conditions, a *concentration* of injected holes, for instance, moves through a semiconductor with a *group* velocity $E\mu_a$, where the ambipolar mobility μ_a is given by

$$\mu_a = \frac{p - n}{n/\mu_h + p/\mu_e}. \tag{5.7}$$

It should be emphasized that the holes themselves move at the drift velocity $E\mu_h$. For example, in a perfectly intrinsic photoconductor, this group velocity is zero. In other words, when photo-injection results in equal concentration changes of holes and electrons in a region of the semiconductor, then, even though the concentration profiles will diminish and spread as recombination and diffusion proceed, the "pulse" of carriers will not drift one way or the other, as it has a net charge of zero; nor will the hole pulse separate from the electron pulse, as to do so would violate the assumption of microscopic electrical neutrality. Rather, both holes and electrons will flow into the pulse region, from opposite directions, and equal numbers will flow out, thus maintaining the pulse profile. On the other hand, in, say, an n-type photoconductor, a pulse of holes will be able to drift in the direction of the field, because the surrounding "gas" of electrons will quickly coalesce into a concentrated pulse to maintain charge neutrality. Therefore, in the limit of infinite electron mobility and concentration, the pulse mobility would be equal to the drift mobility of the holes, μ_h. In general, the ambipolar mobility is chiefly determined by the mobility of the minority carriers.

Further, an ambipolar diffusion constant

$$\mathfrak{D}_a = \frac{n + p}{n/\mathfrak{D}_h + p/\mathfrak{D}_e} \tag{5.8}$$

can be defined, where the respective electron and hole diffusion constants are as indicated, and in general $\mathfrak{D} = k_B T\mu/e$. Moreover, a characteristic diffusion length can be defined as $L = (\mathfrak{D}\tau)^{1/2}$ (assuming equal recombination lifetimes for each carrier). It is actually this distance which must be considered then in a careful treatment of sweepout effects.

Substituting Eq. 5.6 into Eq. 5.5, we get for the gain in an n-type photoconductor:

$$G_n = (b+1)z_h f(z_h) = \frac{(\mu_e + \mu_h)\tau_h E}{l} f(z_h). \tag{5.9}$$

This product saturates at a value of $G_n = (b+1)/2$ when $z > 1$, in other words, due to sweepout.

5.2 Noise in Detectors

It is now germane to begin discussing noise contributions to the output voltage of the detector, as these will determine the ultimate "sensitivity" of the device under various conditions of use. Besides noise sources inherent in the device itself, there are the noise or signal fluctuations present in the optical target, its surroundings, and in the amplification stages to which the detector is connected. Because the first two cannot be eliminated, it has become standard to refer to the signal or background limited performance of a detector (see Appendix 1). To optimize detector performance, it is necessary to cool the first stage of amplification as well as the detector, as the noise level of a room-temperature transistor exceeds the absolute signal strength of most semiconductor detectors. This was considered for these experiments, but not actually implemented (see Chapter VI). Here, only Johnson or Nyquist noise, generation-recombination ("g–r") noise, and $1/f$ or contact noise will be discussed.

The last of these shall be mentioned first. There often appears in semiconductor detectors a noise component with an $I^\alpha f^\beta (\Delta f)^{1/2}$ dependence, where I is the detector current, α is approximately unity, f is the modulation frequency of the signal, $\beta \approx -\frac{1}{2}$, and Δf is the bandwidth. This noise, generally only visible below the kilohertz range, is usually ascribed to surface states, surface leakage currents, or non-ohmic contacts. As yet, no complete theory exists for it, but it is often completely eliminated by careful surface preparation. As it was not problematic in the present experiments (wherein optical modulation was typically between 100 and 1000 Hz), it will not be considered further here.

It can be shown (KRUSE, 1962) that the rms Johnson noise power developed in a semiconductor is $4k_B T \Delta f$. This noise arises from random thermal motion of carriers, or in other words, local velocity "aberrations" resulting in unsteady current, even in the absence of bias.

The g–r noise voltage due to the spontaneous fluctuations in n and p brought about thermally is (LONG, 1980) $2eRG\sqrt{g_{th}\Delta f}$, while that due to "extraneous" background flux

Φ_b is $2eRG\sqrt{\eta\Phi_b A\Delta f}$.*

KRUSE (1962) shows, using the Wiener-Khintchine theorem, that the power spectrum of the g–r noise in an n-type semiconductor is

$$P(f) = \frac{4I_0^2\tau_r}{\overline{N}(1+\omega^2\tau_r^2)}, \tag{5.10}$$

where f is the modulation frequency, as usual, I_0 is the average current, $\overline{N}$ is the average *total* number of free electrons, and $\omega = 2\pi f$. In particular, then, it is seen that a highly doped sample exhibits less g–r noise than a purer one, and that the noise power drops off roughly with the square of the frequency above that frequency corresponding to the recombination lifetime.

Therefore, the total noise voltage arising within the semiconductor itself is

$$V_N = \sqrt{4e\left(e\eta\Phi_b AG^2R^2 + eg_{th}G^2R^2 + \frac{Rk_BT}{e}\right)\Delta f}. \tag{5.11}$$

Because spectral detectivity is in this case (see Appendix 1)

$$D_\lambda^* = \frac{\Re_\lambda(V_s)A^{\frac{1}{2}}(\Delta f)^{\frac{1}{2}}}{V_N}, \tag{5.12}$$

we get

$$D_\lambda^* = \frac{\eta\lambda}{2hc\sqrt{\eta\Phi_b + g_{th}/A + k_BT/G^2RAe^2}}. \tag{5.13}$$

KRUSE (1962) has derived expressions for the detectivities of photoconductors under various limitations. The first is done from a purely materials standpoint. It is theoretically possible to reduce to arbitrarily low levels all noise contributions *except* Johnson noise. Using a set of differential equations expressing charge transport under the influence of fields, and making a set of modest assumptions, an expression for the material-limited detectivity is derived:

$$D_\lambda^* = \frac{E\lambda e^{\frac{3}{4}}\mu_e^{\frac{1}{4}}\tau_r^{\frac{3}{4}}}{2hc(k_BT)^{\frac{3}{4}}n_i^{\frac{1}{2}}}\mathcal{AB}, \tag{5.14}$$

* This result is derived from a model (KRUSE, 1962) wherein it is assumed that the background flux of photons, obeying Bose-Einstein statistics, ultimately fluctuates as a Poisson process, and that for each photon $h\nu \gg k_BT_b$, where T_b is the background temperature. This assumption is valid for light of wavelength less than 30 μ, and a 300°K background.

where

$$\mathcal{A} \equiv \frac{\sinh m + \alpha_2[\cosh m - 1]}{m^{\frac{1}{2}}[(1 + \alpha_1\alpha_2)\sinh m + (\alpha_1 + \alpha_2)\cosh m]},$$

$$\mathcal{B} \equiv \frac{(b+1)a^{\frac{1}{4}}}{b^{\frac{1}{2}}(a+1)^{\frac{1}{4}}(ba+1)^{\frac{1}{4}}},$$

$a \equiv n_0/p_0$, $b \equiv \mu_e/\mu_h$, $m \equiv t/L_a$ (where L_a is the ambipolar diffusion length), $\alpha_1 \equiv s_1\tau_r/L_a$ and $\alpha_2 \equiv s_2\tau_r/L_a$, where s_1 and s_2 are the surface recombination velocities* at the front and back surfaces of the sample, respectively.

If there were no surface recombination, $\mathcal{A}$ could theoretically rise *ad infinitum* as m (or the sample thickness) were decreased. Of course, the practical limits on this thinning are the ever-increasing sample resistance which would load the pre-amp, and the decreasing optical absorption. Secondly, it is found that $\mathcal{B}$ has a maximum, but finite, value when $a = b^{-1/2}$. Still, from the rest of the expression, it appears that detectivity could rise without limit, given a high enough field (which would cause breakdown, eventually), large enough electron mobility and lifetime, and low enough temperature and electron concentration.

As discussed in Appendix 1, however, it is not possible to have infinite detectivity without limiting the field of view to such an extent that no light intensity is measured. The ultimate detectivity has been shown by KRUSE (1962) to be either background fluctuation noise limited or signal fluctuation noise limited. These theoretical limits for any photoconductive detector are also discussed in Appendix 1. A background limited photoconductor (BLIP) can be approached if all other noise sources can be minimized.

In order to achieve BLIP performance then, it is necessary that both g–r and Johnson noise be well below that of the background, or

$$g_{th}/A \ll \eta\Phi_b$$

and

$$k_B T/G^2 RAe^2 \ll \eta\Phi_b. \tag{5.15}$$

From the g–r theorem (VAN VLIET, 1958),

$$p_0 = g_{th}\tau_h/At,$$

* Surface recombination velocity is defined as the recombination rate per unit area per unit excess carrier concentration (evaluated just inside the surface).

so, if $n_0 p_0 = n_i^2$, Eq. 5.15 can be rewritten as

$$\eta n_0 \tau_h / n_i^2 t \gg 1/\Phi_b. \tag{5.16}$$

This implies that to minimize background-linked g–r noise, the lowest operating temperature is best, as n_i^2 increases exponentially with temperature.

Rearranging 5.4, we get

$$RA = l^2/et(nb + p)\mu_h. \tag{5.17}$$

Finally, combining Eq. 5.9 and Eq. 5.17, we get

$$G_n^2 RA = (b + 1)^2[z_h f(z_h)]^2 l^2/et(nb + p)\mu_h . \tag{5.18}$$

It is seen then that maximum gain, and therefore responsivity, can be attained by increasing the effective electron lifetime, by in turn maximizing the hole lifetime. This is often done purposely by providing traps for the holes. Conversely, sweepout lowers the effective lifetime, and hence the gain; but the advantage here is that the response time of the detector is decreased as well (as will be discussed later, overall response speed of a detection system is often limited by *RC* time constants in the circuitry). Further, a high electron:hole mobility ratio will result both in higher gain and better detectivity (too high mobilities give rise to large Johnson noise currents), while a smaller electron concentration, as reflected in n_0, will not effect the gain, but will, in raising R, improve the detectivity.

Extrinsic semiconductor detectors must be cooled in order to provide the same carrier lifetimes, because of greater scattering. Furthermore, the optical absorption is considerably less, lowering responsivity.

5.3 Cyclotron Resonance Photoconductive Detectors

In the case of photon absorption by cyclotron resonance, the number of carriers stays constant, but the mobility, limited predominantly by ionized impurity scattering, which is energy-dependent (see § 2.5), increases, thus increasing the responsivity. In an ideal Putley detector, the signal is proportional to the real part of the conductivity (HINDLEY, 1964).

Impurity transitions, on the other hand, can contribute to an increase in conductivity in a number of ways:

- if the impurity concentration is high enough, the impurities will form a band, albeit of fairly limited conductivity at liquid helium temperatures. However, the higher excited states would be expected to have higher mobility, being quasi-free states;
- the electron may tunnel into the conduction band, induced by the electric field;
- the electron may absorb a second photon;
- the electron may be impact ionized by other, free electrons;
- the electron may exhibit electric field-induced "hopping" between excited states of molecular complexes (CARTER ET AL., 1977);
- but most commonly, especially with respect to indium antimonide at liquid helium temperatures, the electrons absorb or emit phonons in the process of thermal ionization, which, when combined with the original photoexcitation, is termed *photothermal ionization.* This was described in more detail in § 4.2.

5.4 Optical and Plasma Effects

Certain space charge effects in semiconductors will now be discussed. The bulk of a sample may be thought of as a "sea" of electrons anchored to a lattice of largely immobile ion cores. Within this collective "fluid" or plasma, a single electron may be treated as though it were a classical oscillator. The oscillator eigenfrequency is ω_e, with damping γ. The plasma frequency is

$$\omega_p = \sqrt{\frac{4\pi n_o e^2}{m_e^*}}, \tag{5.19}$$

where n_o is the density of oscillators. Generally, this frequency falls in the mid-infrared at high doping levels, e.g., $10^{18}\,\mathrm{cm}^{-3}$, or at lower concentrations (10^{13}–$10^{14}\,\mathrm{cm}^{-3}$) in the millimeter wavelength regime. The index of refraction and the extinction coefficient may be related to the complex dielectric constant as follows (SEEGER, 1982):

$$\begin{aligned} n^2 - \kappa^2 = \kappa_r &= \kappa_0 + \omega_p^2 \frac{\omega_e^2 - \omega^2}{(\omega_e^2 - \omega^2)^2 + \omega^2\gamma^2} \\ 2n\kappa = \kappa_i &= \omega_p^2 \frac{\omega\gamma}{(\omega_e^2 - \omega^2)^2 + \omega^2\gamma^2}. \end{aligned} \tag{5.20}$$

In the case of free carrier absorption, Eqs. 5.20 reduce to

$$\begin{aligned} n^2 - \kappa^2 = \kappa_r &= \kappa_0 + \frac{\omega_p^2}{\omega^2 + \gamma^2} \\ 2n\kappa = \kappa_i &= \frac{\omega_p^2 \gamma}{\omega(\omega^2 + \gamma^2),} \end{aligned} \tag{5.21}$$

in which case $\kappa = \omega_p^2 \gamma / (2\omega^3 \sqrt{\kappa_\infty})$, and

$$\alpha = \frac{4\pi\kappa}{\lambda} = \frac{\mu_0 c}{\sqrt{\kappa_\infty}} \frac{\sigma_0}{(\omega\tau_{DC})^2} \propto \lambda^2 \tag{5.22}$$

($\mu_0 c$ may be estimated as 377 Ω). Here, σ_0 is the DC conductivity, while τ_{DC}, the momentum relaxation time, is in fact just the reciprocal of γ. The λ^2 dependency has been derived classically, but in fact, an examination of various data (SEEGER, 1982) reveals that, for instance, a cubic dependency may prevail. The precise nature of the dependency varies with the dominant scattering mechanism, and this can be treated successfully using quantum mechanics.

Absorption can also be expressed in terms of the rate per volume of transitions R/V of electrons between two k-states: If the photon flux Φ is equal to Nc/nV, where there are N photons in the volume V, then

$$\frac{R}{V} = \frac{Nc\alpha}{nV}. \tag{5.23}$$

The actual monochromatic energy impingent on the sample then is $Nc\hbar\omega/nV$, which must equal the time-averaged Poynting vector, $S = [E \times H]$. It can then be shown by equating these flux energy expressions that

$$\alpha = \frac{2\hbar^2 \mu_0 c R}{A_0^2 V n}, \tag{5.24}$$

where A_0 is the magnitude of the magnetic vector potential in an EM wave.

As mentioned earlier, a free electron cannot absorb a photon, as the energy gained by the electron would require a momentum change much greater than can be supplied by the photon. In a solid, however, the large population of phonons can allow a virtual state of an electron excited by a photon to exist briefly, to be followed by the absorption or

emission of a phonon. In this way, the absorption of a photon is accompanied by a large change in momentum and energy, decreasing the energy-dependent scattering (increasing the mobility), and, hence, the conductivity.

Second-order perturbation theory gives the probability of transition from an initial state k to a final state k'' through an intermediate virtual state k' by the absorption or emission of a phonon of wavevector q as

$$S_{\pm} = \frac{2\pi}{\hbar}\left(\frac{|\mathcal{H}_{k'k}|_{\pm}^2|\mathcal{H}_{k''k'}|^2}{\hbar^2\omega^2}\right)\delta(\epsilon' - \epsilon - \hbar\omega \pm \hbar\omega_q), \tag{5.25}$$

where $\mathcal{H}_{k'k}$ is the Hamiltonian for phonon emission or absorption (+ or −, respectively) and $\mathcal{H}_{k''k}$ is that for photon absorption. The former tends to be q-dependent, but not dependent on k. $\mathcal{H}_{k''k}$ is given by $-(eA_0/2m_0)\mathcal{P}_{k''k}$, and $\mathcal{P}_{k''k}$ is the momentum matrix element given by $-i\hbar\int u_{k''}^*\nabla_r u_k d^3r$, where the u's are Bloch functions. The transition rate is given by integrating Eq. 5.25 over all initial states:

$$R_{\pm} = \frac{2V}{(2\pi)^6}\int d^3k\, d^3k'\, S_{\pm} f(k)[1 - f(k')], \tag{5.26}$$

where a factor of 2 has been included due to spin degeneracy. In the non-degenerate case at electron temperature T_e, if $f(k')$ is neglected; if the photon momentum is neglected, allowing the substitution $\mathcal{P}_{k'k}/m_0 \approx \hbar(k' - k)/m_e^* = \hbar q/m_e^*$; if the parameter $z_{\pm}$ is introduced, being equal to $(\hbar\omega \pm \hbar\omega_q)/2k_BT_e$; and if the parameter ξ is introduced, equal to $\hbar^2q^2/4m_e^*k_BT_e$; then the final expression for rate is given by:

$$R_{\pm} = \frac{Ve^2A_0^2nm_e^{*2}(k_BT_e)^3}{3\pi^3\hbar^9\omega^2N_c}\int_0^{\infty}|\mathcal{H}_{k'k}|_{\pm}^2\exp(z_{\mp})\exp[-\frac{1}{2}(\xi + z_{\mp}^2/\xi)]\xi\, d\xi. \tag{5.27}$$

Therefore, from Eq. 5.24, it can be seen that

$$\begin{aligned}\alpha_{\pm} &= R_{\pm}\frac{2\hbar\mu_0 c}{\sqrt{\kappa_{\infty}}A_0^2\omega} \\ &= \frac{2^{\frac{3}{2}}\mu_0 cne^2m_e^{*\frac{1}{2}}(k_BT_e)^{\frac{3}{2}}V}{3\pi^{\frac{3}{2}}\sqrt{\kappa_{\infty}}\hbar^5\omega^3}\int_0^{\infty}|\mathcal{H}_{k'k}|_{\pm}^2\exp(z_{\mp})\exp[-\frac{1}{2}(\xi + z_{\mp}^2/\xi)]\xi\, d\xi.\end{aligned} \tag{5.28}$$

There are two cases of note with regard to Eq. 5.28: First, for acoustic and optical deformation potential scattering, the matrix element is independent of q. The integral of Eq. 5.28 thus simplifies to

$$|\mathcal{H}_{k'k}|^2_{\pm} \exp(z_{\mp}) 2 z_{\mp}^2 \mathcal{K}_2(|z_{\mp}|), \tag{5.29}$$

where $\mathcal{K}_2$ is a modified Bessel function. On the other hand, for piezoelectric and polar optical scattering, $\mathcal{H}_{k'k} \propto 1/q$, in which case the quantity corresponding to that in Eq. 5.29 is

$$\frac{\hbar^2}{4 m_e^* k_B T_e} \exp(z_{\mp}) 2 |z_{\mp}| \mathcal{K}_1(|z_{\mp}|). \tag{5.30}$$

For ionized impurity scattering with screening neglected, the analogous result is

$$\left(\frac{\hbar^2}{4 m_e^* k_B T_e} \right)^2 e^z 2 \mathcal{K}_0(|z|). \tag{5.31}$$

(In ionized impurity scattering, no phonon is required, and in the above equation, $z = \hbar\omega / 2 k_B T_e$. Second order perturbation theory is still applicable, however, as the third particle is the ion.

Below, then, is the list of absorption coefficient equations for each of the above scattering mechanisms:

- *Acoustic deformation potential scattering:* In this case, the phonon energy is very small, so $z_{\mp} \approx \hbar\omega / 2 k_B T_e$. A treatment (SEEGER, 1982) that accounts for phonon absorption and emission (responsible for a factor of 2 in the expression below), as well as for induced photon emission (by changing the sign of $\hbar\omega$ in Eq. 5.25), yields:

$$\alpha = \frac{\mu_0 c 2^{3/2} n e^2 \varepsilon_{ac}^2 (m_e^* k_B T)^{1/2}}{\sqrt{\kappa_\infty} 3 \pi^{3/2} \hbar^3 c_l \omega} \left(\frac{T}{T_e} \right)^{1/2} \sinh\left(\frac{\hbar\omega}{2 k_B T_e} \right) \mathcal{K}_2\left(\frac{\hbar\omega}{2 k_B T_e} \right), \tag{5.32}$$

  where ε_{ac} is a constant of proportionality known as the deformation potential constant. This reduces to Eq. 5.22 (within a factor of 1.13) when $T = T_e$ (thermal equilibrium), $2 k_B T \gg \hbar\omega$ (high temperatures), and if simply the DC values of mobility and conductivity are substituted. In this case, optical absorption increases with increasing electron temperature.

- *Piezoelectric scattering:*

$$\alpha = \frac{\mu_0 c 2^{1/2} n e^4 \mathcal{K}^2 (k_B T)^{1/2}}{\sqrt{\kappa_\infty} 3 \pi^{3/2} \hbar^2 \kappa_0 \epsilon_0 m_e^{*1/2} \omega^2} \left(\frac{T}{T_e} \right)^{1/2} \sinh\left(\frac{\hbar\omega}{2 k_B T_e} \right) \mathcal{K}_1\left(\frac{\hbar\omega}{2 k_B T_e} \right), \tag{5.33}$$

where $\mathcal{K}$ is the electromechanical coupling coefficient.* In the classical limit, the sinh and $\mathcal{K}_1$ factors are ~ 1, while in the quantum limit their product is $\sim(\pi k_B T_e/\hbar\omega)^{1/2}$, and $\alpha \propto \lambda^{2.5}$, independent of T_e. As the absorption cross-section in this case is inversely proportional to mobility, which is very high for PE scattering at low temperatures, this mode of absorption is usually insignificant.

- *Optical deformation potential scattering:* Once more considering both absorption and emission for both electrons and phonons, the following expression results:

$$\alpha = \frac{\mu_0 c}{\sqrt{\kappa_\infty}} \frac{2^{3/2} n e^2 D^2 m_e^{*1/2}}{3\pi^{3/2}\hbar^4 \varrho \omega_0 \omega^3} (k_B T_e)^{3/2} \times \frac{\sinh(z_+ - z) z_+^2 \mathcal{K}_2(z_+) + \sinh(z_- + z) z_-^2 \mathcal{K}_2(|z_-|)}{\sinh(z)}, \tag{5.34}$$

where D is the optical deformation potential constant of the band-edge. Its behavior is shown in Fig. 5.1. For the longer wavelengths, $\alpha \propto \lambda^2$. The maximum at low temperatures is due to a resonant absorption wherein a photon is absorbed, and the energy immediately released in the emission of a phonon of the same energy.

- *Polar optical scattering:* PO scattering is similar in behavior to OD scattering.

$$\alpha = \frac{\mu_0 c}{\sqrt{\kappa_\infty}} \frac{2\alpha n e^2 (\hbar\omega_0)^{3/2}}{3\pi^{1/2}\hbar^2 \omega^3 m_e^*} (k_B T_e)^{1/2} \times \frac{\sinh(z_+ - z) z_+ \mathcal{K}_1(z_+) + \sinh(z_- + z)|z_-|\mathcal{K}_1(|z_-|)}{\sinh(z)}, \tag{5.35}$$

where α is the so-called polar constant, or polaron coupling constant, defined by

$$\alpha = \frac{1}{137}\sqrt{\frac{m_e^* c^2}{2k_B\Theta}}\left(\frac{1}{\kappa_\infty} - \frac{1}{\kappa}\right), \tag{5.36}$$

where the fine structure constant is $\frac{1}{137} = e^2/(4\pi\kappa_0\hbar c)$, and Θ is the Debye temperature (i.e., $\hbar\omega_{LO} = k_B\Theta$).

* $\mathcal{K}^2/(1-\mathcal{K}^2) = e_{pz}^2/\kappa c_l$, where e_{pz} is the piezoelectric constant, and c_l is the longitudinal elastic constant, given by $\varrho\omega_l^2 q_l^2$, where ϱ is the mass density and the subscript 'l' refers to longitudinal acoustic waves.

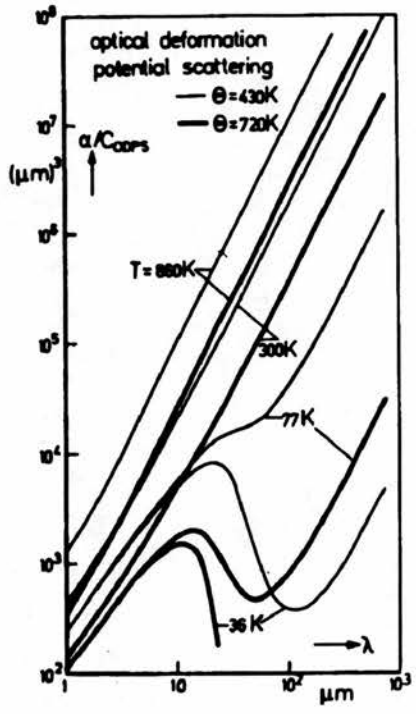

FIG. 5.1: Free carrier optical absorption coefficient α for various temperatures. C_{ODPS} is a constant of proportionality. Reprinted from SEEGER, 1982.

• *Ionized impurity scattering:*

$$\alpha = \frac{\mu_0 cne^6 N_I Z^2 (k_B T_e)^{-1/2}}{\sqrt{\kappa_\infty} 2^{1/2} 3\pi^{3/2} \hbar \kappa_0^2 \epsilon_0^2 m_e^{*3/2} \omega^3} \sinh\left(\frac{\hbar\omega}{2k_B T_e}\right) \mathcal{K}_0\left(\frac{\hbar\omega}{2k_B T_e}\right). \tag{5.37}$$

CHAPTER VI

Experimental Methods

6.1 Sample Preparation

Most of the samples examined in these studies were prepared from commercially available high purity n-type indium antimonide. The material was nominally undoped, with $n \approx 5 \times 10^{13}\,\mathrm{cm}^{-3}$ (but see Chapter VII), and was initially cut in $\sim$1 mm slices from boules. It is in this form that we received it from our supplier, MCP, Ltd. Because the material parameters and electronic and photoconductive properties of indium antimonide may vary widely among samples, the bulk of the work was performed on material from one slice of one boule (IS522T). It was necessary to use numerous samples cut from this slice, as various experiments require samples of very different dimension, and also because of sample breakage (indium antimonide is exceptionally brittle). However, material heterogeneity on a micron scale may be appreciable (see § 4.7). Therefore, sample properties may vary from experiment to experiment. Measurements were also performed to a more limited extent on a material of comparable electron concentration and mobility cut from an entirely different boule (IS520T) in order to afford some comparison. Cyclotron resonance narrowing experiments were performed as well on a highly compensated sample of n-InSb, labeled 6-98(16).

Work was also done on MBE-grown "headers", from RSRE, Malvern (samples 1040-/GMW(24) and 1042/GMW(25)). These were cloverleaf Van der Pauw samples of n-InSb, $\gtrsim 1\,\mu$ depth, grown on a p-type substrate, thus creating an insulating depletion region between them. The quoted figures for the n-type layer were $n = 1.4 \times 10^{16}\,\mathrm{cm}^{-3}$ and $\mu = 208,000$.

Bulk detector slices were cut from the boule wafers by means of the UNIPRESS wire-saw.

This delicate precision instrument comprises a thin tungsten wire (25–60 μ) and bobbin system, and a silicon carbide/oil slurry dispensing system. The wire is coated with a thin layer of the abrasive slurry, and rapidly but lightly run lengthwise, back and forth, over the sample. The sample is thus gradually eroded away, leaving a thin ($\sim$50 μ) swath. The speed of the cutting, the thickness of the cut, the quality of the cut surface, and the allowable size of the sample are all variable over wide limits. A coarser grade of SiC, and more tension, more weight and more slurry on a thicker wire will cut most quickly and most coarsely. However, using careful technique and the most delicate settings, a 30μ slice, $\sim$3 mm $\times$ 5 mm in cross-section, can easily be cut.

The wire-saw is also supplied with a goniometer in order to allow precise directional cutting. This feature was never used in these experiments, however, since indium antimonide has a nearly spherical conduction band, and its crystal orientation is therefore unimportant to first order.

Once the sample has been sliced from the initial slab, it adheres to the surface thereof by virtue of its very light mass and the surface tension of the oil. This position retention, however, is actually quite helpful, as the sample can now be coaxed away from the remaining slab simply by washing it off the face of the slab and onto a cotton swab using a squirt of methanol. This avoids any handling of the sample with anything harder than a droplet of methanol, as, again, it is merely the surface tension of the methanol that retains the sample on the cotton bud. This is important in order to avoid dislocations that lower the electron mobility, as well as to avoid completely obliterating the sample, which is exceedingly fragile.

Despite the delicateness of the instrument, experiments on slices taken directly from the wire-saw, without lapping or polishing, indicate that surface damage remains from the cutting, even with the finest slurry and slowest cutting (see Chapter VIII). It is therefore necessary to polish or etch the samples prior to experimentation. It was not necessary in these experiments to achieve an optically flat finish,* so polishing was omitted in favor of etching only.

First, the samples must be cleaned of all oil and slurry from the cutting process, as well as of the wax used to mount them in the saw. For this, a serial rinse in, successively, boiling

* While not easy to achieve, an optically flat finish may be undesirable as well. A sample with flat parallel sides can act in optical experiments like a small Fabry-Perot interferometer, creating spurious resonances, or "channeling". To avoid this, samples that *are* optically flat are commonly wedge-cut or polished. In the present work, the lozenge- or canoe-shaped cross-section of the samples (formed by virtue of the efficiency of the etchant at the sample edges) and their overall unevenness combine to eliminate this concern (see GORNIK ET AL., 1978, for instance).

trichloroethane, boiling acetone and boiling methanol was done. During this operation, the very fragile sample is suspended in the beakers on a PTFE sieve. The sample is then etched in a 10% Br_2/methanol solution. The same PTFE sieve is used to suspend the sample in the etchant, but constant gentle manual agitation is maintained during the etching to assure evenness over the surface. The etch was invariably continued to the point of sample specularity, but whereas some samples were only lightly etched (for a half minute, just until specularity), some were more radically etched (for minutes), removing $\sim 50\mu$ of material, and, in one case, leaving only $\sim 5\mu$. The etch is stopped and the etchant washed away by serial washes in pure methanol. (It should be noted that the etchant lingers rather tenaciously in the rough edges of the PTFE, so thorough cleaning with repeated washes is necessary.) As contacting is to proceed presently at this stage, the sample is retained under pure methanol; though for longer storage after etching, a nitrogen gas-filled glove-box may be used to avoid oxidation.

Contacting the sample requires some preparation, prior to the etching of the sample. Indium wire, the source of the contacts, is extruded and covered with oil in its manufacture. It is thus necessary to clean the indium thoroughly. This is done by immersing a centimeter length of it in a small beaker of acetone, and immersing this in an ultrasonic bath. Along with the wire is placed a scalpel, glass slide, small glass squares (sample size) and tweezers, which are used in subsequent manipulations of the samples. After a few minutes of cleaning, the indium is placed with the tweezers on the slide, and the broad side of the scalpel is used to flatten the wire into a ribbon. Small triangles of this ribbon ($\sim 0.2\,\text{mm}$) are cut off, each to become a contact on the sample. It is at this ready point that etching is done, such that *immediately* after removing the sample from the methanol, it may be contacted.

The technique for contacting micron thick samples should be mentioned, as it is not trivial: It is not possible to merely affix the sample to a firm substrate by means of adhesive, for the sample would not then be subject to uniform (hydrostatic) pressure once immersed in the pressure medium, both because the sample is irregularly shaped, meaning stresses from contact with the substrate might be uneven, and because the substrate and adhesive themselves are subject to differential contraction. The sample is so fragile that even the force necessary to overcome its slight adherence to the carbon stage of the contacting furnace, after heating, is enough to destroy it.

First, the freshly cleaned small glass square is placed (with tweezers) on the graphite stage of the contacting furnace. The sample, still resting on the etching sieve, is removed from the methanol and placed under a warm light to dry away the methanol. A methanol-wet

cotton swab is gingerly brought to the surface of the sample, at which point the sample clings by methanol surface tension to the cotton swab, and is thus removed from the sieve. It is then gingerly rolled onto the small glass square, cushioned by the drop of methanol surrounding it. Very slight heating from the contacting furnace evaporates the residual methanol. The scalpel is used to transfer the indium "dots" from the slide on to the sample. The dots will adhere to the nib of the scalpel with barely any pressure, and can thus be removed from the slide. If a corner of the dot away from the nib (observed under a microscope) is then lightly pressed onto one of the corners of the sample, the dot will be leveraged off of the nib, and will fall into place on the sample. Four dots, typically, are positioned in this way. Contacting can now begin in earnest.

Once the sample is centered on the stage, the latter is covered with a quartz top through which a reducing gas (typically 10% H_2/90% N_2) flows. Air must be scrupulously excluded, by sealing the top down with silicone grease and maintaining a sufficiently strong gas flow. The heat is gradually increased until the indium dots melt (156°C), as evinced by their becoming highly specular spheres (hence the term "dots"). The heat is lowered at this stage, and HCl vapor is routed through the line, in order to further remove any remaining oxides. After 30 seconds or so, a brownish scale appears on the dots. The HCl is then replaced by reducing gas, and the heat restored, so that annealing may proceed. A temperature of 250–300°C was found to be adequate for this. Excessive heat will damage the sample, actually causing destructive sublimation (see below). The dots begin to wet the surface of the sample, becoming hemispheres, and they assume a lustrous purple sheen, occasionally even a brilliant scarlet, before they revert to a normal neutral specularity.

During this process, two other effects are seen. Fronts of very slight darkening radiate outward from each of the dots, at a rate of a millimeter every few seconds. The dark circles formed may remain, or may disappear with further heating. These may be areas where indium vapor is being adsorbed to the surface, albeit in tiny (non-shorting) concentration.

In addition, prolonged heating will result in the sublimation of the indium antimonide itself, or perhaps its absorption into the dots: After sufficient time, and on very thin samples, craters become apparent around each indium dot. Indeed, the crater may extend completely through the sample to expose the glass below. Even before this point is reached, the indium dot may "sink" through the sample, such that there is an indium hemisphere on each side of the sample. It appears that if annealing is continued this far on very thin samples, the contacts so produced are extremely non-ohmic, and these may be responsible for an otherwise inexplicable failure to detect far-infrared radiation with these samples.

At this point, the heat is turned down, and the reducing gas is allowed to flow while the sample cools. Finally, the sample is removed and mounted into a PTFE ring or onto a pressure bomb stage. For this, thin indium-coated wires are heated, away from the contacts, and the warm ends allowed to melt into the contacts. For the thinnest samples ($< 10\mu$), extremely thin gold or platinum wires must be used. The stress generated by manipulating even 48 s.w.g. copper wire soldered at one end to a sample contact will break the contact and corner off of a very thin detector.

6.2 The Liquid Pressure Cell

Samples were pressurized in clamp cells manufactured by UNIPRESS of Warsaw, Poland (see Fig. 6.1). These cells are cylinders of beryllium/copper alloy of outer diameter 29 mm which fit into the bores of most superconducting magnet coils. BeCu alloy is advantageous in that it is not brittle, a safety feature for a pressure "bomb"; it is hard enough to resist pressure deformation at room temperature for short periods ($\sim$1 day); at liquid nitrogen temperature, it appears to be stable for weeks; it is non-magnetic, even at liquid helium temperatures; and it is reasonably machinable.

Within the cell is a 6.5–7 mm bore, and two pistons, one static and one sliding, which seal it. The pressure medium is a high-boiling (120–160°C) petrol mix, which below 77°K is an amorphous glass, which, through line-broadening studies, has been determined to be hydrostatic to within 1%. The seal between each piston and the bore is made by a rubber O-ring at initial low pressures and by an indium-coated brass gasket at higher pressures. The static piston affords optical access into the working volume by means of a narrow ($\sim$2 mm) tapered bore down its center. The piston is itself sealed in the working space with a 4 mm thick sapphire window, which is initially attached to the highly polished piston end with silicone grease. This bond is itself protected from petrol seepage by a thin PTFE sleeve, heat-shrinkable sleeving, glue, or a varnish layer. Once pressure is applied, forcing the window more tightly against the piston, the system is self-sealing.

The sliding piston provides the pressure application, adjustment and electrical feed-through for the sample and manometer (see below). The electrical feed-through comprises some dozen thin wires sandwiched in a pyrophyllite matrix. Pyrophyllite (hydrous aluminum silicate), obtained in a soft hydrate (gray-blue) form from STL High Pressure Laboratory, sinters on the application of pressure. First, it is baked at 1,000°C for 30 minutes, in a silica dish, to produce the anhydrite (light brown). After manual grinding with an agate mortar and

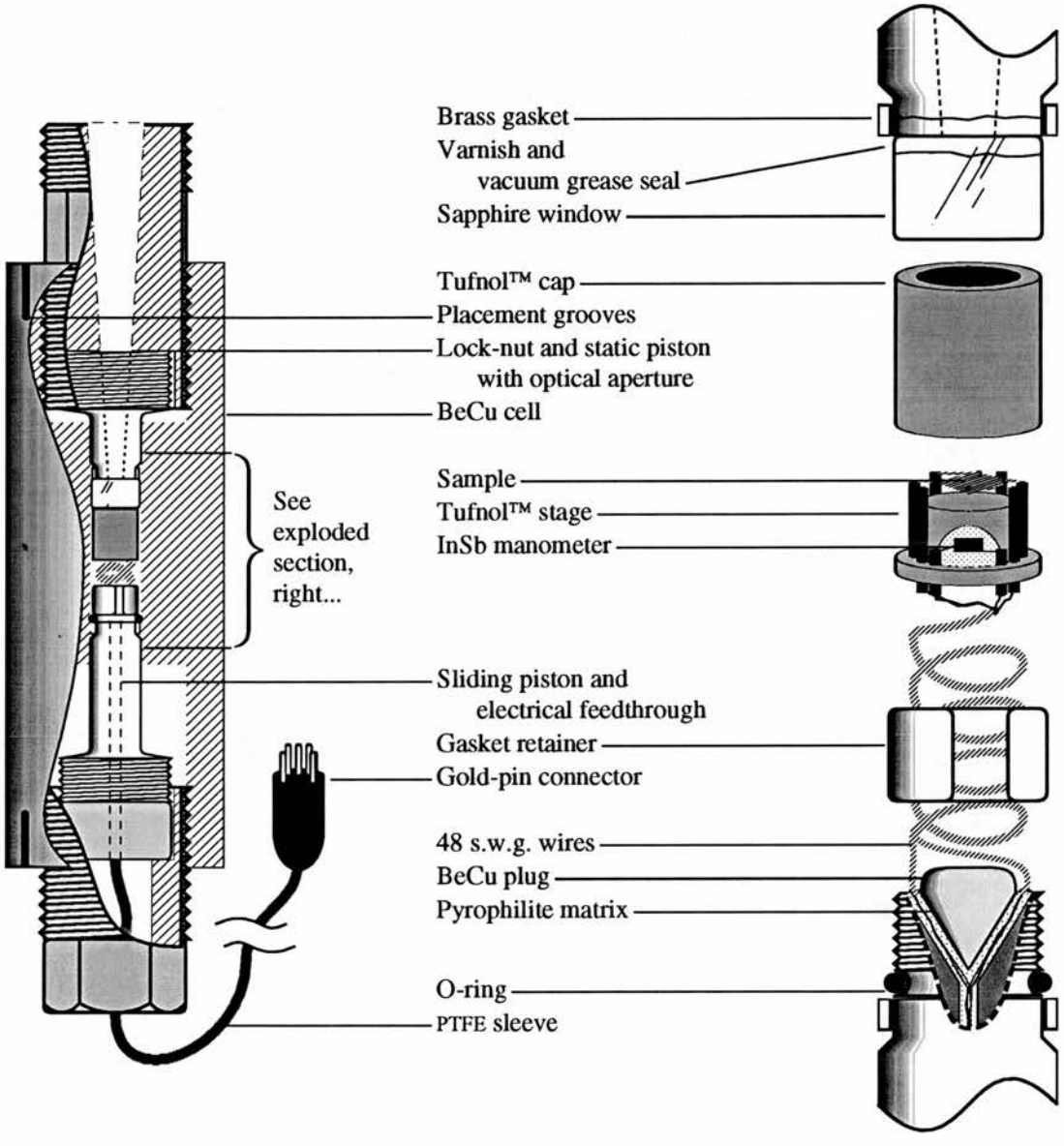

FIG. 6.1: Diagram of the UNIPRESS liquid pressure cell.

pestle, the fine powder* (normally stored in a dessicator) is tamped into the conical cavity at the end of the sliding piston. With a special tool, this "charge" of pyrophyllite is compressed outward to line the cavity. Enamel-insulated wires are fed through the piston, and are splayed

* In order to properly pack and seal, the powder should be made so fine that it begins to assume a clay-like texture, a state that can be achieved only when the particles are so small (generally with a mean diameter on the order of a micron) that inertial forces are comparable to those of adhesion.

out along the inside of the pyrophyllite layer. Another charge of pyrophyllite is added on top of the wires, and a BeCu plug is lodged in this charge (using a table-top hydraulic press), finally, to create the "sandwich", a pressure-tight seal. The wires exit the piston through a PTFE sleeve, to terminate some centimeters later in a gold-pin plug (these small gold-plated pins and sockets are found to be free of intermittency even at low temperatures). The wires entering the working space are tightly coiled into a spring, protecting them from damage and providing shock absorption for the sample stage.

The sample stage is a small Tufnol™ disc, in the rim of which are contacting posts. The wires from the feed-through are connected to the posts on one side of the disc, while the sample is connected on the other. Besides the sample, there is a manometer: A small bar ($\sim$3 mm $\times$ .5 mm $\times$ .5 mm) of highly doped n-type indium antimonide ($n \approx 10^{18}\,\mathrm{cm}^{-3}$), with a resistance that varies parabolically with pressure. This manometer is protected by a smaller Tufnol™ stage placed over it, above which the sample is suspended from its contacts. Over the entire assemblage is placed a protective Tufnol™ cap with a radiation aperture on top. The pressure bomb is first sealed manually with a spanner, to a pressure of approximately 1 kbar ($\sim$100 MPa). It is then transferred to the small hydraulic press, surrounded by polycarbonate safety panels, where it can be pressurized to about 12 kbar (25 kbar for cells with nickel-chromium inserts). Throughout the process, the pressure is monitored by measuring with four contacts the resistance of the manometer.

Immediately upon pressurization, the cell should be cooled to liquid nitrogen temperature or below (even if it is not to be used immediately) in order to prevent its deformation. Further precautions include preserving the cell, especially when cold, from air, as moisture can degrade the electrical feed-through. The cell should not be manipulated when in cryogen, as the enamel wires, if twisted when cold, may begin to short as the enamel cracks.

Depressurization proceeds almost exactly in the reverse order of pressurization. However, the pistons must be extracted from the bore mechanically rather than manually, and a special tool exists for this purpose. Furthermore, the gasket of the static piston is not extracted with the piston itself, as it is in the case of the sliding piston. Therefore, a "punch" is used to push the gasket out once both pistons have been removed.

6.3 The Gas Pressure System and the Pulsed-Power Supply

Pressure experiments in the 3–5 μ region required the use of a pressure medium other than petrol, as this exhibits many sharp absorbtions in the C–H stretch regions.* The gas cell,

* An attempt was made to run these experiments in the liquid pressure cell using a mix of chlor- *(cont'd.)*

similar in construction and size to the liquid cell described above, removed this problem, and further, allowed immediate and easy pressure variation during the experiment (see Fig. 6.2).

The pressure medium in this case is high purity helium gas from a cylinder, although in principle any inert liquid or gas can be used with the compressor. Impure helium, however, is found to solidify at high pressures and low temperatures, impeding the gas flow (the capillary through which the gas flows, described below, is only 0.3 mm inner diameter, and therefore subject to complete blockage quite easily, including by over-flexion).* The gas is transparent to infrared radiation, a major advantage. Furthermore, the gas is compressed into the cell through a long, flexible capillary from a compressor. This allows the gas to be controlled *in situ*, enabling the experimenter to change pressures even when the cell itself is immersed in cryogen.

The compressor has three stages. Gas fed into the system from the cylinder is initially compressed by a modified Diesel oil injection pump to 750 bars, completing Stage I. At this point, the gas inlet is closed off, and Stage II of compression commences. Here, the oil pump drives a piston (a so-called "hydraulic multiplicator") which has five times the surface area at the oil surface as in the gas volume, hence effecting a five-fold increase in the maximum gas pressure, to 3,750 bars. This is achievable of course only because at this point, the working gas volume is quite small. Finally, the gas inlet to Stage III is sealed off, and the oil pump is made to drive the press piston, which achieves 15 kbar in the cell and the capillary (the total volume of Stage III being only $\sim 8\,cm^3$).

For these experiments, a standardized manganin coil, situated in Stage III, is used for pressure measurements. This is because the manganin is calibrated to greater accuracy than is the indium antimonide, is very temperature-stable, and is not required to fit in the bomb itself. While the coil is quite stable, its resistance is nonetheless temperature-dependent, and the biasing used to measure it must be zeroed on a bridge against a standard resistor each time the bridge is used.

The pulsed power supply allows a series of Van der Pauw Hall measurements to be taken over fractions of seconds in rapid succession. The system entails the rapid alternation of magnetic field direction with simultaneous measurement of currents, voltages and sample

(cont'd.) inated and fluorinated organic compounds, i.e., liquids lacking H atoms. Several attempts at random mixtures revealed a large non-hydrostatic effect, to the extent that the samples were actually broken by stress. CS_2 has been used as a pressure medium, but due to its high toxicity was not tried in these experiments.

* It should be noted, however, that solid helium has a very low shear modulus and can be used as a near-hydrostatic pressure medium.

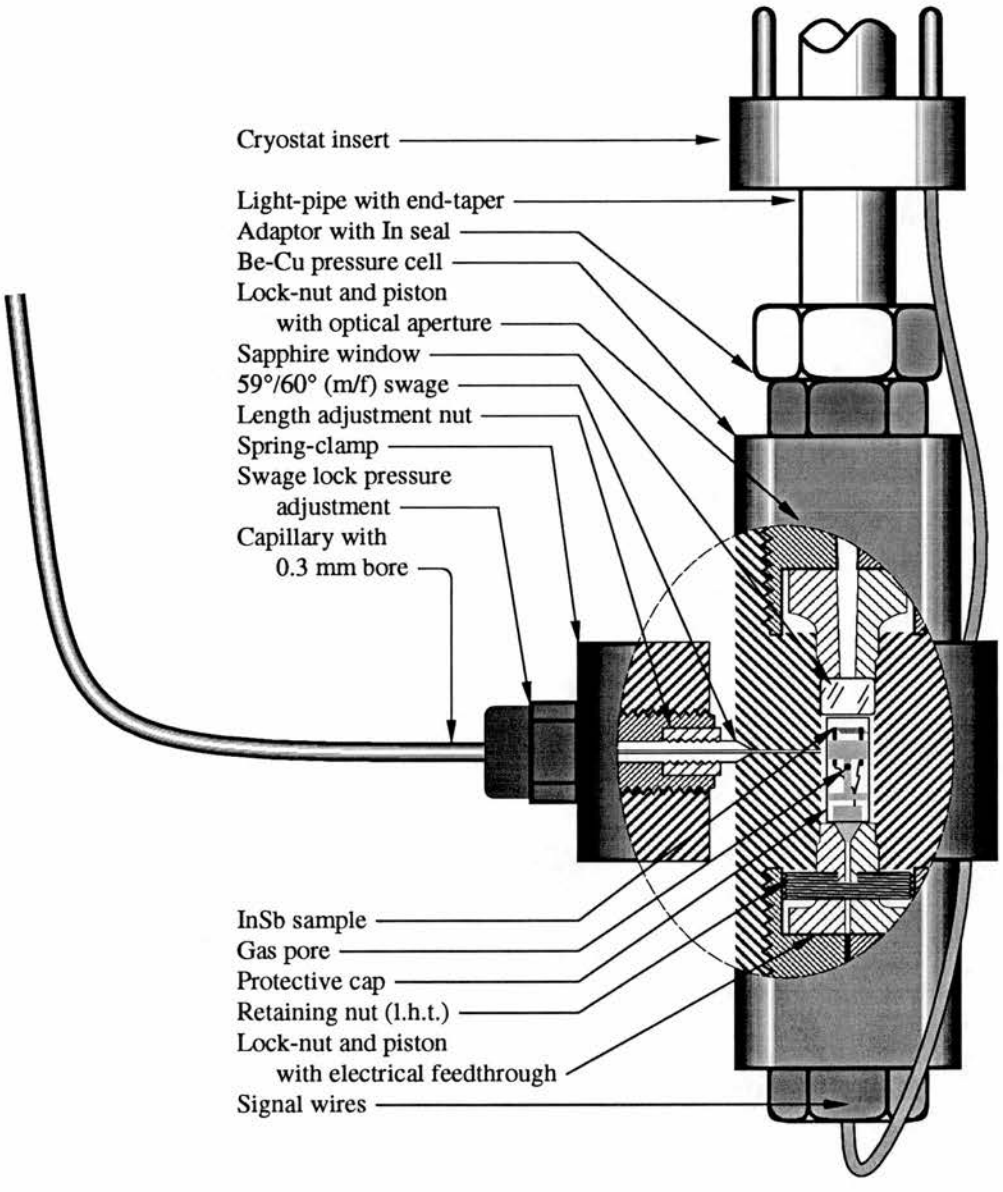

FIG. 6.2: Diagram of UNIPRESS optical access gas pressure cell, as used in the current work.

conditions such as magnetic field strength, temperature and pressure.

In the set-up used for this work, a pair of Helmholtz coils was energized with a 30 amp 40 V pulse of 0.5 s duration. A pause of 0.3 s followed, to allow a "ringing" effect in the magnetic field to subside. At this point, a second, longer pulse of 1.5 s duration was

generated by a Keithley 220 current source. This powered four thyristors which supplied current to the sample in each direction for each pair of current/voltage measurements. These were in turn connected to the input/output bus (4 bits input, 4 bits output) of a Keithley 705 scanner. Voltages were then read and recorded by a Datron voltmeter. It was during this second pulse that the magnetic field as well was measured (i.e., the magnet current was monitored) over a 0.5 s interval.

6.4 Superconducting Magnets

6.4.1 Architecture of Magnet Systems

Various magnets were used for these experiments, depending on availability and ultimate field and sweep rate required. The smallest was the 6.7 T (7.2 T pumped*) Clarendon Laboratory Magnet. This had a very slow sweep, and was not very reliable (i.e., it often tripped) at the highest fields. But because of its small size and that of its cryostat, it could be wheeled out of a corner, lifted into position, evacuated, precooled, and filled with liquid helium in only an hour.

A Thor 4 T/8 T double magnet, originally intended for cyclotron emission studies, but often available cold, was used as well. This was the magnet used for most of the cyclotron resonance narrowing experiments described in Chapter VIII. At St. Andrews University, an Oxford Instruments 12.7 T NMR high homogeneity † fast sweep magnet was kept continuously cold, and was used for cyclotron resonance experiments. At Imperial College, the large magnet available was an Oxford Instruments 13.5 T magnet.

Each of these magnets was fundamentally similar to the small Clarendon magnet.

Each magnet is insulated by means of an outer liquid nitrogen jacket, a vacuum space, and, in the case of the larger magnets, several layers of "superinsulation", i.e., aluminum-coated Mylar™. These components are entirely suspended by thin-walled necks from the top flanges of the cryostat, to prevent heat conduction to the lower regions of the cryostat. Plastic spacers are also present to limit swinging motion, which, as well as bringing inner and outer surfaces into contact, can seriously damage the thin-walled components. Occasionally, as in the Clarendon magnet, there are ports at the bottom of the cryostat that are meant to

* Applying a vacuum of $\sim 10^{-4}$ torr will lower the temperature of liquid helium to as little as 1.8°K. The lower temperature in turn increases the critical magnetic field to which the magnet can be driven. Generally, a large rotary pump with a capacity of 300–450 liters/min is required.

† The magnetic field in this case was rated as being constant to one part in 10^5 within the volume of a 1 cm diameter sphere.

hold windows for optical access. (Flanges in this region, and for the most part throughout the magnet, are sealed not with O-rings, which would freeze, but with indium wire rings, which form cold welds, if scrupulously cleaned of oil.)

Magnetic fields are often calibrated by the use of a Hall probe, which itself is calibrated against a standard field. The calibration of the magnets used in these experiments was carried out by Hall probe at St. Andrews University. The accuracy of the calibration is widely assumed to be approximately 1%.

Use of the magnet, if starting at room temperature, required evacuating the outer jacket to a pressure of typically between 10^{-4} and 10^{-5} torr, corresponding to a mean free path among remaining particles on the order of the vacuum jacket width. This means that the cryogens are heated principally by incoming thermal radiation and heat conduction down the sides of the vessel from the 300°K top flange. Further, more efficient, evacuation proceeded by the cryopumping action of the coolants themselves, especially the liquid helium. Precooling all internal components and surfaces with liquid nitrogen was in all cases necessary, as liquid helium, with a tiny heat of vaporization (20.9 Joules/gram—less than 1% that of water) would be required in immense quantities to accomplish the initial cooling to 77°K. (Liquid helium is quite expensive, and once lost, escapes the earth's gravity and falls to the sun.) Table 6.1 gives some useful information about liquid nitrogen and liquid helium, and the "cooling power" of each. In order to precool the inner space with liquid nitrogen, it first should be rid of moisture, either by flushing it with helium or nitrogen gas, or by evacuation and back-filling. (In the latter case, it is vital that the vacuum jacket be evacuated beforehand, as the thin-walled helium can may be crushed by atmospheric pressure.)

In the case of the small Clarendon magnet, the inner liquid helium space could be filled with liquid nitrogen, then re-emptied by applying a pressurized cylinder of helium or nitrogen gas to blow out the liquid, all in the course of twenty minutes. In contrast, the large Oxford magnet required two days to equilibrate to 77°K, primarily on account of the mass of the solenoid (~50 kg), which is largely a poorly heat-conducting epoxy matrix called the "potting". (In filling the actual coil space of a magnet with liquid nitrogen, it is never a good idea to do it too quickly, as the epoxy resin of the coil matrix is susceptible to thermal shock, and subsequently needs to be able to withstand very large Lorentz forces during a sweep. It is always essential to ensure that virtually all liquid nitrogen is expelled from the cryostat, as otherwise it will freeze within the magnet. Besides having a significant thermal mass, it may provide unwanted insulation of the coil from the liquid helium.)

The solenoid of each magnet is a coil of superconductive multifilamentary copper-

TABLE 6.1: Some practical cryogenic data applicable to the operation of superconducting magnets (Source: Oxford Instruments).

Calorimetric quantities for:		Liquid nitrogen (LN_2)	Liquid helium (LHe^4)	
Boiling point @ 1 atm [°K]		77.3	4.2	
Latent heat of vaporization [J/gm]		198	20.9	
Volume of liquid evaporated by 1 W [l/hr]		0.023	1.38	
Liquid density at b.p., 1 atm [g/ml]		0.808	0.125	
Gas density at NTP [g/ml]		1.25×10^{-3}	1.79×10^{-4}	
Gas @ NTP to liquid volume ratio		648:1	700:1	
Enthalpy change of gas [J/gm]:				
4.2–77.3°K		–	384	
77.3–273.15°K		234	1542	
Cryogen required to cool selected metals [l/kg]				
Cryogen:		He^4	He^4	LN_2
Initial temperature of metal:		300°K	77°K	300°K
Final temperature of metal:		4.2°K	4.2°K	77°K
Cooling only with the latent heat of vaporization	Aluminum	66.6	3.20	1.01
	Stainless steel	33.3	1.43	0.53
	Copper	31.1	2.16	0.46
Cooling with vaporization and the enthalpy of the gas	Aluminum	1.61	0.22	0.64
	Stainless steel	0.79	0.11	0.33
	Copper	0.79	0.15	0.29

impregnated NbTi, typically containing in a single cross-section up to hundreds of filaments 5–10 μ in diameter, with a critical temperature of $\sim$9°K, and critical fields on the order of 10 T. The multifilamentary nature of the superconductor allows for small strands of it becoming "normal", i.e., resistive, as well as for "flux-jumps", explained below.

An "ideal" superconductor is classified as *Type I*. This means it goes from a purely superconducting state, which completely excludes all magnetic fields, to a normal state at a single critical field or temperature. On the other hand, most alloy superconductors fall into the *Type II* category: Above a certain "first critical point", they have small normal regions within that allow magnetic flux to penetrate, while the rest of the superconductor remains flux-free. This has the effect of pinning "fluxoids", quantum bundles of lines of flux, within a superconducting region, as they cannot pass through a superconducting boundary. However, they may from time to time jump from one region to another. The collapse and rise of the associated circulation currents cause local heating, which, on account of the superconductor's small heat capacity and small thermal conductivity, leads to a relatively large temperature increase. This reduces the critical current, which then leads to more flux jumps, and a flux avalanche may develop. However, isolation of the effect can be achieved by limiting the superconductor's dimension to that of the filaments. The copper matrix provides an alternative pathway for currents caught in normal filaments, thus reducing the opportunity for runaway heating.

The Oxford magnet has two inner solenoids composed of Ni:Sn, which is better at high fields ($\gtrsim$ 10 T) than the titanium-rich alloys.

Cooling with liquid helium proceeds by first transferring cold helium gas from a dewar of the liquid through a double-wall evacuated transfer tube, into a funnel at the bottom of the cryostat. Cooling proceeds from the bottom up. As the temperature drops, liquid being forced through the transfer tube can condense, temporarily, and its vaporization further cools surfaces around it by convection. Liquid helium can begin to collect in the Clarendon cryostat after ten minutes or less of pumping, while a large magnet may require three times as long, and many liters of helium.

Each magnet includes some means of gauging the fullness of the helium can. This is quite important, as often an insert is present in the magnet, blocking from view the level of the helium. If the level is higher than it need be to run an experiment, helium is wasted in that the higher the level, the faster the boil-off. Furthermore, if the filling is too fast or the fill level too high, a large boil-off of helium results. This flow is too fast to efficiently cool the system at lower levels in the cryostat, so as the helium gas escapes, it cools the top flanges

and plumbing of the magnet, freezing O-rings and electronics in a potentially disastrous sequence. A large efflux of cold helium gas in this way, or in a quench, can supercool the surrounding liquid nitrogen, leading to "suck-back": The lowering of the nitrogen vapor pressure to the point where air (and moisture) rushes into the liquid nitrogen jacket. This can bring about the icing up of the nitrogen vents (see below). It is important to note that the cooling power of helium is contained mostly in the enthalpy change required to elevate the temperature of the gas from 4.2°K to 300°K, which is almost 50 times that required to vaporize the helium in the first place.

Conversely, it is easy to let the magnet run out of liquid helium altogether, because the low temperature gas remaining at the bottom of the cryostat is still a good refrigerant, and the magnet will remain superconducting for a few degrees above 4.2°K. However, in the case of photoconductivity experiments, when light is being shone down into the sample space, the lack of a good cryogen can allow the sample to heat well above the temperature of interest. More seriously, in the event of a quench, when the magnet goes to a normal state, the absence of liquid helium (which is 700 times as dense as helium at 1 atm and 300°K) would likely result in the thermal destruction of the magnet. Even if there is no quench, but merely a trip (a voltage-inducing current ramp-down resulting from, e.g., a too-high sweep voltage), the heat evolved by the quench protection resistors is also potentially destructive.

While the helium level can be seen from the top flange if there is no insert present, and if a clear plastic lid and flash-light are used, discerning depth this way is still often deceptive. The Clarendon magnet includes a number of silec* diodes down its length. The conductivity of these diodes varies sharply with temperature in the realm of 4.2°K. When surrounded by gas near 4.2°K, a 3 ma current keeps the diodes warm; when surrounded by liquid helium, the resistance rises to such a degree that the associated circuit cuts off the warming current. This saves liquid helium, and the circuit then switches from a red to a green indicator light. The series of indicator lights thus controlled served as a fill monitor. In the case of the Thor magnet, a superconducting wire extends down the inner wall. It is meant, as it becomes warm, to go normal just within that length of wire not submersed, thus changing its resistance as a function of fill depth. However, this system has an "all-or-nothing" action, probably resulting from the entire wire reaching a single temperature, as superconducting wires are also good conductors of heat, even in the normal state (copper wire at 4.2°K can be up to 10 times as thermally conductive as at room temperature (MCCLINTOCK ET AL., 1984)).

* *Si*licon *l*iquid-*e*ncapsulated *C*zochralski-grown.

A large magnet can be a dangerous place, generally speaking, though reasonable care has prevented any mishaps in this laboratory. Cryogens in general are potentially dangerous,* and a magnet with iced-over helium or nitrogen exhaust vents is a potential bomb, in that escaping gas carries away with it much heat: When it is blocked, the temperature of the space below rises, releasing more boil-off, and the system thus exponentially approaches a critical point. Therefore, the use of at least one Bunsen valve (a closed rubber tube with a slit cut in it as a one way escape valve) on a nitrogen jacket is strongly recommended.

When a magnet is kept cold for a very long time (the 12.7 T Oxford NMR magnet at St. Andrews was kept under helium for over a year), small leaks can allow the vacuum jacket to build up quite a large titer of frozen gases on its walls. In the case of gradual warming, and a faulty pressure-release valve, the out-gassing from the walls can create an over-pressure sufficient to implode the thin-walled inner helium vessel, or even to explode the heavy outer can. If the vacuum is lost suddenly, the sudden effusion of helium gas, as well as of nitrogen gas, can be explosive, but it can also rapidly displace most of the oxygen in a small laboratory and lead to asphyxiation. This is in theory possible even in the case of a quench. In the event of a quench, a huge current (over 100 amps in the case of a large magnet) must ramp to 0 very quickly, thus building an enormous back-voltage (tens of thousands of volts, potentially) through the inductance of the solenoid. In the case of poorly insulated or too closely spaced components in the magnet, this can lead to arcing which has been known to drill holes through the metal jackets of magnets, leading to a cryogenic catastrophe as well.

Finally, the magnetic field itself poses certain hazards. The 13.5 T Oxford magnet has an enormous stray field, capable of visibly deflecting large keys over a meter away. Besides the mischief this could cause to magnetic discs, tapes, pacemakers and magnetic furniture in the area, it is also very unstable. The movement within this field of another magnetic object can lead to eddy fields which induce in the solenoid itself eddy currents. As a solenoid has a maximum field and a maximum current that it can sustain before it goes normal, any spurious fields or currents imposed on a coil operating near its maximum are inauspicious things.

Most large magnets have a persistence switch and switch heater, though these were not used in these experiments. The idea is that while a superconducting coil itself evolves no heat as it conducts, the copper cables leading down to it (and, in a large magnet, often carrying over 100 amps) do. Therefore, it is desirable to close the circuit of the coil on itself,

* Besides causing cold-burns, possible asphyxiation (see below) and embrittling plastics, liquid nitrogen condenses liquid oxygen into solution or onto adjacent surfaces, creating a combustion hazard.

allowing the trapped current to persist indefinitely. The switch between the two cables to the magnet is always present, but it is kept normal by a heater, and thus carries no current. If persistent mode is desired, the switch heater need merely be turned off. After a wait of $\sim$1 minute, the switch is superconducting, and the supply current is ramped down. This change in current creates a back-voltage through the inductance of the coil, which in this case supplements, through the persistence switch, the diminishing current from the cables, thereby maintaining full current in the coil at all times.

All magnets include a number of electronic diagnostic, control or safety features. For instance, all magnets have a trip voltage setting, designed to cut the current to the magnet or ramp it down rapidly if the applied voltage reaches a certain preset value. This could happen if the magnet itself begins to quench (i.e., one portion of it goes normal, increasing the resistance and thus the voltage drop), or if it is driven to too high a current. In this case, as no voltage is dropped across a superconducting solenoid, the diagnostics must be made across the output terminals of the power supply.

Because of the presence of parallel resistances (quench protection resistors, voltage sensors, etc.) in a magnet, as the voltage sweeps up, current flows elsewhere than through the coil. As the voltage sweeps down, the same is true, although the parallel currents are in the opposite direction. Therefore, the current going through the coil itself is not a function merely of the total output current from the power supply, but of the sweep rate and parallel resistances as well. To know the exact field at any moment, therefore, it is not sufficient merely to know the output current. It is possible to use a magnetoresistance probe, but two problems arise: First, the voltage across the probe is not linear with field, and therefore not straightforward to read off of a simple uncomputerized display such as a chart-recorder. Second, there still remains a pseudo-hysteresis effect in that the time-constants of the electronics involved will continue to prevent a cyclotron resonance peak, for instance, from appearing at the same field on the down-sweep as on the up-sweep.

Therefore, standard procedure is to take two sweeps at the same rate settings and with the same time-constants, and to ensure that any features of interest are well away from the end-points of the sweeps. In this way, true field can be read as that value exactly half way between any two features—provided there is no "hysteresis" in the sample, as could come about, not through magnetic effects, but by gradual warming of the sample by electrical currents or laser illumination, changes in high hydrostatic pressure over the course of, say, an hour, or by photoionization of metastable states.

Although it was not utilized for these experiments, a so-called "λ-point fridge" was

available on the Oxford 13.5 T magnet. In order to achieve the highest magnetic field possible with a given coil, as noted above, it is necessary to lower the temperature as far as possible. While it is possible to do this simply by pumping on the liquid helium space, this is difficult and inconvenient, especially with a large magnet: A very large rotary pump is required, and an enormous amount of helium is spent in the first hour or so of pumping; access to the helium space (to change inserts, for example) is prohibited; and finally, it is necessary to ensure vacuum-tightness rather than merely gas-tightness. A λ-plate circumvents all of these problems by acting as a convection cooler. The plate sits just above the solenoid in the helium can, and can be filled through a needle-valve operated at the magnet's top flange. A very small quantity of liquid helium in the plate's inner channels is then vacuum-cooled toward 2.17°K, the so-called λ-point of liquid helium, where the superfluid phase begins to form. (Further cooling requires a diffusion pump and a long waiting period.) This cold plate begins to cool the surrounding helium, which is only that in the vicinity of the coil. As the helium reaches the λ-point, it undergoes a phase transition, becoming denser and settling to the bottom of the cryostat, slowly covering the coil. Further cooling may be suspended at this stage, as rather than cooling the superfluid itself, which can sustain no thermal gradients, it will result merely in moving the phase boundary upward from the magnet.

6.4.2 Insert Protocol

In order to position an experimental sample in the center of a supermagnet bore, the sample must be suitably encased, and the magnetic field center position must be known.

Most samples are not immersed directly into liquid helium. Liquid helium, while not dense optically or inertially, is subject to violent turbulence during a quench, which could destroy a fragile sample. The sample could also be effected by thermal shock if submerged too quickly. Therefore, and for general ease of handling, samples are mounted at the end of thin-walled anti-magnetic stainless steel* tubing ("light pipes" in optical work†), and these assemblages are themselves inserted into (generally) more robust outer sleeves, and

* Among common stainless steels, 316 and 321 have the lowest magnetic susceptibilities, of about 300 and 100 emu/g, respectively (WHITE, 1979).

† In the current work, the light pipes were coupled to the sample by short tapered sections, which focus the light onto the sample. One "cone" was electroformed of copper (a smooth conical surface is difficult to machine), while another, for attachment to a pressure cell, was machined out of nickel-chrome alloy, which has a high IR reflectivity.

sealed with an O-ring. Suitable "plumbing" must be present at the top flange of the insert as well: Before any cooling whatsoever can take place, the work-space must be evacuated, as moisture, of any form, will block the infrared radiation typically employed in semiconductor work, and as ice, which expands as it is formed, can damage samples. This work-space is then back-filled with helium gas at an over-pressure from a cylinder or return system, in order to expel any moisture that begins to leak in from the atmosphere.

In order to conserve liquid helium, especially in the case of a (massive) pressure-cell being used, the insert is precooled in liquid nitrogen, a process which can take up to twenty minutes. The rate of cooling of the sample itself, however, which may be accelerated by the presence of the wires connected to it, may occur somewhat faster, and this may have certain undesirable effects, particularly with regard to the population of metastable states (see Chapter IV and § 6.8).

After the insert is precooled, it is lowered slowly into the helium space of the magnet: As the helium gas in the insert cools, it contracts and draws in more warm helium gas from the supply line, increasing the thermal mass. The clearance between the insert and the magnet collar must be sealed, as cold helium gas can otherwise escape, driven both by the over-pressure of helium gas in the magnet itself, and the inrush of the heavier air. This has the doubly bad effect of freezing anything with which the escaping gas comes in contact (such as O-rings or human flesh), and depositing much heat and moisture (and presently, ice) into the magnet. (Once the magnet does become iced—all components down the bore appearing a light gray—it is best to let the magnet thaw (a process which takes days on account of the large thermal mass and the absence of convection), at least prior to a ramp up to high fields. Otherwise, the thermal insulation of the ice could impede adequate cooling of various components, such as the quench protection resistors and the copper leads descending to the coil.) The seal around the descending insert must be suitably flexible and sized correctly. An O-ring, for instance, is usually unsatisfactory, as it tends to grip the insert too tightly if it seals at all, and is forced to roll as the insert descends, which may bind or tear it. Furthermore, an O-ring easily freezes, losing all its resiliency and sealing ability, when briefly exposed to out-rushing helium gas, as in the initial opening of the magnet aperture. One of the best alternatives yet has been the Mecro™ seal, which resembles an O-ring with a square cross-section (preventing rolling as it sits in a square-cut channel), but with a groove cut around the top to allow the seal to change inner diameter without undue force or binding.

The inserts each possess a large thermal mass; therefore, prior to actual insertion, they are cooled in a dewar of liquid nitrogen, typically for at least half an hour. Once cold, they

are lowered into the helium bath, a long insert requiring about twenty minutes to descend, in order not to thermally blast out more helium than necessary. In the case of the Oxford magnet, it is recommended that the insert be electrically insulated with Mylar™ in the vicinity of the solenoid, as the Ni:Sn manufacturing process often results in carbon deposits on the windings' former, which is electrically isolated from the rest of the magnet (i.e., not grounded). This carbon can result in high resistivity shorts, which in the high voltage generated by a quench could cause serious damage via arcing to a neighboring conductor.

It may be necessary at times, or even with each experiment, to locate the center of the magnetic field. Usually, this is unnecessary, as magnets and the stainless steel or aluminum supporting structures and associated implements are fairly rigidly held. Thermally induced variations in the lengths of the struts, due to variable liquid helium and liquid nitrogen fill levels, are negligible, as the magnetic fields within these solenoids are constant (within most experimental precision) over a range of centimeters. Some inserts, however, are meant to be variable height, to allow for different sample mounting configurations. Furthermore, a magnet's coil is held in place by adjustable bolts, which, after many magnet commissionings and recommissionings, may be altered in setting. Therefore, a small bar of semiconductor, or usually the sample itself, can be used to locate the field center by varying its position and noting that height corresponding to the maximum (or minimum) in the magnetoresistance.

If an insert is to be used repeatedly or for an extended period, it may be economical to remove, or elevate, and reinsert it, so as to prevent heat being conducted into the helium bath.

The removal of an insert from the magnet should be slow, on the order of 15 seconds, to prevent an explosive warming of the helium gas, which can blow seals and windows.

Two of the inserts used in the present work were of double-wall construction, with a vacuum space between the two walls, and a thin dielectric spacer at the top to maintain thermal separation. The shorter double-wall insert, used with the Clarendon magnet, was in fact just the normal insert with a removable inner sleeve. Because of this mobility, it was necessary to ensure with each use that the inner sleeve was not in contact with the outer sleeve, which would have presented an unacceptable thermal leak. This was accomplished by electrically isolating the inner sleeve by means of neoprene gaskets. Three bolts and wing-nuts clamping this sleeve to the outer one were adjusted in tightness, against the resistance of the gasket, to tilt the inner sleeve until an ohmmeter indicated the two sleeves were not connecting.

The intention with either insert was to be able to pump on the inner space to lower the

sample temperature to 1.8°K or thereabouts, or to fill it with liquid nitrogen in order to be able to apply a high magnetic field to the sample at 77°K. In practice, the short insert was unable to maintain liquid helium significantly below 4.2°K, as its length created too large a heat gradient.

Finally, an insert must have suitable electronic conductors in order to do Hall measurements, photoconductivity experiments, etc. Typically, some 10–14 wires will be present in an insert to allow, say, six contacts to a sample for a Hall measurement, four additional wires for manometry, and at least two thermocouple wires will be included, as well as connections to a temperature-reference diode, for instance. The wires leading to the sample must be thin enough to avoid heating the sample and boiling off liquid helium due to the large thermal gradient,* but should also be thick enough to withstand manipulation and to keep circuit resistive losses, also helium-expensive, minimal. Finally, long circuit wires that thread through strong magnetic fields are liable to cause great difficulty with noise and distortion, both from microphonic pick-up, where a vibrating conducting loop varies the magnetic flux through it, and from capacitative effects. Therefore, adequate shielding is essential.

In practice, these sometimes divergent requirements were met as follows. On the short insert (~80 cm from top flange to sample), wires were typically ~40 s.w.g. silk-covered copper wires, each in its individual thin-walled stainless steel conduit, of approximately quarter-inch tubing. This arrangement allowed the wires to be cooled directly by the liquid helium so as to avoid heating the sample, and were of negligible resistance. Unfortunately, they are also quite fragile and prone to shorting. Therefore, they are often threaded through loose-fitting PTFE sleeving for protection, both from sharp stainless steel edges and from tangling. The stainless steel tubing surrounding each wire is electrically contiguous with the top flange of the insert, which is kept at ground potential. This prevents the capacitative effects mentioned earlier, but the system is still very microphonic because of the motion of the wires relative to the tubing.

In the longer inserts (~130 cm from top flange to sample), the same system was originally employed. However, as the difficulty of threading thin wires through sleeving and conduits increases exponentially with the lengths involved, a move to coaxial "cryogenic" cable was made. This is extremely thin stainless steel wire surrounded by a thin foil of shielding. While the thermal conductivity is exceedingly low, the resistivity is quite high (~50 Ω for the circuit). Therefore, to get accurate voltages on a sample of low resistance, it is essential

* A few copper radio wires leading down a short insert can transfer 600 mW of thermal power, enough to boil off a liter per hour of liquid helium.

to do four-contact measurements (which are of course the preferred method in any case to eliminate non-ohmic contact effects from the readings).

6.5 The Czerny-Turner Monochromator

Both homemade and production (Bentham) models of the single-beam Czerny-Turner monochromator were employed in order to conduct intrinsic detection experiments in the near-infrared (i.e., the 3–10 μ region). This is a very common laboratory tool, simple in its construction and robust: Concave collimating mirrors provide self-correction for off-axis rays, and offer no wavelength dispersion as do lenses, and the simple sine-bar drive renders an angle, and hence a wavelength, proportional to displacement.

Gratings blazed at $\sim 4\,\mu$ were used,* as the band-edge of indium antimonide falls in the region of 5 μ, varying with temperature, pressure and magnetic field. The maximum theoretical resolution for a given wavelength depends only on the width of the grating (as opposed to its line density), and the Bentham monochromator used gratings of $\sim 40 \times 40\,\text{mm}^2$, replacing the previous 1 inch square grating.

The slit width of the monochromator is determined by a variety of needs: Total power transmitted through the exit slit is approximately proportional to the square of the slit-width (assuming that the slits are set equally), but resolving power is inverse to the width of the exit slit, provided the slit itself does not become narrow enough to appreciably diffract the wavelength of interest: $R = \lambda n f / s(d \cos \theta_i)$, where R is the resolution, n is the order of the reflection, f is the focal length of a collimating mirror, s is the slit-width, d is the line separation, and θ_i is the incident angle. The monochromator was generally run so as to be able to easily resolve the CO_2 doublet, a separation of $\sim 0.03\,\mu$.

In each case, a stepper motor and associated electronics were present in order to register wavelength on either a chart recorder or into a computer data file.

The monochromator was often flushed with nitrogen gas at room temperature, in order to eliminate the large IR absorbances of air-borne moisture. Generally, it was found that $\sim 90\%$ of this absorption could be eliminated, sufficient to prevent it masking any major features. Unfortunately, a series of small water absorptions (vibrational/rotational combination bands) occurs in the region of the indium antimonide band-edge, and these can often obscure or be mistaken for structure.

* Blazed gratings, or echelettes, have their reflecting surfaces oriented such that the first order of the desired wavelength is provided with maximum surface. In this way, typically 80% of the diffracted intensity falls in the desired order.

In combination with the monochromator, of course, was a source of infrared radiation, in this case an Oriel "globar" of silicon carbide heated to ~1000°K, with a maximum emissivity at ~4 μ. It was run at constant voltage (~11 V) and after an initial warm-up period, current was seen to remain constant to within a couple of percent over the term of these experiments. The spectral irradiance (see Appendix 1) was provided by Oriel.

A small chopper was used to modulate the light for PSD measurements.

6.6 The CO_2 and FIR Lasers

An Edinburgh Instruments PL4 continuous wave CO_2 laser, of 50 W maximum polarized power output, was used to pump an EI Model 195 far infrared laser, a passive cavity resonator filled usually with methanol (though formic acid, CH_3OD, and many other lasing vapors can be used). Typically, 100 mW of 118.8 μ radiation can be generated from the latter, along with many other lines.

Each laser was kinematically mounted on aluminum blocks bolted to a granite slab resting on inflated innertubes supported by polystyrene blocks, serving as an optical bench.

6.6.1 Principles of CO_2 and FIR Laser Operation

Light propagation through most media is damped exponentially according to the equation $I(x) = I_0 \exp[-\alpha(\omega)x]$, where $I(x)$ is the intensity as a function of propagation distance and α is the absorption coefficient, a function of the light frequency ω. Such absorption is to be expected in a classical, or Maxwellian system, where an ensemble of atoms in thermal equilibrium is characterized by the Boltzmann distribution, wherein

$$\frac{\mathcal{N}_i}{\mathcal{N}_j} = \exp\left[\frac{-(E_i - E_j)}{k_B T}\right], \tag{6.1}$$

and $\mathcal{N}_i < \mathcal{N}_j$. The absorption coefficient α is given by $\sigma_a(\mathcal{N}_j - \mathcal{N}_i)$, where σ_a is the absorption cross-section. If $\mathcal{N}_i > \mathcal{N}_j$ at any point, the absorption coefficient becomes negative, and thus, a gain coefficient.

Laser action in general relies on such a "population inversion" to enhance stimulated emission of radiation. In an excited system, the total probability of photon emission due to an electron relaxing from a level i to a level j is the sum of that for spontaneous (incoherent) emission, $\mathcal{A}_{ij}$, and that for stimulated (coherent with the stimulating radiation) emission,

$U(\omega)\mathcal{B}_{ij}$, where $U(\omega)$ is the density of the stimulating radiation. $\mathcal{A}$ and $\mathcal{B}$ are the so-called Einstein coefficients, which are related to the lifetime of the transition τ_{ij} as follows:

$$\mathcal{A}_{ij} = \frac{1}{\tau_{ij}} \qquad \text{and} \qquad \mathcal{B}_{ij} = \frac{c^3}{8\pi h \nu_{ij}^3}\mathcal{A}_{ij}. \tag{6.2}$$

Merely providing a flux of stimulating radiation is not sufficient to achieve a population inversion, as an equilibrium between absorption and emission is eventually attained. If $\mathcal{N}_i = \mathcal{N}_j$, the medium becomes transparent.

As such, a third energy level is required at an energy higher than E_i to spontaneously emit radiation while allowing the electron to relax into E_i. In this way, E_i can be populated at a rate greater than that by upward transitions from E_j, and a steady state population inversion is achieved.

If there are four states, with a state E_j separate from the ground state, and in which the electrons have a negligible lifetime prior to decay to the ground state, more efficient inversion is possible, in that less stimulating radiation is channeled into absorption from E_j to E_i.

The CO_2 laser relies on the population inversion depicted in Fig. 6.3.

An electric discharge is used to populate (by collision) the $v = 1$ vibrational level of the ground state of N_2, which, having no dipole moment, cannot emit radiation to relax. This state, then, is metastable, and can become highly populated. This allows efficient selective excitation of the CO_2 from the ground state (00^00) to the vibrational level 00^01, a transition only $18\,cm^{-1}$ larger than that of the N_2. This deficit, which is tiny relative to the overall transition of over $2300\,cm^{-1}$ from the ground state, can easily be made up for in collisional energy transfer.

Emission takes place in the infrared between vibrational levels 00^01 and either 10^00 ($10.4\,\mu$) or 02^00 ($9.4\,\mu$). These vibrational levels include modes that bend the CO_2 molecule away from its equilibrium linearity, producing a temporary dipole moment by virtue of the great electronegativity of the oxygen atom. However, each vibrational level is split into several rotational levels (see Fig. 6.4, for example), which add small rotational quanta ($\sim 1.5\,cm^{-1}$) to the total transition energy sum. The transitions wherein $\Delta J = +1$ (and the transition energy is enlarged) make up the so-called P-branch transitions, whereas those in which $\Delta J = -1$ and the transition energy is reduced comprise the R-branch.

The lower downward transitions take place in the far-infrared. These typically occur much faster than transitions within the IR region, and the transitions from 10^00 and 02^00 to

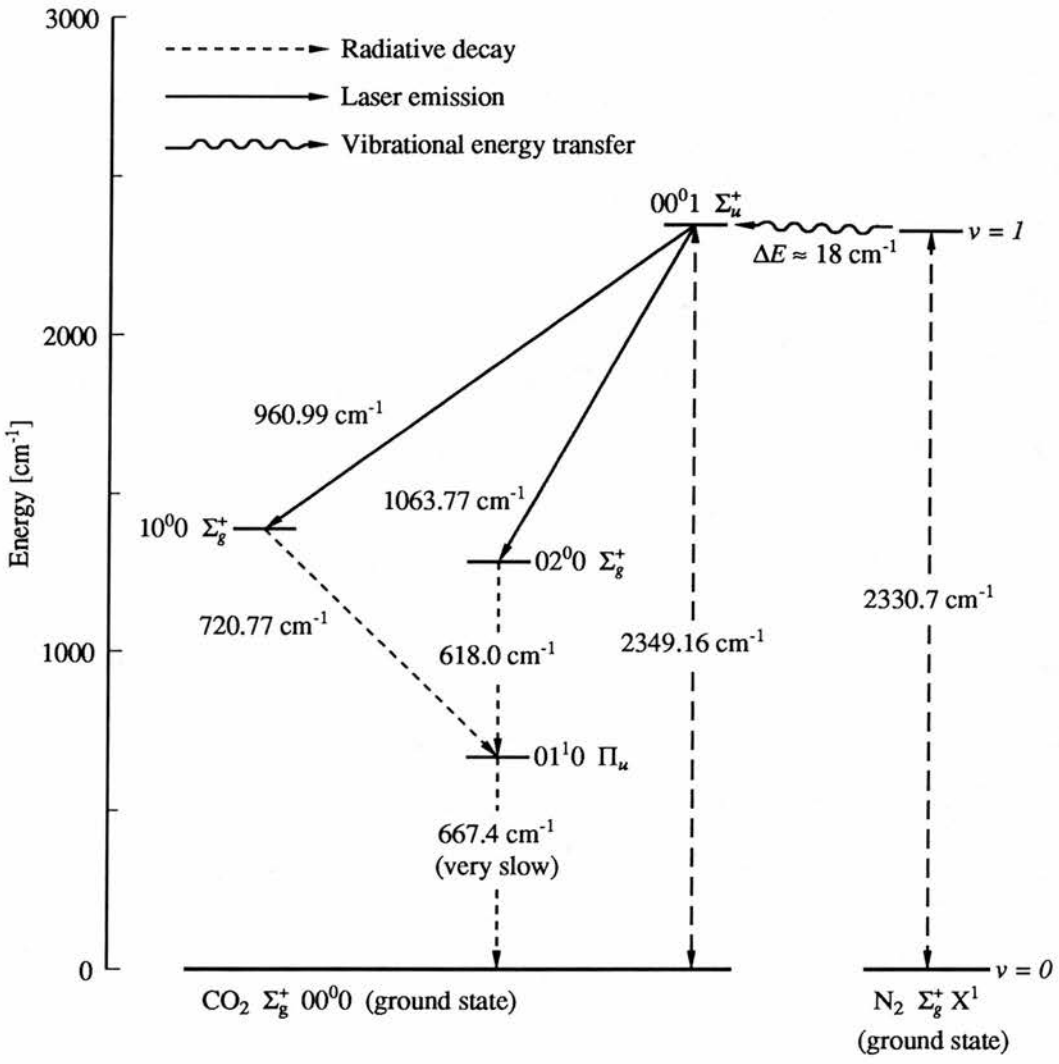

FIG. 6.3: Energy level diagram for CO_2/N_2 laser.

01^10 occur an order of magnitude faster than those from 00^01, thus creating the necessary population inversion between 00^01 and the lower states.

On the other hand, the rate of decay from 01^10 to 00^00 is very slow, and "self-trapping" might occur within the higher levels, stifling the gain, but for the presence of helium gas. Helium, by virtue of its great thermal conductivity, very effectively depopulates the 01^10 state. The same effect can be attained by cooling the gas. The PL4 laser uses a flowing gas mix of 7% CO_2, 18% N_2 and 75% He for this purpose, and includes a running-water-cooled

discharge tube as well.

Also critical to lasing efficiency are the dynamics of the gas involved. The energy density within a constant *volume* of gas increases with pressure. Most efficient pumping is observed when the ratio of the electric field of the discharge to the numerical molecular density is in the neighborhood of $10^{16}\,\mathrm{V\,cm^2}$. This means that for a longitudinal discharge of 1 m in length, in a gas at 1 atm, about 10^6 V are required. This threshold can be lowered by preionizing the gas with transverse electrical discharges at atmospheric pressures (TEA), which also lower the overall circuit inductance so that very short pulse risetimes are possible.

Optimally, 70% of the power of a discharge may be channeled to $CO_2(00^01)$ and $N_2(v = 1)$. Since the quantum efficiency in this case is 0.41, the overall efficiency of such a laser is $\sim$30%.

An optically pumped far-infrared laser (or OPFIRL) works, of course, on the same principles as above: Pumping radiation must be closely matched to the absorption frequency of a molecule with a dipole moment which in this case must be permanent, as the FIR lines correspond to rotational states of this moment, with the emission strength directly proportional to the dipole moment. The rule of thumb for an appreciable transition probability is $\mu_d \gtrsim 1$ Debye (1 Debye $\equiv 10^{-18}$ esu cm), where μ_d is the dipole moment. Typically, methanol (CH_3OH), deuterated methanol (CD_3OD), fluoromethane (CH_3F), formic acid (HCOOH) and ammonia (NH_3) are employed. (While ammonia does not have permanent dipole moment in the strict sense, it occupies only two states of opposite parity, which give rise to two sets of rotational levels.)

A schematic energy-level diagram for a suitable permanent dipolar molecule such as methane is shown in Fig. 6.4.

As mentioned earlier for the case of the CO_2 laser, each vibrational mode is associated with a series of rotational levels. These levels are specified with two quantum numbers, J and K, called the rotational level and the second rotational quantum number, respectively. J may take on the values 0, 1, 2..., while M, the quantum number representing the angular momentum component in the direction of rotational symmetry ($= M\hbar$) may take on any value $-J, (J-1), \ldots 0 \ldots, J$. K is a quantum number associated with rotation of the molecule about its symmetry axis, and is usually reserved for non-linear molecules. These molecules in general have three different moments of inertia. If all are equal, the molecule is said to be a spherical top. If only two are equal, a symmetric top, as in the case of fluromethane and methanol. At any rate, K, like M, is limited to values 0, ± 1, $\pm 2, \ldots$,

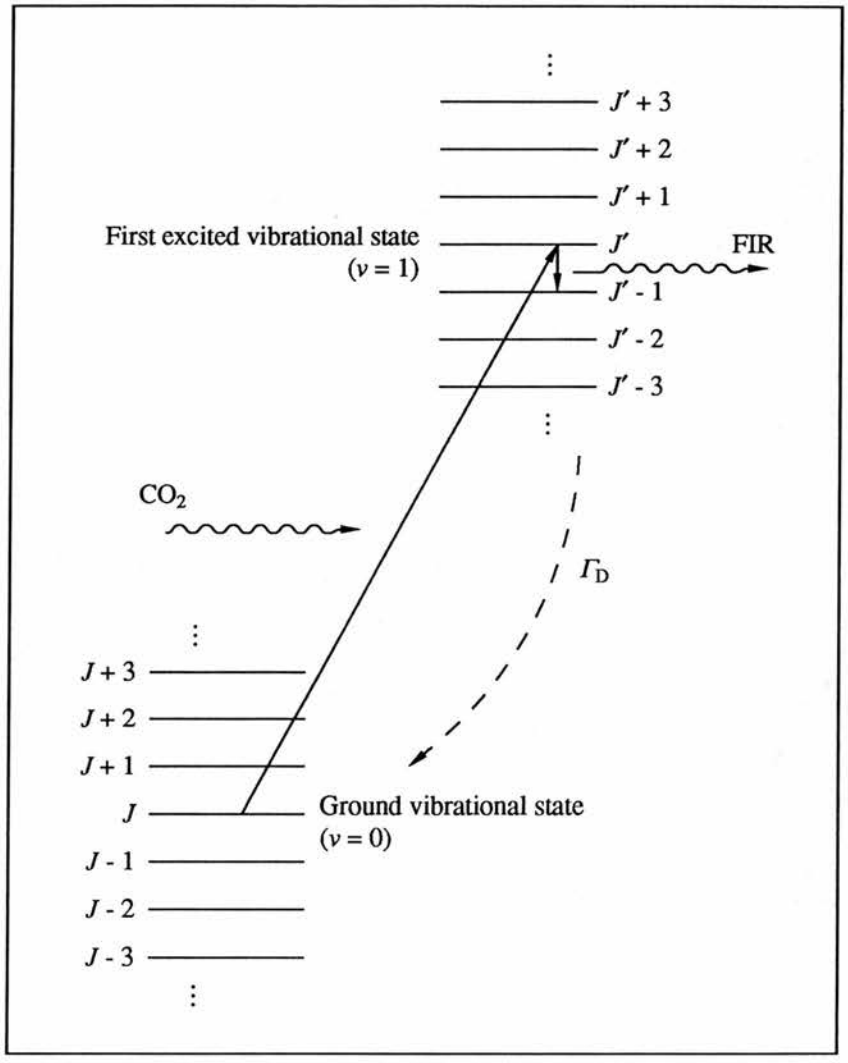

FIG. 6.4: Vibrational/rotational state diagram of CH_3OH for OPFIRL

and since energy depends on K^2, all levels except $K = 0$ are twofold degenerate. The selection rule for a lasing transition is that $\Delta J = -1$ and $\Delta K = 0$.

At 300°K, typically, only the ground state vibrational level is occupied. Optical excitation results in the elevation of electrons to the corresponding rotational levels in the first excited vibrational level, resulting in a population inversion with respect to two adjacent rotational levels in the upper vibrational state. Radiative decay may occur through cascading

transitions. In mid-infrared lasers, there is likely to be self-absorption in the ground state, but in FIR lasers, anharmonic bonding terms result in small variation in rotational interstate energies, preventing this problem.

Population inversion in an OPFIRL is maintained by ensuring that the state $J' - 1$ in Fig. 6.4 depopulates quickly enough to avoid self-absorption. The rate of this relaxation back to the ground state, Γ_D, is determined mostly by the rate at which vibrational energy can be lost through collisions with other molecules and with the resonator walls. $\Gamma \propto 1/Pd^2$, where P is the pressure, and d is the diameter of the resonator. A pressure between 30 and 300 mtorr is generally employed, and 100 μbar was standard with the Model 195.

At such low pressures, the mean free path of the molecules is quite large, as are the mean free velocities, and appreciable Doppler broadening, to an extent far greater than the natural pumping linewidth, results. Doppler broadening is given by $\Delta\nu = 2\nu_0(v_z/c)$, where ν_0 refers to the central exciting frequency, and v_z is the longitudinal component of molecular velocity. Since the velocity distribution is largely bimodal (i.e., to and fro), rotational groups are split into two populations.

It can be shown that the power available from an OPFIRL is approximately

$$P_{FIR} = \frac{Q_q Q_c}{\left(1 + \frac{g_2}{g_1}\right)} \left[\frac{\alpha_{IR} L}{(\Gamma_{IR} + \alpha_{IR} L)}\right] P_{IR}, \tag{6.3}$$

where Q_q is the quantum efficiency, $\hbar\omega_{FIR}/\hbar\omega_{IR}$; Q_c is the cavity efficiency, $(1 + \mathcal{A}/\mathcal{T})^{-1}$, where $\mathcal{A}$ is the net cavity loss from absorption at end mirrors, waveguide losses, scatter, etc. (but not transmission) and $\mathcal{T}$ is the transmission per round trip; g_1 is the degeneracy within the ith K-rotational level; α_{IR} is the absorption coefficient for the pumping radiation; L is the cavity length; Γ_{IR} is the empty cavity loss for the pumping radiation; and P_{IR} is the input power of pumping radiation. The bracketed term is thus the portion of pump power absorbed by the gas. On the surface, it appears then that increasing the pressure, which increases α_{IR} proportionately, should increase the output power. However, above a critical pressure P_c, relaxation processes dominate, and P_{FIR} rapidly drops to zero. In fact, P_c is independent of pump power, all other things being equal.

Eq. 6.3 breaks down at very low pressures near a resonant driving field, or when the pumping radiation is offset from the absorption transition by more than the Doppler width, but is intense enough to drive multiphoton absorption processes nonetheless. In these cases, the coherent pumping model is required, a semi-classical model incorporating Schrödinger's equation for multiphoton kinematics.

6.6.2 *The PL4 CO_2 Infrared Laser*

While the PL4 is suited to operation in either cw or pulsed mode, power *per se* was not generally a problem in deriving signal from indium antimonide, one of the world's most sensitive detectors of IR radiation. Furthermore, as most of the experiments were conducted with the small sample mounted in the pressure-bomb, where it was completely immersed in glassified hydrocarbons of presumably poor heat-conducting capability, sample heating was a real concern (see below), and intensities were purposely kept low, occasionally even to the extent of introducing into the optical path PTFE filter discs to lower the 10.6 μ radiation component, which penetrated the windows of the OPFIRL. Therefore, only cw operation was used, although the output was chopped at ~250 Hz, typically, to allow PSD electronics to detect the photoconductivity changes, which are on the order of only 1% or less. This speed seemed to work best for the elimination of ground loop noise and $1/f$ noise (see Chapter V).

The PL4 is capable also of running in a sealed mode, as when expensive isotopic mixtures of CO_2, which can generate different lines, are being used. However, in these experiments, only the flowing gas mode, which better prevents thermalization, was employed.

The laser is supported and thermally stabilized (structurally speaking) by invar rods, the discharge tube itself by perspex (polyethylene) plates. The tube is a 9 mm periodically corrugated bore* glass tube surrounded by a water jacket and a gas jacket which, by channeling the gas over the water jacket, precools the gas. The tube ends are O-ring sealed on air-cooled ZnSe Brewster windows that are wedged in order to frustrate interference effects, and which optically couple, with minimum loss, the radiation from the low-pressure region to the rest of the system, and protect other components from the discharge. They also render the output vertically polarized. 90% of this output is in the TEM_{00n} mode,† with a nearfield beam diameter (at the $1/e^2$ points) of approximately 7.5 mm, and a divergence of < 2 mrad.

The laser requires 30 kV at up to 30 mA, and filtered cooling water at a rate of 2–3 liters/min. The above described gas mixture is supplied at a pressure of ~30 mbar, but discharge should be commenced at about half that.

* Corrugation (in this case on the order of 1 cm) frustrates off axis modes and allows coupling to end windows.

† i.e., no longitudinal field components, and n wavelengths in the cavity.

The laser is tuned by means of a water-cooled blazed diffraction grating at its back end and a piezoelectrically translated output coupler. Tuning was in fact not trivial. While the lines are broad enough to find easily, the stability during the first ten minutes or so of operation was generally unsatisfactory, necessitating allowance for a (literal) warm-up and equilibration period, occasionally as long as two hours. This is was apparently on account of the variation in cavity length with temperature, though if this is the only reason, a steady state temperature was ostensibly never reached. Over the course of ten minutes of spectra taking (which may require close to half an hour for each direction in the extreme case of high fields, long time constants and dense structure), the laser stability was often called into question, though at times it was unclear whether inconstancy of signal was due to sample heating, sample pressure loss, or instability of the FIR laser. A slight instability in the pumping radiation can result in large fluctuations in the FIR output, as heating can affect the FIR cavity as well as the gas itself, which beside thermalizing can chemically deteriorate; and if the pumping radiation is near threshold intensity, it can exponentially vary the output. A line stabilizer, which worked by receiving signal feedback from the detector and inputting this to the piezo-drive, was available but remained unused: It was found to be ineffectual, possibly because of its reliance on the constancy of the signal output.

Alignment of the laser by users is possible, and instructions are to be found in the manuals. However, the laser was aligned by the manufacturers *in situ* prior to these experiments. The laser is mounted on a makeshift optical bench as described above, and appears to be quite free of vibrational problems or disalignment.

The only problem to have come up in this respect was a mysterious, and large, disalignment of the associated steering optics for directing the PL4 radiation into the OPFIRL. The nearfield not-quite-Gaussian mode pattern of the PL4 is such that, running at its maximum (and typical) output power of 60 W, it can ignite wood over approximately a 1 cm diameter. It appears that this intensity was too much for the polymeric grub screws which held in place the mirror on a newly purchased optical mount. As they were tightened with some force, and as the first steering mirror (see Fig. 6.5) is over a meter away from the input coupler of the OPFIRL, it is likely that the grub screws were softened sufficiently to "creep" slightly, and thus completely misdirect the PL4 radiation from the pinhole of the input coupler (see below).

A list of all available pumping lines and their output, as well as the induced FIR radiation wavelength, was provided with the laser manuals. A portion of this tabulature, listing those lines employed in the current work, is reproduced in Table 6.2.

6.6.3 *The Edinburgh Instruments OPFIRL*

The EI Model 195 FIR laser is a non-flowing mode, gas-filled Fabry-Perot waveguide resonator, capable of using numerous gases, and is widely tunable. The laser consists of an outer Pyrex™ tube serving as a gas envelope, an inner waveguide of either brass or Pyrex™, and sealed housings at either end, one of which is adapted to allow gas exchange and input coupling, and the other of which comprises the output coupler and fine-tuning mechanisms.

As explained above, a permanent dipole molecular gas, such as methanol of spectral grade (used exclusively in the present work) serves as an active medium in an OPFIRL, and must be maintained at a pressure of $\sim$100 μbars. In this case, the gas is maintained statically within a Pyrex™ envelope, while thermalization is prevented by rapid collisions of the molecules with the waveguide, rather than with each other, and by the chopped nature of the radiation. Because the gas is not continuously replenished, and because many optional gases are either corrosive (formic acid) or radioactive (CH_3OD), the laser is sealed at the end houses with ultra-high vacuum (UHV) fittings. These include thick warp-resistant stainless steel flanges and oxygen-free copper gaskets, which are sealed by means of knife-edge rims on the flanges, which are bolted to one another with typically 8 or 12 bolts placed circumferentially. Tightening proceeds by doing opposite bolts in sequence around the circumference, and continuing the process repeatedly until the increase in resistance to tightening indicates that the knife-edge has penetrated the copper. No rubber or other polymeric components are present.

The Pyrex™ envelope is bonded to the inner stainless steel flange of each end house by means of a glass-to-metal seal and rolled bellows, which beside providing a hermetic seal, isolate the Pyrex™ from differential thermal expansion of the rest of the laser, which is thermally stabilized by three invar rods.

The 1.5 m waveguide of the OPFIRL may be either Pyrex™ or brass, though in the present work, only the latter was used. While brass takes longer to outgas than Pyrex™ (an important consideration—see below), it allows a greater range of wavelength to be attained than does the Pyrex™, which can be used for wavelengths only up to $\sim$500μ. This would have been unsatisfactory in the present work. The waveguide, of 24.9 mm inner diameter, is highly polished on its inner surface.

The input coupler is in the form of a ZnSe window of approximately 25 mm diameter, positioned $\sim$14 cm in front of a 45 mm diameter concave aluminized glass mirror with

a 1.2 mm pinhole through its center, through which the radiation from the PL4 must be focused. This mirror is positioned by three screws pressing it against a wavy circular spring (see paragraph on alignment, below). The output coupler is an aluminized glass mirror of similar diameter, in the center of which is a silicon window of ~1 cm diameter, held in with epoxy. This window is the standard adjustment window, and as such is mounted on the front of a stainless steel bellows, allowing it about 2 cm of movement. Besides there being an output translator for this movement, three micrometers can angle the mirror by differentially compressing the eight springs that surround the bellows and terminate on the front plate. These micrometers terminate with ball bearings, which are seated against kinematic mounts (an indentation, a groove and a plane) inset in the outer face of the output coupler.

Alignment of the lasers (of the OPFIRL relative to the PL4, and the mirrors and cavity of the OPFIRL relative to each other) is conveniently carried out using one or two He-Ne lasers (and a small beam-splitter if only one is used), and numerous mirror mounts. First, the steering optics are adjusted by aiming the He-Ne down the center of the OPFIRL cavity with both couplers removed. It is very difficult to simply point the He-Ne down the center, as the acceptable angular range is very small. It is best to remove the He-Ne by two meters or so, and line up its apparent direction (judged simply by that of its plastic case) with that of the laser, taking a sightline over the the top of the OPFIRL. Once the He-Ne beam is propagating directly through the waveguide, two Lucite™ discs, etched with cross-hairs, which fit into the ends of the waveguide, can be used to easily ensure that the He-Ne is aligned with the laser to much better than the required 1°. As two mirrors are all that is required to collinearize one light beam with another, the two mirrors closest to the OPFIRL are used to steer the He-Ne beam along the path defined by the PL4 and the first mirror in front of it. This path can be easily demarcated by mounting, along the approximate path, two small sheets of paper affixed to optic mounts. If the PL4 is switched on, well off its central peak, just enough power will emerge to slowly brown the first sheet of paper. A scalpel can then be used to scrape out this small burn to leave an aperture through which the second sheet of paper may be browned. (The heat sink/shutter should always be down when operations near the invisible beam are carried out, and goggles or glasses of some form should be worn constantly.) With the PL4 laser off, the He-Ne can be switched back on and the two mirrors adjusted to steer it through the apertures defined by the PL4. Once the path is thus adjusted, it may be necessary to fine tune it. This can be done by mounting the input coupler mirror (with the pinhole) and sending low-intensity PL4 radiation through it. A fluorescent screen, comprising small panels of differing sensitivity, can then be mounted in front of the output

end of the waveguide, and a fluorescent light shone on it. When the intense laser IR impinges upon this screen, it quenches the fluorescence and thus makes itself visible as a dark spot. A correctly directed IR beam will show up on these panels as a series of fine concentric circles, which should not be asymmetrically fragmented or shaded, in the ideal case. Small adjustments with the steering mirrors will allow this pattern to emerge. The input angle at this stage of alignment can in fact be judged visually, as the highly focused input beam will cause the edge of the pinhole to glow when the former is displaced slightly from the optic axis. (It should be noted that the screen, while having heat sinks, will become quite hot, and a sensitive panel on it may actually burn quite easily.)

The OPFIRL is aligned by first translating the He-Ne toward the edge of the waveguide. This is in order to make use presently of the reflecting surfaces of the cavity mirrors, which do not cover the axial center. First, using a beam-splitter and several mirrors, the He-Ne beam is steered into the input end of the waveguide, and the output coupler mirror is affixed and adjusted to send the He-Ne beam back along its path, thus ensuring (since the He-Ne is already parallel to the optic axis) that the mirror is perpendicular to the optic axis. A small mirror is affixed, solidly, to the *outside* of the output mirror, such that the original, unsplit He-Ne beam is incident on it. The reflection of the He-Ne off of this external mirror is traced to a wall or other suitably immobile marker, and the reflected beam's position recorded. Thus, the output coupler mirror can be later repositioned by adjusting it with the micrometers so as to make the He-Ne's reflection coincident with that of the original.

At this point, the output coupler mirror is removed, the input coupler mirror is affixed so as to send the first He-Ne beam back along itself (making the mirror normal to the optic axis), and the output coupler mirror is repositioned.

In order to prevent contamination of one gas with another, or contamination of the laser cavity with residue of previous reagents, which can dramatically lower signal strength and contribute to line instability, the cavity should be scrupulously cleaned. The waveguide can be washed in a mild detergent, followed by several liberal rinses with distilled water, and rinsed with isopropyl alcohol to degrease it and to displace the water (which can freeze and kill IR propagation), while mirrors and flanges must be similarly rinsed and degreased. The waveguide should be handled only with gloves. In particular, the vacuum pump (see below) must have an oil mist filter and cold trap. Failure to supply this leads, after a short time, to the collection of pools of low-vapor-pressure oil within the bellows and other internal nooks of the laser. While this does not in itself appear to kill laser operation, it is difficult if not impossible to remove, and if bakeout of the Pyrex™ envelope is attempted, all components,

mirrors included, will be covered with oil—which will kill the lasing action.

In order to ensure optimal operation, the laser cavity should be evacuated overnight to a pressure of $\sim 10^{-7}$ torr. The active gas must then be purified (de-aired), which will result in markedly lower threshold powers and higher output power (often by a factor of two or three). This is achieved with the freeze-pump-thaw technique, which is carried out by means of the needle valve and test-tube connected to the input manifold: The methanol, for instance, is frozen by immersing the test-tube, as it extends from the manifold, in a small bath of liquid nitrogen. It is then vacuum pumped to remove gaseous impurities. As it is thawed, usually by the warmth of the hand, other liquid components of lower vapor pressure than the methanol start to escape, although if this is continued for too long, the vapor pressure of the methanol itself will rise to the point that it is lost up the vacuum system. Therefore, this cycle must be repeated a few times, until no more bubbling is seen as the methanol thaws.

Afterward, the methanol is allowed to enter the cavity by means of the same needle valve, up to a pressure of $\sim 100\,\mu$bars.

6.6.4 Laser Artifacts

Because of mixed modes (i.e., lines of different frequency) emerging from the PL4, and because even a single line typically gives rise to two lines from the OPFIRL, mixed modes emerging from the OPFIRL can be expected, and are also problematic. Fortunately, it is usually possible to distinguish one mode from another by using the translator to vary the cavity length. As micron adjustment is possible, it is easy to track the disappearance and reemergence of specific lines as the cavity length proceeds through successive multiples of $\lambda/2$, provided the wavelengths are not too close: The 70.51 μ and 699.4 μ lines are easily discernible this way (provided the 70.51 μ line is visible at all: As practically the shortest wavelength mode available on the laser—though weaker lines are available down to 37 μ—it is the most vulnerable to laser disalignment or mirror contamination by oil). Observing the intensity of signal as a function of micrometer distance allows the identification of the wavelength of a particular mode. If too many modes are present to do this easily, or if the noise level is such that signal identification is uncertain, filters can be interposed between the output coupler and the brass light-pipe to eliminate unwanted wavelengths. For instance, PTFE transmits only about two thirds as much 70.51 μ radiation as it does 699.4 μ. The pumping and output lines most commonly used in this work are shown in Table 6.2.

TABLE 6.2: Typically, each CO_2 pumping line stimulates at least two strong FIR lines. Methanol, the most versatile of the FIR lasing gases, gives rise to over one hundred lines. The strongest of those lines, often used in the current work, as well as their relative strengths, are shown below. It should be borne in mind that output power is not indicative of the strength of the detector's response, necessarily (see Chapter V). (Data selected from Edinburgh Instruments printout.)

CO_2 Pumping line (wavelength [μ] and branch)	FIR Wavelength [μ]	Relative power
9.52P16	1223.658	-1
	570.5678	0
	369.1137	0
	223.50	0
	164.60038	0
9.68P34	699.4	+2
	486.1	+1
	70.51163	+2
	63.36954	0
10.14R38	469.0233	0
	251.1398	0
	163.03353	0
9.33R10	232.93906	-1
	164.7832	+1
	96.52239	+1
9.69P36	170.57637	+2
	118.83409	+1

One artifact that appears to have arisen from the mixing of modes is the broadening of a cyclotron resonance linewidth (see Chapter VIII). In particular, a resonance corresponding to 170 μ stimulation was found to be anomalously broad, even though bias and temperature were as low as usual. The likely explanation for this is that the resonance was appearing on the shoulder of that due to the much more intense 118.8 μ, and prolonged exposure to the latter resulted in substantial sample heating.

A similar problem, occasionally exacerbated by mixed modes in the laser, is one of shifting quadrature. This was especially troublesome with the 699.4 μ line at low magnetic

fields: In this case, free carrier concentration is very high (not having been magnetically frozen out yet) and λ^2 is also at practically the largest value available from the laser, typically at a high intensity. Absorption therefore is at a maximum, even in a very thin sample (see Chapter III), and apparently sample heating occurs. As resonance proceeds through its range of magnetic field, one observes the PSD signal change phase by up to 180°. This indicates that conductivity is perhaps being stanched by thermal effects, far beyond those of modest notching (see below). These thermal effects, moreover, would be expected to have time constants more on the order of the optical chopper frequency than of the electron relaxation time, thus swaying the phase of the output as well as its sign.

One problem possibly encountered in the current work is that of thermoelectric effects. Because of the great heating power and coherence of the laser, small areas of a sample may become significantly warmer than others. In the case of a contact to a copper wire becoming warmer than a neighboring contact, this can lead to a large voltage being induced in the sample. In cyclotron resonance spectra, this evinces itself as a (possibly) very large negative peak at the point of greatest absorption, as the thermovoltage is not necessarily of the same direction or phase (i.e., time dependence) as the photovoltage.

A final problem occasionally leading to difficulty in identifying resonances or transitions is that of "notching". In this case, a high intensity photoconductive peak is apparently split, resembling the expected outcome from Zeeman splitting or second Landau level transitions. STILLMAN ET AL. (1985) proposed that this effect was due to the alteration of material optical constants at the highest absorption levels. In these experiments, notching was not generally observable, as the samples were made as thin as possible to achieve a true lineshape, and power levels were kept low.

6.7 Hall Measurements

Several Hall measurements were undertaken in Warsaw, Poland at UNIPRESS, the high pressure research center, on a sample of indium antimonide.

The material tested was high-purity, high-mobility bulk n-type indium antimonide from MCP, Ltd., nominally of electron concentration $n \approx 5 \times 10^{13}\,\mathrm{cm}^{-3}$ and mobility $\mu \approx 600{,}000\ \mathrm{cm}^2\,\mathrm{V}^{-1}\mathrm{sec}^{-1}$ at 77°K.* For these measurements, a small, square cross-sectional slice ($\sim 3\,\mathrm{mm} \times 3\,\mathrm{mm} \times 0.5\,\mathrm{mm}$) was notched to form a Van der Pauw "cloverleaf", etched

* These measurements, however, were taken by the manufacturer under conditions, especially magnetic field strength, unknown to us. Furthermore, as is explained in Chapter II, measurements of n are complicated by the presence of various scattering processes which alter its proportionality to the Hall coefficient. Finally, the heterogeneity of the ingot sampled introduces wide variations into the *(cont'd.)*

in a bromine/methanol solution to high specularity to a final thickness of $\sim 150\,\mu$, and contacted with undoped indium dots. Hall measurements were taken from 77°K to 290°K only, involving no optical excitation. The applied magnetic field used was usually ~ 0.13 T, though fields as low as ~ 0.03 T and as high as ~ 0.16 T were used as noted.

The gas-pressure system and the pulsed power supply described above were used in order to be able to vary pressure while the sample was cold, both in a metastably pretreated state and in the "normal" state.

Metastable pretreatment, or high pressure freeze-out (HPFO), involved pressurizing the sample to a pressure above 7 or 8 kbars while at 290°K, then cooling it by filling the cryostat in which the pressure-cell was lowered with liquid nitrogen from a pressurized dewar. The pressure, which is maintained by "locking in" the gas, drops as the temperature of the cell is lowered, but only by a limited amount (on the order of 10%), as the volume of gas cooled is only a small portion of the total volume under pressure. The rate of cooling by this method at any one temperature is highly erratic, depending on the instantaneous turbulent flow characteristics of the liquid and gaseous nitrogen phases. Therefore, it is difficult to determine precisely how extensive impurity freeze-out will be, as the number of carriers trapped on *DX* centers depends strongly on the exact pressure and rate of cooling at ~90°K.

6.8 Cyclotron Resonance Experiments

Cyclotron resonance and shallow impurity spectra were taken for a number of indium antimonide samples. Previously (WASILEWSKI, 1982), it had been noted that some n-InSb samples remained low resistance at high pressures an low temperatures, and did not show narrowing, but that certain compensated samples (e.g., sample 6-98(16), also used in this work) attained extremely high resistance ($\gtrsim 10\,\mathrm{M}\Omega$) above 8 kbars at 4.2°K, which degraded the signal obtainable from them, as the preamp was loaded. One sample, however, IS522T, of especially high mobility, proved to offer good signal through a range of pressures, and exhibited narrowing over most of this range.

The mode structure and polarization of the laser were largely inconsequential in the current studies, as the brass light-pipe and metal mirrors, the integrating cone which focuses the radiation on to the sample by tapering down from ~15 mm to ~5 mm, and the integrating hemisphere behind the sample all serve to "homogenize" the radiative field and average the

(cont'd.) actual donor concentrations. We are therefore unable to rely on the precision of the quoted figures. Our own measurements in fact indicate that $n \approx 9 \times 10^{13}\,\mathrm{cm}^{-3}$ and $\mu \approx 780,000\,\mathrm{cm}^2\,\mathrm{V}^{-1}\mathrm{sec}^{-1}$ at 77°K.

intensities. All spectra were taken with the sample in the Faraday geometry (i.e., $\boldsymbol{E} \perp \boldsymbol{B}$). Theoretically, certain interstate transitions are prohibited in this geometry by selection rules. However, by virtue of the finite thickness and misorientation of the sample, and the multiple reflections of the radiation within the optics just described, Voigt configuration components are in fact present as well.

All work in the far-infrared region (i.e., $> 50\,\mu$) employed a TPX (poly-4, methyl pentene-1) filter $\sim$1 mm thick, usually unpolished, as the wavelengths transmitted are large relative to surface roughness features. Black polyethylene located either at the bottom of the insert or at the output aperture of the FTS was used as a 300°K or optical radiation filter.

Samples were cooled to 4.2°K by insertion into the magnetic bore. Because of the pressure-cell's robustness, it has a large thermal mass which is very expensive to cool in terms of cryogen. In order to conserve liquid helium, the insert in which samples in the bomb were mounted was first precooled in liquid nitrogen in a styrofoam bucket. As explained in Chapter IV, the population of metastable states is very sensitive to the precise rate of cooling in the region of 100–120°K. While the mass of the bomb was such that it took approximately 20 minutes to reach 77°K when cooled in the insert in this manner, it appears that cooling of the sample itself through the sensitive region may not have been uniform from trial to trial, as linewidths appear to have varied by more than normally expected (see Chapter VIII), possibly due to varying numbers of ionized donors.

The general set-up for these FIR measurements is depicted in Fig. 6.5, which includes elements such as the pressure cell, superconducting magnet and lasers described above. Also included is the electronics used, i.e., PSD and biasing components.

Cyclotron resonance during metastable freeze-out was examined using the HPFO technique by mounting the long magnet insert near the gas compressor and using a cylinder of helium to back-fill the insert to avoid icing. The sample was pressurized at room-temperature to $\sim$12 kbars, and cooled to 77°K by pumping liquid nitrogen through a supply line into a small styrofoam bucket surrounding the cell. The final pressure attained in the one successful trial, after leakage and cooling, was $\sim$9.1 kbars. The pressure in the vicinity of 90–100°K, and the rate of cooling in that region, which strongly determine metastable state occupation, was not recorded.

Special long-handled "spanners" were used to disengage the capillary from the pressure-cell while both were still immersed in the cryogen. The assembly of insert, cell, helium gas cylinder, and bucket of liquid nitrogen was then wheeled quickly into the laser laboratory. It is not known what effect, if any, exposure of the sample to liquid nitrogen had on the

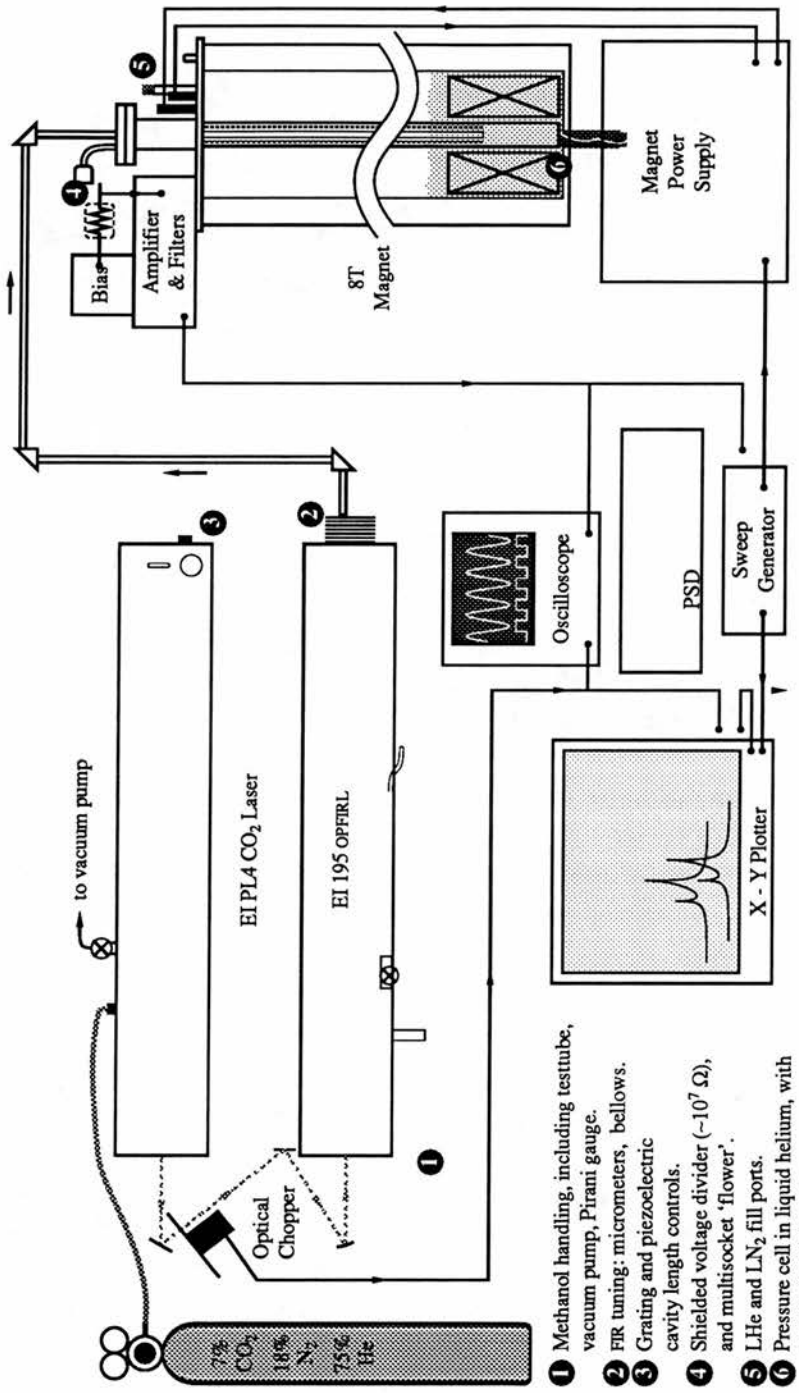

FIG. 6.5: Experimental set-up for cyclotron resonance photoconductivity measurements.

experiment. While the liquid itself may not have surrounded the sample (as the aperture into the cell is only ~0.3 mm in diameter, and any small quantity of liquid nitrogen entering may have gasified), certainly nitrogen gas remained in the sample space. The insert was quickly removed from the bucket and inserted into a sleeve which had been bunged closed, back-filled with helium and precooled in liquid nitrogen. It is not possible to say how much warming or icing the sample suffered during this transition. It is not likely that much water vapor entered through the aperture, both because of its small size relative to that of the sample space, but also on account of the effusing nitrogen gas. It is likely that the icing stopped at the aperture. The sample was then inserted into the superconducting magnet and brought to 4.2°K reasonably quickly. Any nitrogen gas remaining in the cell would have frozen, but whether it was deposited on the sample, and, if so, what effect it had, are difficult to judge.

6.9 Intrinsic Detection Experiments

Intrinsic detection experiments were conducted on most samples mentioned above, but the most extensive work was done on IS522T. A Czerny-Turner monochromator and gas compressor were used to examine pressure- and wavelength-dependent response to IR radiation in the 1–10 μ range at 77°K. Samples were also examined at 4.2°K in a magnetic field, though not with the gas-pressure system, as an explosion or sudden depressurization could have been devastating for an expensive superconducting magnet. The mix of petroleum spirits needed to employ the liquid pressure cell was not compatible with the near-IR wavelengths being studied, so no successful pressure work was carried out in this case.

The general set-up was as depicted in Fig. 6.6. Most of the components involved have been described above. In order for the pressure-cell in this case to be cooled, however, it was necessary to immerse the end of a supported insert into a bucket of liquid nitrogen, as the optical access to the cell necessitates the use of a side-entering gas capillary, and this extents outward from the cell several inches.

In order to successfully control sample conditions when the gas-pressure system was utilized, many components of the experiment required remote control, as the gas compressor, and all components at high pressure were isolated behind a polycarbonate screen. Thus, a small telescope and mirror were used to read the grating position on the monochromator, and a pumping dewar was required to fill, through a long rubber hose, the liquid nitrogen bucket in which the sample insert was submerged. Biasing control and stepper-motor control also had to be extended outside of the gas compressor enclosure. Because the S/N ratio

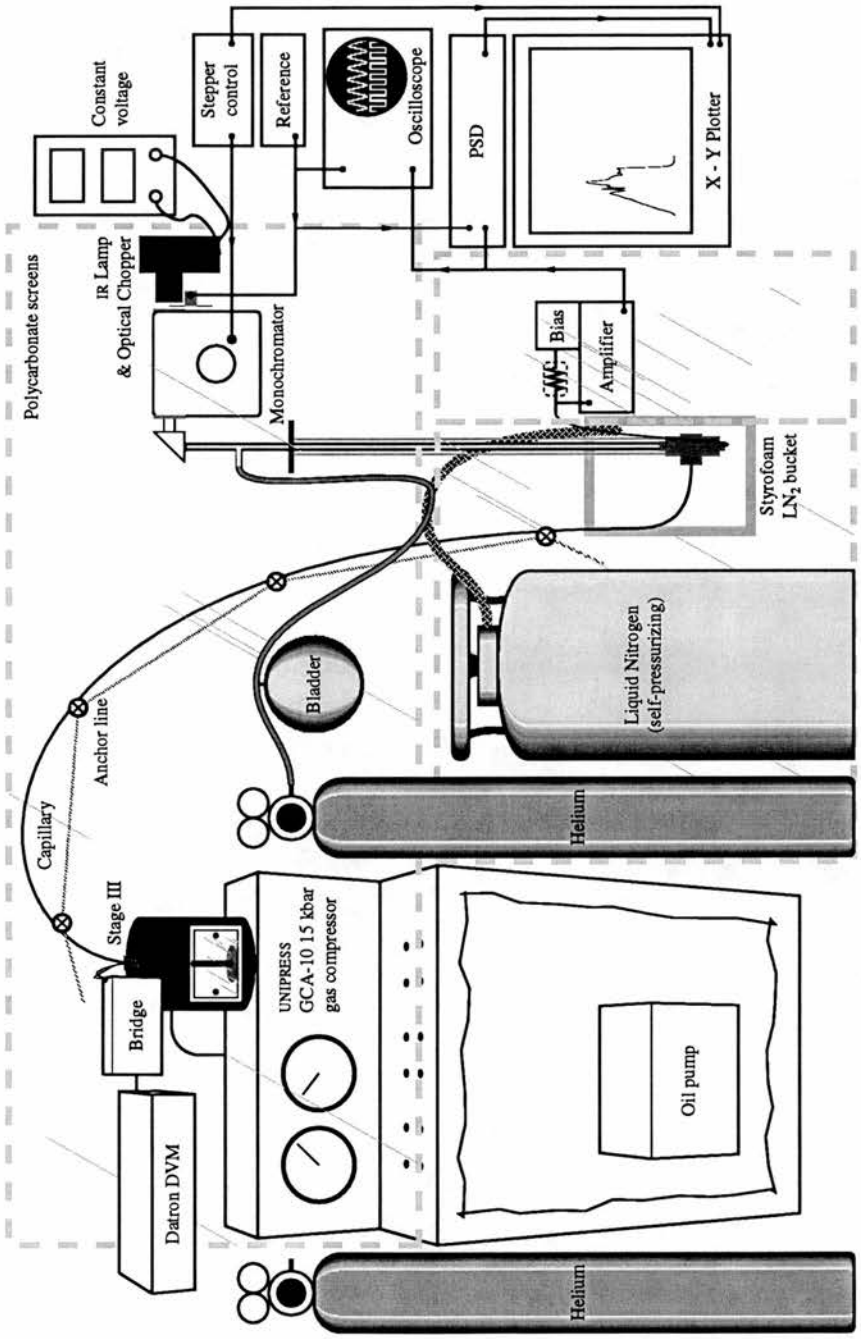

FIG. 6.6: Experimental set-up for achieving metastable HPFO in a sample prior to cyclotron resonance experiments. All manipulations must be conducted behind protective screens, while allowing signals, control voltages, cryogens, etc., to pass through.

decreased dramatically as the length of conductor connecting the sample to the first stage of amplification was increased, the preamp was positioned immediately above the liquid nitrogen bucket, and connected to the wires emerging from the pressure-cell with short lengths of coaxial cable. This was also the case for the biasing power supply.

All intrinsic (i.e., near-infrared, or 2–10 μ) experiments employed a sodium chloride filter of $\sim$4 mm thickness, highly polished (to optical transparency), and which was stored in a dessicator. NaCl is transparent in the near-infrared up to $\sim$50 μ. This is also the region where $dn/d\lambda$ is least for NaCl (HADNI, 1967).

6.10 Computer Modeling

Finally, all mobility and lineshape calculations and models were conducted using *Mathematica 2.0*, implemented with a remote kernel on an IBM RISC System 6000 work-station, and front end on a Macintosh II.

CHAPTER VII

Hall Measurements on Indium Antimonide

Discussed in this chapter are the results and interpretation of the Hall measurements described in the previous chapter. The sample was one which had shown both dramatic narrowing of the cyclotron resonance linewidth under hydrostatic pressure (see Chapter VIII on FIR results) and *DX*-like metastability (see Chapter IV). The Hall data provide information on donor levels and carrier properties responsible for these phenomena.

7.1 Results at 290°K

The first measurements reflect the sample's Hall behavior at ~290°K during slow pressurization to (and subsequent depressurization from) 12 kbar. The applied magnetic field nominally ranged from 0.126 T to 0.133 T, but these figures may be about 15% too low (see below). The plot of electron concentration (n) against hydrostatic pressure in kbar (P) is presented in Fig. 7.1, from which various important parameters can be deduced.

First, at 290°K, the sample is virtually intrinsic ($n_i \approx 10^{16}\,\mathrm{cm}^{-3}$, where n_i is the intrinsic electron concentration), so $n = n_i$. The experimental value of n at ambient pressure was apparently $\sim 1.5 \times 10^{16}\,\mathrm{cm}^{-3}$. Results cited by HILSUM & ROSE-INNES (1961) (see Fig. 7.2) indicate that $n \approx 1.6 \times 10^{16}\,\mathrm{cm}^{-3}$.

However, as explained in § 2.6, a fair degree of uncertainty is inherent in all these measurements by virtue of the unevaluated Hall factor, r_H, which takes into account the appropriate averages for various scattering mechanisms, and which can be almost as large as 2. Again, r_H is normally defined in the low magnetic field limit where $\mu B \ll 1$; in indium antimonide, this corresponds to a field at 77°K of $\ll 0.02$ T, or at 290°K of $\ll 0.15$ T, neither of which was true in these experiments. Therefore, for the time being, the Hall factor will

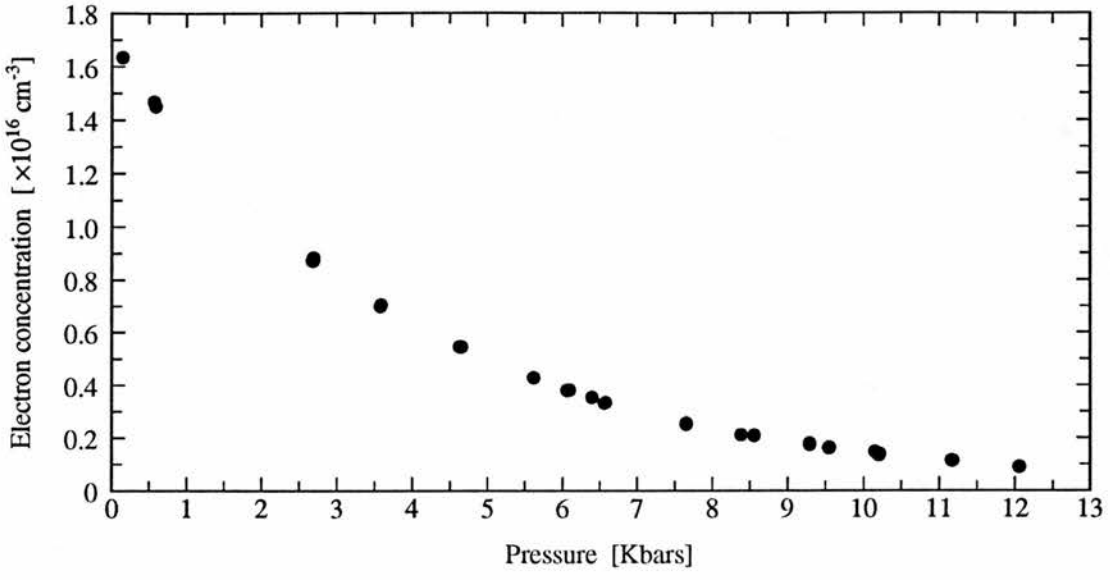

FIG. 7.1: Electron concentration in n-InSb *vs.* pressure (290°K).

be assumed to be unity. The results presented in Fig. 7.2 are also uncorrected for r_H, so the discrepancy between the values quoted above is minor.

Further uncertainty in our measurements of n arises from the non-uniform thickness of the very thin etched sample, for in a Hall measurement, n is inversely proportional to the sample thickness. The imprecision of the geometry of the sample's contacts, while not as great as that of the thickness, increases the uncertainty. Finally, an error in the assumed sample temperature of only 5°K would result in a discrepancy of almost 15% in n. Hence, the above quoted electron concentration is very approximate. On the other hand, we measured the mobility μ to be $88,000\,\mathrm{cm^2\,V^{-1}sec^{-1}}$, a value which exceeds the accepted published results ($77,000\,\mathrm{cm^2\,V^{-1}sec^{-1}}$ when polar optical scattering is dominant (LANDOLT-BÖRNSTEIN)), by about 15%.

This could be explained if the actual magnetic field were 15% higher than originally assumed, as the mobility is inversely proportional to the magnetic induction in a Hall measurement, while being independent of the largely uncertain sample thickness. While n is directly proportional to the magnetic induction, the discrepancy in the above values of n due to an incorrect value for the induction is largely concealed by that due to the unknown thickness.

Throughout this chapter, therefore, the values of μ quoted or used in calculations, and

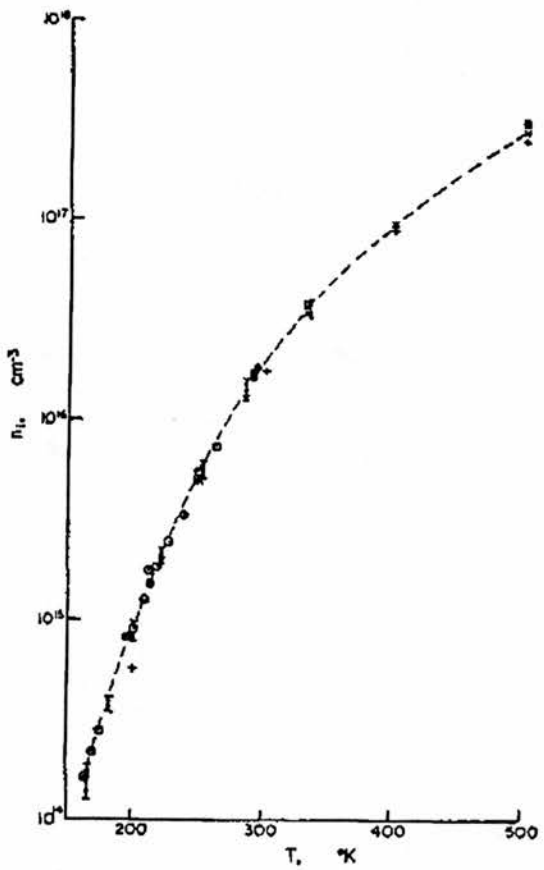

FIG. 7.2: Intrinsic electron concentration (logarithm) in indium antimonide *vs.* temperature: Various experimenters' results, taken from HILSUM & ROSE-INNES (1961) (Hall data uncorrected for the low-field scattering factor r_H).

those depicted in the figures, are corrected as above by ~15% (see Fig. 7.3). Values of n are corrected for the uncertainty in thickness by ~7% so as to be consistent with Hilsum's figure at 290°K.

Because n_i is a function of the band-gap energy E_g, which is known very accurately, the data of n_i *vs.* P can be used to determine dE_g/dP. Furthermore, because the experimental dependence of ln n on pressure (Fig. 7.4) is a quite straight line, at least up to 7 kbars, dE_g/dP can be taken as roughly constant (this is justified in § 2.3) to facilitate the forthcoming calculations.

dE_g/dP at 290°K can be determined from the slope of the curve of Fig. 7.4 by taking the natural logarithm of each side of Eq. 2.8. (The slope, as opposed to the y-intercept,

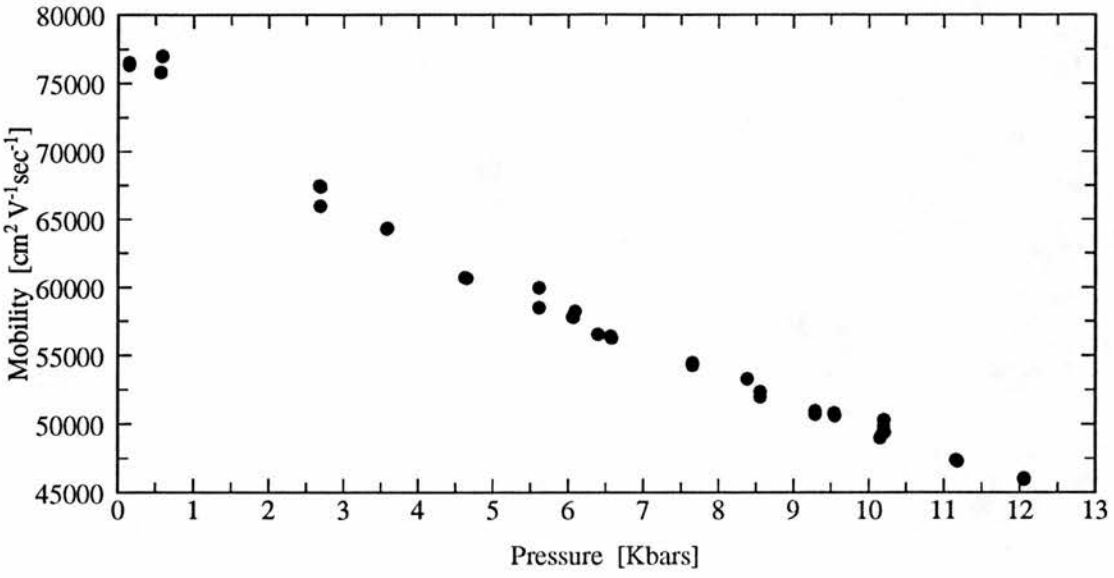

FIG. 7.3: Electron mobility in n-InSb *vs.* pressure (290°K).

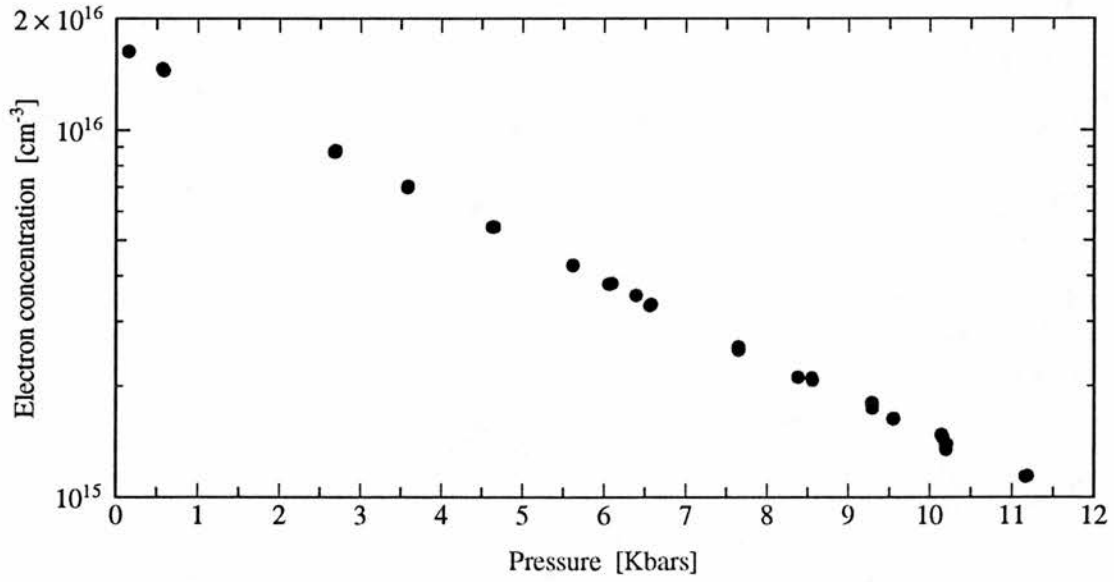

FIG. 7.4: Electron concentration (logarithmic) in n-InSb *vs.* pressure (290°K).

or as opposed to attempting a best fit, is the feature considered, as the uncertainty in n makes a close fit unwarranted, and because, as pointed out above, the dE_g/dP term will

dominate the slope). Using a value of 0.17 eV for the band-gap at 290°K, a value of $0.012\,\text{eV kbar}^{-1}$ is deduced, substantially less than the widely quoted $0.015\,\text{eV kbar}^{-1}$ of Porowski and others (although a value of $14\,\text{meV kbar}^{-1}$ deduced from cyclotron resonance measurements is quoted by HUANT ET AL., 1984). (An error in n of a constant—that is, pressure-independent—multiplicative factor, due for instance to an error in sample thickness or temperature measurement, would not account for this discrepancy. r_H, however, could be pressure-dependent, and therefore could conceivably alter the slope of ln n *vs.* P.)

Eq. 2.8 can also be invoked to determine a value for m_e^{DS} at 290°K of 0.016. In principle, this would allow Eq. 2.7 to be used to determine a Fermi energy at 290°K of −0.028 eV. (In fact, this value for ϵ_F results from using Eq. 2.3 as well). However, if this value is substituted with the value of m_e^{DS} above into Eq. 2.5, a value for n emerges of 1.47×10^{16} cm^{-3}, in disagreement with the initial value of n by ~10%. This illustrates the limited applicability of Eq. 2.7, especially when the Fermi energy is very close to the conduction band.

Using the derivative of Eq. 2.17 with respect to pressure and the zero-pressure band-edge mass of 0.013 at 290°K, various values for dm_0^*/dP can be determined:

$$\frac{dm_0^*/dP}{m_0} \times 10^4 = \begin{cases} 10.56 & \text{at 0 kbar} \\ 10.08 & \text{at 6 kbar} \\ 9.72 & \text{at 12 kbar} \end{cases} \qquad \text{at 290°K.}$$

7.2 Results at 77°K

The sample was cooled to 77°K, pressurized to ~13.5 kbar and depressurized. These data can be analyzed in a set of calculations similar to those just displayed above.

Fig. 7.5 shows that at 77°K, n at ambient pressure is $\sim 10^{14}\,\text{cm}^{-3}$. Using a 77°K value for the band-gap of 0.228 eV and an approximate value for m_e^{DS} of 0.014, Eq. 2.8 gives a value for n of $\sim 2 \times 10^9\,\text{cm}^{-3}$. This implies that the semiconductor is not intrinsic at this temperature, and therefore neither m_e^{DS} nor ϵ_F can be evaluated by the above methods. The following values of dm_0^*/dP result from assuming the value of 0.014 for m_0^* (STRADLING AND WOOD, 1968), and by assuming that dE_g/dP is temperature-independent:

$$\frac{dm_0^*/dP}{m_0} \times 10^4 = \begin{cases} 8.43 & \text{at 0 kbar} \\ 8.10 & \text{at 6 kbar} \\ 7.86 & \text{at 12 kbar} \end{cases} \qquad \text{at 77°K.}$$

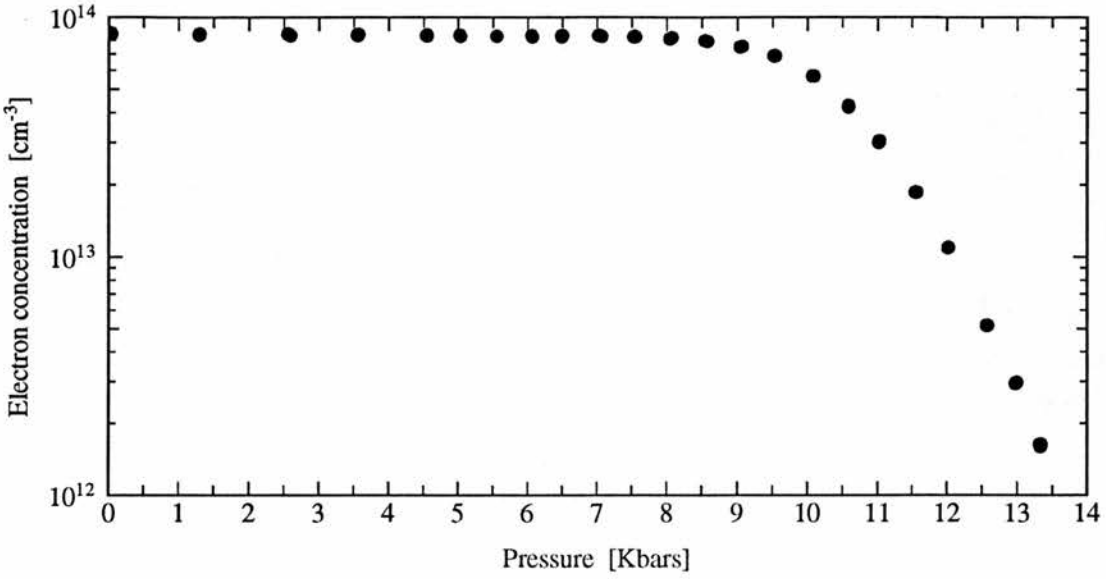

FIG. 7.5: Electron concentration (logarithm) in n-InSb *vs.* pressure (77°K).

While room-temperature mobility is dominated by polar optical scattering (although the deformation potential scattering of acoustic phonons also plays a significant role), these mechanisms are secondary at 77°K to charged impurity scattering. Electron mobility tends to decrease with increasing pressure due to the concomitant increase in electron effective mass and decrease of the dielectric constant.

Comparing Figs. 7.3 and 7.6 illustrates that while at 290°K the drop in mobility with increasing pressure is the only visible trend, at 77°K, mobility, overall much higher than at 290°K, begins to rise at high pressure, due to the freeze-out of impurity ions as the band-gap increases. In fact, charge-center-scattering-limited mobility (μ_{CC}) may at times be used to determine, via the Brooks-Herring or Conwell-Weisskopf formulae, for instance, the concentration of ionized impurities (see Chapter II).

However, in the present case this exercise is complicated by the fact that, as seen in Fig. 7.7, the mobility increases with decreasing temperature, even though no more impurities are freezing out.

Because Fig. 7.5 shows a virtually constant n ($\sim 10^{14}\,\mathrm{cm}^{-3}$) at the lowest few kilobars, it is apparent that in this region the donors and acceptors are all ionized, and therefore that $n = N_D - N_A$, where N_D and N_A are the donor and acceptor concentrations, respectively.

In Fig. 7.6, the mobility can be seen to decrease with increasing pressure, as explained

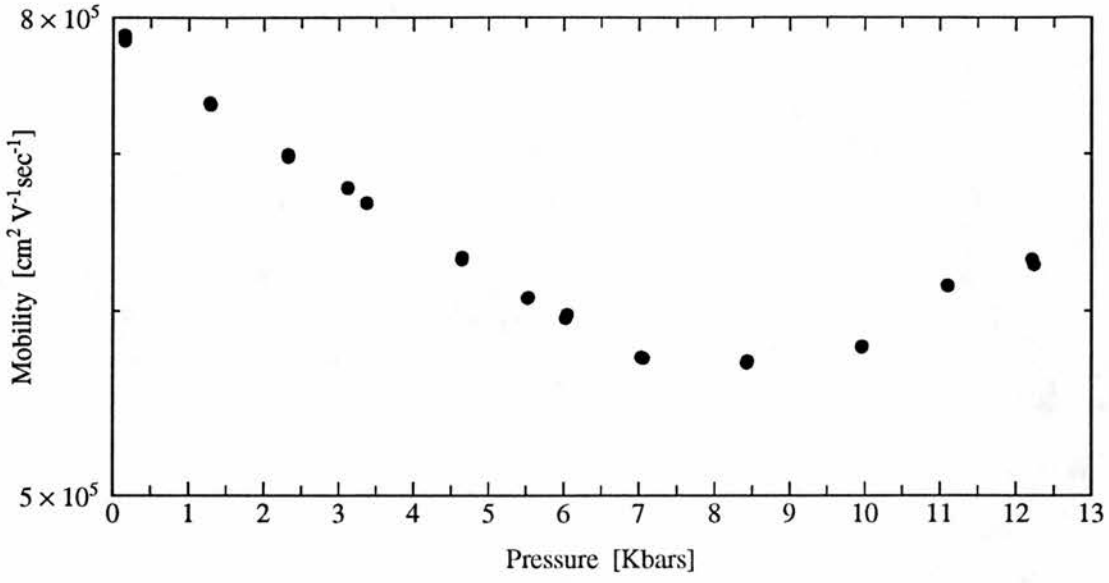

FIG. 7.6: Electron mobility (logarithm) in n-InSb *vs.* pressure (77°K).

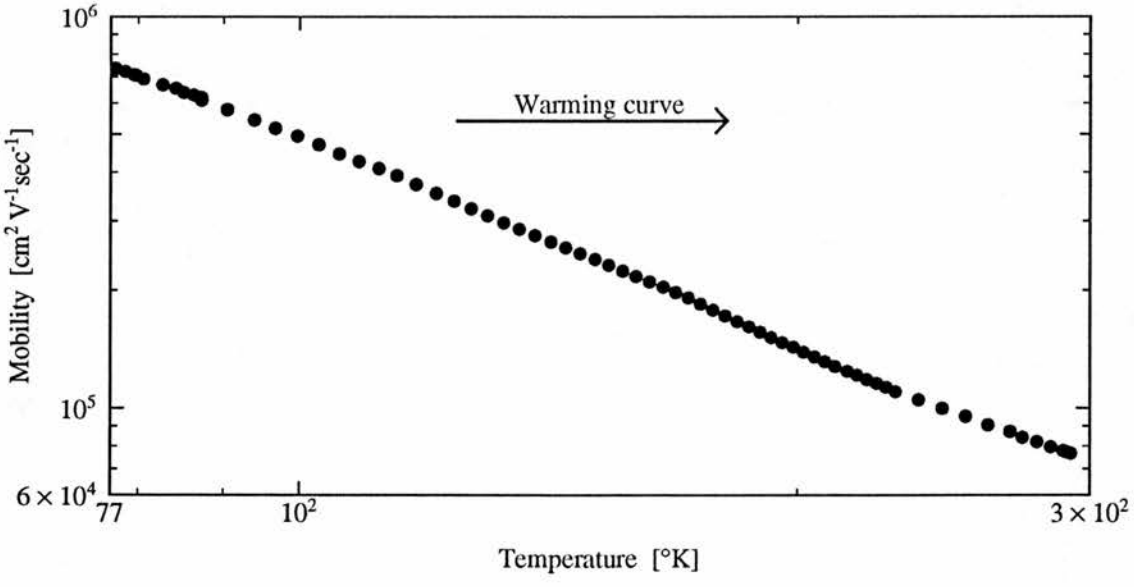

FIG. 7.7: Electron mobility in n-InSb *vs.* temperature (logarithm of each): Warming curve at ambient pressure.

above, until about 9 kbar. Beyond this point, as donors begin to freeze out, and ionized impurity scattering is diminished, the mobility increases, eventually plateauing roughly at

its value at 5 or 6 kbar of $\sim 630,000\ \mathrm{cm^2\,V^{-1}sec^{-1}}$.

If the equations of Chapter II linking ionized impurity-limited mobility to donor concentration (Eqs. 2.36, 2.38, 2.39 and 2.41, for example) were correct, N_D and N_A could be deduced from Fig. 7.6 as follows: At zero pressure, none of the impurities have frozen out, so the total number of scatterers is $N_D + N_A$. It is also known that $n \approx 10^{14}\,\mathrm{cm^{-3}}$ and that $\mu \approx 780,000\ \mathrm{cm^2\,V^{-1}sec^{-1}}$. Using the Brooks-Herring model, for instance, assuming Eqs. 2.38 and 2.39 were valid in this regime, and using Eqs. 2.3 and 2.5 to determine m_e^{DS}, it is found that $\beta_{BH} = 13.6$ and $N_I = N_D + N_A \approx 1.4 \times 10^{15}\,\mathrm{cm^{-3}}$. Since $N_D - N_A = 10^{14}\,\mathrm{cm^{-3}}$, one could conclude that N_A and N_D were $\sim 6.5 \times 10^{14}\,\mathrm{cm^{-3}}$ and $7.5 \times 10^{14}\,\mathrm{cm^{-3}}$ respectively. This is probably too high, implying that N_A and N_D are within 15% of each other.

Applying the Conwell-Weisskopf model, N_I can be found by solving Eqs. 2.36 and 2.38 self-consistently. The results in this case are $N_D \approx 5.2 \times 10^{14}\,\mathrm{cm^{-3}}$ and $N_A \approx 4.2 \times 10^{14}\,\mathrm{cm^{-3}}$, still rather close.

Finally, applying Eqs. 2.40 and 2.41, the results are $N_D \approx 5.5 \times 10^{14}\,\mathrm{cm^{-3}}$ and $N_A \approx 4.5 \times 10^{14}\,\mathrm{cm^{-3}}$.

Looking at the other extreme of the data, however, at 13 kbar where virtually all of the donors have been frozen out,* the same equations can be solved using the high-pressure values for μ, m_e^*, κ and n. However, N_I will also be different: Here, if freeze-out were complete, the original number of ionized centers, $N_D + N_A$, would have decreased by the original number of conduction band electrons, $N_D - N_A$, leaving $2N_A$ ionized sites; but there is still, according to Fig. 7.5, an electron concentration of $\sim 2 \times 10^{12}\,\mathrm{cm^{-3}}$. This figure must be added to the total number of ionized donors. Again, different models give different answers. In the Brooks-Herring model, the value for β_{BH} shoots up to almost 100, but N_A and N_D work out to be only ~ 2.7 and $3.7 \times 10^{14}\,\mathrm{cm^{-3}}$, respectively. These are less than half of the respective values calculated above based on the ambient pressure results. The enormous variation of β_{BH} gives some clue why: The bracketed term in the Brooks-Herring equation (Eq. 2.38) varies by a factor of two, while the actual change in screening is not that dramatic; once the electron concentration has fallen well below that of the scatterers, it is no longer possible for them to effectively screen themselves, so the screening term cannot be changing significantly.

Performing the same exercise with the Conwell-Weisskopf and Zawadzki-Szymańska

* The plateauing indicates that not quite all the donors have frozen out: If they had, it would be expected that mobility would have continued to drop precipitously with increasing electron effective mass.

models, one arrives at values for N_A and N_D of $\sim$3.4 and $4.4\times10^{14}\,cm^{-3}$ with the former, and $\sim$3.0 and $4.0\times10^{14}\,cm^{-3}$ with the latter. These are each higher pairs of concentrations than given by the Brooks-Herring model, but are in fact likely to be too high.

It therefore appears that none of the prominent models of CC-scattering is *alone* accurate or sufficient for the present case. If there were another significant contribution to the scattering, all of the above numbers would decrease accordingly to more realistic values. It was for this reason that the extensive mathematical exercise depicted in Appendix 2 was attempted, so that the mobility, which is also limited by PO scattering, could be modeled as successfully as in LITWIN-STASZEWSKA (1981).

7.3 Donor energy

An estimation can be made of the deep non-metastable donor energy relative to the Γ-minimum (i.e., its ionization energy) as a function of pressure. This can be done using Eq. 2.12. The resulting plot of ϵ_D vs. P, using the values of N_A and N_D derived above from the high pressure regime, is illustrated in Fig. 7.8.

At low pressures ($\lesssim$ 7 kbar) n is virtually constant as the donor is above the Γ-minimum, making deductions about the donor energy level impossible. In the high-pressure regime, however, it is apparent that the donor binding energy increases at $\sim$.01 eV $kbar^{-1}$. This is in agreement with the results of POROWSKI (1980) concerning the non-metastable donor associated with the L-minimum.

7.4 Metastable Donors

7.4.1 Metastable Donor Concentration

Presented here are some results of the Hall investigation of metastable donors. Fig. 7.9 depicts the examination of electron concentration after the sample has been pressurized to about 12 kbar at room temperature, cooled to liquid nitrogen temperature, thus trapping electrons on numerous metastable donor sites, and depressurized while at 77°K, reionizing only the non-metastable donors.

The figure shows an exponential increase in n as pressure is removed, below about 4.5 kbar. This is typical of intrinsic electron concentration (as in Fig. 7.4) as a function of pressure. However, the measured electron concentration at ambient pressure is $\sim1.8\times10^{12}$ cm^{-3}, and Eq. 2.8 indicates that the intrinsic electron concentration at 77°K in indium antimonide should be $\sim2\times10^{9}\,cm^{-3}$.

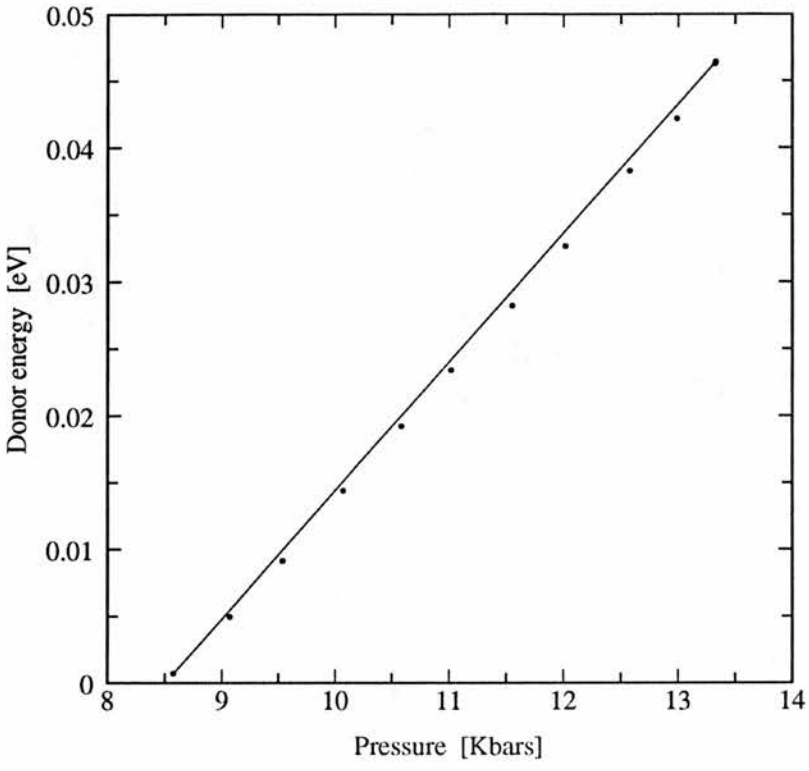

FIG. 7.8: Energy of the L-associated donor state *vs.* pressure (77°K), exhibiting a slight curvature (possibly due to other donors) against a straight line.

Eq. 2.8 does not, however, correct for the extreme nonparabolicity of the conduction band of indium antimonide. The "empirical" intrinsic electron concentration of indium antimonide as a function of temperature can be determined by "straightening out" Fig. 7.2 by plotting $\ln(n_i\, T^{-3/2})$ vs. $1000/T$, and extrapolating, as in Fig. 7.10.

A best-fit program resulted in the approximate relation

$$\ln(n_i T^{-\frac{3}{2}}) = -1.41\left(\frac{1000}{T}\right) + 33.63. \tag{7.1}$$

From this equation, n_i at 77°K would be at least $3 \times 10^{10}\,\mathrm{cm}^{-3}$ at ambient pressure, a full order of magnitude above that predicted by Eq. 2.8, but still only one sixtieth of that actually observed.

Although the liquid nitrogen used in these experiments was no more than three days old, and was kept in a closed dewar, it is conceivable that enough O_2 had been absorbed

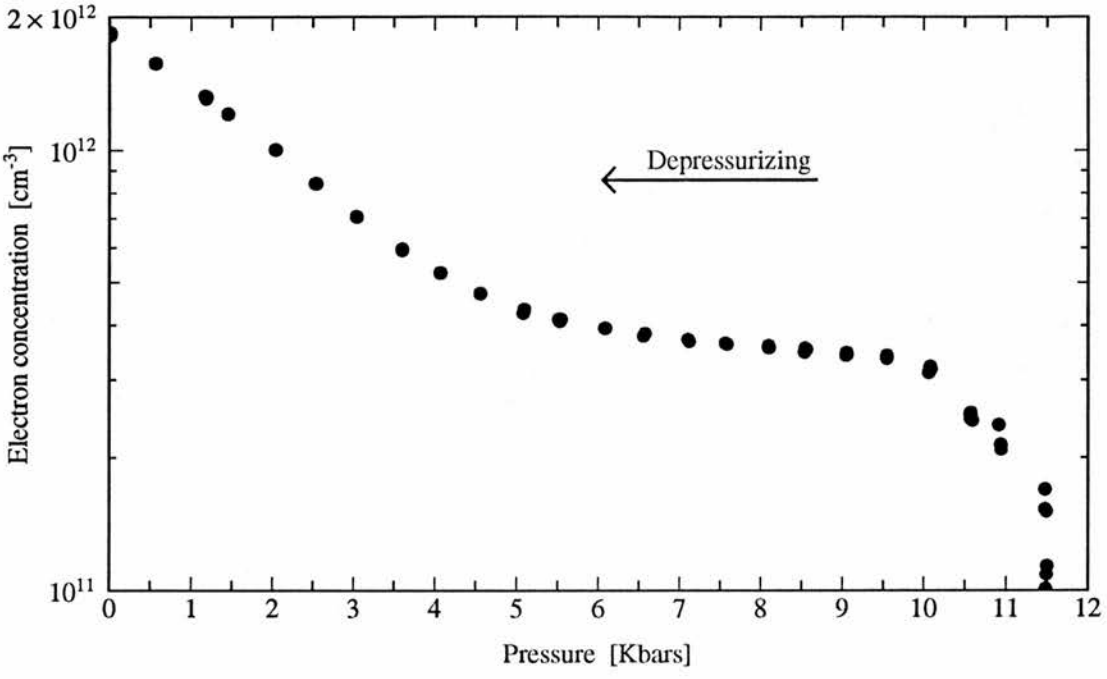

FIG. 7.9: Electron concentration (logarithm) in n-InSb *vs.* pressure (77°K): Depressurizing as indicated from 11.5 kbar, with metastable *DX* centers frozen out.

from the air to raise the temperature slightly, as no independent temperature calibration was employed. In the extreme case where virtually all the cryogen was in fact oxygen, its temperature would be 90°K. The intrinsic electron concentration at this temperature, from Eq. 7.1, would in fact be $5.4 \times 10^{10}\,\mathrm{cm}^{-3}$.* However, if the slope of the data points in the question in Fig. 7.9 is examined, it is found to be ~0.32 (on a natural log basis). On the other hand, from Eq. 2.8, one finds that the slope should be ~1.13, practically a factor of four off. While it is true that Eq. 2.8 does not correct for nonparabolicity, the slope of its logarithm is dominated by the energy gap pressure dependence. It therefore appears that this increase may be another donor species, located right at the band-edge, that is swamped in Fig. 7.5 by the presence of electrons from donor "*A*". If it is assumed that the number of these donors is governed by an $\epsilon_D/k_\mathrm{B}T$ factor, then the donor energy can be estimated as in the previous section, and it is found to decrease with pressure at a rate of ~3 meV/kbar.

* As pointed out previously, a modicum of uncertainty will persist regarding the concentration figures, as the scattering term r_H in the Hall coefficient has not been calculated; nor have various geometric factors, including the exact thickness of the sample, been precisely treated.

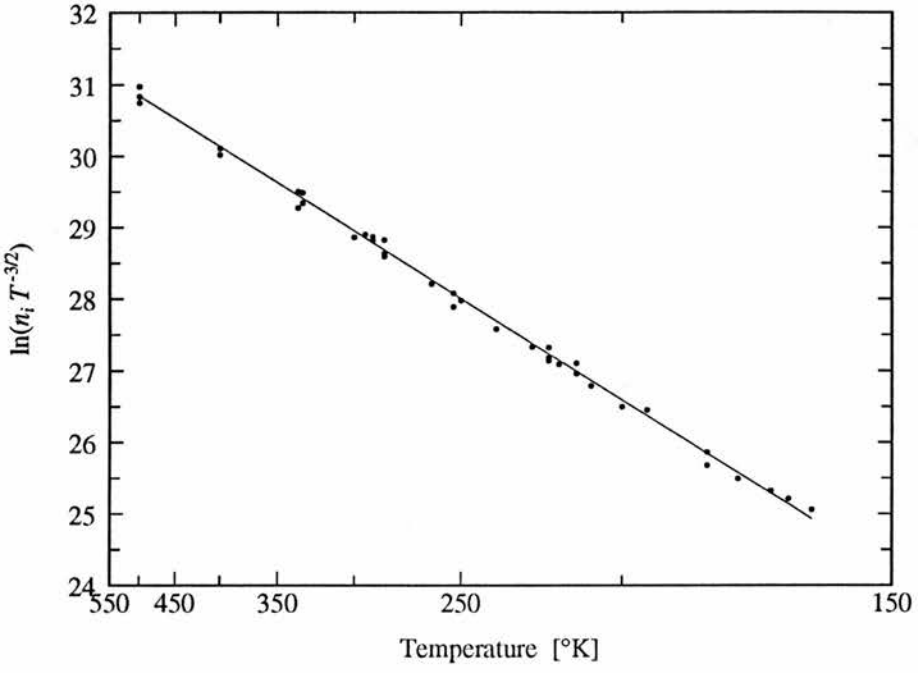

FIG. 7.10: The "straightening" of Fig. 7.2 by plotting $\ln(n_i T^{-3/2})$ *vs.* $1/T$, displaying a slight curvature (due to nonparabolicity of the conduction band) against a straight line.

This is in fact consistent with what is seen in Fig. 7.11 (see below).

In Fig. 7.11, which begins where Fig. 7.9 left off, pressure was removed from the sample at 77°K, and the sample was then rewarmed to 290°K. This result (shown in solid black circles as well in curve (B)) is contrasted with warming curves generated both at ambient pressure (curve (A)) and at constant high pressure (curve (C)).

Curve (C) resulted after the sample had been fully pressurized at ambient temperature, and then cooled with liquid nitrogen (the gas-generated pressure on the sample ranged from 11 kbar at 77°K to 12 kbar at 290°K). The curve is shown only above 100°K. The data below this temperature have been suppressed in this figure because they, as well as those of curve (B), are dependent on the rate at which the sample was cooled, and therefore the two curves cannot be meaningfully compared. This is because, at high pressure, when the sample is cooled at any finite rate, metastable donors become occupied. At 77°K, these metastable sites have a time constant on the order of one year, and therefore do not equilibrate during the experiment. The extent to which they become occupied depends quite strongly on the rate of cooling in the neighborhood of 100°K. Because this experiment was concerned

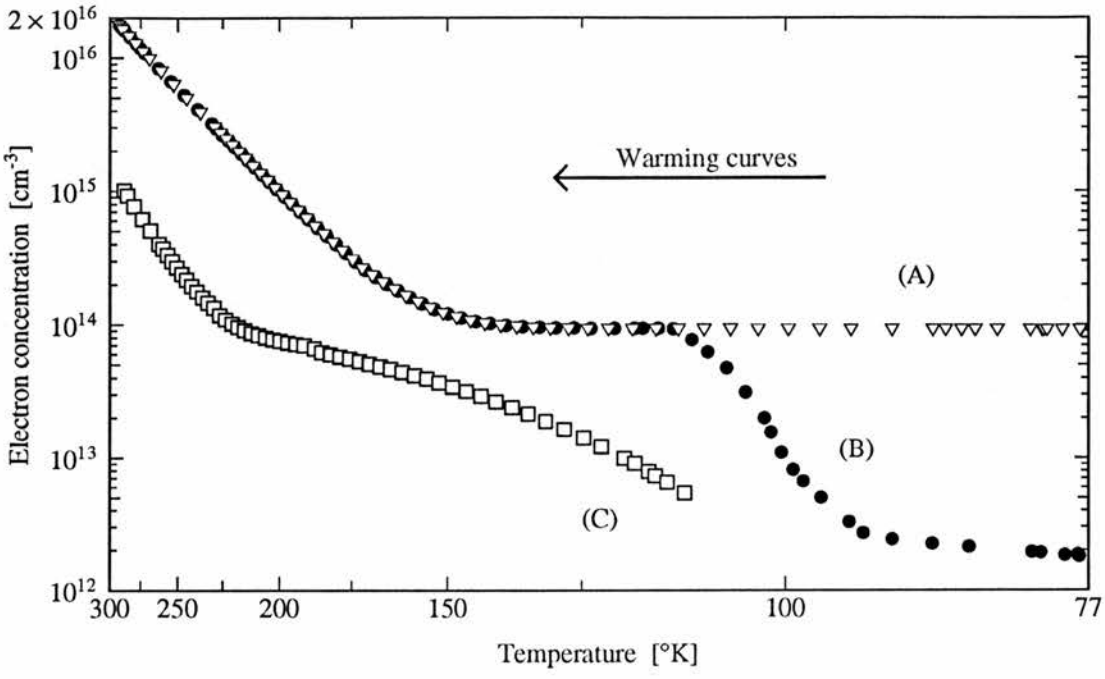

FIG. 7.11: Electron concentration (logarithm) in n-InSb *vs.* reciprocal temperature (warming curves): Curve (A) ($\triangledown$) was taken at ambient pressure, with no pressure treatment. Curve (B) ($\bullet$) resulted from depressurizing from 12 kbar to ambient pressure (see Fig. 7.9) prior to warming. Curve (C) ($\square$) was generated while approximately 11 kbar was maintained on the sample.

primarily with warming curves, cooling was effected simply by pumping liquid nitrogen into the sample insert. With rapid cooling, a large fraction of the deep lying metastable states becomes occupied. Because the donor species responsible for this metastable state is identical to that for the non-metastable state (see § 4.5), the number of available non-metastable donor sites decreases dramatically. This allows a larger number of electrons to remain in the conduction band than would be present during equilibrium cooling. Above ~110°K, in contrast, the electron transfer time to non-metastable states is $\ll$ 1 second, implying that the electrons reach thermal equilibrium well within the experimental time-frame.

An examination of curve (B) reveals a slight change in the number of carriers between 77°K and 90°K. This may be due to the increase in the intrinsic electron concentration as the sample was warmed. The observed change is $\sim 5 \times 10^{11}$ cm^{-3}, while that expected from intrinsic carriers, according to Eq. 7.1, is $\sim 10^{12}$ cm^{-3}, assuming the temperature calibration is correct. If the temperature is as widely off as speculated above, i.e., if the range in question is between 90°K and 103°K, then the electron concentration at the higher temper-

ature would be $\sim 4.4 \times 10^{12}\,\mathrm{cm}^{-3}$, almost twice that measured. Therefore, it is unlikely that the calibration is off by that much, and the possibility of a shallow donor responsible for the observed rise in electron concentration in Fig. 7.9 cannot be excluded.

Fig. 7.11 can be used to obtain a lower limit to the number of metastable donors, by subtracting the electron concentrations at each of the two plateaus in the warming curve, and by assuming that the value at the higher plateau is $N_D - N_A$. This yields $N_{D_M} \approx 8 \times 10^{13}$ cm^{-3}, meaning perhaps one third to one half of the donors had been frozen out metastably at 11 kbars, as expected from central cell results (STRADLING, 1985) (although with a high degree of compensation, it is highly unlikely that all donor "*A*" sites would be occupied). A reexamination of Fig. 7.9 reveals that at the highest pressures, the electron concentration drops precipitously, as the deepening non-metastable donor sites freeze out virtually all the remaining electrons of the conduction band, and does *not* saturate. Therefore, a small unknown number of non-metastable donor "*A*" sites remains unoccupied.

Fig. 7.12 shows the high-pressure warming curve in full, along with one taken at lower pressure: That is, the sample was pressurized to 10.2 kbar at ambient temperature, rapidly cooled to 77°K (during which time the pressure within the cell declined to 9.2 kbar) and then slowly warmed (on the order of 1°K per second). Again, at low temperatures, r_H may be changing in unknown ways, and may be contributing to the unusual apparent elevation in carrier concentration seen below 100°K.

A comparison with the results presented in Chapter IV is appropriate at this point, and Fig. 4.4 has been reproduced here for convenience. The figure, it will be remembered, shows the results of Hall measurements of an *uncompensated* sample cooled down to 77°K at a variety of "cool-down" pressures P_c, then reversibly, isothermally, pressurized and depressurized from ambient pressure to almost 14 kbars. If we assume that $r_H = 1$ for the sake of argument, then the actual electron concentration is calculated by using $R_H = 1/ne$. In curve (A), the sample has been cooled to 77°K at a variety of pressures, all below 7 kbar. In this case, all the results of sweeping through the pressure range were identical. It is seen that at ambient pressure, the electron concentration is $\sim 1.4 \times 10^{15}\,\mathrm{cm}^{-3}$, and that it decreases at the highest pressure to a saturation value of $\sim 1.1 \times 10^{15}\,\mathrm{cm}^{-3}$; in other words, $\sim 3 \times 10^{14}\,\mathrm{cm}^{-3}$ electrons have been frozen out onto non-metastable sites, which are saturated at the highest pressures. Curve (B) corresponds to a cool-down pressure of 8.5 kbar. Here, $\sim 2.5 \times 10^{14}$ cm^{-3} donors are frozen out metastably in the cool-down process, while another $\sim 5 \times 10^{13}$ cm^{-3} are frozen out reversibly on remaining sites, which again become saturated at the upper end of the pressure range. Finally, in curve (C), cool-down has taken place at 11 kbar,

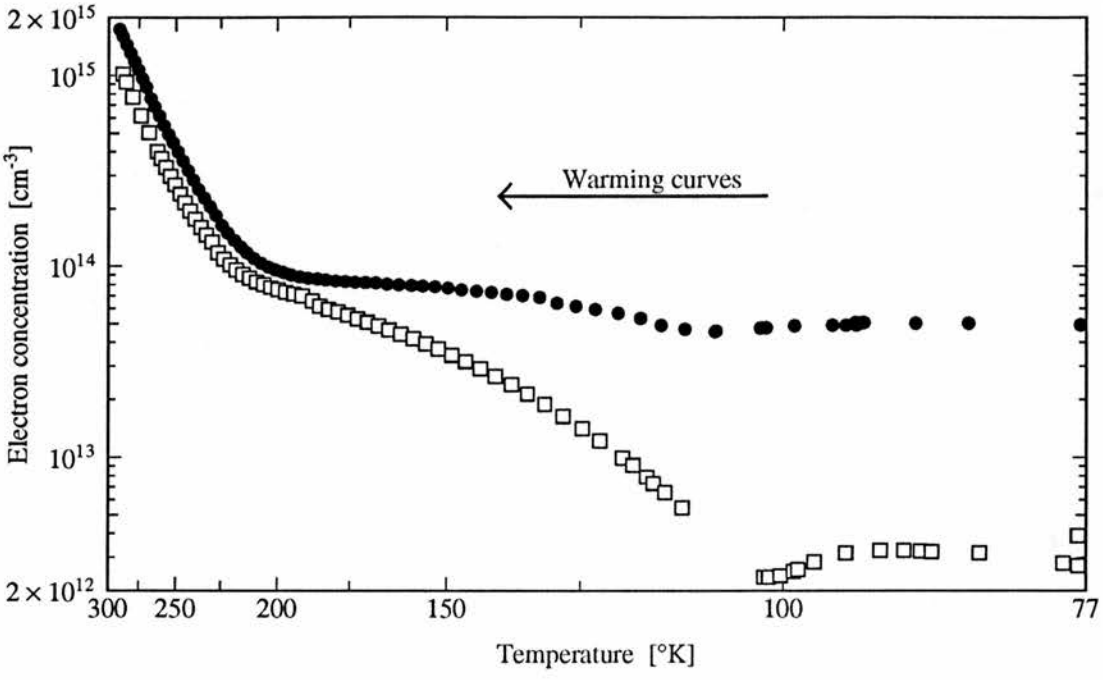

FIG. 7.12: Electron concentration (logarithm) in n-InSb *vs.* reciprocal temperature (warming curves): The lower curve (□) was generated while approximately 11 kbar was maintained on the sample. After pressurization, at room temperature, it had been non-equilibrium cooled to 77°K, preventing substantial freeze-out. The upper curve (●) shows the same process at a pressure of 9.2 kbar.

metastably freezing out practically all the sites of donor "*A*".

It must be pointed out once more that this saturation could occur *only* with *uncompensated* samples, such that there remain in the conduction band a sufficient number of electrons to completely saturate the available donor "*A*" sites. In the sample examined in the present work, the extent of compensation, as shown in Fig. 7.5, is such that at 77°K and ambient pressure, the electron concentration is fully an order of magnitude lower than in the sample depicted in Fig. 4.4 (compare to curve (A)). When, in the current work, high hydrostatic pressure was applied to the sample during cool-down (see Fig. 7.9), the electron concentration dropped a further three orders of magnitude, again showing no signs of saturation, even at the highest pressures (compare to Fig. 4.4, curve (C)).

A reproduction of **FIG.4.4** (see text).

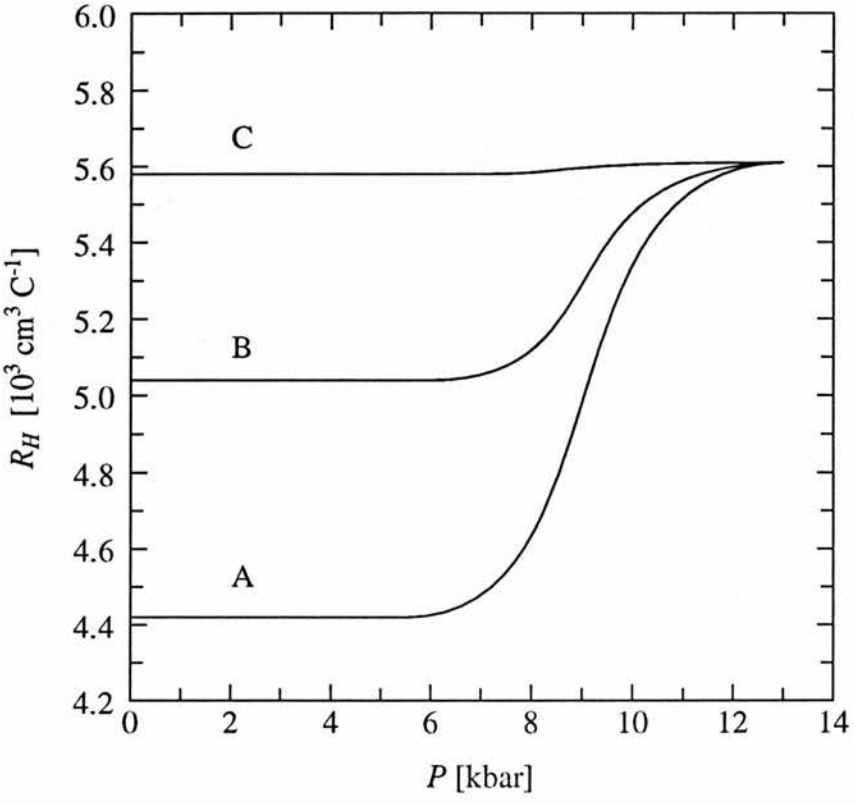

7.4.2 Mobility in the Metastable State

Mobility measurements taken simultaneously with the concentration measurements depicted in Figs. 7.5, 7.9, and 7.11 are shown in Figs. 7.13 and 7.14.

There are two salient features in these figures. Most obvious of course is the increased mobility when the metastable donors are frozen out, visible in each figure. Assuming no significant change in PO-scattering between the normal and the pressure-treated states of the sample, and ignoring neutral impurity scattering, it can be allowed that the difference in mobilities is due entirely to a difference in II scattering. This argues against the negative-U model, unless correlation of ionic scatterers is invoked, as the pairs of ionized centers would be expected to lower mobility. However, this result can be examined using the equations invoked and the results obtained above. In particular, if the change in the N_D due to metastable donors is $8 \times 10^{13}\,\mathrm{cm}^{-3}$, as discussed in the previous section, Eqs. 2.38 and 2.41 can be used to estimate the expected proportional change in mobility. If a total donor concentration

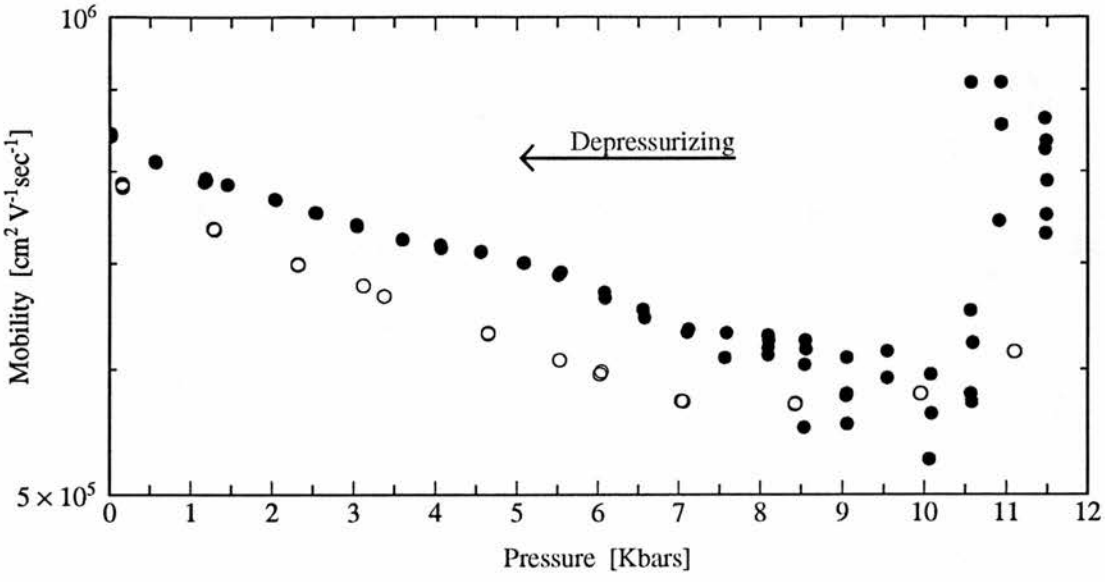

FIG. 7.13: Comparison of electron mobilities (logarithm) in n-InSb against pressure at 77°K: ●— metastable centers frozen out (see Fig. 7.9); ○— metastable centers unoccupied (reproduced from Fig. 7.6).

of 4×10^{14} cm^{-3} is assumed, metastable freeze-out would be expected to result in an increase in mobility of 25%, at least twice as large as that seen in the figure. In other words, *DX* center freeze-out is apparently not removing as many ionized centers as might be expected, thus in fact reinforcing the negative-*U* model.

Also obvious is the upturn near 12 kbar of the data points associated with metastable freeze-out. Not only is this absent in the other curve, but there is in fact a very slight apparent downturn or saturation in the non-metastable case.

A third feature is more subtle, visually, but apparently quite reproducible. Centered at ~5.5 kbars in Fig. 7.13, and at ~160°K in Fig. 7.14, is a very shallow, broad peak in the mobility. This peak appears to be entirely absent in the untreated sample at 77°K and in the high pressure curve in Fig. 7.14.

Finally, conspicuous in its absence from Fig. 7.14 is the anomalous behavior evident in Fig. 4.7 (*c*). This may imply that the sample measured in the current work is highly homogeneous compared to that of PIOTRZKOWSKI ET AL. (1986).

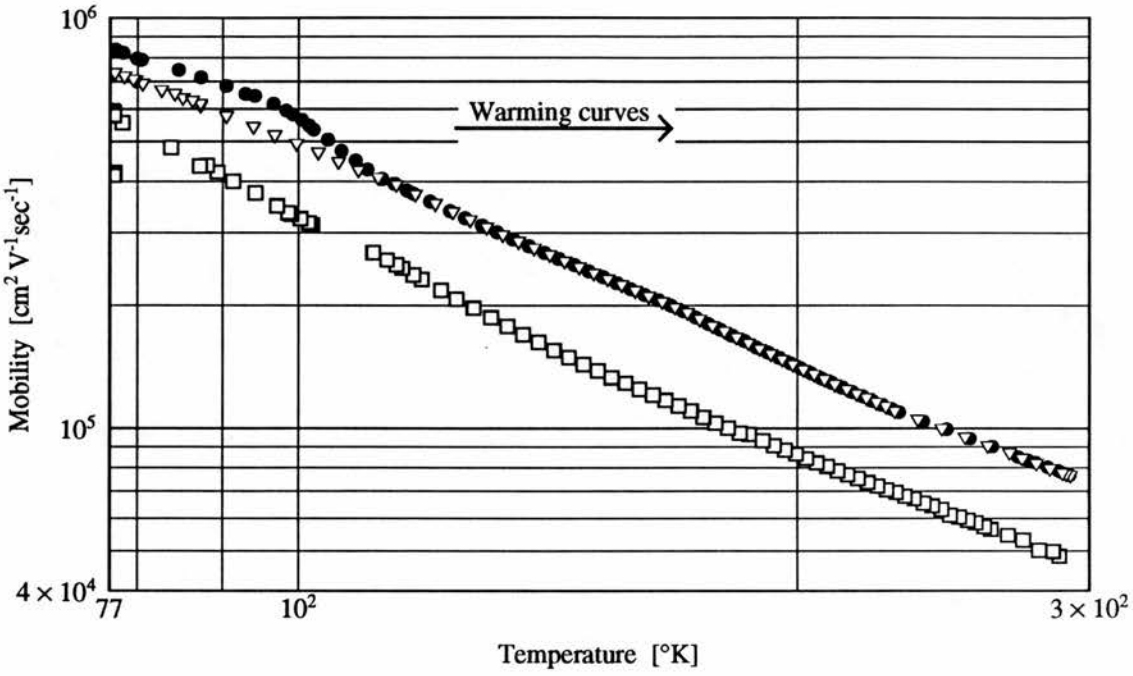

FIG. 7.14: Electron mobility in n-InSb *vs.* temperature (logarithm of each), warming after metastable cycling: Curve (A) (▽) was taken at ambient pressure with no pressure treatment; curve (B) (●) resulted from depressurizing from 12 kbars to ambient pressure (see Fig. 7.9) prior to warming; and curve (C) (□) was generated while approximately 11 kbars was maintained on the sample. (See Fig. 7.11, which concerns the same experiments as this figure. All curves are delineated by corresponding tokens and labeled accordingly.)

CHAPTER VIII

Photoconductivity in Indium Antimonide under Hydrostatic Pressure

8.1 Indium Antimonide as an Intrinsic Photoconductor

A variety of n-type indium antimonide samples was examined for intrinsic detection behavior under a range of hydrostatic pressures, temperatures and magnetic fields, as described in Chapter VI. In the initial photoconductivity experiments, n-type indium antimonide was examined at 77°K without hydrostatic pressure, and the very first samples were unetched. The photoconductive spectra (derived as explained in Chapter VI) were characteristically peaked at the band-edge (as seen, for example in Fig. 8.5, which, however, was taken at 4.2°K). This is a well-known effect in an unetched or poorly etched sample, wherein radiation of supra-gap energy is immediately absorbed within the first micron or so of the sample's surface. An unetched surface exhibits a high recombination velocity, dramatically attenuating the photoconductive (recombination) lifetime, and hence, as explained in Chapter V, the gain.

Normal etching, as described in Chapter VI, clearly improved the surface quality of the detector, and removed the band-edge peak (as in Fig. 8.3). However, at 4.2°K, even after etching, a very narrow peak at the band-edge becomes evident (see Fig. 8.5). Further, the first experiments wherein the sample was put under hydrostatic pressure (see below) also evinced this band-edge peaking, even at 77°K, thus raising the possibility of excitons or perhaps some variable surface recombination speed mechanism. This behavior was investigated as detailed in the next subsection.

The MBE-grown samples from RSRE described in Chapter VI, observed under intrinsic radiation in a magnetic field at 4.2°K, did not exhibit the peaking. This is consistent with the

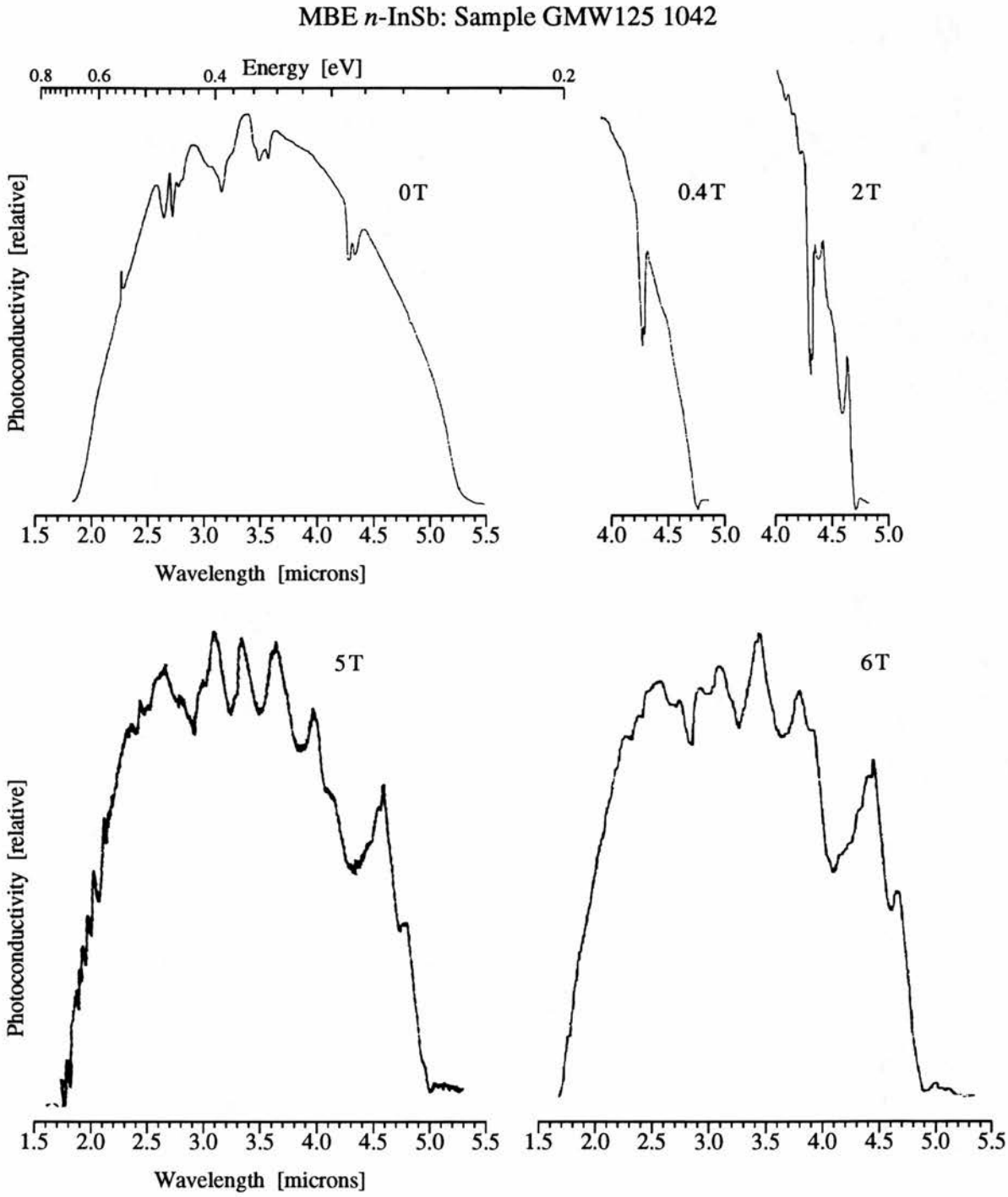

FIG. 8.1: The photoconductivity spectra of n-type MBE-grown indium antimonide on a p-type substrate at 4.2°K in several different magnetic fields, exhibiting both a band-edge shift and Landau level shifts with field. (See Fig. 8.2.)

notion of the peaking arising from surface damage, as an epitaxial surface would be expected to be largely damage-free. However, also missing from the spectrum (see Fig. 8.1 at 0 T) was a sharp absorption edge, possibly indicative of either damage or strain, although the substrate was *p*-type indium antimonide, so lattice matching was not the problem. Unlike any bulk samples observed in this work, the MBE samples exhibited photoconductivity oscillations as the wavelength was varied, as indicated in Fig. 8.2. A comparison of the positions of these peaks and valleys with the magneto-optical transmission data reported in indium antimonide by PIDGEON ET AL. (1967) reveals the dependence of the photoconductivity signal on the absorption of the sample, with the oscillations reflecting the Landau level spacing. Oscillations are in this case visible because the epilayer was only 1 μ thick: Normally, these oscillations are "ironed out" by virtue of the over-absorption of the bulk, even in the 3-5 μ thick slice.

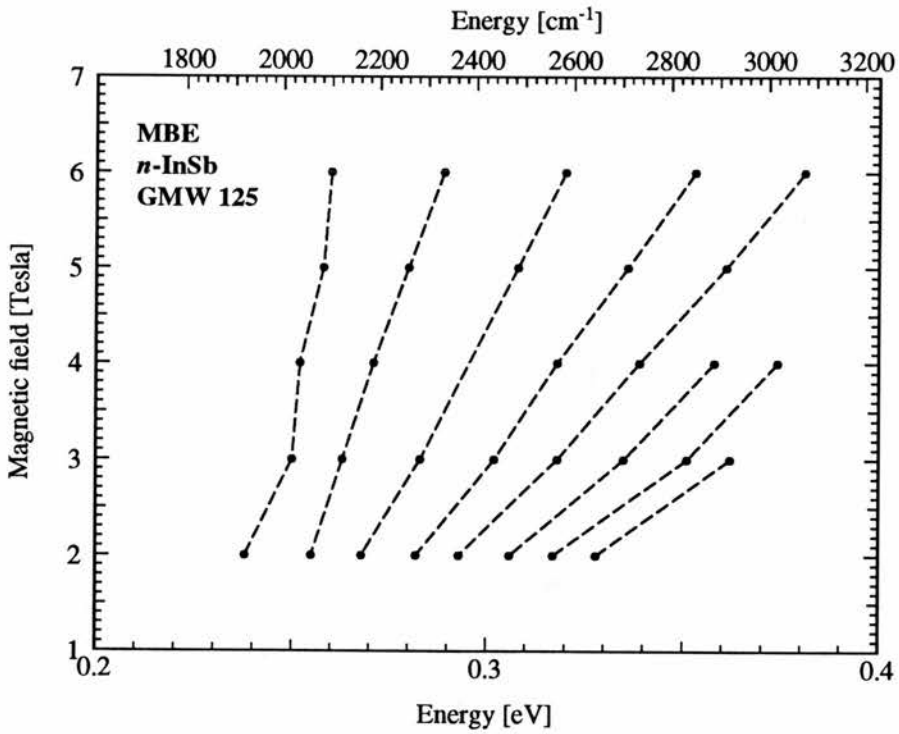

FIG. 8.2: The positions of the "valleys" in the photoconductivity spectra of Fig. 8.1 *vs.* B, corresponding to successive Landau levels. The curvature results from the extreme nonparabolicity of the conduction band.

8.1.1 Intrinsic Photoconductivity with Hydrostatic Pressure

The first spectra of indium antimonide photodetection under hydrostatic pressure obtained with the gas compressor were at the very lowest pressures, e.g., ~1 kbar (see Fig. 8.3). It is apparent in the figure that modest pressure has brought about a four-fold increase in responsivity.* At these low pressures, the resistivity of the sample was found to remain fairly constant as pressure was increased. According to the simple model presented in Chapter V, it would appear that the concomitant increase in responsivity would therefore be due to an increased electron recombination lifetime. This increase is possibly due to hydrostatic pressure-induced variation of the energy of hole-traps (as seen by PIOTRZKOWSKI, 1984 in a similar sample of indium antimonide, in which a similar increase in photoresponse occurred at ~3 kbar).

At slightly higher pressures, however (see Fig. 8.4), the sample exhibits an intense band-edge peaking accompanied by a severe attenuation of the remainder of the spectrum, thus behaving like an unetched sample.

A further interesting feature in these spectra was the appearance beyond the band-edge of a large response peak, ostensibly due to carriers from impurities (see Fig. 8.4*b*). The smaller peak and absorption at slightly lower wavelength appears to have been attenuated somewhat by the coincidence at this point of the CO_2 absorption, which in this experimental set-up could not be removed entirely. Therefore the true relative intensities of these spectral features are difficult to appraise. Why this extrinsic peak should show so intensely at 4.4 kbar, and not, for example, at 3.5 kbar, is not clear.

Experiments were conducted in which a sample of indium antimonide was simultaneously subjected to hydrostatic pressure and to magnetic fields up to 6 T (such as in Fig. 8.5). At ambient pressure, it was seen that the peak position deepens at a rate of ~3 meV/T, while the band-edge deepens at ~4 meV/T. This would not exclude excitonic behavior, though the existence of excitons in indium antimonide at 77°K, where the thermal energy is about three times as great as the excitonic binding energy at zero field, was viewed with some skepticism. Furthermore, the rate of deepening observed was only about two thirds that predicted using the model of nonparabolicity-corrected excitonic energies developed by JOHNSON (1967) and VREHEN (1968).

* In this figure and in subsequent ones, NIR spectra have not been normalized with respect to the blackbody spectrum of the globar source.

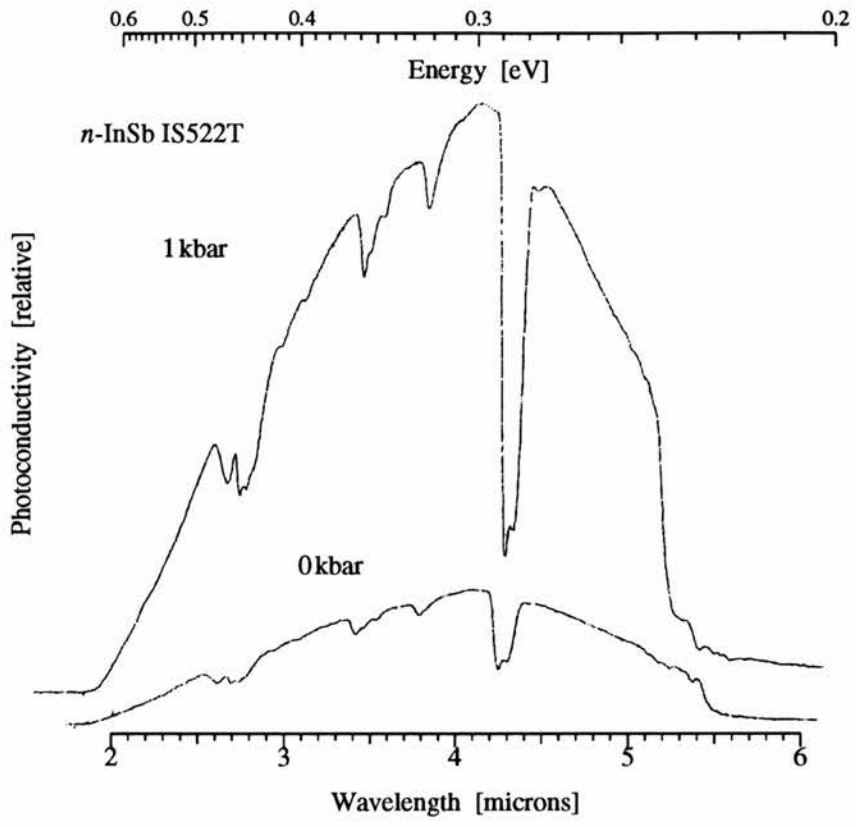

FIG. 8.3: The effect of 1 kbar hydrostatic pressure on the photoconductive response of n-InSb at 77°K to near infrared radiation. The spectral amplitudes are shown to scale, with a slight vertical displacement.

Another possible explanation of the peaking was proposed by WASILEWSKI. A sample which is etched enough to not *spectrally* exhibit surface recombination at ambient pressure may nonetheless possess a damaged surface: The recombination lifetime in the bulk is sufficiently short to become the limiting factor; i.e., the low recombination speed at a good surface allows carriers to recombine in the bulk. On the other hand, when hydrostatic pressure is applied and the bulk lifetime is extended because of trap freeze-out, the limiting factor may be the surface recombination time.

However, were this the case, the amplitude of the "attenuated" portion of the high pressure peaked spectrum would still be expected to exceed that of the zero pressure spectrum. In Fig. 8.4, not only is the responsivity at short wavelengths lower than for an unpressurized sample, but the signal-to-noise ratio has obviously suffered as well.

Alternatively, a model wherein the surface recombination speed changed with both tem-

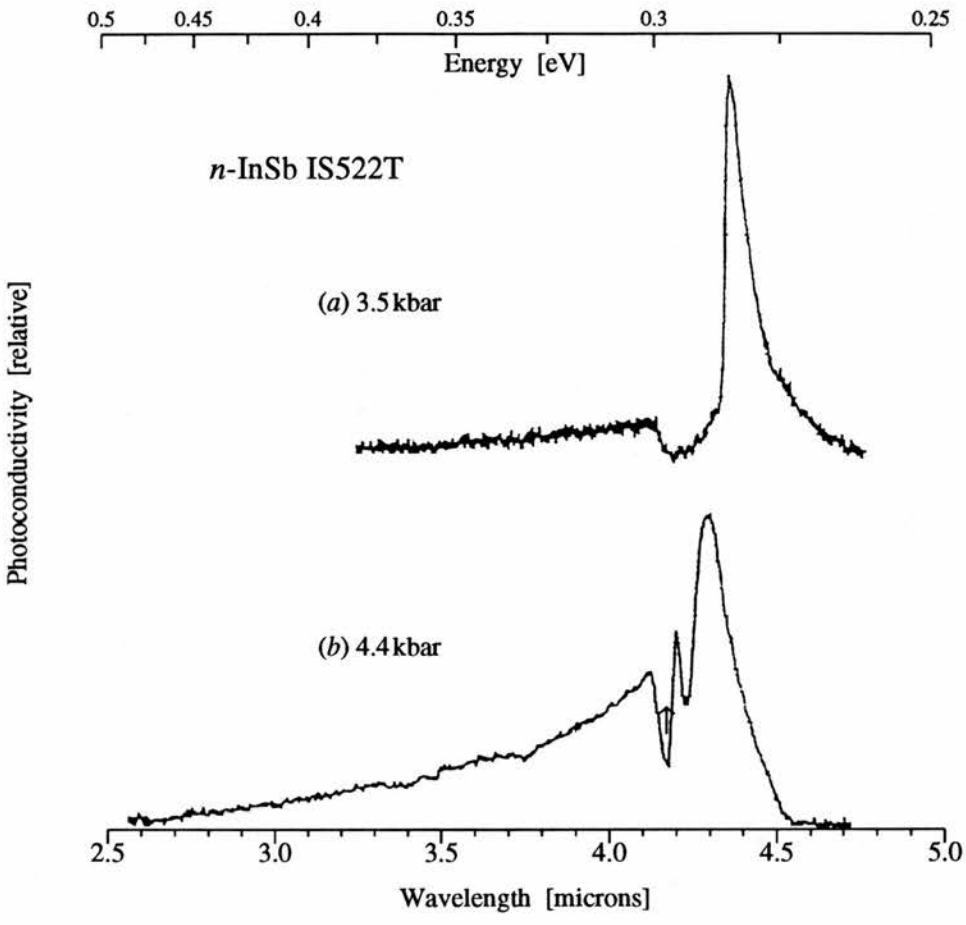

FIG. 8.4: Photoconductive response of n-type indium antimonide under approximately (*a*) 3.5 kbars and (*b*) 4.4 kbars of helium pressure at 77°K. In (*b*), the arrow marks the approximate position of the band-edge (as determined from the applied hydrostatic pressure, which was seen to predict the band-edge position to within ~1%), implying the large peak in response to its right may be extrinsic photoexcitation.

perature and pressure was proposed. In order to minimize the effects of damage, however minimal and however deep, therefore, a sample of indium antimonide (IS520T) was etched down to a thickness of only 5 μ, thus removing about 50 μ of material after the slice was cut from the wire-saw. Because the petroleum spirits used in the liquid cell absorbs strongly in the near and mid-infrared, it was decided to use the gas pressure system (described in Chapter VI) to avoid spurious or confusing absorptions in the spectrum. With these modifications in the set-up, a detector was produced which exhibited a greatly increased responsivity at

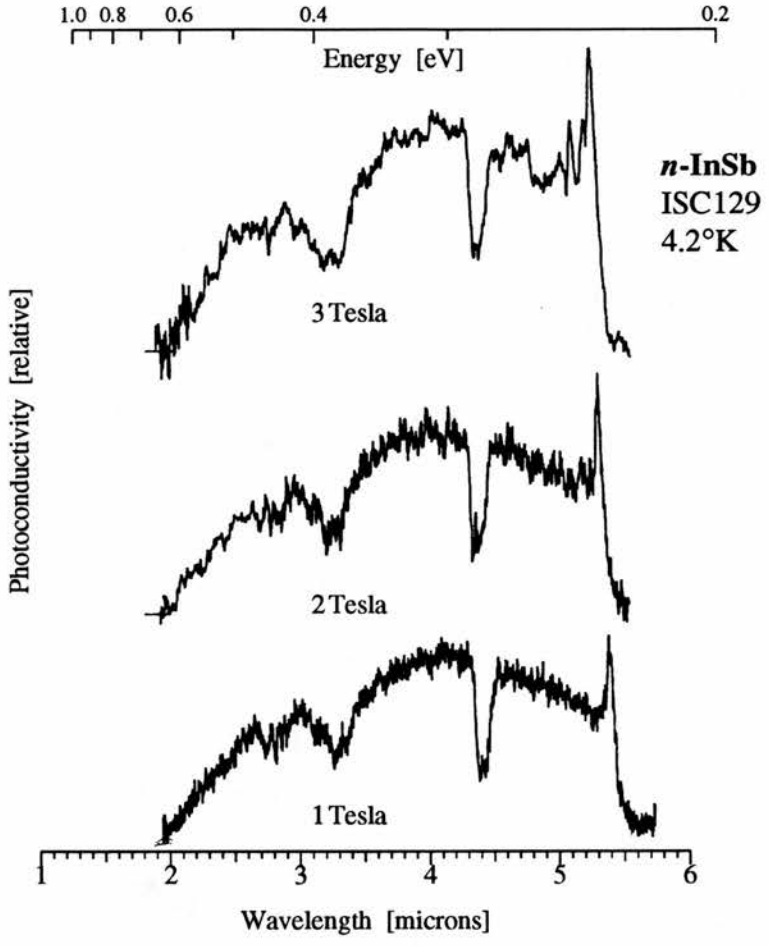

FIG. 8.5: The figure shows the shift with magnetic field of the band-edge peak in a sample of indium antimonide at 4.2°K. As noted in the text, the rate of shift does not correspond closely to that of an excitonic peak.

$\sim$10 kbar relative to that at ambient pressure, and which showed no band-edge peaking at all, thus apparently confirming that the peaking had resulted from surface damage. The spectra obtained in these runs are shown in Fig. 8.6.

The responsivity at 2.9 μ of the sample is seen in this case to increase upon pressurization to 12 kbar by approximately two orders of magnitude, though this was observed to vary substantially from sample to sample. In all cases, the resistivity of the sample was observed to increase over this pressure range by roughly the same amount, which is to be expected from the fact that the photoconductive gain is proportional to $\Delta\sigma/\sigma_0$ (as discussed in § 5.1); however, the change in responsivity was in some cases a factor of two or three higher still (perhaps on account of increased recombination lifetimes, as mentioned above with

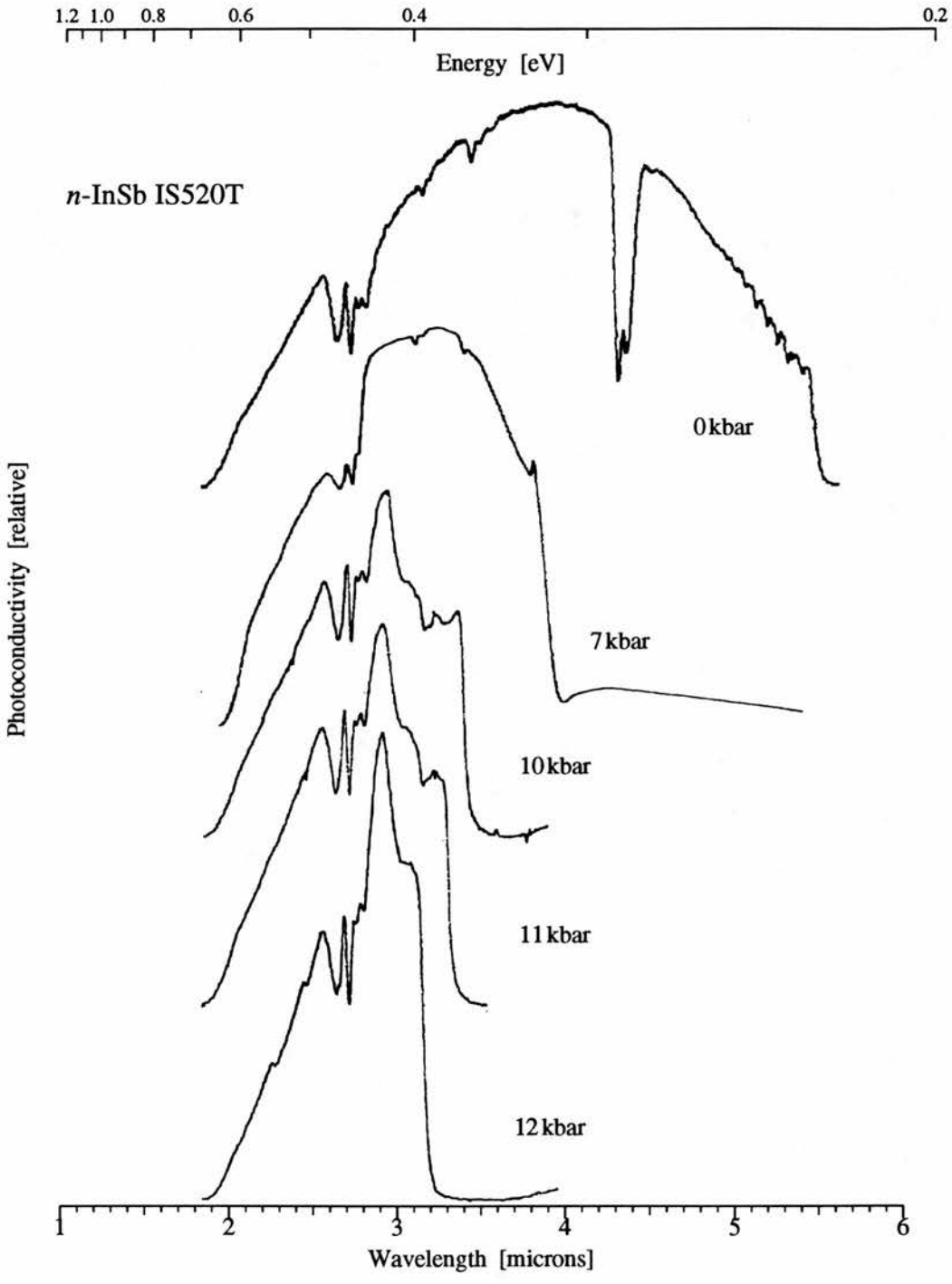

FIG. 8.6: NIR photoconductive spectra taken at high hydrostatic pressure: While the ambient pressure run, shown for comparison, exhibits the spectral envelope of the blackbody source, the higher pressure runs ($\gtrsim 5$ kbar) feature an apparent absorption at $\sim 3\,\mu$ which does not shift with pressure, and which appears in the metastable state as well, as in Fig. 8.7. The responsivity of the sample at $2.9\,\mu$ at 12 kbar is approximately 100 times that at ambient pressure, as is the resistivity.

regard to Piotrzkowski's results), while at other times it was lower, perhaps on account of mechanically induced damage.

8.1.2 HPFO in an Intrinsic Detector

The near-infrared spectrum of indium antimonide in a metastable HPFO (high pressure freeze-out) state is shown in Fig. 8.7. In this case, the sample had been pressurized to 12 kbar, cooled to 77°K, and depressurized while cold. The two salient features of this result are the appearance of an absorption at ~0.4 eV, and an increase in the sample resistivity to ~350 Ω. After warming and recooling at ambient pressure, the resistance dropped to ~110 Ω (about 10% higher than the original resistance), and the normal blackbody spectrum-shaped response curve was restored.

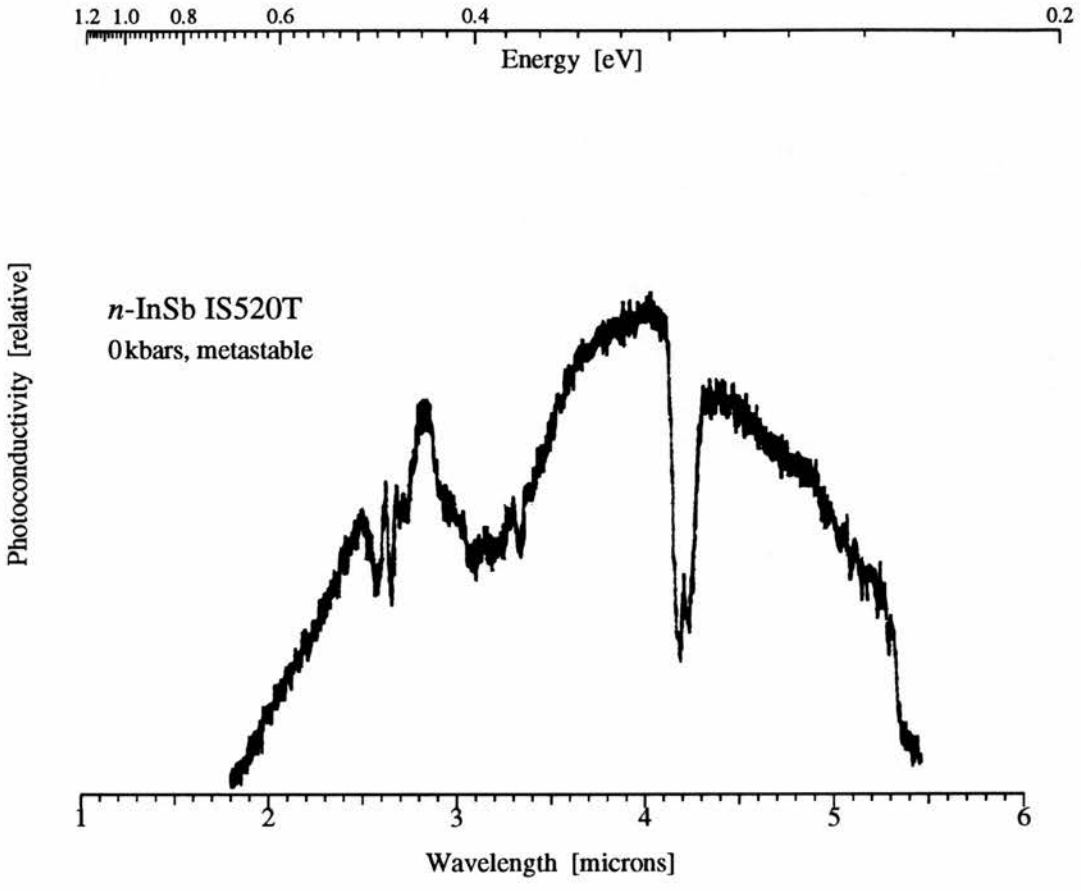

FIG. 8.7: NIR spectrum of indium antimonide in the metastable HPFO state at 77°K, 0 kbar, after being pressurized at room temperature to 12 kbar.

The behavior the resistivity exhibits is quite different from that expected from the sample examined in the previous chapter, IS522T, even though the two samples appeared to be similar. In particular, the product of the mobility and the electron concentration of sample IS522T when in the metastable state would be approximately 1/30th that in its normal state, implying a resistance an order of magnitude higher during metastable freeze-out than that actually seen with IS520T.

8.2 Cyclotron Resonance in Indium Antimonide under Hydrostatic Pressure

Here follows a discussion of the effects of hydrostatic pressure on cyclotron resonance linewidth, as observed in three samples of n-type indium antimonide: 6-98(16), IS520T and IS522T. As mentioned in Chapter VI, the last of these samples (the Hall characterization

of which was the subject of Chapter VII) had displayed a dramatic cyclotron resonance narrowing over a fairly wide range of applied pressures, in contrast with the first of the samples, which, while displaying the narrowing (WASILEWSKI, 1982), became too noisy at 4.2°K above 8 kbar ($\gtrsim 10\,\mathrm{M}\Omega$) to observe signal in (see discussion below); and at lower pressures, there had been no noticeable narrowing. The middle sample, IS520T, with Hall characteristics approximately equal to those of IS522T, was examined for comparison.

Measurements of cyclotron resonance linewidth must proceed with some care, as there are several variables involved. Particular care must be taken to minimize lattice or carrier heating by the electric field or from the absorption of laser radiation. Experimentally, for instance, as was remarked in Chapter III, linewidth is dependent on lattice temperature, though only above ~30°K. While this would not at first sight appear to pose a problem in the current work, where all measurements were conducted in the bore of a liquid helium-cooled superconducting magnet, an anomalous linewidth due to carrier warming *can* in fact arise. When such carrier warming was clearly present, the results were discarded.

By virtue of the experimental set-up, i.e., constant wavelength excitation and varying magnetic field, there is some distortion of the cyclotron resonance peak away from a true Lorentzian lineshape. Furthermore, in high magnetic fields, increasing numbers of electrons freeze out onto impurity sites, changing the nature of the sample being observed (see discussion in § 3.3.1).

Another major experimental determinant of cyclotron resonance linewidth in n-type indium antimonide is the precise conditions of cooling; in particular, the rate of cooling in the region of 100°K when the sample is under pressure $\gtrsim 7$ kbar (see discussion in the previous chapter). Varying cooling rates lead to differing amounts of freeze-out, affecting, predominantly, the ionized impurity concentration in the bulk (low conduction band electron concentration is not an important variable), which influences linewidth (see Chapter III) approximately as $N_{\mathrm{II}}^{1/2}$. As explained in Chapter VI, once the "bomb" was pressurized, the magnet insert was immediately immersed in a liquid nitrogen dewar to prevent deformation and loss of pressure, and to conserve liquid helium. While the procedure itself was highly uniform, the magnitude of the variation in frozen-out electron concentration in this method has not been evaluated.

A final experimental variable of potentially great influence on linewidth is the applied bias. Biases were kept as low as possible to avoid hot electron effects, but minimum biases were necessary in order to overcome background noise, photovoltaic effects, etc. No measurements of linewidth against bias were conducted at ambient pressure, but IS520T was

pressurized to ~10 kbar in order to see the effects at high pressure. The results are plotted in Fig. 8.8, while the spectra themselves are visible in Fig. 8.9.

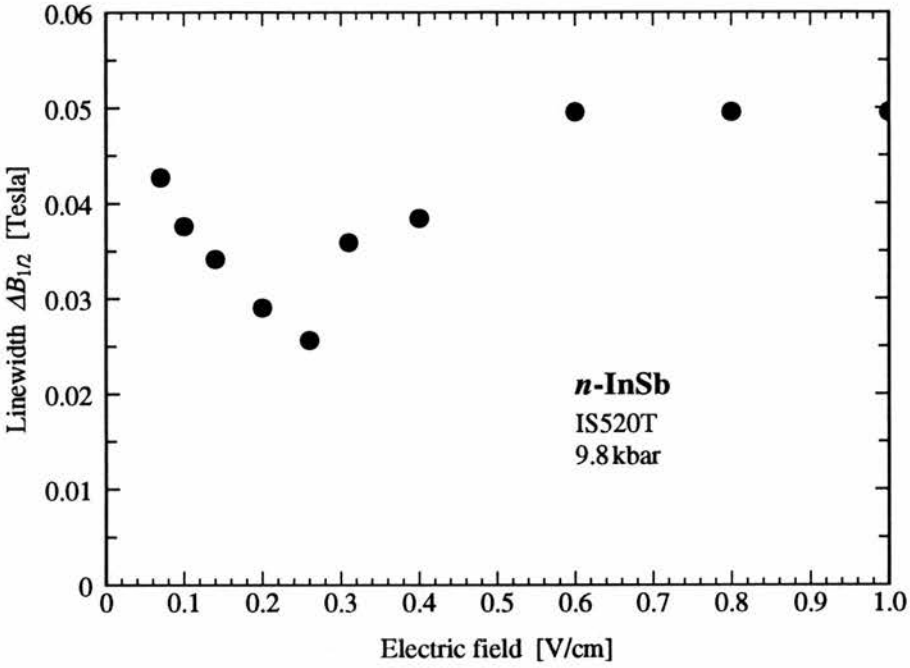

FIG. 8.8: Cyclotron resonance linewidth *vs.* approximate electric field in n-type indium antimonide at ~10 kbar. The linewidths are those measured on the low-field side of the right-hand (cyclotron resonance) peaks of Fig. 8.9.

Hot electron effects are somewhat moderated at 10 kbar because of the large increase in effective mass. It is rather surprising to see a *decrease* in linewidth, however, up to 260 mV/cm, possibly due to the prevalence of small angle ballistics or increased screening.

Fig. 8.10 shows the variation of responsivity for the same data, as measured simply by the height of the cyclotron resonance line in Fig. 8.9, against electric field.

According to PUTLEY (1965), the responsivity varies with applied bias in proportion to the quantity βV, where β is the variation of conductivity with electric field, $(1/\sigma)[d\sigma/d(E^2)]$, and V is the applied bias. Furthermore, higher order terms of E are expected to enter the dependence when $E > 0.1$ V/cm. As seen in Fig. 8.10, there is a strong power curve dependence in responsivity up to ~400 mV/cm, beyond which point, apparently, hot electron effects dominate. In fact, a best-fit revealed an $E^{3.4}$ dependence. Unfortunately, no analytic expression for the electric field dependence of a Putley detector is available for comparison.

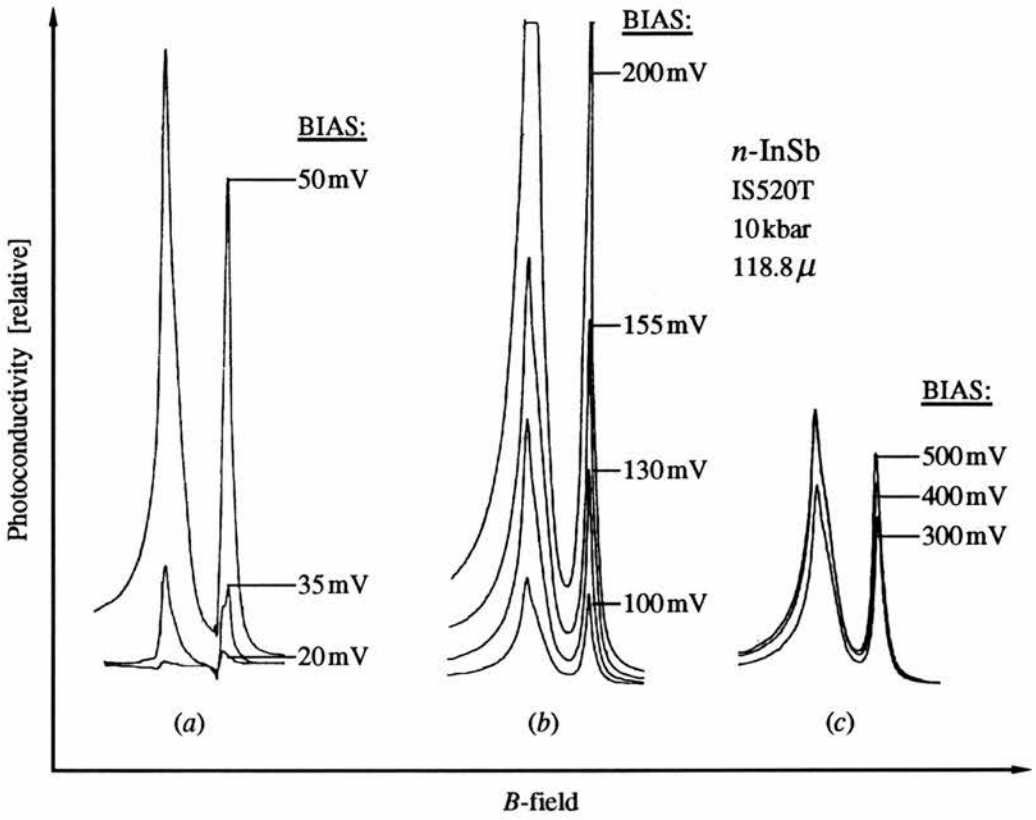

FIG. 8.9: Cyclotron resonance at 118.8 μ in n-type indium antimonide at ~10 kbars varying with bias. The sample dimensions are ~5 mm × 5 mm × 0.2 mm, with the bias applied along the greater dimensions. The curves at the lowest biases (in (*a*)) show some distortion due to photovoltaic effects. (*a*), (*b*) and (*c*) are each on different vertical scales. The variation of responsivity with bias is plotted in Fig. 8.10.

Other complications in measuring resonance linewidths involve the fundamental physics of the semiconductor itself. Because of the nonparabolicity-induced inhomogeneity of the line-broadening, for instance, it is difficult to appraise a "true" cyclotron resonance linewidth, i.e., one that is determined purely by τ_{CR}, the relaxation time described in § 3.3. To minimize the uncertainty, the linewidth was *often* measured based on the low-field halfwidth of only the cyclotron resonance peak, which is reasonably accurate for collision time estimation (STRADLING[b]). However, appraising this width from the combined signal trace of two partially resolved pseudo-Lorentzian curves can be deceptive, in that the FWHM of the actual individual resonance is considerably smaller than that apparent from the sum trace. For this reason, a large number of sums of two (homogeneous) Lorentzian curves were computer-generated in order to produce output replicating the experimental trace. This output was

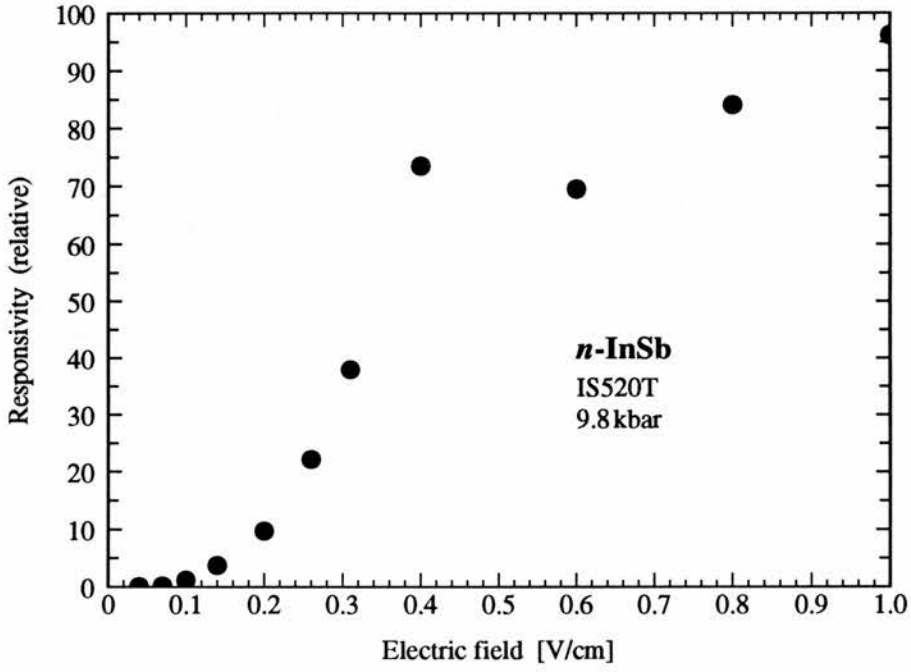

FIG. 8.10: Responsivity (simply the height of the cyclotron resonance peak in Fig. 8.9) *vs.* electric field.

used as a guide to estimate Γ, the halfwidth at half maximum. However, occasionally the *high-field* side of the peak was the narrower, because the low-field side was distorted by its summation with the more rapidly rising portion of the ICR peak. Finally, as can be seen in many of the upcoming traces, various long-wavelength low field lineshapes are very non-Lorentzian in appearance, either because of the appearance of the "shoulders" of subsidiary peaks, or possibly on account of biasing effects (although as was seen in Figs. 8.9 and 8.8, the variation with bias of linewidth was very small at high pressure, in the regime in which the measurements were made). It is in this long-wavelength region, furthermore, that the most dramatic changes in lineshape are visible, in that at ambient pressure, the CR and ICR peaks, even in the thinnest samples, are almost entirely unresolved, whereas rather rich structure is evident within the long-wavelength regime at even low pressures.

Fig. 8.11 exhibits the narrowing effect seen on the same sample (6-98(16)) by WASILEWSKI (1982). Not only is the narrowing visible over only a quite limited pressure range, but the character of the cyclotron resonance peak is quite different from that of sample IS522T (see e.g., Fig. 8.12): In particular, even when several volts per centimeter were applied to the sample, the amplitude of the CR peak was minute compared to that of the ICR peak

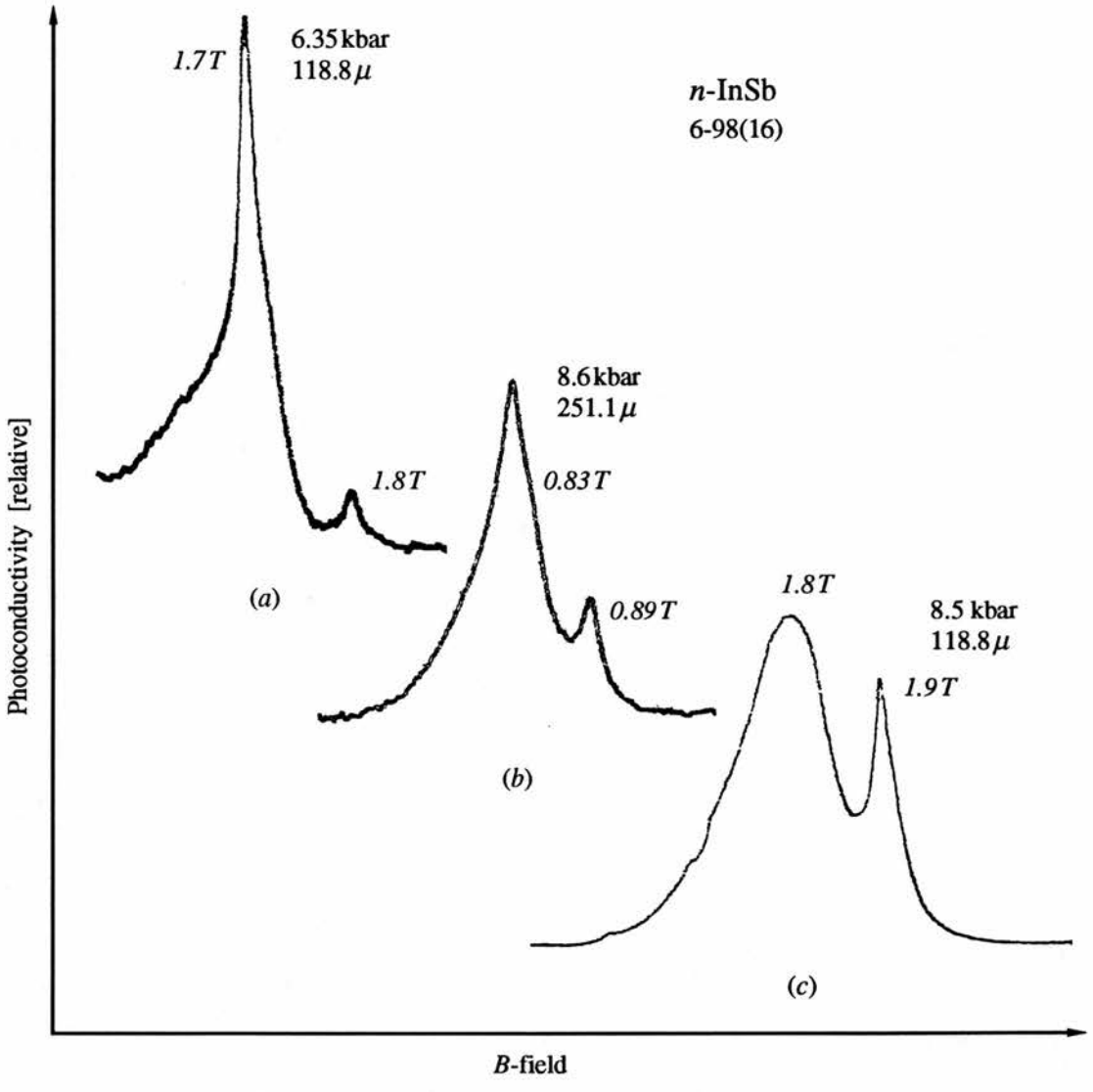

FIG. 8.11: Cyclotron resonance narrowing in n-type indium antimonide sample 6-98(16), as reported previously by WASILEWSKI (1982), over a small range in pressure. Even though the bias ranges as high as several hundred millivolts per centimeter, the cyclotron resonance peak (on the right) is very small due to freeze-out. The magnetic fields quoted are the peak values.

because of the high pressure freeze-out of the conduction band electrons. In Fig. 8.12*a*, for example, the trace corresponding to 6.2 kbar was obtained with a bias of only ~30 mV (< 100 mV/cm). Sample IS520T, as will be seen, usually tends to show CR amplitudes lying between the two other samples.

Another point of slight difference between 6-98(16) and IS522T is that of high pressure S/N behavior: In each sample, S/N degrades markedly at pressures on the order of 10 kbar,

but IS522T continues to exhibit good S/N at least a kilobar higher than 6-98(16). The reason for this behavior is not clear. While it is true that the high resistance of the samples loads the preamplifier, this cannot account for the large amount of noise that appears. If the Piotrzkowski model of growth striations in the material is valid, the increase in noise could be explained as the result of all the current being channeled through a very small volume, thus possibly creating an avalanche effect and an increase in shot/current noise. Alternatively, as there may exist many different paths through the striations, the noise may represent rapidly changing current paths. If correlation is the reason for the narrowing, it is conceivable that the increased dipole concentration at higher pressures presents a greater cross-section to the electron current, creating more opportunities for impact ionization of the anion, resulting in a higher shot/current noise superposed on a much lower signal current.

Fig. 8.13 presents a similar set of spectra for the two MCP samples, taken with 251.1 μ radiation, and again illustrates the sample-dependent nature of the linewidths, in that the cyclotron resonance at ambient pressure in IS520T is narrower than that of IS522T with almost 4 kbar on it. What is more, the former sample was $\sim$200 μ thick, inviting over-absorption broadening, while the latter was only 50 μ thick.

Figs. 8.14 through 8.16 show the cyclotron resonance spectra of the MCP samples at the extremes of wavelength, and the great difference in effect that hydrostatic pressure has in these instances.

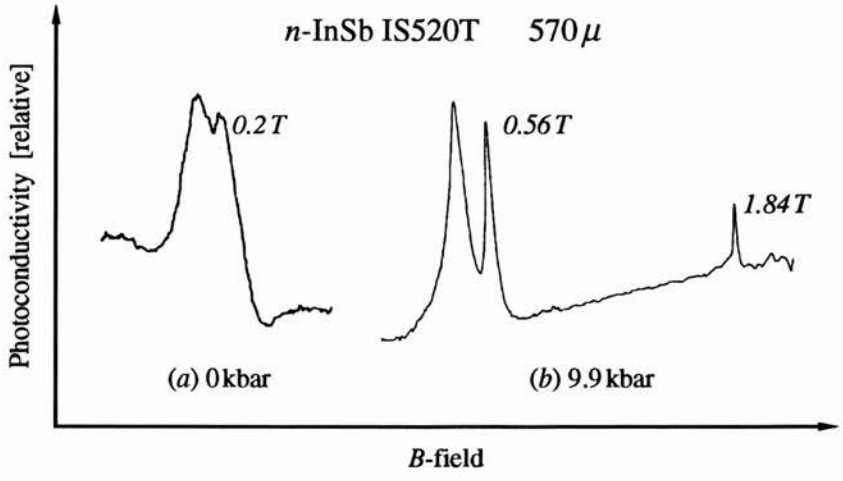

FIG. 8.15: Hydrostatic pressure can dramatically resolve low energy resonances such as this at 570 μ. (*b*) shows a spin-flip transition upfield from the cyclotron resonance. This is discussed in § 8.2.2.

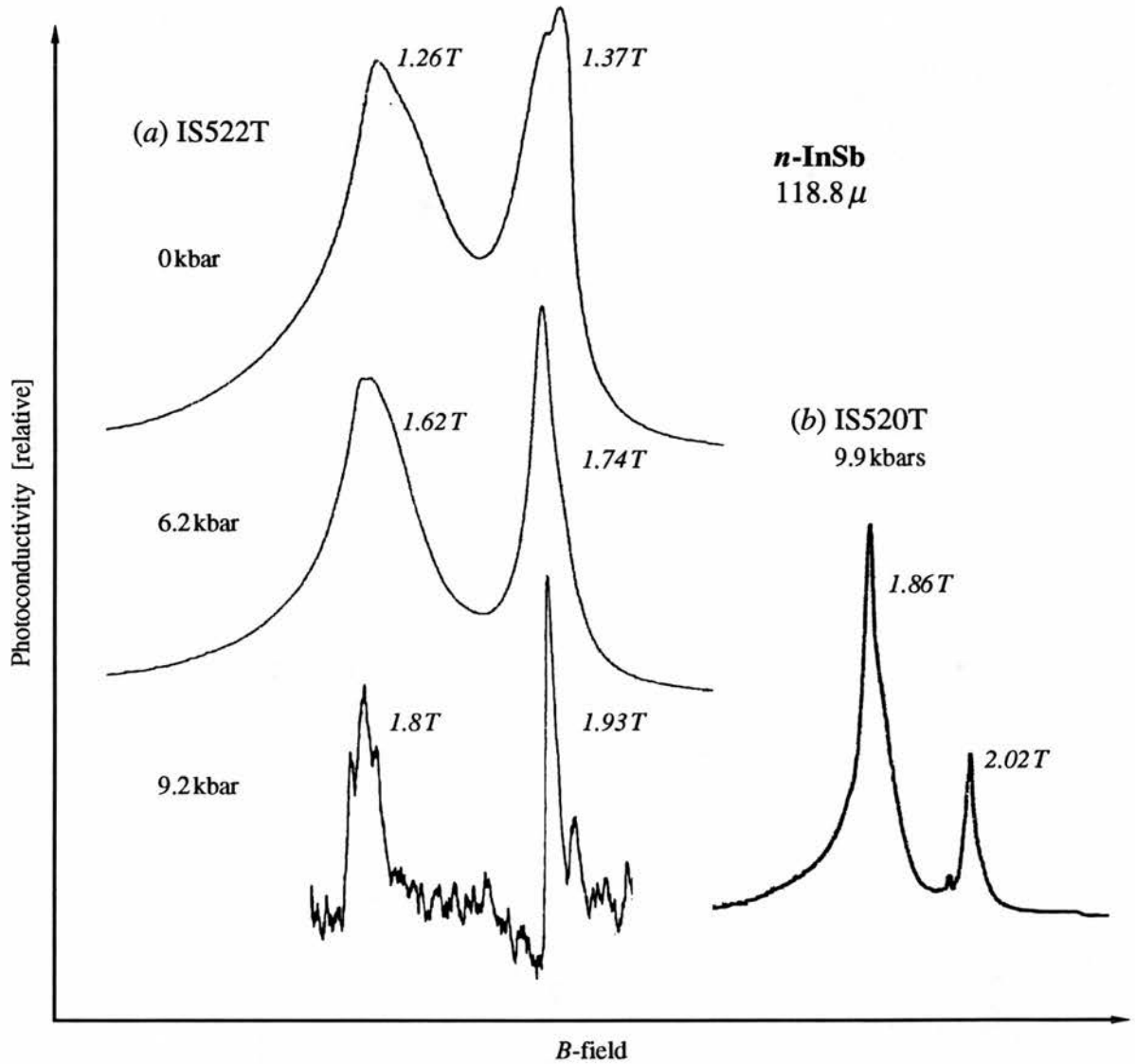

FIG. 8.12: The gradual narrowing of the CR and ICR peaks with hydrostatic pressure for IS522T is shown in (*a*), revealing substantial narrowing even under 7 kbar. At 9.2 kbar, the sample resistance is so high (> 20 MΩ) that it loads the preamplifier. While IS520T in (*b*) shows comparable narrowing, it did not exhibit as dramatic an effect as IS522T within the pressure range studied. The magnetic fields quoted are the peak values.

The linewidths ($\Delta B_{1/2}$ = HWHM) are plotted against pressure for the different wavelengths tested in Figs. 8.17 through 8.21.

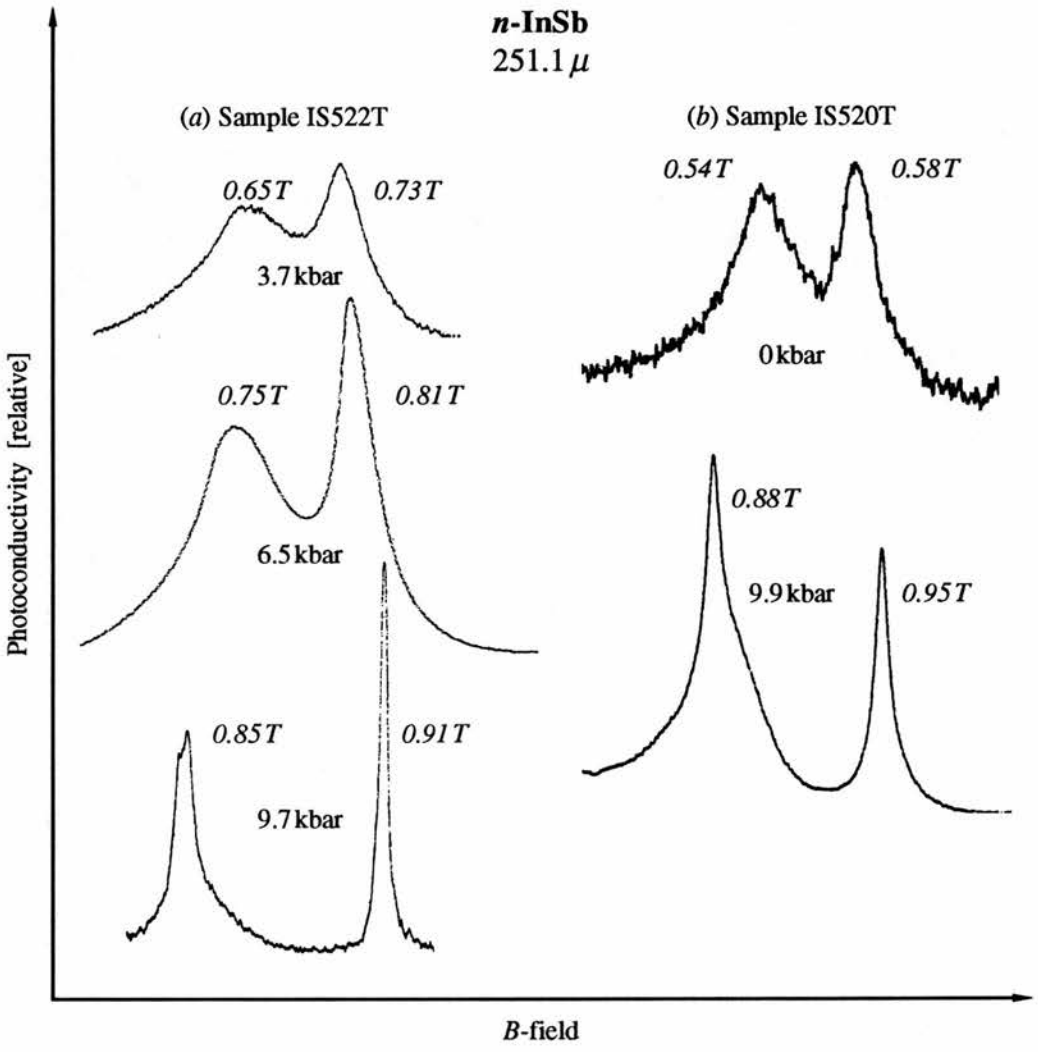

FIG. 8.13: Narrowing of the 251.1 μ CR and ICR peaks. Note in (*b*) that the resonances at ambient pressure are narrower than those at 3.7 kbar in (*a*), even though IS520T is a substantially thicker slice ($\sim$200 μ). The magnetic fields quoted are the peak values.

In order to compare these results with the work cited in Chapter III, the linewidths can be plotted against magnetic field at a constant pressure.* Those figures that have the most data tend to show a linewidth that reaches a minimum value, about 0.01 T, at a magnetic field of $\sim$1–1.5 T, with the higher pressures pushing the minimum toward higher fields. This behavior is in general agreement with the results of Kaplan discussed in § 3.3.4. In particular,

* Not all these data were taken at the same time; therefore, the actual pressure corresponding to a given point may vary somewhat from the quoted pressure.

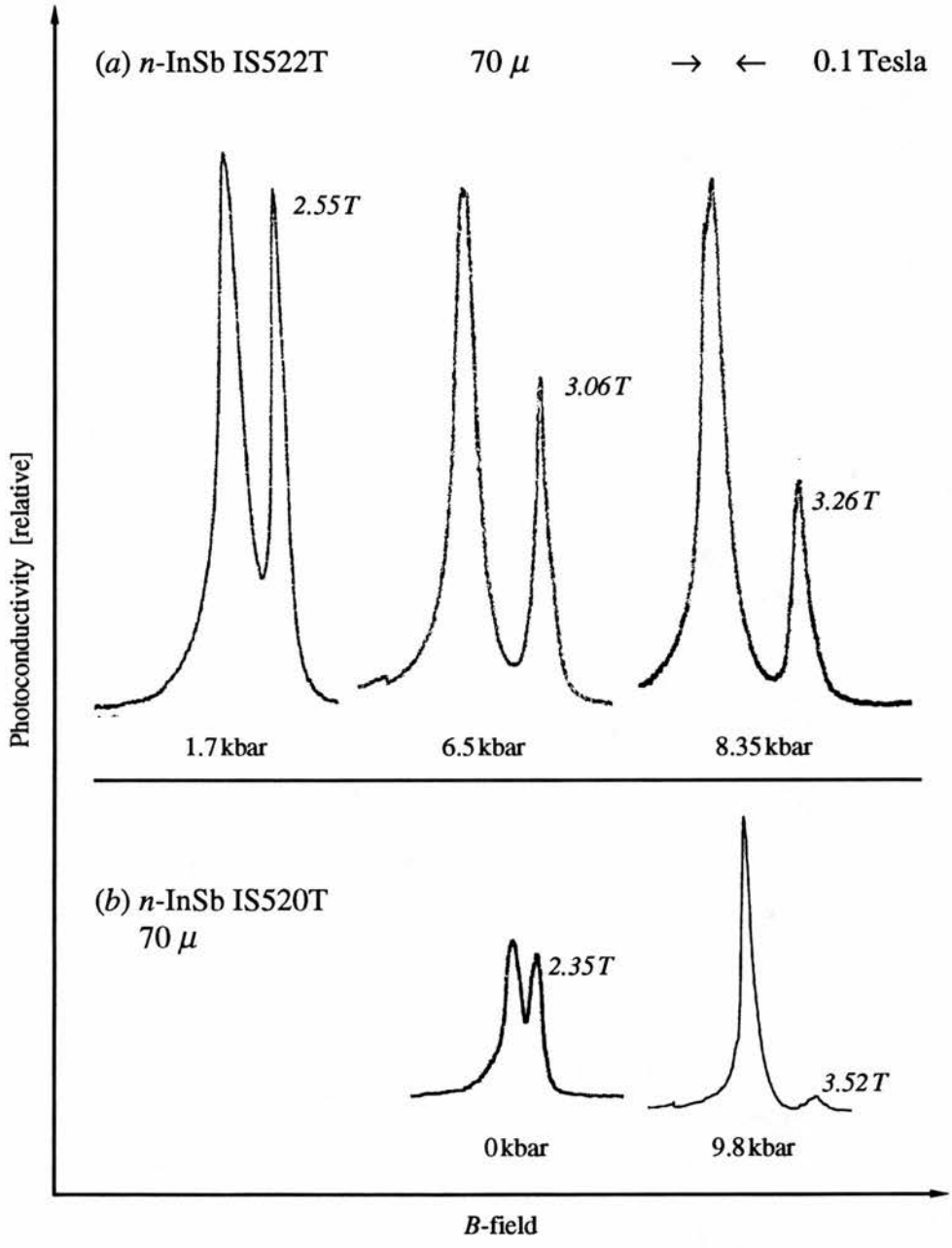

FIG. 8.14: Narrowing with hydrostatic pressure of the 70 μ cyclotron resonance in n-type indium antimonide. While narrowing relative to the CR and ICR separation is apparent, absolute linewidth stays more or less constant (see Fig. 8.17).

the quantity l/a_i is proportional to $(m_e^* n)^{1/4}$ for a given magnetic field; or equivalently, the magnetic field of the minimum is proportional to the square root of the effective mass. Therefore, in the regime of lower pressures (< 10 kbar) where n is fairly constant, the

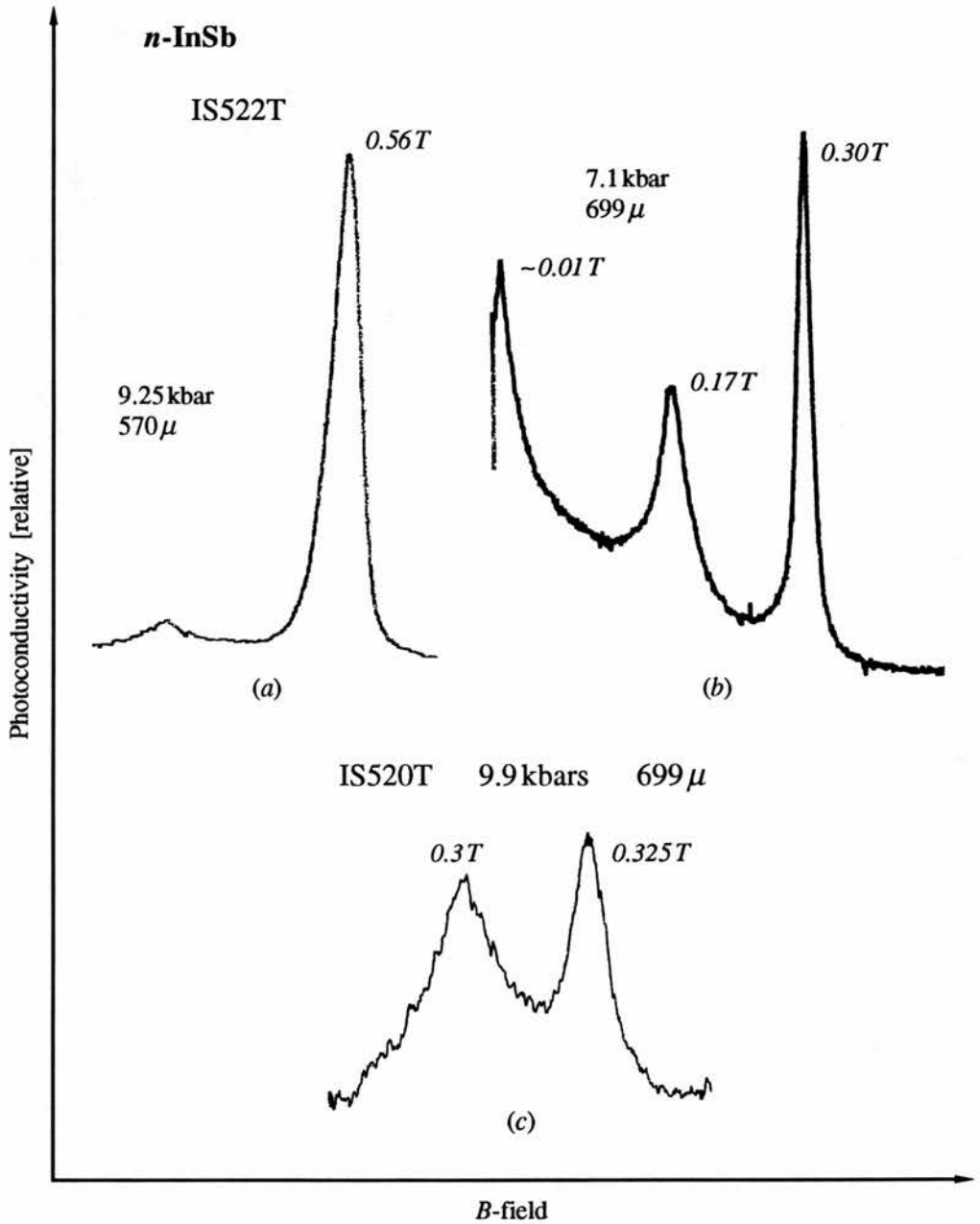

FIG. 8.16: More narrowing of low energy resonances. Again, IS522T shows a more dramatic effect than IS520T. In (*b*), for example, the three peaks shown are entirely unresolved in the ambient spectrum. The peak at ~0.01 T has not yet been identified: It may correspond to free electron absorption.

change of effective mass governs the position of the minimum, pushing it toward higher magnetic field as it increases with pressure. At the highest pressures used in this study, the minimum would be expected to be about 30% higher than at ambient pressure; a fair

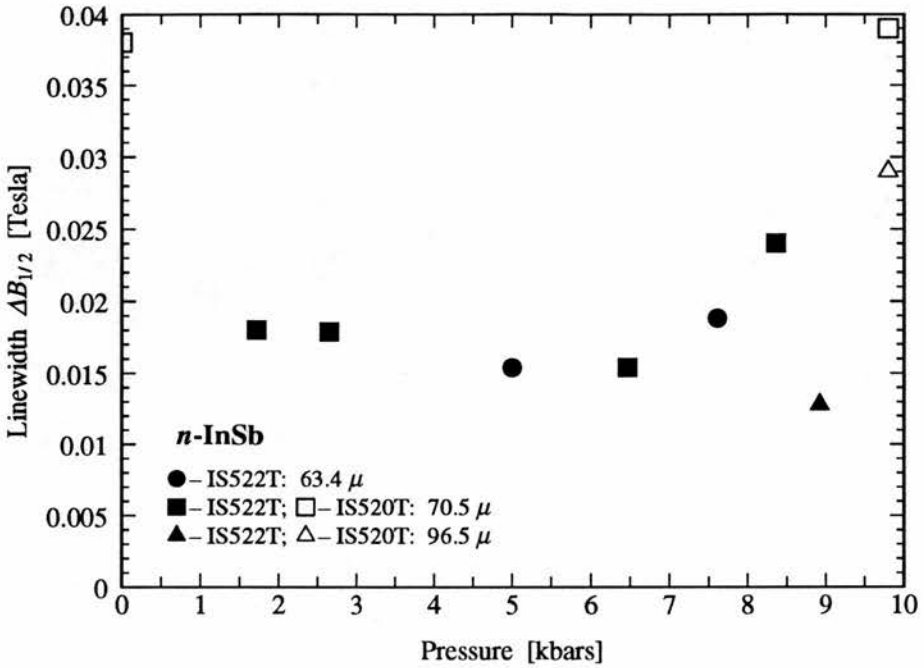

FIG. 8.17: Linewidth *vs.* pressure: Short wavelengths.

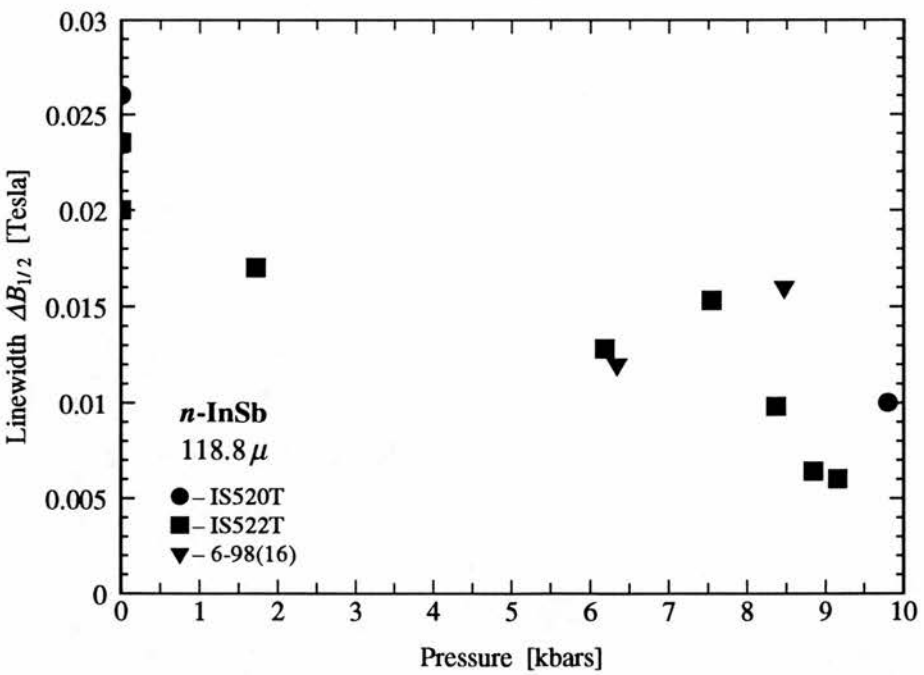

FIG. 8.18: Linewidth *vs.* pressure: 118.8 μ.

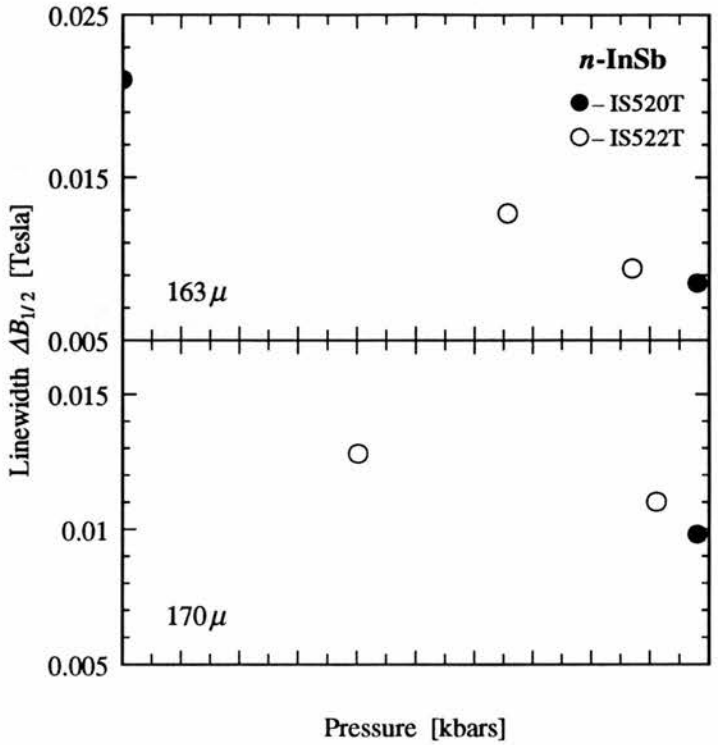

FIG. 8.19: Linewidth *vs.* pressure: 163 and 170 μ.

agreement, given the roughness of the curves.

Comparing the above results with those of Kobori *et al.*, as presented in Table 3.1, a correction or normalization for various pressure-dependent parameters can be made for inter-Landau level scattering by multiplying the linewidths by the factor

$$\left(\frac{N_{\rm I}(P)}{N_{\rm I}(0)}\right)\left(\frac{m_{\rm e}^*(P)}{m_{\rm e}^*}\right)\left(\frac{\kappa(P)}{\kappa(0)}\right)^{-2}\left(\frac{B_{\rm CR}(P)}{B_{\rm CR}(0)}\right)^{-3/2},$$

where the argument (0) refers to the corresponding quantity at ambient pressure, and $B_{\rm CR}$ is the field of the central maximum of the cyclotron resonance peak. The values of $N_{\rm I}$ used are taken from Fig. 7.5, by assuming that the electron concentration is $N_{\rm D} - N_{\rm A}$ and that $N_{\rm A}$ is $4 \times 10^{14}\,{\rm cm}^{-3}$. The equivalent expression for intra-Landau level scattering is

$$\left(\frac{N_{\rm I}(P)}{N_{\rm I}(0)}\right)\left(\frac{m_{\rm e}^*(P)}{m_{\rm e}^*}\right)^{1/2}\left(\frac{\kappa(P)}{\kappa(0)}\right)^{-2}\left(\frac{B_{\rm CR}(P)}{B_{\rm CR}(0)}\right)^{-1}.$$

However, these corrections are in fact only of the order of a few percent, even at the highest pressures, while it is seen in Fig. 8.20, for example, that the linewidths may change by an

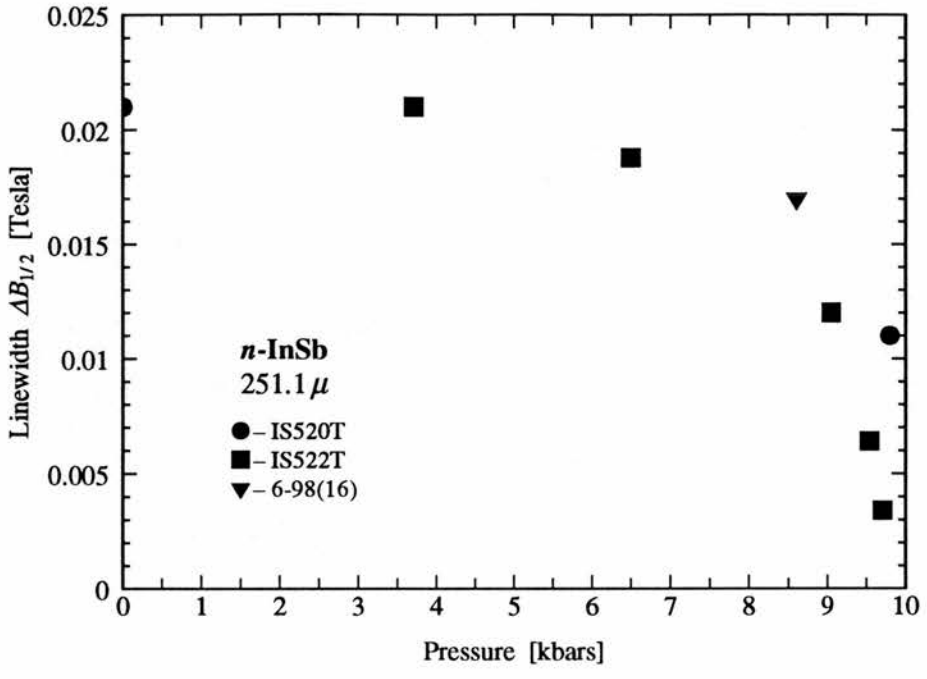

FIG. 8.20: Linewidth *vs.* pressure: 251 μ.

order of magnitude with pressure. This argues for an extra influence, such as heterogeneity or correlation. Because none of the mobility anomalies due to heterogeneity, discussed in § 4.7, were observed in these studies, it is tempting to ascribe the anomalous narrowing to correlation.

8.2.1 Cyclotron Resonance in Metastable Indium Antimonide

In the study of cyclotron resonance in indium antimonide in the metastable HPFO state (see § 6.8), it was possible to perform measurements at one pressure only (~9.1 kbar) on the sample (IS522T). The spectra taken both during HPFO and afterward, when the sample had been warmed and recooled, are compared in Fig. 8.30. While the spectrum taken after HPFO is virtually identical to that taken before the treatment (as in Fig. 8.12), that taken during HPFO (when, from Fig. 7.11, $n \approx 2 \times 10^{12}\,\mathrm{cm}^{-3}$) shows comparatively sharp CR and ICR peaks, with abruptly widening "wings". This is indicative of an energy-dependent scattering mode becoming dominant in this state, as discussed in § 3.3.

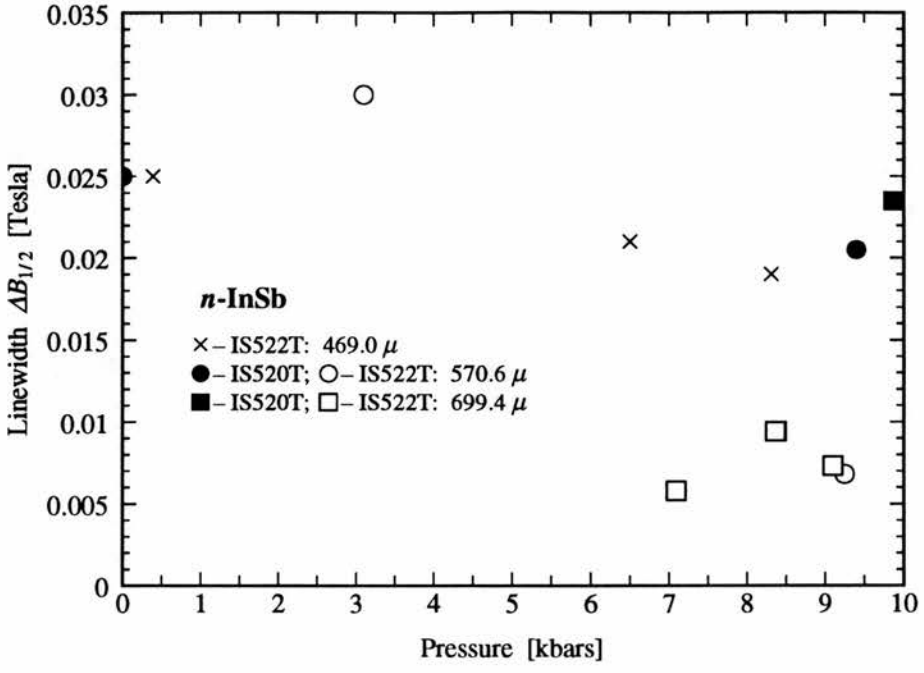

FIG. 8.21: Linewidth *vs.* pressure: Long wavelengths. It was not possible to measure many linewidths at low pressure in this case as they were unresolved, and occasionally of unusual shape or structure.

8.2.2 *Spin-Associated Effects under Hydrostatic Pressure*

In both MCP samples, IS520T and IS522T, effects of spin splitting became apparent with the application of hydrostatic pressure. In the pressure range of ~7.5 kbar to 8.5 kbar, spin-split spectra such as that of Fig. 8.31 were typical. These structured spectra varied in amplitude from sample to sample and did not always appear. Why the spin-splitting was never observed outside of this regime is not clear.

Both samples, but IS520T especially, also exhibited spin flip transitions at elevated pressures. These resonances are typically very sharp, as in Fig. 8.32, and of much lower amplitude than the cyclotron resonances. These have been studied previously as a function of pressure (KUCHAR, MEISELS ET AL., 1984), and therefore were not investigated further.

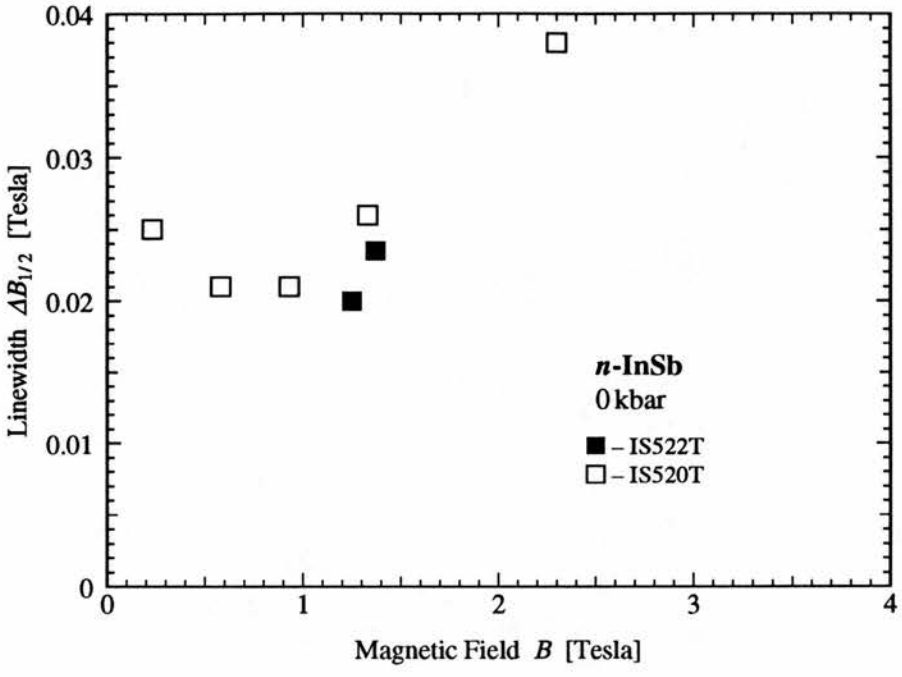

FIG. 8.22: Linewidth *vs.* magnetic field: Ambient pressure.

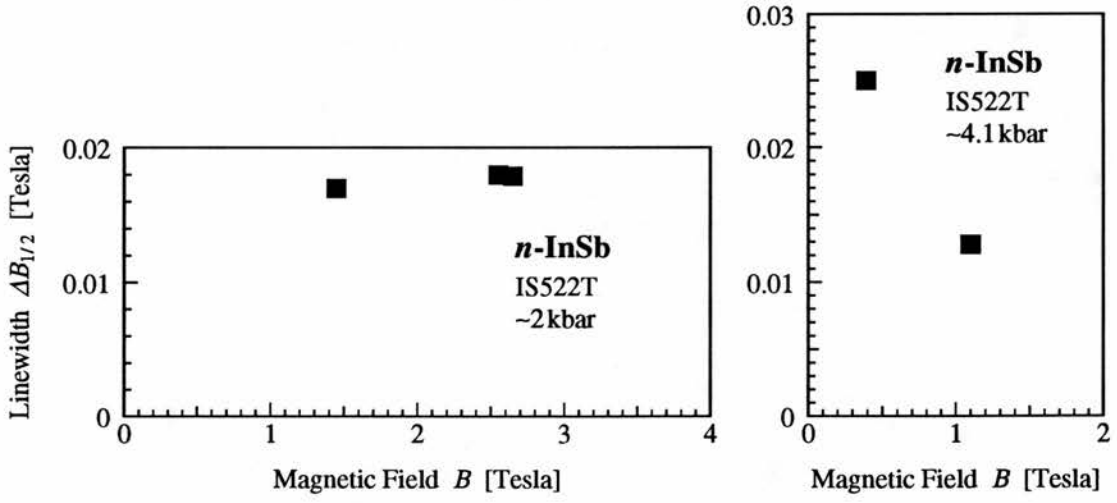

FIG. 8.23: Linewidth *vs.* magnetic field: 2 and 4 kbar.

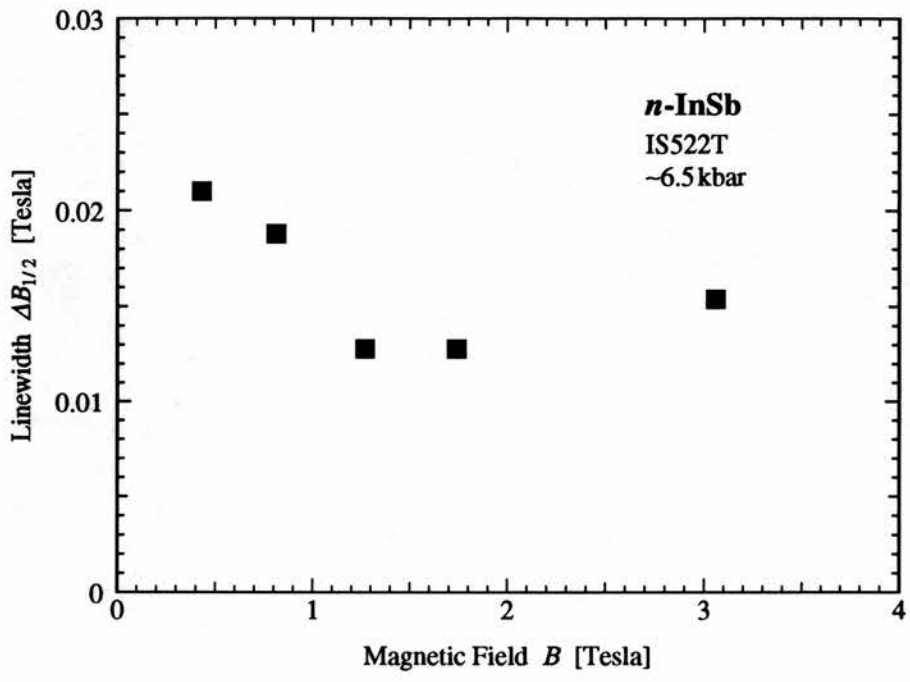

FIG. 8.24: Linewidth *vs.* magnetic field: 6.5 kbar.

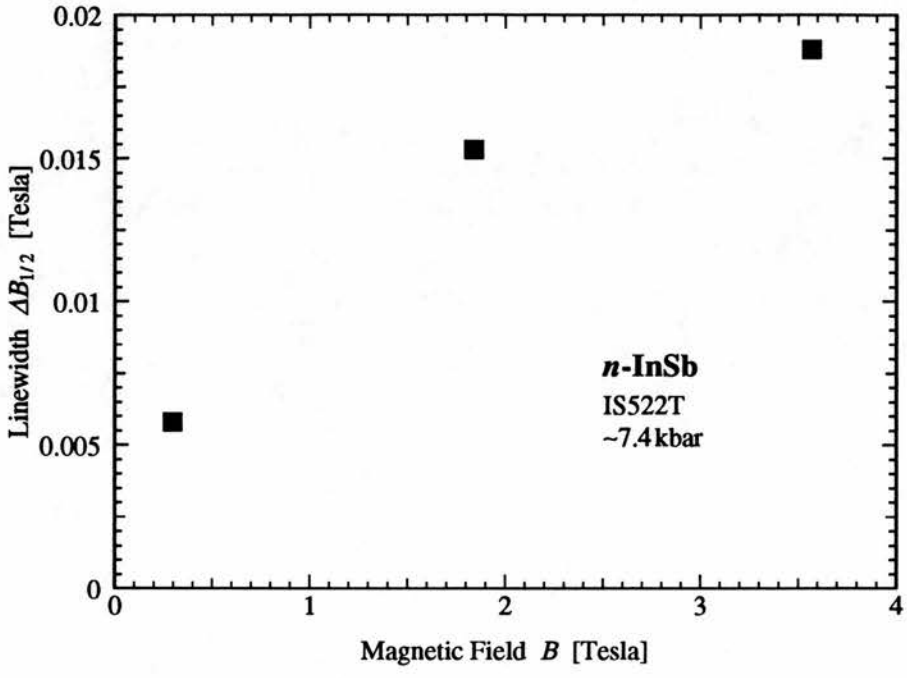

FIG. 8.25: Linewidth *vs.* magnetic field: 7.4 kbar.

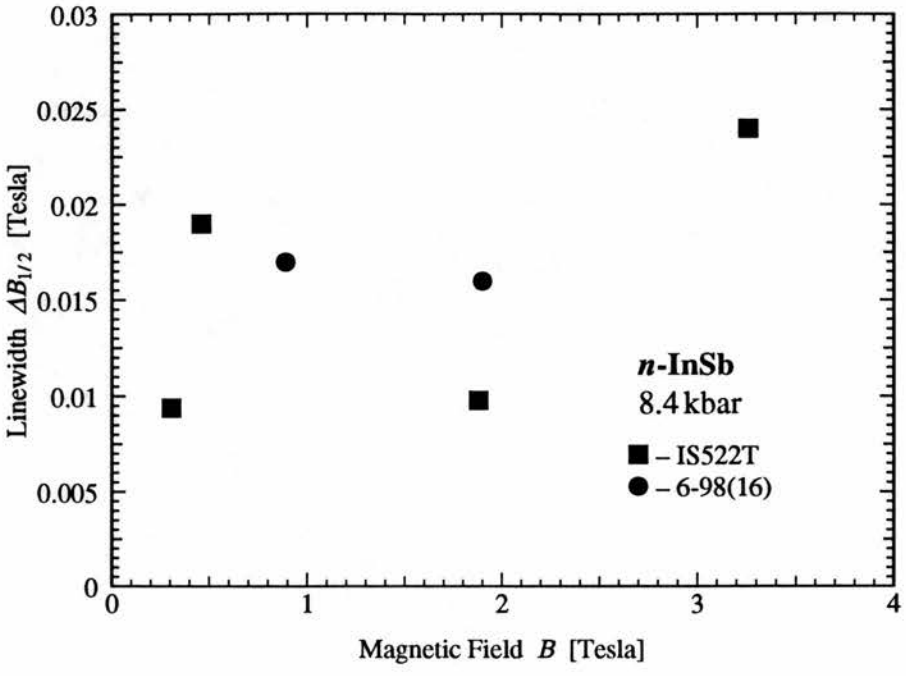

FIG. 8.26: Linewidth *vs.* magnetic field: 8.4 kbar.

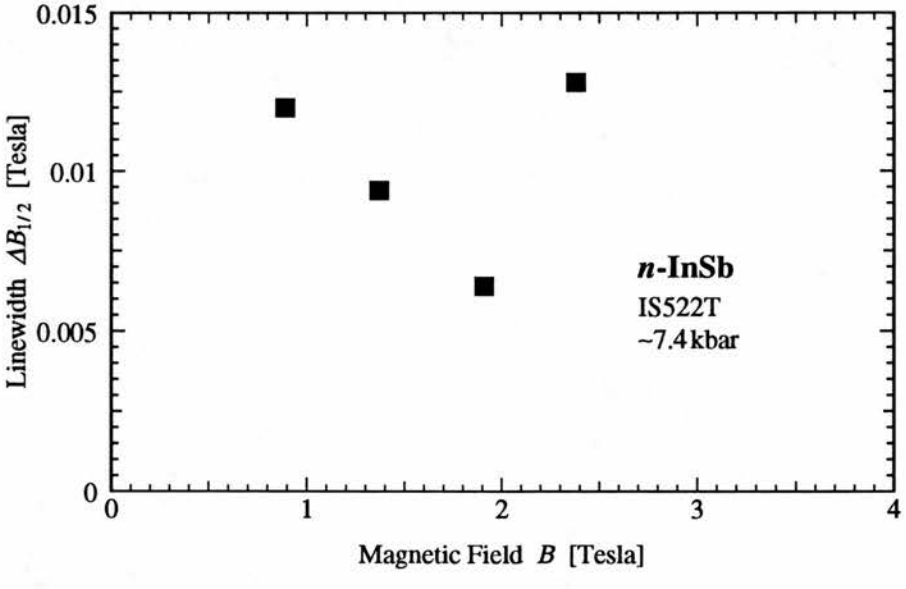

FIG. 8.27: Linewidth *vs.* magnetic field: 8.8 kbar.

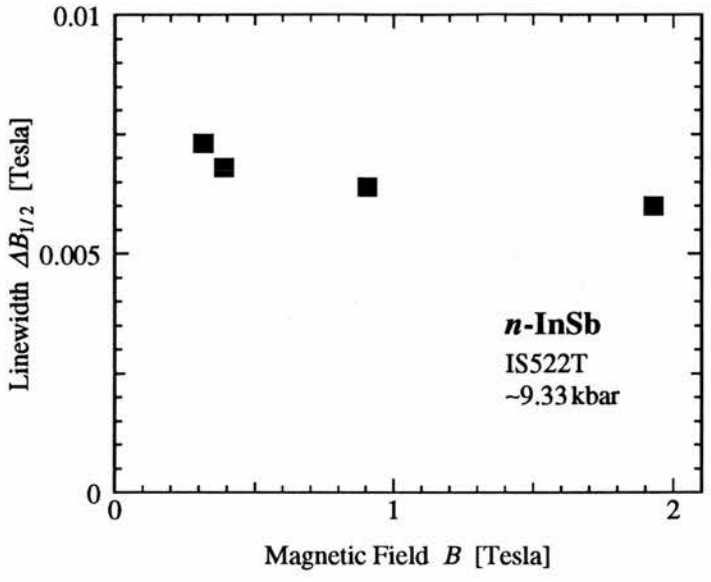

FIG. 8.28: Linewidth *vs.* magnetic field: 9.3 kbar.

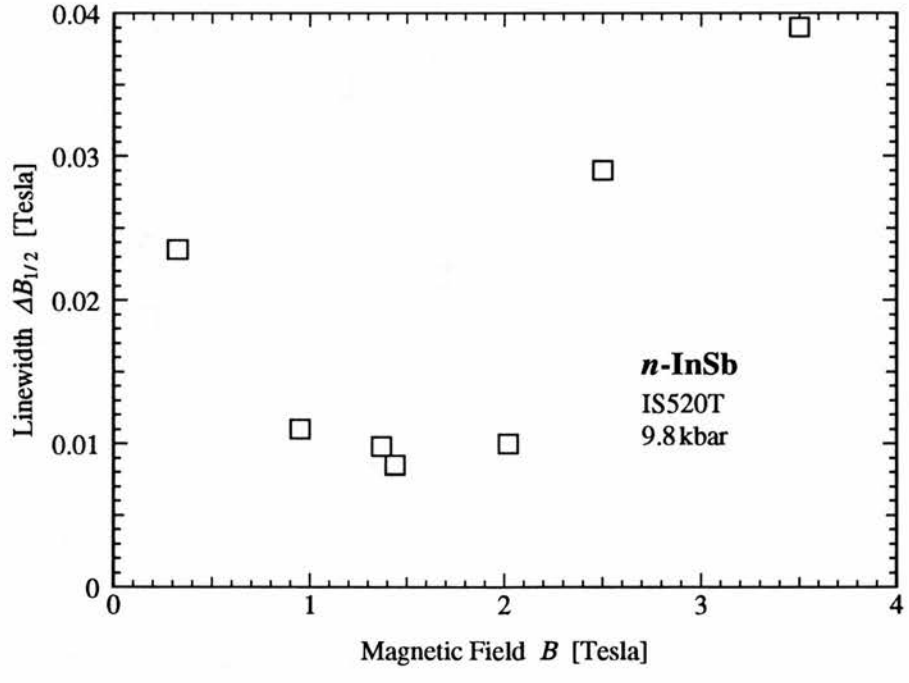

FIG. 8.29: Linewidth *vs.* magnetic field: 9.8 kbar.

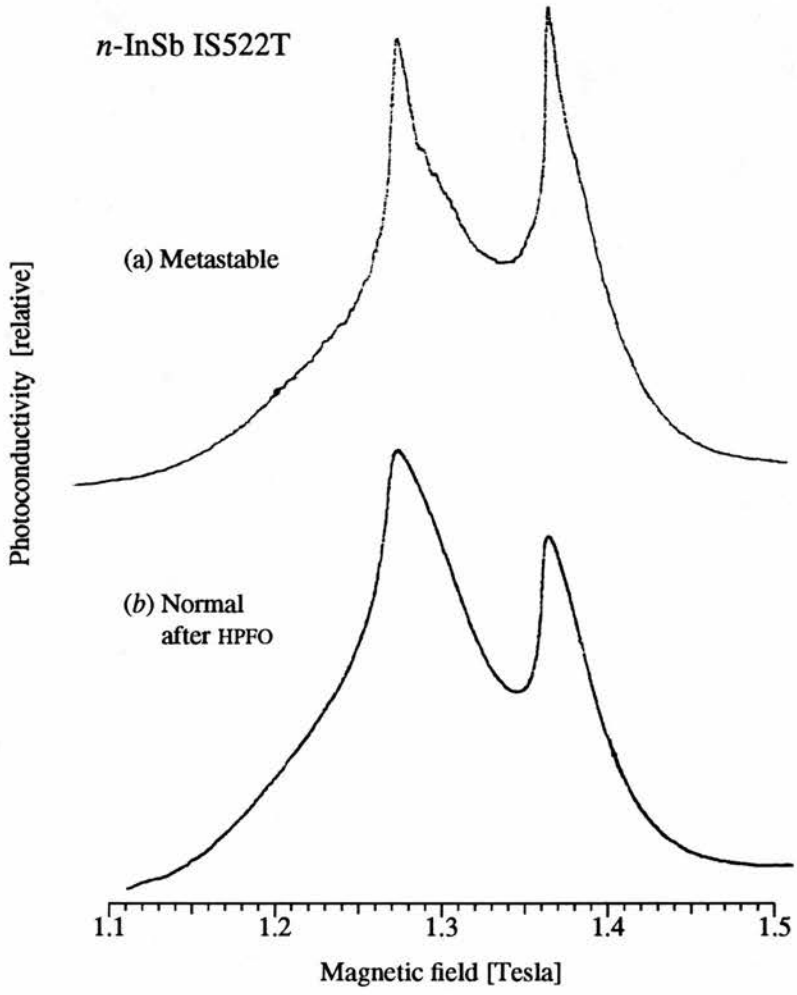

FIG. 8.30: Comparison of cyclotron resonance in indium antimonide at ambient pressure in a metastable HPFO state at 4.2°K (prior to which it had been pressurized to ~9 kbar, cooled to 77°K and depressurized) (*a*) with that in its normal state (*b*).

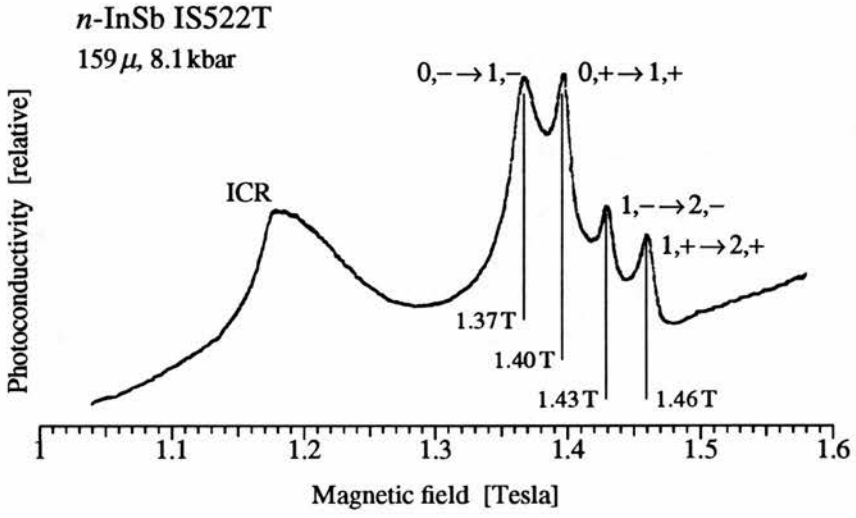

FIG. 8.31: Spin-splitting of the CR and ICR peaks in n-type indium antimonide. The magnetic fields shown are those calculated from Eq. 3.19 based on the stated pressure and wavelength.

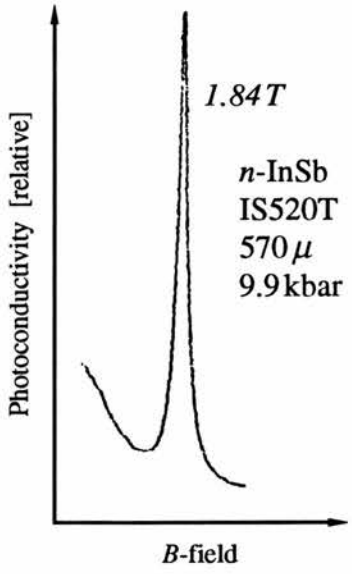

FIG. 8.32: The sharp spin-flip resonance with hydrostatic pressure.

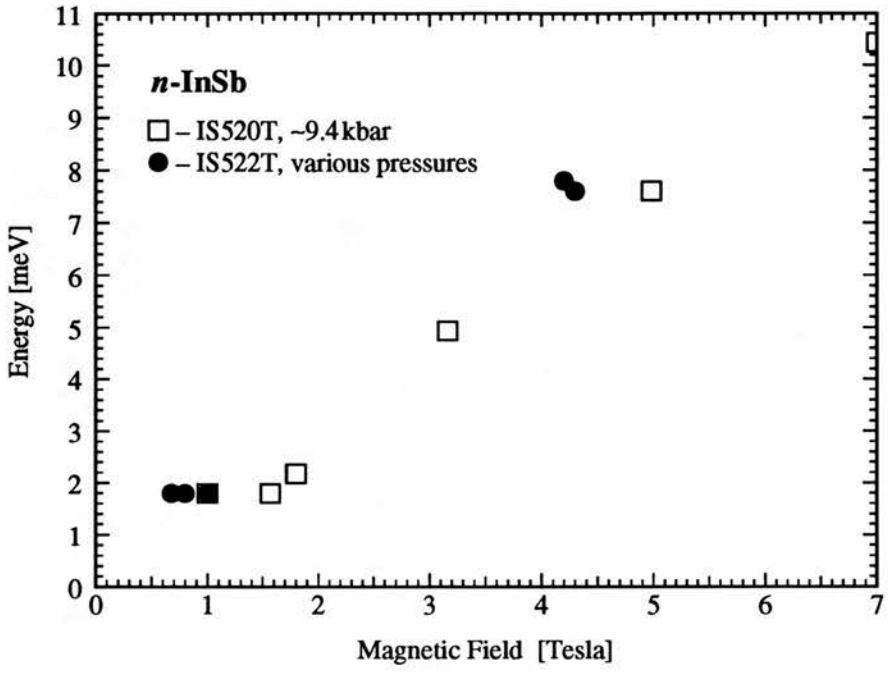

FIG. 8.33: The variation with magnetic field of $0, - \rightarrow 1, +$ spin-flip transition energy.

CHAPTER IX

Conclusions

This chapter presents a summary of the results and conclusions arrived at in the preceding chapters and in this work over all. § 9.1 discusses the significance of the Hall measurements undertaken in Warsaw. § 9.2 itemizes the observations made on n-type indium antimonide samples subjected to hydrostatic pressure and magnetic fields at low temperature, while § 9.3 reviews observations concerning cyclotron resonance linewidth and lineshape in the same samples.

9.1 Hall Measurements on Compensated Indium Antimonide

Hall measurements in indium antimonide are complicated by the inexact knowledge of the Hall factor r_{H}, which is dependent on modes of scattering, temperature, magnetic field, and possibly pressure; but because the resistivity of indium antimonide itself changes quite rapidly with magnetic field (even the small fields used in most Hall experiments), there is no straightforward way to arrive at the magnetic field dependence of r_{H}. Therefore, it was assumed throughout this work to be equal to unity.

Using pressure to vary electron concentration in a compensated sample of n-type indium antimonide (as pressure forces certain donor impurities below the conduction band minimum), a value for the band-gap pressure-dependence of 0.012 eV kbar^{-1} was deduced, $\sim$15% less than the accepted value. This may reflect the dependence on pressure of the Hall factor. The pressure coefficient of the effective mass at the bottom of the conduction band was also estimated at various pressures at both 77°K and 290°K.

Three models of ionized-impurity-limited mobility (Brooks-Herring, Conwell-Weisskopf and Zawadzki-Szymańska) were invoked in an effort to arrive at impurity concentrations in the sample tested based on mobility measurements. None of the models appeared to give

wholly plausible results in this respect, always predicting suspiciously similar values for acceptor and donor concentrations. An extensive model due to SZYMAŃSKA AND DIETL (1978) was invoked in an effort to include polar-optical mode scattering, but this hefty numerical program failed to converge.

An estimation was done of the non-metastable ("L-like") donor energy as a function of pressure, and the result, $\sim$0.01 eV kbar^{-1}, agrees closely with that of POROWSKI (1990).

Numerous Hall measurements were performed on indium antimonide involving its metastable donors. When these donors were frozen out (by pressurizing the sample to above 7 kbars at 290°K and cooling to 77°K), depressurization revealed an exponential increase in electron concentration well above that predicted for known donors, apparently revealing a new shallow donor.

The Hall measurements performed were inconclusive with respect to the existence of the negative-U effect in indium antimonide: Metastable freeze-out was found to increase mobility, while in the simplest negative-U model, it would be expected that mobility would decrease with pressure; on the other hand, that expectation is reversed if correlation effects are allowed. In fact, however, the increase in mobility observed was only half that expected due to freeze-out alone, implying that the (uncorrelated) negative-U effect may be present after all.

9.2 Indium Antimonide's Photoconductivity in the Near Infrared

Most conspicuous in the investigations of photoconductivity in indium antimonide under hydrostatic pressure was the behavior of the band-edge portion of the spectrum: While band-edge peaking (due to surface recombination) has long been noticed in poorly etched samples even at ambient pressure, pressurized samples exhibited this effect even after being etched to a nominally sufficient extent to remove surface recombination. The fact that this peaking disappeared with more radical etching, and was not present at all in MBE-grown samples, indicates that it was likely caused by damage extending more deeply into the sample, or by some other surface feature not removed by lighter etching. The possibility remains that the application of hydrostatic pressure, which was not attempted with the epitaxial samples, increases the surface recombination rate, leading to the attenuation of photoconductive signal at high energies.

It is highly unlikely that the peaks observed at 77°K are excitonic in nature, given the large thermal energy present; and even those observed at 4.2°K are unlikely to be excitonic, given the shift of these peaks with magnetic field.

Of most interest in the case of intrinsic photoconductivity is the enhancement of infrared responsivity with the application of hydrostatic pressure. This was seen to rise on average by two orders of magnitude in an uncompensated sample, as would be expected to first order from the similar increase in the sample's resistivity. In fact, enhancements both substantially less and greater than two orders of magnitude were also observed. The greater enhancements appear to be due to an increase in ~~energy~~ electron lifetime due to hole freeze-out, while the smaller enhancements may have resulted from mechanical damage inflicted on the very thin and fragile samples.

Most unexpected was the appearance of a very large absorption at approximately 0.4 eV in the NIR spectrum of uncompensated indium antimonide which had been metastably cycled (pressurized, cooled to liquid nitrogen temperature and depressurized). This absorption was seen to disappear after the sample had been "relaxed", i.e., rewarmed to room temperature, and recooled to 77°K subsequently. Thus it appears to correspond to some higher lying metastable donor.

9.3 Cyclotron Resonance in Indium Antimonide's under Hydrostatic Pressure

Because a large number of factors can influence cyclotron resonance lineshape and linewidth, an attempt was made to determine the effect of some of them, or to at least bring them under control, i.e., standardize them.

The broadening of linewidth by high electric fields, due to hot-electron effects, is well-known at lower pressures. It was examined in the present work at high hydrostatic pressure (~10 kbar), where the effective mass of the electrons is about twice as high as at ambient pressure. The surprising result was that up to an electric field intensity of ~0.25 V/cm, the linewidth exhibited a marked *decrease* of some 50%, perhaps due to an increase in small-angle ballistics or increased screening. The linewidth was seen to rapidly increase above this voltage, and to then plateau, at voltages as high as 1 V/cm, most likely due to hot electron effects.

Electric field intensity was also observed to increase the infrared responsivity of the sample, following a power curve of exponent 3.4, up to 0.4 V/cm. Beyond this, the responsivity levels off quite sharply, in fact dropping slightly as the field intensity approached 0.6 V/cm, prior to slowly climbing again.

Prior to this work, the narrowing (by up to an order of magnitude) of cyclotron resonance peaks in indium antimonide had been observed over only a very limited pressure range (WASILEWSKI, 1982), and exhibited very little amplitude in the free electron ("CR") peak

relative to the impurity-shifted peak ("ICR"), due to freeze-out. Furthermore, when the same sample used in the original work was investigated in this work, it was observed that even with biases of several volts per centimeter, the amplitude of the CR peak remained very low.

Both the uncompensated and the compensated sample investigated additionally in this work exhibited cyclotron resonance narrowing over almost the entire range of applied pressures, up to ~10 kbar, with the uncompensated sample yielding narrower peaks, presumably due to reduced scattering. Furthermore, both the amplitude and the integrated intensity of the CR peak were comparable to those of the ICR peak, even though biases were kept low to avoid heating effects (which proved minor at the highest pressures anyway). Also observed in these samples was the dramatic narrowing at high pressures of spin-flip transitions, while, between ~7.5 and 8.5 kbars, spin-split states were observable, even at very low magnetic field. Finally, the signal-to-noise ratio observed in the resonances of these latter samples was very high relative to that of the original sample, and was observed, in the cases of all samples, to degrade at successively higher pressures (although the propensity of the highest resistance samples to load the preamplifier may have played a rôle in this). However, if the original sample contained growth striations separating relatively pure and impure phases (PIOTRZKOWSKY ET AL., 1986), current may have been channeled through the restricted volume of the purer phases, giving rise, conceivably, to avalanching and increased shot noise. Alternatively, rapidly switching current paths could also be responsible. The increased dipole concentration resulting at higher pressures within a correlated material could also give rise to increased impact ionization and shot noise at these pressures.

The behavior of the narrowing itself was seen to agree qualitatively with the work of KAPLAN ET AL. (1973), where a minimum linewidth of ~0.1 T appears in the neighborhood of 1 T applied magnetic field, which figure tends to rise with pressure. Applying the equations given by KOBORI ET AL. (1990), a narrowing of the cyclotron resonance linewidths by approximately 28% was predicted, but this figure is far away from the order of magnitude narrowing often observed. Thus it is concluded that an additional factor, other than net impurity ion concentration, dielectric constant or effective mass, is responsible for the narrowing; the two chief contenders at this juncture being heterogeneity effects as reported by Piotrzkowsky, or correlation. In the absence of even any hint of the anomalous mobility effects observed by Piotrzkowsky, it appears that correlation is responsible for the lion's share of the narrowing.

Finally, the effect on cyclotron resonance lineshape was investigated, in one trial only, for the case of high-pressure metastable freeze-out, wherein the sample was pressurized to

~9 kbar, cooled to 77°K, depressurized and exposed to FIR radiation in a magnetic field to elicit cyclotron resonance. The resulting resonance lineshape featured both a broadening in the "wings" and a sharpening of the apices of the normally more Lorentzian curves. This lineshape is associated with energy-dependent scattering processes, though the exact form of the dependence is not deducible from the available data. The original Lorentzian lineshape was restored after the sample had been rewarmed to room temperature and then reexamined at 4.2°K, with no pressure treatment.

APPENDIX 1

Figures of Merit

In order to compare the quality or sensitivity of optical detectors of varying modes of operation (i.e., photoconductors, photomultipliers, pyroelectric detectors, etc.), it is necessary to specify a number of parameters, and to define a number of standards against which the detector under consideration may be judged. The following casual discussion, however, will be geared mainly to "figures of merit" applicable to photoconductors.

Perhaps the most basic figure of merit for a detector is the so-called *responsivity*, $\Re$. This is generally defined as the current *or* voltage change in or across the detector per watt of incident radiant power. Further, it is generally specified as a *spectral responsivity* $\Re_\lambda[(v)$ *or* $(i)]$. Note, however, that no account is taken of either the signal-to-noise ratio (S/N) or the conditions of the detector's use, including its construction. The quality of the detector then, or the intrinsic sensitivity of the material used, for instance, is left open to question.

The *noise equivalent power*, or NEP, is defined as that radiant power incident on the detector which will yield a response with a S/N of unity. Its reciprocal, the *detectivity*, D, is then the extrapolated S/N per watt of incident radiation, although the two are not generally proportional, of course. As such, D is rarely if ever used. Often, the reference bandwidth is specified with the NEP, which itself is rarely used with infrared detectors, but more often with optical detectors. Assuming the spectral responsivity of a detector covers the right wavelength, then, S/N is certainly the main criterion of sensitvity in choosing an individual detector to do a particular job; for if the responsivity is low, it can always be amplified; but if the S/N is low, no amount of amplification will help.

Ultimately though, neither NEP nor D is a good figure to discriminate between different materials or geometries, for example, in rating a detector. This is because the S/N of a detector, especially a photoconductor, depends on its area, bandwidth and field of view. In a simple model, if the exposed area of a detector is, say, quadrupled, it will receive four times the radiation, create four times the photocurrent, and therefore yield four times the signal as before. The rms noise, on the other hand, increases by a factor of only two, that is, by the square root of the change in area, following a stochastic model. S/N, then, increases by the

square root of the area. The bandwidth dependence is exactly analogous to that of the area, so that a fourfold increase in the bandwidth, assuming a flat response, results in a doubling of the S/N.

In order to compare the "intrinsic" S/N of two detectors independently of areas and bandwidths, D^* (*"dee-star"*) has been introduced. This is simply the detectivity D divided by the square roots of both the exposed area A and the bandwidth Δf. More often, the *spectral detectivity* D^*_λ is specified, this being limited to a specific wavelength with a 1 Hz bandwidth. Alternatively, a blackbody-referenced detectivity can be defined for BLIP.

Because it may be necessary to detect a target embedded within a broad background of radiation, often a 290°K ambient, it has become standard practice, when possible, to restrict the field of view of the detector from 2π steradians to only that solid angle sufficient to view the target, using a cooled (ideally non-radiating) optical channel or light pipe. This has the effect of eliminating background blackbody noise. A simple derivation, treating the target as a point source, disregarding signal fluctuation noise, assuming no reflection within the shield, and assuming a Lambertian* detector, has been introduced by KRUSE (1962). If the uniformly distributed background light intensity from a 2π steradian solid angle is integrated from a conical axis (see figure) to a half-angle θ, weighting the contribution by $\cos\theta$ to account for the Lambertian response, it is found that total detected noise power goes as $\sin^2\theta$, and therefore that the detectivity varies as $1/\sin\theta$. Therefore, to standardize detectors against varying fields of view, D^{**}, or *"dee double star"* has been introduced, equal to $D^* \sin\theta$. KRUSE (1962) has shown that there are two fundamental limitations on the ultimate detectivity of a photoconductor exposed either to a 2π steradian blackbody noise background or even to a "pure" signal.

When a photoconductor's S/N is limited only by the background noise (in other words, all intrinsic noise contributions are well below that of the background), it is said to operate in the BLIP mode.† The theoretical limit of D^* for a detector with a cut-off wavelength λ_{co}, corresponding to a cut-off frequency ν_{co}, a spectral quantum efficiency of $\eta(\nu)$, aimed at a monochromatic source of frequency ν_s, and staring into an ambient background at T_b, is shown to be

$$D^*_\lambda = \eta(\nu_s) \Big/ h\nu_s \left\{ \int_{\nu_0}^{\infty} \frac{4\pi\eta(\nu)\nu^2 \exp(h\nu/k_B T_b) d\nu}{c^2[\exp(h\nu/k_B T_b) - 1]^2} \right\}^{\frac{1}{2}} . \qquad \text{(A1.1)}$$

* Lambertian detectors or emitters, by definition, absorb or emit diffuse light from a surface with an intensity that varies as the cosine of the angle between the sightline and the normal to the surface.

† *B*ackground *L*imited *I*nfrared *P*hotodetector

When $h\nu_s/k_B T \gg 1$, this reduces to

$$D^*_\lambda = \frac{\eta(\nu_s)}{h\nu_s}. \tag{A1.2}$$

APPENDIX 2

The *Mathematica* Program

Below is the *Mathematica* program that allowed evaluation of the complicated formulae presented in Chapter II. Most of the file is fairly self-explanatory, as the syntax is very straightforward and quite common (multiplication signs (*) are optional, and take precedence over addition, for example). As in *C*, comments are bracketed by `(*...*)`. One possible point of confusion is the meaning of `N[`⟨*argument*⟩`]`, which means, generally, to evaluate as a number, rather than symbolically (i.e., `N[Pi]`, for example, would be numerically calculated and expressed, rather than left as `[Pi]` in the final answer). Also, the percent sign, %, symbolizes the previous result. It should be noted that the evaluation of the individual matrix elements d_{ij} may take up to 12 hours on the IBM RISC 6000.

```
Delta = 1.441971 10^-12;
q = 4.8 10^-10;
qcoul = 1.60219 10^-19;
m0 = 9.1066 10^-28;
me = 1.274924 10^-29;
mh = 4.09797 10^-28;
kappainf = 15.7;
kappa0 = 17.9;
kappaL = kappa0 - kappainf;
omegaTO = 34810000000000.;
omegaLO = 37070000000000.;
hbar = 1.054592 10^-27;
kB = 1.38 10^-16;
Psp = 1.45318633 10^-19;
Aprime = 0;
M = -5.5;
Lprime = -2.7;
Nprime = -4.4;
```

```
(*********************  ADJUST  ****************************)
eF = -.0275 eV;
T = 77;
Ni = 10^15;
n = 10^14;
P = 0;
(************************************************************)
Eg := (0.237 - 6 10^-4 T^2/(500 + T)) eV + P 0.015 eV
f[e_] := 1/(E^((e - eF)/(kB T)) + 1)
dfe[e_] := D[f[e],e]
k[e_] := Sqrt[ ((e + Eg) (e + Eg + Delta) e)/(Psp^2 (e + Eg
         + (2/3) Delta) )]
dke[e_] := D[k[e],e]
(* DO THIS FIRST: ADJUST eF TO MAKE nfermi = n *)
nfermi = N[(1/Pi^2)] NIntegrate[f[e] k[e]^2 dke[e],
         {e, 0, .1 eV}, AccuracyGoal->2,
WorkingPrecision->4]
meff[e_] := hbar^2 k[e] D[k[e], e]
Dabc[e_] := ((Delta + 1.5 (e + Eg))(Delta + e + Eg)(e + Eg)
         + (Delta + e + Eg)^2 e  + .5 e (e + Eg)^2 )
a[e_] := Sqrt[(1/Dabc[e]) (Delta + 1.5 (e + Eg))
         (Delta + e + Eg) (e + Eg)]
b[e_] := Sqrt[(Delta^2/(3 Dabc[e])) e]
c[e_] := Sqrt[(2/(3 Dabc[e])) (Delta + 1.5 (e + Eg))^2 e]
lambda = N[Sqrt[kappa0 kB T/(4 Pi q^2 n)]];
xi[e_] := 4 k[e]^2 lambda^2
A[e_] := b[e]^2 (b[e]/2 - c[e] Sqrt[2])^2 - (b[e]^2 + c[e]^2)
B[e_] :=  -(b[e]^2) (b[e]/2 - c[e] Sqrt[2])^2
         + (b[e]^2 + c[e]^2)^2
Fcc[e_] := Log[1 + xi[e]] - xi[e]/(1 + xi[e])
         + 4 A[e] (1 + 1/(1 + xi[e])
              - (2/xi[e]) Log[1 + xi[e]])
         + 2 B[e] (1 - 4/xi[e]
              + (6/xi[e]^2) Log[1 + xi[e]]
```

```
            - 2/(xi[e] (1 + xi[e]))  )
tauCC[e_] := N[(hbar^3 k[e]^3 kappa0^2)
        /( 2 Pi q^4 Ni meff[e] Fcc[e])]
(*IN ORDER TO PLOT THE FUNCTIONS ABOVE TO DISCOVER THEIR NORMAL-
IZATION FACTORS (SEE BELOW), OR TO USE THE 'NORMALIZED VARIABLE'
ARGUMENT [e eV] (WHICH IS IN FACT JUST AN IMMEDIATE VALUE) FOR
INTEGRATING THEM (ALSO SEE BELOW), IT IS NECESSARY TO GIVE THEM
IMMEDIATE = ASSIGNMENTS, WHICH ARE INDICATED BELOW BY THE INITIAL
'N'. *)
NtauCC[e_] = tauCC[e];
Plot[NtauCC[e eV],{e, 0, .1}]
Nk[e_] = k[e];
Plot[Nk[e eV]^2,{e, 0, .1}]
Ndke[e_] = dke[e];
Plot[Ndke[e eV],{e, 0, .1}]
Plot[Ndke[e eV]^-1,{e, 0, .1}]
Ndfe[e_] = dfe[e];
Plot[Ndfe[e eV],{e, 0, .1}]
Nf[e_] = f[e];
Plot[Nf[e eV], {e, 0, .1}]
Nmeff[e_] = meff[e];
Plot[Nmeff[e eV], {e, 0, .1}]
(****************** BARRIE'S PROCEDURE FOR MU ******************)
(*IN ORDER FOR THE INTEGRATION BELOW---AND ALL SUBSEQUENT
INTEGRATIONS IN THE FILE---TO WORK PROPERLY, CONSIDERING
THE EXTREMES IN THE VALUES OF THE FACTORS, THEIR EXTREME
DIFFERENCES, AND THE EXTREMELY SMALL ABSCISSA VALUES, THE
"NORMALIZED" ABSCISSA [e eV] MUST BE USED AS THE VARIABLE
OF INTEGRATION, AND EACH AMPLITUDE MUST ALSO BE NORMALIZED
BY A CONVENIENT FACTOR. THESE VARIOUS FACTORS ARE THEN
CORRECTED FOR OUTSIDE OF THE INTEGRAL.*)
NIntegrate[NtauCC[e eV] 10^11 Nk[e eV]^2 10^-12
        Ndke[e eV]^-1 10^20 (-Ndfe[e eV]) 10^-9,
        {e, 0, .1}] 10^-10  eV
```

```
N[% q/(3 hbar^2 Pi^2 n)]
% 10^7 1.6 10^-19/(4.8 10^-10)
(***************** BOLTZMANN EQ AND PO SCATTERING ***************)
Nq = 1/(E^(hbar omegaLO/(kB T)) - 1);
eplus[e_] := e + hbar omegaLO
eminus[e_] := e - hbar omegaLO
hminus = If[ e >= hbar omegaLO, this=1, this=0];
Plot[hminus, {e, 0, .1 eV}]
rho0[x_] :=  (   (a[e] a[x])^2 + 0.25 (b[e] b[x])^2
         - (b[e] b[x]) (b[e] c[x]
              + c[e] b[x])/Sqrt[2]
         + (b[e] c[x] + c[e] b[x])^2/2   )
rho1[x_] := 2 a[e] a[x] (b[e] b[x] + c[e] c[x])
rho2[x_] := ( 0.75 (b[e] b[x])^2
         + b[e] b[x] (b[e] c[x] + c[e] b[x])/Sqrt[2]
         + 2 b[e] b[x] c[e] c[x]
         - 0.5 (b[e] c[x] + c[e] b[x])^2 + (c[e] c[x])^2 )
KVplus[x_] := k[x] + k[e]
KVminus[x_] := k[x] - k[e]
phi[e_, i_] := (e/(kB T))^(i-1)
Nphi[e_, i_] = phi[e,i];
Vplus[e_, i_] := (
0.5 (phi[e, i] - ((k[eplus[e]]^2 + k[e]^2)/(2 k[e]^2))
              * phi[eplus[e], i])
    * ( rho0[eplus[e]]
      + rho1[eplus[e]](k[eplus[e]]^2 + k[e]^2)
        /(2 k[e] k[eplus[e]])
      + rho2[eplus[e]] ((k[eplus[e]]^2 + k[e]^2)
        /(2 k[e] k[eplus[e]]))^2)
    * (Log[(1+lambda^2 KVplus[eplus[e]]^2)
        /(1+lambda^2 KVminus[eplus[e]]^2)]
      - (4 lambda^2 k[eplus[e]] k[e])
        /((1+lambda^2 KVplus[eplus[e]]^2)
          *(1+lambda^2 KVminus[eplus[e]]^2)))
```

```
+ ( -(phi[e, i] - ((k[eplus[e]]^2 + k[e]^2)/(2 k[e]^2))
        * phi[eplus[e], i])
    * ( rho1[eplus[e]] (1/(4 lambda^2 k[eplus[e]] k[e]))
      + rho2[eplus[e]] ( (k[eplus[e]]^2 + k[e]^2)
            /(4 lambda^2 k[eplus[e]] k[e]) )  )
    + phi[eplus[e], i]/(4 lambda^2 k[e]^2)
      * (rho0[eplus[e]] + rho1[eplus[e]](k[eplus[e]]^2 + k[e]^2)
            /(2 k[e] k[eplus[e]])
        + rho2[eplus[e]] ((k[eplus[e]]^2 + k[e]^2)
              /(2 k[e] k[eplus[e]]))^2)   )
* (4 lambda^2 k[eplus[e]] k[e]
    - 2 Log[(1+lambda^2 KVplus[eplus[e]]^2)
        /(1+lambda^2 KVminus[eplus[e]]^2)]
    + (4 lambda^2 k[eplus[e]] k[e])
        /((1+lambda^2 KVplus[eplus[e]]^2)
            * (1+lambda^2 KVminus[eplus[e]]^2)) )
+ ((rho2[eplus[e]]/(8 lambda^4 k[e]^2 k[eplus[e]]^2))
    * (phi[e, i] - ((k[eplus[e]]^2 + k[e]^2)/(2 k[e]^2))
        * phi[eplus[e], i])
    -  phi[eplus[e], i]
      * (rho1[eplus[e]] (1/(8 lambda^4 k[eplus[e]] k[e]^3))
        + rho2[eplus[e]] ( (k[eplus[e]]^2 + k[e]^2)
            /(8 lambda^4 k[eplus[e]]^2 k[e]^4)))  )
* (4 lambda^4 k[eplus[e]] k[e] (k[eplus[e]]^2 + k[e]^2)
    - 8 lambda^2 k[e] k[eplus[e]]
    + 3 Log[(1+lambda^2 KVplus[eplus[e]]^2)
      /(1+lambda^2 KVminus[eplus[e]]^2)]
    - (4 lambda^2 k[eplus[e]] k[e])
        /((1+lambda^2 KVplus[eplus[e]]^2)
          * (1+lambda^2 KVminus[eplus[e]]^2)) )
+ (phi[eplus[e], i] rho2[eplus[e]]
/(16 lambda^6 k[e]^4 k[eplus[e]]^2))
* (3 lambda^2 (KVplus[eplus[e]]^2 - KVminus[eplus[e]]^2)
    - lambda^4 (KVplus[eplus[e]]^4 - KVminus[eplus[e]]^4)
```

```
    + (1/3) lambda^6 (KVplus[eplus[e]]^6 - KVminus[eplus[e]]^6)
    -4 Log[(1+lambda^2 KVplus[eplus[e]]^2)
       /(1+lambda^2 KVminus[eplus[e]]^2)]
    + (4 lambda^2 k[eplus[e]] k[e])
      /((1+lambda^2 KVplus[eplus[e]]^2)
        * (1+lambda^2 KVminus[eplus[e]]^2)) ) )
Vminus[e_, i_] := (
0.5 (phi[e, i] - ((k[eminus[e]]^2 + k[e]^2)/(2 k[e]^2))
             * phi[eminus[e], i])
    * ( rho0[eminus[e]]
      + rho1[eminus[e]](k[eminus[e]]^2 + k[e]^2)
        /(2 k[e] k[eminus[e]])
      + rho2[eminus[e]] ((k[eminus[e]]^2 + k[e]^2)
        /(2 k[e] k[eminus[e]]))^2)
    * (Log[(1+lambda^2 KVplus[eminus[e]]^2)
        /(1+lambda^2 KVminus[eminus[e]]^2)]
      - (4 lambda^2 k[eminus[e]] k[e])
        /((1+lambda^2 KVplus[eminus[e]]^2)
          *(1+lambda^2 KVminus[eminus[e]]^2)))
+ ( -(phi[e, i] - ((k[eminus[e]]^2 + k[e]^2)/(2 k[e]^2))
        * phi[eminus[e], i])
    * ( rho1[eminus[e]] (1/(4 lambda^2 k[eminus[e]] k[e]))
      + rho2[eminus[e]] ( (k[eminus[e]]^2 + k[e]^2)
            /(4 lambda^2 k[eminus[e]] k[e]) )  )
    + phi[eminus[e], i]/(4 lambda^2 k[e]^2)
      * (rho0[eminus[e]] + rho1[eminus[e]](k[eminus[e]]^2 + k[e]^2)
            /(2 k[e] k[eminus[e]])
        + rho2[eminus[e]] ((k[eminus[e]]^2 + k[e]^2)
                /(2 k[e] k[eminus[e]]))^2)   )
* (4 lambda^2 k[eminus[e]] k[e]
    - 2 Log[(1+lambda^2 KVplus[eminus[e]]^2)
        /(1+lambda^2 KVminus[eminus[e]]^2)]
    + (4 lambda^2 k[eminus[e]] k[e])
        /((1+lambda^2 KVplus[eminus[e]]^2)
```

```
            * (1+lambda^2 KVminus[eminus[e]]^2)) )
+ ((rho2[eminus[e]]/(8 lambda^4 k[e]^2 k[eminus[e]]^2))
    * (phi[e, i] - ((k[eminus[e]]^2 + k[e]^2)/(2 k[e]^2))
        * phi[eminus[e], i])
    -  phi[eminus[e], i]
      * (rho1[eminus[e]] (1/(8 lambda^4 k[eminus[e]] k[e]^3))
        + rho2[eminus[e]] ( (k[eminus[e]]^2 + k[e]^2)
            /(8 lambda^4 k[eminus[e]]^2 k[e]^4)))  )
* (4 lambda^4 k[eminus[e]] k[e] (k[eminus[e]]^2 + k[e]^2)
    - 8 lambda^2 k[e] k[eminus[e]]
    + 3 Log[(1+lambda^2 KVplus[eminus[e]]^2)
      /(1+lambda^2 KVminus[eminus[e]]^2)]
    - (4 lambda^2 k[eminus[e]] k[e])
        /((1+lambda^2 KVplus[eminus[e]]^2)
          * (1+lambda^2 KVminus[eminus[e]]^2)) )
+ (phi[eminus[e], i] rho2[eminus[e]]
/(16 lambda^6 k[e]^4 k[eminus[e]]^2))
* (3 lambda^2 (KVplus[eminus[e]]^2 - KVminus[eminus[e]]^2)
    - lambda^4 (KVplus[eminus[e]]^4 - KVminus[eminus[e]]^4)
    + (1/3) lambda^6 (KVplus[eminus[e]]^6 - KVminus[eminus[e]]^6)
    -4 Log[(1+lambda^2 KVplus[eminus[e]]^2)
       /(1+lambda^2 KVminus[eminus[e]]^2)]
    + (4 lambda^2 k[eminus[e]] k[e])
      /((1+lambda^2 KVplus[eminus[e]]^2)
        * (1+lambda^2 KVminus[eminus[e]]^2)) ) )
NVplus[e_, i_] = Vplus[e, i];
NVminus[e_, i_] = Vminus[e, i];
TauPO[e_, i_] := ( (q^2 kappaL omegaTO^2
    /(hbar^2 kappainf^2 omegaLO f[e] k[e]))
    (Nmeff[eplus[e]] Nf[eplus[e]] NVplus[e, i] (Nq+ 1) +
    Nmeff[eminus[e]] Nf[eminus[e]] NVminus[e, i] Nq hminus))
Plot[q^2 kappaL omegaTO^2/(hbar^2 kappainf^2 omegaLO Nf[e eV]
        Nk[e eV]), {e, 0, .1}]
NTauPO[e_, i_] = TauPO[e, i];
```

```
Plot[NTauPO[e eV, 1], {e, 0, .1}]
Plot[NVplus[e eV, 1], {e, 0, .1}]
Plot[NVminus[e eV, 1], {e, 0, .1}]
L[e_, i_] := (meff[e]/q) TauPO[e, i]
     + phi[e, i] meff[e]/(q tauCC[e])
NL[e_, i_] = L[e, i];
Plot[NL[e eV, 1], {e, 0, .1}]
Plot[TauPO[e eV, 1], {e, 0, .1}]
(* hbar omegaLO = 3.9 10^-14 erg = .024 eV *)
d[i_, j_] := NIntegrate[ -Ndfe[e eV] 10^-11 Nphi[e eV, i]
         NL[e eV, j] 10^-2
         Nk[e eV]^3 10^-18, {e, 0, 0.1}] 10^31 eV
d[1,1]
a0[i_] := NIntegrate[ -Ndfe[e eV] 10^-11 Nphi[e eV, i]
     Nk[e eV]^3  10^-18, {e, 0, 0.1}] 10^29 eV
a0[1]
(* INDICES DO NOT AGREE WITH S&D: 0,0 -> 3,3 vs.  1,1 -> 4,4 *)
dmatrix = Table[d[i, j], {i,4}, {j,4}]
da0a0 = Det[{{0,   a0[1],   a0[2],    a0[3],  a0[4]},
      {a0[1],  d[[1,1]],  d[[1,2]],   d[[1,3]],  d[[1,4]]},
      {a0[2],  d[[2,1]],  d[[2,2]],   d[[2,3]],  d[[2,4]]},
      {a0[3],  d[[3,1]],  d[[3,2]],   d[[3,3]],  d[[3,4]]},
      {a0[2],  d[[4,1]],  d[[4,2]],   d[[4,3]],  d[[4,4]]}}]
dd = Det[d]
sigma = N[(q/3) Pi^2 (da0a0/dd)]  (*cgs!*)
mu = sigma/(n q)  (*cgs*)
% 10^7 1.6 10^-19/(4.8 10^-10)
Det[d]
```

Bibliography

AMBEGAOKAR V, HALPERIN B I & LANGER J S (1971), *Phys. Rev. B*, **4** (8), 2612.

ANDERSON P W (1958), *Phys. Rev.*, **109** (5), 1492.

ARMISTEAD C J (1986), doctoral thesis, St. Andrews University.

ARMISTEAD C J, DAVIDSON A M, KNOWLES P, NAJDA S P, STRADLING R A, NICHOLAS R J & SESSIONS S J (1982), *Lecture Notes in Physics 177 (Proc. of the Int'l. Conf. on the Applications of High Magnetic fields to Semiconductors, Grenoble, 1982)*, Springer-Verlag, 289.

ARNOLD D, KLEM J, HENDERSON T, MORKOC H & ERICKSON L P (1984), *Appl. Phys. Lett.*, **45**, 764 and references therein.

BAGGULEY D M S, STRADLING R A & ROBINSON M L A (1963), *Phys. Lett.*, **6**, 143.

BAJ M, DMOWSKI L, KOŃCZYKOWSKI M & POROWSKI S (1976), *Phys. Stat. Sol. (a)*, **33**, 421.

BARANOVSKIĬ S D, ÉFROS A L, GEL'MONT B L & SHKLOVSKIĬ B I (1979), *J. Phys. C: Solid State Phys.*, **12**, 1023.

BARANOVSKIĬ S D, SHKLOVSKIĬ B I & ÉFROS A L (1980), *Sov. Phys. JETP*, **51** (1), 199.

BARRIE R (1956), *Proc. Phys. Soc., London*, (B) **69**, 553.

BATE R T, BAXTER R D, REID F J & BEER A C (1965), *J. Phys. Chem. Solids*, **26**, 1205.

BLEANEY B I & BLEANEY B (1976), *Electricity and Magnetism*, 3rd edn., Oxford University Press.

BOURGOIN J C, FENG S L & VON BARDELEBEN H J (1989), *Phys. Rev. B*, **40** (11), 7663.

BOWERS R & YAFET Y (1959), *Phys. Rev.*, **115** (5), 1165.

BOYLE W S & BRAILSFORD A D (1957), *Phys. Rev.*, **107**, 903.

BRUNEL L-C, HUANT S, BAJ M & TRZECIAKOWSKI W (1986), *Phys. Rev. B*, **33** (10), 6863.

CARTER A C, CARVER G P, NICHOLAS R J, PORTAL J C & STRADLING R A (1977), *Solid State Comm.*, **24**, 55.

CHADI D J & CHANG K J (1988), *Phys. Rev. Lett.*, **61** (7), 873.

CHADI D J, CHANG K J & WALUKIEWICZ W (1989), *Phys. Rev. Lett.*, **62** (16), 1923.

CHEN Y, GIL B & MATHIEU H (1986), *Solid State Comm.*, **59** (11), 777.

COHEN M H, FRITZSCHE H & OVSHINSKY S R (1969), *Phys. Rev. Lett.*, **22** (20), 1065.

COWAN D (1985), doctoral thesis, St. Andrews University.

CUEVAS M (1967), *Phys. Rev.*, **164** (3), 1021.

DAVYDOV B I & SHMUSHKEVICH I M (1940), *Zh. éksp. teor. Fiz.*, **10**, 1043.

DMOCHOWSKI J E, LANGER J M & JANTSCH W (1988), IOP Conf. Ser., (invited).

DMOCHOWSKI J E, STRADLING R A, WANG P D, HOMES S N, LI M, MCCOMBE B D & WEINSTEIN B (1991), *Semicond. Sci. Technol.*, **6**, 476.

DMOCHOWSKI J E, WANG P D & STRADLING R A (1991), *Semicond. Sci. Technol.*, **6**, 118.

DMOCHOWSKI J E, WASILEWSKI Z & STRADLING R A (1990), *Materials Science Forum*, **65 – 66**, 449.

DMOWSKI L, BAJ M, IOANNIDES P & PIOTRZKOWSKI R (1982), *Phys. Rev. B*, **26** (8), 4495.

DMOWSKI L, KOŃCZYKOWSKI M, PIOTRZKOWSKI R & POROWSKI S (1976), *Phys. Stat. Sol. (b)*, **73**, K131.

DOBACZEWSKI L, DMOCHOWSKI J E, LANGER J M (1988), *8th Int'l. School on Defects, Szczyrk, Poland,* (Singapore: World Scientific).

EHRENREICH H (1957), *J. Phys. Chem. Solids*, **2**, 131.

EHRENREICH H (1959), *J. Phys. Chem. Solids*, **9**, 129.

ÉFROS A L (1976), *J. Phys. C: Solid State Phys.*, **9**, 2021.

ÉFROS A L & SHKLOVSKIĬ B I (1975), *J. Phys. C: Solid State Phys.*, **8**, L49.

ERGINSOY C (1950), *Phys. Rev.*, **79**, 1913.

FALICOV L M & CUEVAS M (1967), *Phys. Rev.*, **164** (3), 1025.

FUJITA S & LODDER A (1976), *Physica*, **83B**, 117.

FUKAI F, KAWAMURA H, SEKIDO K & IMIA I (1964), *J. Phys. Soc. Jap.*, **19** (1), 30.

GEL'MONT B L & ÉFROS A (1977), *JETP Lett.*, **25** (2), 67.

GOLKA J, TRYLSKI J, SKOLNICK M S, STRADLING R A & COUDER Y (1977), *Solid State Comm.*, **22**, 623.

GORCZYCA I (1982), *Phys. Stat. Sol. (b)*, **112**, 97.

GORNIK E, CHANG T Y, BRIDGES T J, NGUYEN V T, MCGEE J D & MÜLLER W (1978), *Phys. Rev. Lett.*, **40** (17), 1151.

HADNI A (1967), *Essentials of Modern Physics Applied to the Study of the Infrared*, Pergammon Press.

HASEGAWA H & HOWARD R E (1961), *J. Phys. Chem. Solids*, **21** (3/4), 179.

HINDLEY N K (1964), *Phys. Stat. Sol.*, **7**, 67.

HILSUM C & ROSE-INNES A C (1961), *Semiconducting III-V Compounds*, Pergamon Press.

HJALMARSON H P & DRUMMOND T J (1986), *Appl. Phys. Lett.*, **48**, 656.

HUANT S, DMOWSKI L, BAJ M & BRUNEL L-C (1984), *Phys. Stat. Sol. (b)*, **125**, 215.

JACKSON J D (1975), *Classical Electrodynamics*, 2nd edn., Wiley & Sons, Inc.

JOHNSON E J (1967), *Phys. Rev. Lett.*, **19**, 352.

KAHLERT H & BAUER G (1973), *Phys. Rev. B*, **7**, 2670.

KANE E O (1957), *J. Phys. Chem. Solids*, **1**, 249.

KAPLAN R (1966), *J. Phys. Soc. Jap. Suppl.*, **21**, 249, in: *Proc. of the XVth Int'l. Conf. on Phys. of Semiconductors (Kyoto).*

KAPLAN R (1969), *Phys. Rev.*, **181** (3), 1154.

KAPLAN R, KINCH M A & SCOTT W C (1969), *Solid State Comm.*, **7**, 883.

KAPLAN R, MCCOMBE B D & WAGNER R J (1973), *Solid State Comm.*, **12**, 967.

KAWABATA A (1967), *J. Phys. Soc. Jap.*, **23**, 999.

KAWAMURA H, SAJI H, FUKAI F, SEKIDO K & IMIA I (1964), *J. Phys. Soc. Jap.*, **19** (3), 288.

KEYES R W & SLADEK R J (1956), *J. Phys. Chem. Solids*, **1**, 143.

KINCH M A & ROLLIN B V (1963), *Br. J. Appl. Phys.*, **14**, 672.

KIREEV P S (1978), *Semiconductor Physics*, 2nd edn., Mir Publishers, Moscow.

KOBORI H, OHYAMA T & OTSUKA E (1990), **(I)**, *J. Phys. Soc. Jap.*, **59** (6), 2141.

KOBORI H, OHYAMA T & OTSUKA E (1990), **(II)**, *J. Phys. Soc. Jap.*, **59** (6), 2164.

KOGAN SH M, NGUEN V L & SHKLOVSKIĬ B I (1980), *Sov. Phys. JETP*, **51** (5), 971.

KOHN W (1957), *Advances in Solid State Physics*, **5**, 257.

KOŃCZEWICZ L, LITWIN-STASZEWSKA E & POROWSKI S (1977), *Proc. of the IIIrd Int'l. Conf. on the Physics of Narrow-Gap Semiconductors (Warsaw)*, PWN Warszawa, 1978.

KOŃCZEWICZ L & TRZECIAKOWSKI W (1983), *Phys. Stat. Sol. (b)*, **115** (2), 359.

KOŃCZYKOWSKI M, POROWSKI S & CHROBOCZEK J (1972), *Proc. of the XIth Int'l. Conf. on the Physics of Semiconductors*, **2**, 1050.

KOSSUT J, WILAMOWSKI Z, DIETL T & ŚWIATEK (1990), *Proc. of the XXth Int'l. Conf. on the Physics of Semiconductors (Thessaloniki)*, 613.

KRUSE P W, MCGLAUCHLIN L D & MCQUISTAN R B (1962), *Elements of Infrared Technology: generation, transmission, and detection*, Wiley & Sons, Inc.

KUBO R (1957), *J. Phys. Soc. Jap.*, **12**, 570.

KUCHAR F, KAPLAN R, WAGNER R J, COOKE R A, STRADLING R A & VOGL P (1984), *J. Phys. C: Solid State Phys.*, **17**, 6403.

KUCHAR F, MEISELS R, STRADLING R A & NAJDA S P (1984), *Solid State Comm.*, **52**, 5.

LANDAU L D & LIFSHITZ E M (1960), *Electrodynamics of Continuous Media*, Pergammon Press.

LANDOLT-BÖRNSTEIN (1987), *Numerical Data and Functional Relationships in Science and Technology, New Series III/22a*, (Madelung O, ed.), Springer-Verlag.

LANG D V & LOGAN R A (1977), *Phys. Rev. Lett.*, **39**, 635.

LANG D V & LOGAN R A (1979), *Phys. Rev. B*, **19**, 1015.

LANG I G (1961), *Fiz. Tverd. Tela*, **3**, 2573.

LARSEN D M (1968), *J. Phys. Chem. Solids*, **29**, 271.

LARSEN D M (1973), *Phys. Rev. B*, **8** (2), 535.

LARSEN D M (1975), *Phys. Rev. B*, **11** (10), 3904.

LARSEN D M (1979), *Phys. Rev. B*, **20** (12), 5217.

LITTLER C L & SEILER D G (1985), *Appl. Phys. Lett.*, **46**, 986.

LITWIN-STASZEWSKA E, POROWSKI S, FILIPCHENKO A S (1971), *Phys. Stat. Sol. (b)*, **48**, 525.

LITWIN-STASZEWSKA E, SZYMAŃSKA W, PIOTRZKOWSKI R (1981), *Phys. Stat. Sol. (b)*, **106**, 551.

LONG D (1977), *Optical and Infrared Detectors*, (Keyes R J, ed.), Springer-Verlag, p.101.

LORRAIN P & CORSON D (1970), *Electromagnetic Fields and Waves*, 2nd edn., W H Freeman & Co.

MADELUNG O (1964), *Physics of III-V Compounds*, Wiley & Sons, Inc. and references therein.

MAKADO P C & MCGILL N C (1986), *J. Phys. C: Solid State Phys.*, **19**, 873.

MATSUDA O & OTSUKA E (1979), *J. Phys. Chem. Solids*, **40**, 809.

MAUDE D K, PORTAL J C, DMOWSKI L, FOSTER T, EAVES L, NATHAN M, HEIBLUM M, HARRIS J J & BEALL R B (1987), *Phys. Rev. Lett.*, **59** (7), 815.

MAUDE D K, EAVES L, FOSTER T J & PORTAL J C (1989), *Phys. Rev. Lett.*, **62** (16), 1922.

MCCLINTOCK P V E, MEREDITH D J & WIGMORE J K (1984), *Matter at Low Temperatures*, Blackie & Son, Ltd.

MCCOMBE B D, KAPLAN R, WAGNER R J, GORNIK E & MÜLLER W (1976), *Phys. Rev. B*, **13** (6), 2536.

MEYER H J G (1962), *Phys. Lett.*, **2** (5), 259.

MIZUTA M, TACHIKAWA M, KUKIMOTO H & MINOMURA S (1985), *Jap. J. Appl. Phys.*, **24**, L143.

MOONEY P M (1990), *J. Appl. Phys.*, **67** (3), R1.

MOONEY P M (1991), *Semicond. Sci. Technol.*, **6**, B1, in: *DX-Centers and other Metastable Defects in Semiconductors: Proc. of the Int'l Symposium*, Adam Hilger.

MORGAN T N (1986), *Phys. Rev. B*, **34** (4), 2664.

MOTT N F (1967), *Advan. Phys.*, **16**, 49.

NICHOLAS R J & SARKAR C K (1982), *Solid State Comm.*, **41** (12), 943.

NISHINCHI K N, MIMURA T, KURODA S, HIYAMIZU S, NISHI H & ABE M (1983), *IEEE Trans. ED-30*, 1569.

O'REILLY E P (1989), *Appl. Phys. Lett.*, **55** (14), 1409.

PALIK E D, PICUS G S, TEITLER S & WALLIS R F (1961), *Phys. Rev.*, **122** (2), 475.

PASTOR K (1988), *Acta Phys. Polonica*, **A73** (3), 361.

PASTOR K & SADOWSKI M L (1988), *Phys. Lett. A*, **133** (9), 506.

PASTOR K (1988), *Phys. Rev. B*, **37** (15), 8895.

PAUL W (1968), *Proc. of the IXth Int'l. Conf. on the Physics of Semiconductors (Moscow)*, 16.

PIDGEON C R, MITCHELL D L & BROWN R N (1967), *Phys. Rev.*, **154**, 737.

PIDGEON C R & BROWN R N (1966), *Phys. Rev.*, **146**, 575.

PIDGEON C R & GROVES S H (1969), *Phys. Rev.*, **186**, 824.

PIOTRZKOWSKI R (1984), *Phys. Stat. Sol. (b)*, **124**, 411.

PIOTRZKOWSKI R, LITWIN-STASZEWSKA E & SUSKI T (1986), *Acta Phys. Polonica*, **A69**, 907.

POROWSKI S, KOŃCZEWICZ L, KOŃCZYKOWSKI M, AULOMBARD R & ROBERT, J L (1980), *Proc. of the XVth Int'l. Conf. on Phys. of Semiconductors (Kyoto)*, 271.

POROWSKI S, KOŃCZEWICZ L, KOWALSKI J, AULOMBARD R L & ROBERT J L (1981), *Phys. Stat. Sol. (b)*, **104**, 657.

POROWSKI S, KOŃCZYKOWSKI M & CHROBOCZEK J (1974), *Phys. Stat. Sol. (b)*, **63**, 291.

POROWSKI S, SMITH J E, MCGRODDY J C, NATHAN M I & PAUL W (1969), *Les Proprietés des Solides sous Pression (Editions CNRS No. 188)*, p.217.

POROWSKI S & SADOWSKI M L, to be published.

POROWSKI S & SOSNOWSKI L (1976), *High Temperature—High Phys. Rev. VICHP*, p.716.

POROWSKI S & TRZECIAKOWSKI W (1983), *Helv. Phys. Acta*, **56**, 331.

PRASAD M (1982), *Phys. Stat. Sol. (b)*, **109**, 11.

PUTTLEY E H (1965), *Appl. Optics*, **4** (1), 649.

PUTLEY E H (1977), *Semiconductors and Semimetals, Vol. 12*, (Willardson R K & Beer A C, Eds.), Academic Press, p.143.

RAVITCH J (1965), *Fiz. Tverd. Tela*, **7**, 1821.

RIDLEY B K (1988), *Quantum Processes in Semiconductors*, 2nd edn., Oxford University Press.

ROBERT J L (1979), *The Shubnikov-de Haas Effect and the Magnetic Freeze-out* in *Narrow-Gap Semiconductor Physics and Applications (Nîmes)*, (Zawadzki W, Ed.).

ROBINSON L C (1973), *Methods of Experimental Physics: Physical Principles of Far-Infrared Radiation*, Academic Press.

SADOWSKI M L & PASTOR K (1989), *Acta Phys. Polonica*, **A75** (2), 203.

SAXENA A K (1981), *Phys. Stat. Sol. (b)*, **105**, 777.

SEEGER K (1982), *Semiconductor Physics*, 2nd edn., Springer-Verlag.

SHIN E E H, ARGYRES P N & LAX B (1972), *Phys. Rev. Lett.*, **28**, 1634.

SHOCKLEY W (1950), *Phys. Rev.*, **79**, 191.

SMITH R A, JONES F E & CHASMAR R P (1968), *The Detection and Measurement of Infra-red Radiation*, Oxford University Press.

SRINIVAS T K, CHAUDHURY S & FUJITA S (1983), *J. Phys. Chem. Solids*, **9**, 417.

SRINIVAS T K, CHAUDHURY S & FUJITA S (1983), *J. Phys. Chem. Solids*, **9**, 931.

STILLMAN G, LARSEN D M & WOLFE C M (1971), *Phys. Rev. Lett.*, **27**, 989.

STILLMAN G E, LOW T S & LEE B (1985), *Solid State Comm.*, **53**, 1041.

STILLMAN G E, WOLFE C M & DIMMOCK J O (1977), *Semiconductors and Semimetals, Vol. 12*, (Willardson R K & Beer A C, Eds.), Academic Press, p.169.

STONEHAM A M (1975), *Theory of Defects in Solids*, Clarendon Press, Oxford.

STORMER H L, GOSSARD A C, WIEGMANN W & BALDWIN K (1981), *Appl. Phys. Lett.*, **39**, 912.

STRADLING R A (1980), *Proc. of the NATO Advanced Study Institute on Theoretical Aspects and New Developments in Magneto-Optics (Antwerp)*, Plenum Press, p.449.

STRADLING R A (1985), *Festkörperprobleme*, **XXV**, 591.

STRADLING R A[a], personal communication.

STRADLING R A[b], to be published.

STRADLING R A & WOOD R A (1968), *J. Phys. C (Proc. Phys. Soc.)*, **1**, 1711.

SUMMERS C J, ET AL. (1968), *Phys. Rev.*, **170**, 755.

SZYMAŃSKA W, BOGUSŁAWSKI P & ZAWADZKI W (1974), *Phys. Stat. Sol. (b)*, **65**, 641.

SZYMAŃSKA W & DIETL % (1978), *J. Phys. Chem. Solids*, **39**, 1025.

TACHIKAWA M, FUJISAWA T, KUKIMOTO H, SHIBATA A, OOMI G & MINOMURA S (1985), *Jap. J. Appl. Phys.*, **24**, L893.

THEIS T N & MOONEY P M (1990), *Mat. Res. Soc. Symp. Proc.*, **163**, 729.

TOYOZAWA Y (1978), *Solid State Electron.*, **21**, 1313.

TRZECIAKOWSKI W, BAJ M, HUANT S & BRUNEL L-C (1986), *Phys. Rev. B*, **33** (10), 6846.

TRZECIAKOWSKI W & KRUPSKI J (1982), *Solid State Comm.*, **44** (11), 1491.

VAN VLIET K M (1958), *Proc. Inst. Radio Engrs.*, **46**, 1004.

VAN VLIET K M (1967), *Appl. Optics*, **6** (7), 1145.

VREHEN Q H F (1968), *J. Phys. Chem. Solids*, **29**, 129.

WALLIS R F (1958), *J. Phys. Chem. Solids*, **4**, 101.

WALLIS R F & BOWLDEN H J (1958), *J. Phys. Chem. Solids*, **7**, 78.

WASILEWSKI Z, personal communication.

WASILEWSKI Z (1985) doctoral thesis, Polish Academy of Science.

WASILEWSKI Z, DAVIDSON A M, STRADLING R A & POROWSKI S (1982), *Lecture Notes in Physics 177 (Proc. of the Int'l. Conf. on the Applications of High Magnetic fields to Semiconductors, Grenoble, 1982)*, Springer-Verlag, 233.

WASILEWSKI Z & STRADLING R A (1986), *Semicond. Sci. Technol.*, **1**, 264.

WASILEWSKI Z, STRADLING R A & POROWSKI S (1986), *Solid State Comm.*, **57** (2), 123.

WHITE G K (1979), *Experimental Techniques in Low-Temperature Physics*, Clarendon Press, Oxford.

WINTGEN D & FRIEDRICH H (1986), *J. Phys. B: At. Mol. Phys.*, **19**, 991.

YAFET Y, KEYES R W & ADAMS E N (1956), *J. Phys. Chem. Solids*, **1**, 137.

YAMAGUCHI E, SHIRAISHI K & OHNO T (1990), *Proc. of the XX$^{\underline{th}}$ Int'l. Conf. on the Physics of Semiconductors (Thessaloniki)*, 501.

ZAWADZKI W (1974), *Advances in Physics*, **23**, 435.

ZAWADZKI W & SZYMAŃSKA W (1971), *J. Phys. Chem. Solids*, **32**, 1151.

ZAWADZKI W & SZYMAŃSKA W (1971), *Phys. Stat. Sol. (b)*, **45**, 415.

ZAWADZKI W & WŁASAK J (1984), *J. Phys. C: Solid State Phys.*, **17**, 2505.

ZIMAN J M (1967), *Electrons and Phonons*, Clarendon Press, Oxford.

ZIMAN J M (1968), *J. Phys. C: Solid State Phys.*, **1**, 1532.

ZIMAN J M (1969), *J. Phys. C: Solid State Phys.*, **2**, 1230.